



Universidade do Minho
Escola de Engenharia

Manuel Andrés Hormazábal Fuentes

Time-Dependent Dynamic Identification: A new Approach for Structural Health Monitoring Through Vibration Measurements

outubro de 2024

Time-Dependent Dynamic Identification: A new Approach for Structural Health Monitoring Through Vibration Measurements

Manuel F. Hormazábal

UMinho | 2024



Institute for
Sustainability and
Innovation in Structural
Engineering



Agencia
Nacional de
Investigación
y Desarrollo

Ministerio de Ciencia,
Tecnología, Conocimiento
e Innovación

Gobierno de Chile



Universidade do Minho
Escola de Engenharia

Manuel Andrés Hormazábal Fuentes

Time-Dependent Dynamic Identification: A new Approach for Structural Health Monitoring Through Vibration Measurements

Tese de Doutoramento
Programa Doutoral em Engenharia Civil
Área de especialização: Estruturas e Engenharia Sísmica

Trabalho efetuado sob a orientação do

Professor Doutor Daniel Vitorino de Castro Oliveira
Professora Doutora Maria Giovanna Masciotta

outubro de 2024

DIREITOS DE AUTOR E CONDIÇÕES DE UTILIZAÇÃO DO TRABALHO POR TERCEIROS

Este é um trabalho académico que pode ser utilizado por terceiros desde que respeitadas as regras e boas práticas internacionalmente aceites, no que concerne aos direitos de autor e direitos conexos.

Assim, o presente trabalho pode ser utilizado nos termos previstos na licença abaixo indicada.

Caso o utilizador necessite de permissão para poder fazer um uso do trabalho em condições não previstas no licenciamento indicado, deverá contactar o autor, através do RepositóriUM da Universidade do Minho.

Licença concedida aos utilizadores deste trabalho



Atribuição-NãoComercial-CompartilhaIgual
CC BY-NC-SA

https://creativecommons.org/licenses/by-nc-sa/4.0/

ACKNOWLEDGEMENTS

The present research was conducted in the Institute for Sustainability and Innovation in Structural Engineering (ISISE), in the Department of Civil Engineering of the University of Minho, campus Azurém, Guimarães, Portugal.

This work was partly funded by the Chilean National Agency for Research and Development (ANID) through the programme Becas Chile, under reference ANID BECAS/DOCTORADO EXTRANJERO 72204431. Additionally, this work was partly financed by FCT / MCTES through national funds (PIDDAC) under the R&D Unit Institute for Sustainability and Innovation in Structural Engineering (ISISE), under reference UIDB/04029/2020 (doi.org/10.54499/UIDB/04029/2020), and under the Associate Laboratory Advanced Production and Intelligent Systems ARISE under reference LA/P/0112/2020.

The research was supervised by Professor Dr Daniel V. Oliveira of the University of Minho and co-supervised by Professor Dr Maria Giovanna Masciotta of the G. d'Annunzio University of Chieti e Pescara. I want to express my sincere gratitude to Professor Oliveira and Professor Masciotta for their supervision, support and tutelage, for introducing me to the Structural Health Monitoring, Structural Engineering, and Seismic Engineering fields, and for their support and supervising this research.

I would like to especially thank Dr Alberto Barontini of the University of Minho, for his encouragement and outstanding guidance in the development of this thesis. His knowledge and help were precious for the current work. Additionally, I want to thank Professor Dr Pedro Rosário from the University of Minho, for encouraging me to pursue further academic degrees and for all the support and help received. Also, I want to thank Professor Dr Francisco Fernández from the University of Cádiz for helping me in the initial development of this idea, and I want to thank Professor Dr Luis Mariscal from the University of Cádiz as well, for making the question that started it all: “Why don't you use wavelets?”.

Finally, my biggest acknowledgements and heartfelt gratitude are to my beloved parents, Manuel and Sonia, for their relentless effort, unwavering love and unconditional support and encouragement, no matter the situation or the distance. Without their guidance, care, and sacrifices, I would not be where I am today. Thank you both for being the light that guides my path.

STATEMENT OF INTEGRITY

I hereby declare having conducted this academic work with integrity. I confirm that I have not used plagiarism or any form of undue use of information or falsification of results along the process leading to its elaboration.

I further declare that I have fully acknowledged the Code of Ethical Conduct of the University of Minho.

IDENTIFICAÇÃO DINÂMICA DEPENDENTE DO TEMPO: UMA NOVA ABORDAGEM PARA MONITORIZAÇÃO DA INTEGRIDADE ESTRUTURAL ATRAVÉS DE MEDIÇÃO DE VIBRAÇÕES

RESUMO

Os algoritmos mais frequentemente usados para a análise de vibrações e a identificação dinâmica na Engenharia Civil não são capazes de capturar variações nas propriedades modais durante uma única aquisição. Além disso, estes métodos não podem realizar identificação dinâmica na presença de não linearidades. Para superar essas limitações, apresenta-se um novo algoritmo não paramétrico para identificação dinâmica dependente do tempo. Este algoritmo, denominado Enhanced Modal Identification for Long-term Integrity Assessment (EMILIA), desenvolve-se em três etapas principais, nomeadamente: decomposição de dados wavelet, análise tempo-frequência através da transformada de Hilbert e inferência Bayesiana. A combinação dessas três etapas garante uma estimativa robusta das propriedades modais dinâmicas instantâneas dependentes do tempo (ex: frequências e modos naturais) dentro de uma única aquisição, bem como um conjunto geral estático de frequências naturais para cada aquisição, independentemente da estacionariedade dos registos e do nível de contaminação sonora.

O algoritmo e as suas principais componentes são descritos, testados e validados através de três casos de estudo: (i) uma ponte 2D simulada sem dano e com danos artificiais gerados através da redução local de rigidez; (ii) uma torre de alvenaria simulada em 3D sujeita a fortes excitações sísmicas; (iii) uma estrutura metálica real monitorizada sob diversas condições de rigidez num ambiente controlado de laboratório. As análises efetuadas revelam o sucesso do algoritmo EMILIA quando comparado com métodos tradicionais e bem estabelecidos para resolver problemas de identificação dinâmica linear e invariante no tempo. As análises demonstraram que o algoritmo EMILIA é adequado para processar as respostas estruturais não lineares altamente transitórias e contaminadas por ruído, superando as limitações de muitos desses métodos tradicionais. Por último, as análises apresentaram resultados promissores ao integrar o algoritmo EMILIA numa estratégia de identificação de dano baseada em vibrações, capaz de detetar prontamente variações repentinas nas propriedades modais.

Palavras Chave: Análise Modal Operacional; Dependente do Tempo; Engenharia Estrutural; Engenharia Sísmica; Identificação Dinâmica; Monitorização da Integridade Estrutural.

TIME-DEPENDENT DYNAMIC IDENTIFICATION: A NEW APPROACH FOR STRUCTURAL HEALTH MONITORING THROUGH VIBRATION MEASUREMENTS

ABSTRACT

Most commonly used algorithms for vibration analysis and dynamic identification for civil engineering purposes are not able to capture variations in the modal properties during a single acquisition. Furthermore, these methods cannot perform dynamic identification in the presence of non-linearities. To overcome these limitations, a novel nonparametric algorithm for time-dependent dynamic identification is hereby presented. This algorithm, called Enhanced Modal Identification for Long-term Integrity Assessment (EMILIA), relies on three main stages, namely a wavelet data decomposition, a time-frequency analysis through Hilbert transform and Bayesian inference. The combination of these three stages ensures a robust estimation of both dynamic time-dependent instantaneous modal properties (i.e. natural frequencies and mode shapes) within a single acquisition as well as a static overall set of natural frequencies for each acquisition, irrespective of the stationarity of the records and the level of noise contamination.

The algorithm and its main components are described, tested, and validated through the use of three case studies: (I) a simulated 2D bridge structure in sound and artificial damaged conditions generated by locally reducing its stiffness; (II) a simulated 3D masonry tower subject to strong seismic excitations; (III) a real shear-type metal structure monitored under varying stiffness conditions in a controlled laboratory environment. The conducted analyses successfully compared the EMILIA algorithm against traditional, well-established methods for solving linear and time-invariant dynamic identification problems. They demonstrated the algorithm's suitability for processing high-transient, noise-contaminated non-linear structural responses, surpassing the limitations of many of those methods. Finally, they showcased promising results by integrating EMILIA into a vibration-based damage identification strategy, capable of promptly detecting sudden variations in the modal properties.

Keywords: Operational Modal Analysis; Time-Dependent; Structural Engineering; Seismic Engineering; Dynamic Identification; Structural Health Monitoring.

IDENTIFICACIÓN DINÁMICA DEPENDIENTE DEL TIEMPO: UNA NUEVA PROPUESTA PARA MONITOREO DE LA SALUD ESTRUCTURAL A TRAVÉS DE MEDICIONES DE VIBRACIONES

RESUMEN

Los algoritmos más comúnmente utilizados para el análisis de vibraciones e identificación dinámica para aplicaciones en ingeniería civil no logran capturar variaciones en los parámetros modales durante un único registro de datos. Adicionalmente, estos métodos no son capaces de realizar identificación dinámica en presencia de datos no lineales. Para superar estas limitaciones, un nuevo algoritmo no paramétrico para la identificación dinámica dependiente del tiempo es aquí presentado. Este algoritmo, nombrado Enhanced Modal Identification for Long-term Integrity Assessment (EMILIA), está basado en tres etapas principales: descomposición de datos por wavelet, análisis en tiempo y frecuencia mediante la transformada de Hilbert e inferencia Bayesiana. La combinación de estas tres etapas garantiza una sólida estimación dinámica dentro de una sola medición de datos de no sólo los parámetros modales instantáneos y dependientes del tiempo (frecuencias y modos de vibración), sino que también de frecuencias modales estáticas, sin importar la estacionariedad de los registros y el nivel de contaminación de ruido presente en los datos.

El algoritmo y sus principales componentes se describen, prueban y validan mediante el análisis de tres casos de estudio: (I) una estructura 2D tipo puente simulada en escenarios sin daño estructural, y con daño generado al reducir localmente su rigidez; (II) una torre de mampostería simulada en 3D y sujeta a excitaciones sísmicas; (III) una estructura metálica real monitoreada en diferentes condiciones de rigidez en un entorno de laboratorio controlado. Los análisis realizados compararon con éxito el algoritmo EMILIA con métodos tradicionales bien establecidos, para resolver problemas de identificación dinámica lineal e invariante en el tiempo. Se demuestra la idoneidad del algoritmo para procesar respuestas estructurales no lineales con fuertes transientes y contaminadas con ruido, superando las limitaciones de muchos de los métodos tradicionales. Finalmente, se obtuvieron resultados prometedores al integrar EMILIA en una estrategia para la identificación de daños estructurales basada en registros de vibraciones y capaz de rápidamente detectar súbitas variaciones en las propiedades modales.

Palabras clave: Análisis Modal Operacional; Dependiente del Tiempo; Ingeniería Estructural, Ingeniería Sísmica; Identificación Dinámica; Monitoreo de la Salud Estructural.

To my parents, Manuel and Sonia...

...and in the beloved memory of Emilia.

TABLE OF CONTENTS

ACKNOWLEDGEMENTS III
STATEMENT OF INTEGRITY IV
RESUMO V
ABSTRACT VI
RESUMEN VII
LIST OF ACRONYMS XI
LIST OF FIGURES XIII
LIST OF TABLES XVIII

1 INTRODUCTION 1

1.1 MOTIVATION 2
1.2 RESEARCH OBJECTIVES 4
1.3 THESIS OUTLINE 5

2 STATE OF THE ART 7

2.1 INTRODUCTION 8
2.2 MODAL ALGORITHMS: NOMENCLATURE AND CLASSIFICATIONS 9
2.3 FREQUENCY DOMAIN ANALYSES 12
2.4 TIME-FREQUENCY ANALYSIS TECHNIQUES 16
2.5 DATA DECOMPOSITION ALGORITHMS 24
2.5.1 Parametrical Decompositions 24
2.5.2 Nonparametric Decompositions 27
2.6 DYNAMIC IDENTIFICATION METHODS 28
2.7 VIBRATION-BASED DAMAGE IDENTIFICATION METHODS 33
2.8 CHAPTER CONCLUSIONS AND FINAL REMARKS 39

3 THE EMILIA ALGORITHM 41

3.1 INTRODUCTION 42
3.2 THE EMILIA ALGORITHM 43
3.2.1 Stage 01: Data decomposition 43
3.2.2 Stage 02: Time and frequency domain analysis 52
3.2.3 Stage 03: Probability analysis 58
3.3 DECOMPOSITION ALGORITHMS BENCHMARKING TEST 62
3.4 CHAPTER CONCLUSIONS AND FINAL REMARKS 69

4 TEST AND VALIDATION OF THE EMILIA ALGORITHM 71

4.1 INTRODUCTION 72

4.2 CASE STUDY I: 2D BRIDGE MODEL 73

4.2.1 Model description, eigenvalue analysis and simulated monitoring 73

4.2.2 Operational modal analysis and algorithm validation 77

4.2.3 Time-dependent dynamic identification 86

4.3 ALGORITHM TESTS: PARAMETERS SETTING, ROBUSTNESS AND SENSITIVITY 91

4.3.1 Setting the decomposition level 92

4.3.2 Setting PDF distribution: Kernel vs Gauss and frequency resolution 96

4.4 CHAPTER CONCLUSIONS AND FINAL REMARKS 99

5 NON-LINEAR TIME-DEPENDENT DYNAMIC IDENTIFICATION 101

5.1 INTRODUCTION 102

5.2 CASE STUDY II: FE MODEL OF A MASONRY TOWER 103

5.2.1 Model description, eigenvalue analysis and simulated monitoring 103

5.2.2 Operational modal analysis 110

5.2.3 Time-Dependent Damage Identification 115

5.3 CASE STUDY III: LABORATORY TEST OF A SHEAR-TYPE STEEL STRUCTURE 120

5.4 CHAPTER CONCLUSIONS AND FINAL REMARKS 131

6 CONCLUSIONS 133

6.1 THESIS SUMMARY, MAIN CONCLUSIONS, AND FINAL REMARKS 134

6.1.1 Linear dynamic identification and OMA with reduced amounts of data 135

6.1.2 Non-linear dynamic identification and OMA with strong motion seismic data 137

6.1.3 Time-dependent dynamic identification and damage assessment 138

6.2 FUTURE LINES OF RESEARCH 139

BIBLIOGRAPHIC REFERENCES 141

ANNEXE 155

LIST OF ACRONYMS

SHM	Structural Health Monitoring
SISO	Single Input Single Output
MISO	Multiple Inputs Single Output
MIMO	Multiple Inputs Multiple Outputs
SDOF	Single Degree of Freedom
FRF	Frequency Response Function
EMA	Experimental Modal Analysis
OMA	Operational Modal Analysis
DFT	Discrete Fourier Transform
FFT	Fast Fourier Transform
PSD	Power Spectral Density
CPSD	Cross Power Spectral Density
TFA	Time-Frequency Analysis
STFT	Short Time Fourier Transform
HT	Hilbert transform
AS	Analytic Signal
WT	Wavelet Transform
CWT	Continuous Wavelet Transform
DWT	Discrete Wavelet Transform
SVD	Singular Value Decomposition
HHT	Hilbert-Huang Transform
EMD	Empirical Mode Decomposition
IMF	Intrinsic Mode Function
DWPT	Discrete Wavelet Packet Transform
MODWT	Maximum Overlap Discrete Wavelet Transform
MODWPT	Maximum Overlap Discrete Wavelet Packet Transform
WSST	Wavelet Synchro Squeezed Transform
EWT	Empirical Wavelet Transform
VMD	Variational Mode Decomposition

PP	Peak-Peaking
MDOF	Multi Degree of Freedom
FFD	Frequency Domain Decomposition
EFDD	Enhanced Frequency Domain Decomposition
IRF	Impulse Response Functions
RDT	Random Decrement Technique
ITD	Ibrahim Time-Domain method
ERA	Eigensystem Realization Algorithm
SSI	Stochastic Subspace Identification
CE	Complex Exponential
AR	Auto-Regressive
LSCE	Least Square Complex Exponential
PRCE	Polyreference Complex Exponential
ARMA	Auto-Regressive Moving-Averages
MA	Moving-Averages
HR	High-resolution
BBS	Blind Source Separation
PCA	Principal Component Analysis
ICA	Independent Component Analysis
SOBI	Second-Order Blind Identification
MUSIC	Multiple Signal Classification algorithm
MAC	Modal Assurance Criterion
MSF	Modal Scale Factor
COMAC	Coordinate Modal Assurance Criterion
FE	Finite Element
NSA	Negative Selection Algorithm
EMILIA	Enhanced Modal Identification for Long-term Integrity Assessment
PDF	Probability Density Function
KPDF	Kernel Probability Density functions
BPDF	Bayes Probability Density functions
MEV	Most Expected Value
SNR	Signal-to-Noise Ratio

LIST OF FIGURES

Figure 2.1: Superposition output (bottom) of three standing waves (top). 8
Figure 2.2: Idealised undamped dynamic system and its associated inputs and outputs in the time and frequency domain. 11
Figure 2.3: Comparison between an FFT spectrum (top) and a PSD spectrum (bottom). 15
Figure 2.4: STFT spectrogram computed with a Hanning time window of 500 samples. 17
Figure 2.5: STFT spectrogram computed with a Hanning time window of 25 samples. 17
Figure 2.6: Flat Hilbert spectrogram computed from a single broadband raw acceleration data. 18
Figure 2.7: Hilbert spectrogram computed from decomposed acceleration data. 19
Figure 2.8: CWT scalogram computed using a *Bump* continuous wavelet. 22
Figure 2.9: (a) Continuous Morlet wavelet, (b) discrete Daubechies 4 wavelet, (c) discrete Coiflets 4 wavelet. 23
Figure 3.1: Undamped SDOF model. 42
Figure 3.2: EMILIA algorithm workflow applied to the case study of Figure 3.1 processed with a four-level MODWPT decomposition. For the sake of brevity, only the first, the seventh, and the sixteenth subsequences are presented. 43
Figure 3.3: Example of the convolution process of continuous Wavelet analysis. The plots show Morlet wavelets with different dilatations (red colour), plotted against the normalized SDOF example data (blue colour). The light blue colour highlights the absolute area between the two functions. 44
Figure 3.4: Schematic representation of a three-level DWT decomposition. 46
Figure 3.5: Schematic representation of a three-level MODWPT decomposition. 48
Figure 3.6: A Daubechies 8 scaling function (a) and its corresponding Daubechies 8 mother wavelet function (b), with its corresponding low-pass (c) and high-pass (d) analysis filters (decomposition algorithm), and the pair of low-pass (f) and high-pass (g) synthesis filters (for the reconstruction of the data). 50
Figure 3.7: A Daubechies 20 scaling function (a) and the Daubechies 20 mother wavelet function (b), with its corresponding low-pass (c) and high-pass (d) analysis filters (decomposition algorithm), and the pair of low-pass (f) and high-pass (g) synthesis filters (for the reconstruction of the data). 51

Figure 3.8: EMILIA algorithm first stage workflow: 1st (left), 7th (middle), and 16th (right) subsequences. 52
Figure 3.9: SNR from the example SDOF raw data. The natural frequency of 4 Hz is highlighted in blue against the background noise presented here in orange colour. 53
Figure 3.10: SNR computed from the seventh MODWPT subsequence. The natural frequency of 4 Hz is highlighted in blue against the background noise presented here in orange colour. 53
Figure 3.11: Comparison between different approaches for computing instantaneous frequency. At the top of the image, the original data is in red colour. 56
Figure 3.12: Examples of instantaneous amplitude and frequency data computed from the first, seventh and sixteenth subsequences. 57
Figure 3.13: Time-dependent probability spectrums computed from the first, seventh and last subsequences obtained from the example SDOF data..... 60
Figure 3.14: Complete time-dependent probability spectrum computed by the EMILIA algorithm from the SDOF example data. 61
Figure 3.15: Hilbert spectrogram computed using the HVD decomposition algorithm. 63
Figure 3.16: Hilbert spectrogram computed using the EWT decomposition algorithm. 63
Figure 3.17: Hilbert spectrogram computed using the VMD decomposition algorithm..... 64
Figure 3.18: Hilbert spectrogram computed using the EMD decomposition algorithm. 65
Figure 3.19: Hilbert spectrogram computed using the MODWT decomposition algorithm. 65
Figure 3.20: Hilbert spectrogram computed using the MODWPT decomposition algorithm. 66
Figure 4.1: 2D bridge model schematic view. The damage location is highlighted in orange. 73
Figure 4.2: First ten eigenvectors and eigenvalues computed for the *ST00* stiffness configuration. 74
Figure 4.3: At left, white-noise inputs applied to X and Y axes of node N°15, located in the middle of the main span of the model. At right, the simulated output accelerations computed on the same node for X and Y axes. 76
Figure 4.4: Distribution of the points selected for the application of random excitations (top, yellow dots). Deployment of the nodes selected for measuring the acceleration response (bottom, green dots)..... 76
Figure 4.5: Time-dependent probability spectrum computed from *ST00* stiffness configuration using all available channels, with a Daubechies 45 mother wavelet function and a six-level MODWPT decomposition. 79

Figure 4.6: Time-dependent probability spectrum computed from *ST01* stiffness configuration using all available channels, with a Daubechies 45 mother wavelet function and a six-level MODWPT decomposition. 80

Figure 4.7: Time-dependent probability spectrum computed from *ST02* stiffness configuration using all available channels, with a Daubechies 45 mother wavelet function and a six-level MODWPT decomposition. 80

Figure 4.8: MAC test results for *Mode B* computed by EFDD, SSI and the EMILIA algorithms against the reference eigenvector. 82

Figure 4.9: MAC test results for the fifth mode shape computed by EFDD, SSI and the EMILIA algorithms against the reference eigenvector (SSI information is not presented since this mode was not identified by that estimator). 83

Figure 4.10: *Mode A* and *Mode B* dynamic MAC results of the EMILIA algorithm instantaneous mode shapes of the undamaged bridge against the static shapes from the other methods. 84

Figure 4.11: *Mode C* and *Mode D* dynamic MAC results of the EMILIA algorithm instantaneous mode shapes of the undamaged bridge against the static shapes from the other methods. 85

Figure 4.12: Mode shapes computed by the EMILIA algorithm for the *ST00* configuration and relative instantaneous MAC against the numerical eigenvectors. 86

Figure 4.13: Time-dependent probability spectrum computed across all stiffness configurations. Close-up of *Mode A* dynamic variation of the instantaneous frequency values. 87

Figure 4.14: Evolution of *Mode A* and *Mode B* shapes and instantaneous MAC values with progressive damage. 88

Figure 4.15: Evolution of *Mode C* and *Mode D* shapes and instantaneous MAC values with progressive damage. 89

Figure 4.16: Time-dependent MAC results with progressive damage for the four modes of interest. 90

Figure 4.17: Hilbert spectrogram showing the first mode's instantaneous frequency evolution across the three stiffness configurations (white continuous line shows a moving average of the same data) 91

Figure 4.18: Second and third modal shapes mixed in the results of the four-level decomposition analysis from Table 4.7. 94

Figure 4.19: Time-dependent probability spectrum computed from the bridge in sound condition and resorting to an eight-level MODWPT decomposition. For better visualisation of the computed outputs, the spectrum is here presented until 25 Hz. 95

Figure 4.20: EMILIA algorithm time complexity computed by increasing decomposition levels. 96
Figure 4.21: Time-dependent probability spectrum showing the probability analyses outputs computed by using a Gaussian parametric distribution (blue lines), and by using a Kernel nonparametric distribution (red lines). 98
Figure 4.22: First mode Kernel PDFs and Bayesian PDFs computed using data from the *ST00* stiffness configuration. For the left plot, a resolution of 1024 FFT lines is used; whilst for the right plot, a resolution of 10240 FFT lines is used. 99
Figure 5.1: First six eigenvectors and eigenvalues of the masonry tower. 105
Figure 5.2: PGA map from 2009 L'Aquila 6.3 Mw main shock (Image courtesy of USGS). 106
Figure 5.3: (a) 2009 L'Aquila earthquake accelerogram, (b) pseudo-acceleration response spectrum. 107
Figure 5.4: Computed acceleration outputs on the four base-level nodes. Plot (a) is from the north base node, plot (b) is from the east base node, plot (c) is from the south base node, and plot (d) is from the west base node. 108
Figure 5.5: Computed acceleration outputs on the four top-level nodes. Plot (a) is from the north top node, plot (b) is from the east top node, plot (c) is from the south top node, and plot (d) is from the west top node. 108
Figure 5.6: Principal-strain results computed in the upper side of the FE model's main door. The two blue nodes show the closest output nodes to the location of the induced damage. 109
Figure 5.7: Crack-widths results computed at 35.73 seconds of the NLTH analysis. 110
Figure 5.8: First five eigenvectors and corresponding examples of instantaneous mode shapes computed by the EMILIA algorithm. The blue colour lines highlight the south edge where *Node A* is located. 112
Figure 5.9: Hilbert Spectrogram of the tower X axis responses to the L'Aquila earthquake's data. 113
Figure 5.10: Hilbert Spectrogram of the tower Y axis responses to the L'Aquila earthquake's data. .. 113
Figure 5.11: Displacement mode shapes computed for the 3573 time-step ($Ts = 35.73$ seconds): (a) Mode 2; (b) Mode 3; (c) Mode 4; (d) Mode 5. The blue line shows the displacements of the south edge. The orange line shows the modal curvatures for the same edge. Mode 1 is not considered due to the lower damage presented in Figure 5.12. 114
Figure 5.12: Mode 1 time-dependent MAC results. 115
Figure 5.13: Mode 2 time-dependent MAC results. 116
Figure 5.14: Mode 3 time-dependent MAC results. 116

Figure 5.15: Mode 4 time-dependent MAC results. 117
Figure 5.16: Mode 5 time-dependent MAC results. 117
Figure 5.17: On top: (a) A perspective view, (b) an X-Z plane, (c) and Y-Z plane of a pair of selected fifth mode instantaneous mode shapes computed before the earthquake. On the bottom: (d) A perspective view, (e) an X-Z plane, (f) and Y-Z plane of a pair of selected fifth mode instantaneous mode shapes computed after the earthquake. 118
Figure 5.18: Fifth mode linear-elastic time-dependent MAC (middle) compared with the non-linear time-dependent MAC (bottom). A reference of the output acceleration it can be seen at top. 119
Figure 5.19: (a) Full view of specimen and setup with area of stiffness reduction marked in red, (b) transducer detailed view, (c) external side view of the mode joints showing the removed bolts, (d) internal view of the column joints showing the removed bolts 122
Figure 5.20: Examples from the shear model's instantaneous mode shapes: (a) first mode; (b) second mode. 124
Figure 5.21: Time-dependent probability spectrums computed from the sound condition scenarios.. 125
Figure 5.22: A six-Level Daubechies 45 MODWPT Hilbert spectrogram computed from the shear-structure in sound condition, same record processed in Figure 5.21. 125
Figure 5.23: Bayes f_{MEV} results, standard deviation, and probability density, for all the 32 tests for the structure in sound condition and measured during daytime. 126
Figure 5.24: Bayes f_{MEV} results, standard deviation, and probability density, for all the 32 tests for the structure in sound condition and measured during nighttime. 127
Figure 5.25: Bayes f_{MEV}results, standard deviation, and probability density, for all the 32 tests for the structure in damaged condition and measured during daytime..... 127
Figure 5.26: Bayes f_{MEV} results, standard deviation, and probability density, for all the 32 tests for the structure In damaged condition and measured during nighttime. 128
Figure 5.27: First and second modes f_{MEV} mean, standard deviation and variance for all the eight data sub-sets. 129
Figure 5.28: Time-dependent probability spectrums computed from the records containing the manual damaging procedure: (a) complete spectrum; (b) spectrum zoomed around first mode; (c) spectrum zoomed around second mode. 131
Figure 5.29: Hilbert spectrograms computed from the records containing the manual damaging procedure: (a) complete spectrogram; (b) spectrogram zoomed around first mode; (c) spectrogram zoomed around second mode. 132

LIST OF TABLES

Table 2.1: Commonly used modal estimation methods and their related classifications..... 10
Table 3.1: Instantaneous frequency statistics computed through the methods in Figure 3.11..... 55
Table 3.2: Maximum probability density and variance from the first, seventh, and last subsequences. 59
Table 3.3: Frequency-domain decomposition algorithms instantaneous frequency output statistics..... 67
Table 3.4: Time-domain decomposition algorithms instantaneous frequency output statistics..... 68
Table 3.5: Instantaneous frequency statistics computed resorting to the different decomposition algorithms applied to the time series containing the modal information. 69
Table 4.1: Eigenvalues and effective masses of the first ten numerical modes of the bridge. 75
Table 4.2: Eigenvalues of the bridge for the three stiffness configurations and percentage variation.... 75
Table 4.3: Numerical vs experimental frequencies computed for the *ST00* scenario..... 78
Table 4.4: Numerical vs experimental frequencies computed for the *ST01* scenario..... 78
Table 4.5: Numerical vs experimental frequencies computed for the *ST02* scenario..... 78
Table 4.6: EMILIA f_{MEV} results and percentage difference amid the three stiffness configurations.... 87
Table 4.7: *ST00* four-level Kernel results. 94
Table 4.8: *ST00* two-level Kernel results..... 94
Table 4.9: *ST00* eight-level Kernel results. 95
Table 4.10: *ST00* six-level Kernel results..... 95
Table 4.11: *ST00* six-level Kernel results. 97
Table 4.12: *ST00* six-level Gauss results. 97
Table 5.1: FE material properties adopted for the numerical model. 103
Table 5.2: L'Aquila earthquake overall information. 107
Table 5.3: Identified time steps showing the higher principal strain results..... 109
Table 5.4: Identified time steps with the biggest crack widths results. 110
Table 5.5: EMILIA f_{MEV} results of the first six modes.. 111
Table 5.6: Natural frequency results mean and standard deviation computed from all test setups.... 123
Table 5.7: First mode's statistics from different data lengths of the model in sound condition..... 129
Table 5.8: Second mode's statistics from different data lengths for the model in sound condition..... 129
Table 6.1: Thesis secondary objectives distribution summary. 136

1 INTRODUCTION

1.1 Motivation

Civil engineering structures and infrastructures require large investments and demand prolonged periods for their construction and commissioning (Thoft-Christensen 2012). For these investments to remain sustainable, these assets need to ensure an adequate level of performance during and beyond their original design working life, and to this end, they should be properly maintained and evaluated during their life span. This is even more relevant for heritage buildings, as their cultural and historical significance renders them irreplaceable and their loss would be unaffordable for society.

Vibration-based Structural Health Monitoring (SHM) is an emerging cutting-edge approach to civil engineering and infrastructure management. It leverages the natural vibrations of a structure in response to any natural and anthropogenic dynamic source, recorded through sensors strategically located on it, to estimate its modal properties (i.e. natural frequencies, damping ratios and mode shapes). This provides an almost real-time insight into the structure's condition, allowing for proactive maintenance and timely interventions, since modal properties are inherent characteristics of the structure, directly influenced by its mass, stiffness, and damping properties, which tend to change when the structure sustains damage. These alterations reflect shifts in the modal properties that can be promptly detected by SHM techniques. Therefore, vibration-based SHM offers a non-intrusive and cost-effective means of ensuring the safety, reliability, and longevity of critical assets and heritage buildings, enhancing the knowledge of these systems' physical and material characteristics as well as their current conditions.

The modal properties can be estimated by following two approaches, namely methods that perform a comparison between the input excitations and the output responses of the system, where both must be measured and known, and methods that only interpret the measured structural response to unknown inputs. For the second approach, it is usual to let ambient sources of vibrations randomly excite the structure.

Traditional methods for estimating the modal properties of a structure from output-only measures require significant assumptions. Among them, stationarity, time-invariance, and linearity of the investigated processes, with constant broadband spectrum inputs, are among the most influential. Indeed, in many practical situations, the unknown excitations affecting the structure are filled with unexpected events, potentially violating one or more of these critical assumptions. Excluding earthquakes, the main natural sources of vibrations, such as wind, rain, hail or sea waves, affect structures both from the air and from the ground and can comprise a huge spectrum of frequencies

involved, from components of very few cycles per second, as in the case of vibrations induced by ocean waves, up to frequency components of several thousand Hertz due to rain or hail. Vibrations produced by human activity, instead, correspond mostly to vehicular traffic, service machinery and human movement within the structure. In general, the vibrations produced by human activity present a low amplitude, but like natural vibrations, they have an enormous spectrum of frequencies that goes from a few cycles per second, in the case of human walking, to components of several thousand cycles per second in the case of electrical noise or magnetically induced vibrations.

Variations, even significant, in the operational and environmental conditions of a structure are common and compounding along its life span can finally lead to significant alterations in its dynamic properties and behaviour (Barontini et al. 2021; Pellegrini et al. 2023), however, these variations may be often considered to be slow when compared to the duration of an acquisition, allowing to assume a stationary nature of the process.

An interesting example of the opposite emerges from the dynamic identification conducted by the University of Sheffield on the Bradford Lifts Stand, situated in the east section of the Bradford and Bingley Stadium in Bradford, West Yorkshire, UK (Peeters et al. 2007). The stand can hold a maximum of 4500 supporters and considering an average weight of 75 kg per spectator, when the stand reaches full attendance to a match, there is an increment of more than 330 tons of mass that cannot be assumed as equally distributed. Moreover, the effect of the crowd is not static and constant over time, encompassing actions such as jumping, moving, or gathering at specific points. This dynamic action is expected to induce sudden variation in the structural response violating all the aforementioned assumptions.

Highways bridges and viaducts can be seriously affected by such sudden variations in the sources of vibrations. A case of wide public knowledge is the one from the Tacoma Narrows suspension bridge, which structurally collapsed due to design flaws that caused the bridge to resonate with the vibrations caused by wind vortices (Von Kármán vortex streets) (Matsumoto et al. 2003; Arioli and Gazzola 2017).

Like the two previous examples, vibrations generated from seismic activities present two main challenges: on one hand, they violate the aforementioned assumptions, generating vibrations in the spectrum of low and very low frequencies, with amplitudes that can vary enormously and suddenly, on the other hand, they may cause a rapid outbreak or evolution of damage. It is therefore essential to develop and test methodology that can effectively identify the dynamic properties and their fast variation in time, relying on signals for which common assumptions do not hold true.

1.2 Research Objectives

The main objective of this research is to develop, test and validate an output-only dynamic identification method based on a nonparametric algorithm for assessment of large civil structures and heritage buildings. The algorithm must be suitable for working in seismic-prone areas, being capable of processing time-invariant and time-variant structural data, relying on signals obtained under ambient vibrations as well as under seismic inputs and dealing with close spectral frequency components, high noise-contamination, and low-frequency spectrum range.

The proposed method aims to be used as a SHM analysis tool in tasks ranging from the pre- and post-event dynamic identification for condition assessment, to the online and nearly real-time evaluation of the structural response during seismic events. The method is expected to play a key role in the rapid detection of anomalies in the structural behaviour of ordinary and strategic structures and infrastructures, including heritage buildings.

According to the main objective aforementioned, the following secondary objectives were identified. Hence, in this research, the proposed nonparametric algorithm performance and capability are tested and analysed for:

(1) Application for linear modal analysis.

(2) Application for non-linear modal analysis.

(3) Perform time-dependent dynamic identification.

(4) Perform time-dependent damage identification.

(5) Perform modal analysis with reduced amounts of data

(6) Use strong motion seismic data for dynamic identification.

Aiming at the previous objectives, the current research methodology relies on theoretical developments, numerical simulations, experimental measurements, and statistical analysis.

The thesis work is essentially developed as an applied research, based on the generation and processing of numerical and experimental results with the proposed algorithm.

Additionally, benchmarking tests against traditional well-established alternative methods are conducted.

1.3 Thesis outline

In order to pursue the aforementioned objectives, this thesis is organised into six Chapters:

Chapter 1 is the current introduction, shedding light on the motivation, research framework, main objectives, research methodology and topics, and the general outline of the present document.

Chapter 2 reviews the current state of the art at the moment of the writing of this thesis. The bibliographic review comprehends the traditional and current time-frequency analysis methods, the most used modal analysis methods, and some of the most used damage identification techniques based on the assessment of ambient vibrations of civil engineering systems.

Chapter 3 offers an in-depth review of the algorithm itself, with a presentation of its workflow, a detailed description of its three main stages and a discussion of benchmarking tests against similar mathematical tools.

Chapter 4 presents the validation of the proposed algorithm by performing the dynamic identification of a 2D simulated bridge in sound and artificial damage conditions generated through the local reduction of Young's modulus. Additionally, tests of the main algorithm components are conducted to establish a generalisable parameter setting.

In Chapter 5 the proposed algorithm is exploited to analyse the non-linear and time-variant structural response of a simulated 3D masonry tower subjected to strong motion seismic data and a real scaled metallic shear frame structure in different stiffness conditions induced in a laboratory environment. The algorithm is adopted to estimate the modal properties of these systems and support their damage identification.

Finally, Chapter 6 offers a global review of the results of each chapter, summarises the main general conclusion of this thesis and outlines the most relevant future scopes of research.

PAGE INTENTIONALLY LEFT BLANK

2 STATE OF THE ART

2.1 Introduction

The present chapter aims to provide a systematised overview of the research conducted in the field of vibration tests and dynamic identification for civil engineering purposes.

In physics, the superposition principle is a mathematical concept that can properly explain wave phenomena including interference, diffraction, and standing waves on linear systems. The principle states that when two or more waves overlap in space, the resulting disturbance is equal to the algebraic sum of the individual original waves (see Figure 2.1).

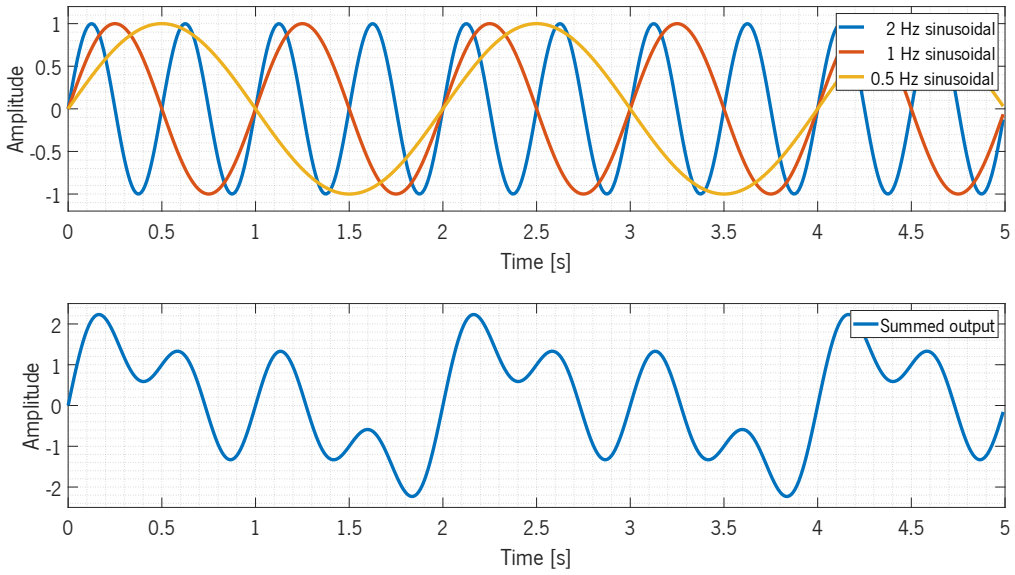


Figure 2.1: Superposition output (bottom) of three standing waves (top).

Superposition applies to any kind of waves and has been extensively used in physics and engineering since many physical systems can be represented with sufficient reliability as linear time-invariant (Ljung 2001).

Under this assumption, the relationship between the input $x(t)$ and the computed output data $y(t)$ can be mapped linearly, and whenever an input $x(t + \tau)$ is applied to the system, the computed $y(t + \tau)$ output is also delayed the same τ units in time. According to the previous, the behaviour of any linear time-invariant system can be described by the mathematical relationship presented in Equation 2.1 and formerly known as the convolution integral.

$$y(t) = (x * h)(t) = \int_{-\infty}^{\infty} x(\tau) \cdot h(t - \tau) d\tau \qquad \text{(Eq. 2.1)}$$

where $h(t)$ is the system's linear response to an impulsive input, also known as the transfer function.

This simplified approach makes these systems easier to analyse, as a large set of mathematical techniques is available. However, since physical systems are generally only approximately linear, the superposition principle is only an approximation of the true physical behaviour as well.

For instance, structural acceleration measurements performed resorting to ambient vibrations include a high amount of stochastic data and the recorded structural response often exhibits non-linear behaviour in the case of high transient excitations under natural or anthropogenic actions, making this type of data potentially inappropriate to conduct dynamic analysis with traditional linear and parametric estimators.

Nonetheless, many time-frequency analysis procedures, modal identification methods, and data decomposition algorithms currently used for professional and research activities in civil engineering and structural analysis rely on the superposition principle, thus, they inherit its limitations.

The present state-of-the-art aims to briefly present and describe some of the most used methods for vibration-based structural dynamic analysis and damage identification. First, a quick insight into the nomenclature, methods, and common classifications is provided. Parametric methods and data decomposition algorithms are presented after, followed by currently well-established nonparametric solutions. Then, an important section of the present chapter is devoted to the description of traditional modal analysis methods based on ambient vibration measurements and the presentation of some of the recently developed nonparametric algorithms. Finally, a brief overview of the applications of dynamic identification for structural damage identification purposes is provided. Closing the current chapter, the conclusions summarise and help shed light on the main motivation, objectives, and framework of the present research.

2.2 Modal algorithms: nomenclature and classifications

Several methods to analyse and decompose data have been developed in the last century and different authors have made various attempts to classify them under distinct paradigms. Table 2.1 shows some of the most currently used dynamic Identification methods together with some of the related classifications. Further information and in-depth reviews of the classification of modal identification methods and data decomposition algorithms can be found in (Luís F. Ramos 2007; D. J. Ewins 2009; Noël and Kerschen 2017; Civera and Surace 2021).

One of the most commonly used classifications for dynamic identification methods is based on the domain where the data analysis or the data decomposition is conducted (third column of Table 2.1). Indeed, this can be performed in the frequency domain or in the time domain. Whilst most of the

frequency domain methods are based on the superposition principle, in the time domain it is possible to find a vast number of different approaches.

Table 2.1: Commonly used modal estimation methods and their related classifications.

Name	Acronym	Domain	DOF	Used Data
Peak-Peaking	PP	Frequency	SISO	Output
Circle-Fit	CF	Frequency	SISO	Input-Output
Rational Fraction Polynomial	RPF	Frequency	SIMO	Input-Output
Frequency Domain Decomposition	FDD	Frequency	MIMO	Output
Enhanced FDD	EFDD	Frequency	MIMO	Output
Stochastic System Identification	SSI	Time	MIMO	Output
Auto-Regressive Moving-Averages	ARMA	Time	MIMO	Output
Ibrahim time-domain method	ITD	Time	MIMO	Output
Eigensystem Realization Algorithm	ERA	Time	MIMO	Output
Least Square Complex Exponential	LSCE	Time	MIMO	Output
Polyreference Complex Exponential	PRCE	Time	MIMO	Output
Complex Exponential	CE	Time	MIMO	Output
Hilbert-Huang Transform	HHT	Time	MIMO	Output

Another frequently used classification is related to the type and number of inputs and outputs considered to conduct the modal estimation (fourth column of Table 2.1). Single Input Single Output (SISO) methods consider only one structural excitation input and one measured output; thus, they are not suitable for in-situ assessment of structures located in places where environmental conditions or ambient excitations cannot be properly identified, and they are mostly suitable to assess local behaviours only. Multiple Inputs Single Output (MISO) methods can work with more excitation sources but a single response measurement, thus one channel of data acquisition, so they can be applied to many types of structures but mostly for global structural response assessment. Multiple Inputs Multiple Outputs (MIMO) methods can be successfully used in all professional applications as they include multiple sources and multiple response measurements (Polyreference) that allow the assessment of local and global structural dynamic behaviour.

A third classification approach focuses on the previously known information required for the application of the methods (fifth column of Table 2.1). Direct formulation methods refer to the ones that make use of a spatial model or general matrix equation of dynamic equilibrium for estimating modal parameters, where fully knowing all the mechanical characteristics of the structure is mandatory. However, the direct solution to the dynamic problem, whether through the exact formulation or a numerical approximation, is not always possible, especially when dealing with structures with poor characterisation of the material and mechanical properties, or when there is no prior knowledge of the

real dimensions nor the actual size and extension of the structure. Examples are heritage or large and complex structures like bridges, tunnels, and dams. Due to that, the inverse formulation of the dynamic problem becomes the only viable solution to identify the modal parameters of the structure of interest and, from that, to characterise its unknown physical parameters. Indirect methods work based on a modal representation for computing dynamic parameters. This approach is known as black-box or grey-box, reliant on the level of knowledge of the structural model (Maia 1988; Katayama 2004; Ljung 2008).

Figure 2.2 illustrates this concept. In the top-left corner of the figure, 10 seconds of normally distributed Gaussian noise are reported as the input/excitation $F(t)$ of an undamped Single Degree of Freedom (SDOF) inverted pendulum. The corresponding time domain system output $u(t)$ is presented in the top-right corner. The bottom of the figure shows the double-sided Frequency Response Function (FRF) of the input (bottom-left), and the output data (bottom-right). The bottom middle hosts the FRF of the undamped SDOF system. This system FRF is the main goal of the identification through modal analysis and is estimated by performing a comparison of the input excitations and the measured outputs or by resorting to the output data exclusively.

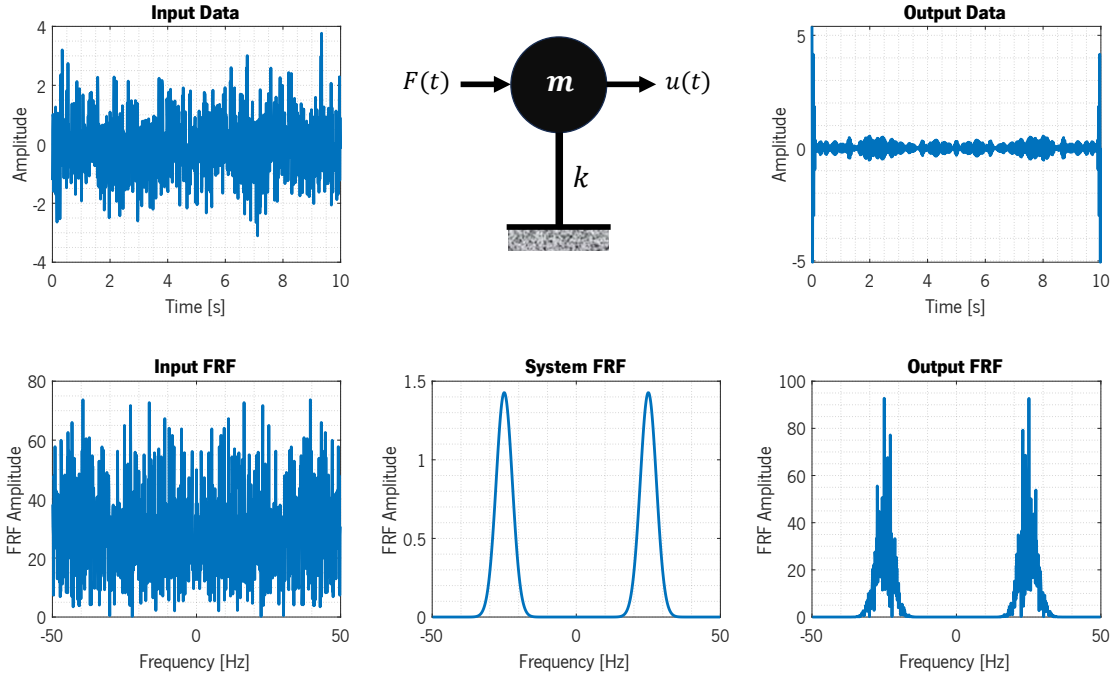


Figure 2.2: Idealised undamped dynamic system and its associated inputs and outputs in the time and frequency domain.

Indeed, some methods, classified as input-output, are designed to work with known inputs. For this kind of analysis having a certain control over the excitations that affect the structure during measurements is mandatory. Other methods work with output-only acquisitions, which allow the assessment of any kind of building under any normal operational conditions.

The assessment of structures with input-output methods is known as Experimental Modal Analysis (EMA), thus the structure is excited by one or more well-known and controlled dynamic forces. The output response of the structure is measured and then correlated to input force measurements for the FRF estimation. On the other hand, the structural assessment with methods that work with output-only data are known as Operational Modal Analysis (OMA) and dynamic parameters are extracted directly from in-situ measurements using the structural response to ambient and inner functioning vibrations, also called operational loadings or operational forces. Commonly, the only suitable modal analysis techniques for large and complex structures and heritage buildings are OMA methods, these having negligible interference with the structure operation, requiring minimum previous information regarding the structure's main characteristics, and preventing any harm to it.

More details on the algorithms listed in Table 2.1 and recent emerging techniques for dynamic identification are provided in Section 2.6. Most of these algorithms rely on Fourier's theory which is briefly introduced in Section 2.3, where its main limitations are discussed as well. The novel algorithm presented and validated within the present thesis overcomes these limitations by employing time-frequency analysis methods, that are presented in Section 2.4. Since an essential step of modal analysis, both in the frequency domain and in the time-frequency domain, is the decomposition of time-series into subsequences to enhance the robustness of the identification, an overview of existing decomposition strategies is provided in Section 2.5. Finally, in Section 2.7, well-established approaches to leverage dynamic identification outputs for condition monitoring of structural systems are described, since, in the next chapters, the novel algorithm is employed to inform damage detection strategies in both artificial and real case studies.

2.3 Frequency Domain Analyses

Traditional frequency domain analysis techniques are based on the theory proposed by *Joseph Fourier* in his revolutionary work *Théorie Analytique de la Chaleur* (Fourier 1822), on which he set the basis of all current state-of-the-art frequency and time-frequency domain methods, namely, the analytic integral transform named after him and presented here on Equation 2.2 in its analytic form.

$$X(\omega) = \mathcal{F}\{x(t)\} = \frac{1}{\sqrt{2\pi}} \int_{-\infty}^{\infty} x(t)\, e^{-j\omega t} dt \qquad \text{(Eq. 2.2)}$$

where t is the time, j is the imaginary unit, $x(t)$ is the continuous function to transform, and ω is the angular frequency expressed in radians.

Despite the importance of the analytical form, this is not a suitable option for performing real computations of sampled data. To this end, the Discrete Fourier Transform (DFT) has been developed to convert a finite sequence of equally spaced samples of a data stream, or a time series, into a same-length sequence of equally spaced samples, which is a complex-valued function, in the frequency domain. If $x[n]$ is a discrete function to transform, where $x_0, \dots, x_{N-1}$ are complex numbers, then the DFT is mathematically defined by the following expression:

$$X[\omega_k] = \sum_{n=0}^{N-1} x[n]\, e^{-j2\pi kn/N} \qquad \text{(Eq. 2.3)}$$

Where n is the current sample, N is the total number of samples, and whereas $k = 0, \dots, N-1$ are the discrete frequencies. According to Equation 2.3, the DFT is obtained by decomposing a sequence of discrete values into a set of components with different frequencies. This operation is extremely useful in many fields but computing it directly from the definition is often too slow to be practical. It is called Fast Fourier Transform (FFT) any algorithm capable of more efficiently computing the DFT of a given data stream by using divide and conquer methods on Equation 2.3, factorising the DFT matrix into a product of sparse (mostly zero) factors. As a result, it manages to reduce the complexity of computing the DFT from $O(N^2)$ operations, which arises if one simply applies Equation 2.3, to $O(N \log N)$, where N is the data length (Cochran et al. 1967).

All currently known FFT algorithms require the same number of calculations, although there is no known proof that lower complexity is impossible. The difference in computing speed can be massive, especially for real SHM data sets, where the number of samples (per channel) can easily reach millions (J. Cooley, Lewis, and Welch 1967b; 1967a; Van Loan 1992).

Therefore, the FFT algorithms are designed exclusively to perform a rapid computation of Fourier's spectrums over discrete digital signals, where most modern mathematical suites or signal processing software are based and make use of the FFTW3 algorithm (Frigo and Johnson 2005; J. W. Cooley and Tukey 2006).

It is worth noting that the FFT computation involves complex numbers, and that the complete resulting spectrum has a mirrored negative and positive part, which is known as a double-sided FFT spectrum. However, referring to the single-sided FFT spectrum (positive part) is common. The most substantial issue of the Fourier theory is that it decomposes the analysed data into a finite sum of infinite continuous trigonometric components, so it is only possible to analyse and transform periodic

and linear data and the Heisenberg uncertainty principle holds true. Thus, it is not possible to gain resolution both in time and frequency at the same time.

The Power Spectral Density (PSD) is a spectral representation of the energy of the analysed signal based on the FFT. The PSD was originally obtained through an averaging process of several consecutively computed spectral densities over time-windowed chunks of data, formerly known as periodograms (Welch 1967).

The PSD is currently one of the most commonly used frequency domain representations in several fields of engineering and physics. However, the most common approach currently used by most professional software and mathematical suites to compute a PSD is through the FFT of the discrete autocorrelation function $R_{xx}[n]$ (Equation 2.4), which is a measure of the correlation of a stream of data against a delayed version of itself. According to the previous, in the discrete domain, the PSD of a $x[n]$ function is typically computed as follows.

$$PSD[\omega] = S_{xx}[\omega] = \sum_{k=-\infty}^{\infty} R_{xx}[k]\, e^{-j\omega k} \quad \text{(Eq. 2.4)}$$

where,

$$R_{xx}[k] = E\big[x[n], x^*[n-k]\big] \quad \text{(Eq. 2.5)}$$

whereas k is the time delay used to compute the autocorrelation function, $E[\ ]$ is the expected value operator, and x^* is the complex conjugate of x. As aforementioned, the PSD is computed through an averaging process, thus, it finally discards random and non-deterministic information on the analysed data, computing clearer and smoother spectrums than the common FFT (Brandt 2019). The previous statement can be observed in Figure 2.3, that shows the absolute value of the single-sided FFT and the PSD spectrums computed from an example data containing a 100 Hz sinusoid, a 250 Hz sinusoid and a zero-mean Gaussian white-noise.

Both spectrums presented in the figure are capable of identifying the sinusoidal data in the signal against the background noise. However, the PSD spectrum is smoother and with noticeably less background noise, being this proof of how the averaging inner process on the PSD calculation improves the obtained spectrum.

Moreover, in the same spectrums, despite an easy identification of the frequency components with reasonable accuracy, there is null evidence of when, in time, the obtained frequency domain

results occurred, thus demonstrating how Fourier's theory is directly affected by the Heisenberg's uncertainty principle, as previously mentioned.

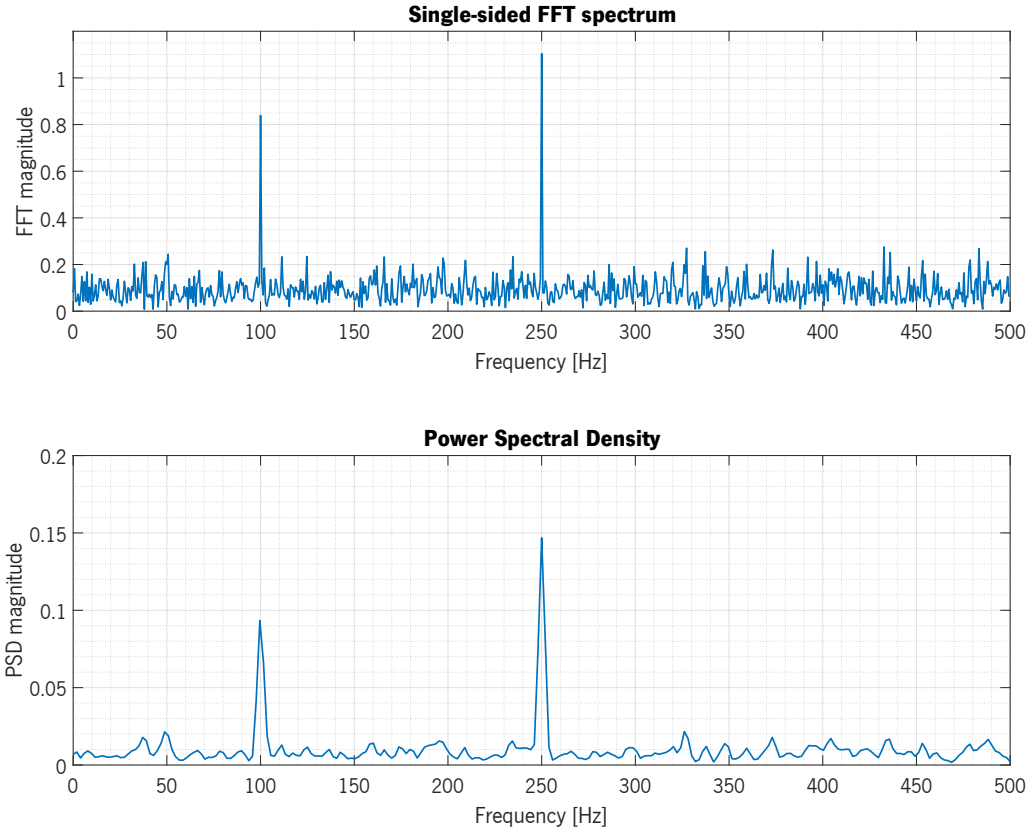


Figure 2.3: Comparison between an FFT spectrum (top) and a PSD spectrum (bottom).

It is worth noting that both FFT and PSD only gather spectral information from a single signal. However, sometimes there is a need to perform a comparison between two (or more) signals or data streams to identify common characteristics or to test for aliased data. Cross-spectral analysis relies on mathematical tools capable of determining the relationship between two time series in the frequency domain. Indeed, Cross-Power Spectral Density (CPSD) is extensively used in many fields of engineering, especially in telecommunications and signal processing applications. In practice, CPSD and the Magnitude Square Coherence function (a normalised CPSD) are by far the most used cross-spectral analysis methods to measure linear statistical relationships between two time series. Similar to the PSD that is computed through the Fourier transform of the auto-correlation function (see Equation 2.4), the CPSD is computed through the Fourier transform of the cross-correlation function $R_{xy}[n]$. Giving the aforementioned, the PSD can be defined as a special case of the CPSD being computed between the signal and itself. The Cross-Correlation function R_{xy} determines the relationship between two stochastic time series in continuous time and is mathematically defined in Equation 2.6.

$$R_{xy}[k] = E\left[x[n], y^*[n-k]\right] \quad \text{(Eq. 2.6)}$$

hence, the $S_{xy}[\omega]$ is mathematically defined as follows:

$$CPSD[\omega] \; = \; S_{xy}[\omega] \; = \sum_{k=-\infty}^{\infty} R_{xy}[k]\, e^{-j\omega k} \quad \text{(Eq. 2.7)}$$

2.4 Time-Frequency Analysis Techniques

As mentioned above, traditional Fourier-based frequency domain analyses lack any temporal information, as they consider that the spectrum is constant throughout the whole observation period. An emerging approach capable of overcoming such an issue is the Time-Frequency Analysis (TFA).

TFA methods and algorithms can capture information from the analysed data both in the frequency and in the time domains simultaneously, allowing further and deeper analyses of the analysed signals.

Gabor's Short Time Fourier Transform (STFT) is an effort to escape from the limitations imposed by the superposition principle on the basic FFT in order to make it possible to analyse and assess non-periodic data and non-linear data obtained from linear time-variant systems (Gabor 1946). The STFT is mathematically defined as:

$$STFT(\omega, \tau) \; = \; \frac{1}{\sqrt{2\pi}} \int_{-\infty}^{\infty} x(t) w(t-\tau) e^{-j\omega t} dt \quad \text{(Eq. 2.8)}$$

where $w(t-\tau)$ is the time-window function, whereas τ is the window time displacement. According to Equation 2.8, the STFT is obtained by discretising the frequency spectrum into time segments of a preferred length τ, and then iteratively computing FFTs along each time window $w(t-\tau)$.

A commonly used graphical representation showing the time (usually on the X axis), the frequency information (usually on the Y axis), and amplitude data (generally in the form of a colour scale), is formally known as a Spectrogram. For instance, a pair of STFT spectrograms showing the two sinusoids of the same example data previously utilized in Figure 2.3 can be seen in Figure 2.4 and in Figure 2.5, where the first spectrogram is computed using Hanning time windows with a length of 500 samples, whilst the second one is computed using Hanning windows of 25 samples.

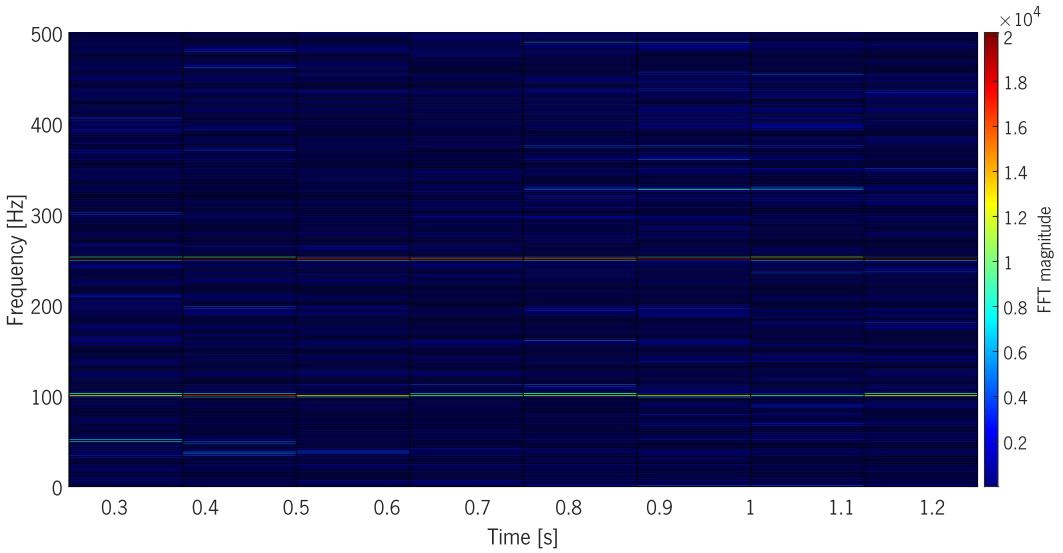


Figure 2.4: STFT spectrogram computed with a Hanning time window of 500 samples.

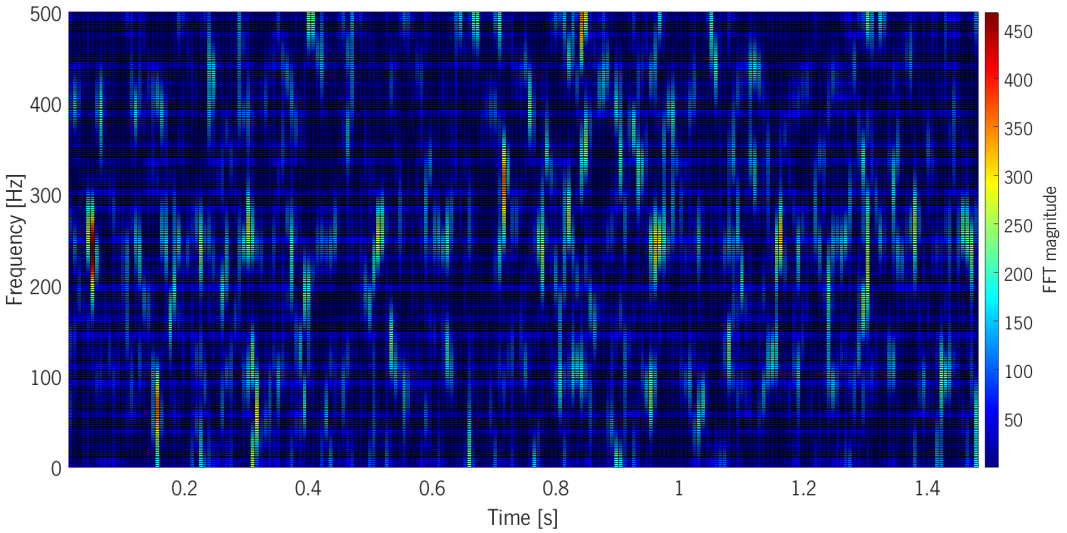


Figure 2.5: STFT spectrogram computed with a Hanning time window of 25 samples.

It is notorious how requesting a higher resolution in time by using the 25 samples Hanning window, the computed output exhibits an enormous loss of resolution in the frequency domain, which is once again evidence of the limitations imposed by the uncertainty principle in traditional Fourier analysis.

The Hilbert transform (HT) is defined as the response of a quadrature filter to a real function $x(t)$ (Equation 2.9) and it is essential for constructing an Analytic Signal (AS). The AS $z(t)$ is the representation of any signal, or data stream, as a complex pair where the imaginary part is the HT of the real part (Equation 2.10). The modulus operation of AS provides the Instantaneous Amplitude

A_{inst} and the time derivative of the AS complex angle provides the Instantaneous Frequency ω_{inst}, which are both time-dependent outputs of the Hilbert analysis.

$$HT = \hat{x}(t) = x(t) * \frac{1}{\pi t} = \frac{1}{\pi} \int_{-\infty}^{\infty} \frac{x(\tau)}{t-\tau}\, d\tau \qquad \text{(Eq. 2.9)}$$

$$\mathrm{AS} = z(t) = x(t) + j\hat{x}(t) \qquad \text{(Eq. 2.10)}$$

It is worth noting that similar to an FFT or a PSD, the HT of a discrete Gaussian white noise will be a flat spectrum, theoretically computing as many different instantaneous frequency values as the number of samples on the original signal. Therefore, broadband signals are not good candidates for Hilbert analysis. It is better to process, or band filter the raw data before any further analysis so that HT is applied to mono-component or pseudo-mono-component signals.

Any ideal structural free vibration response $x(t)$ can also be expressed as a linear combination of well-behaved sinusoidal modal functions where the HT can be successfully applied, but ambient vibration measurements have deterministic data hidden between stochastic random data from sources like sea waves, wind, traffic, seismic waves, etc. Thus, in order to properly apply HT analysis, it is highly recommended to first decompose the ambient vibration records into SDOF or pseudo-SDOF modal components to ensure obtaining well-behaved outputs.

Figure 2.6 presents a Hilbert spectrogram computed directly from the raw example data of Figure 2.3, whilst in Figure 2.7 the spectrogram computed from the example data previously processed through a frequency domain data decomposition (Variational Mode Decomposition) can be observed.

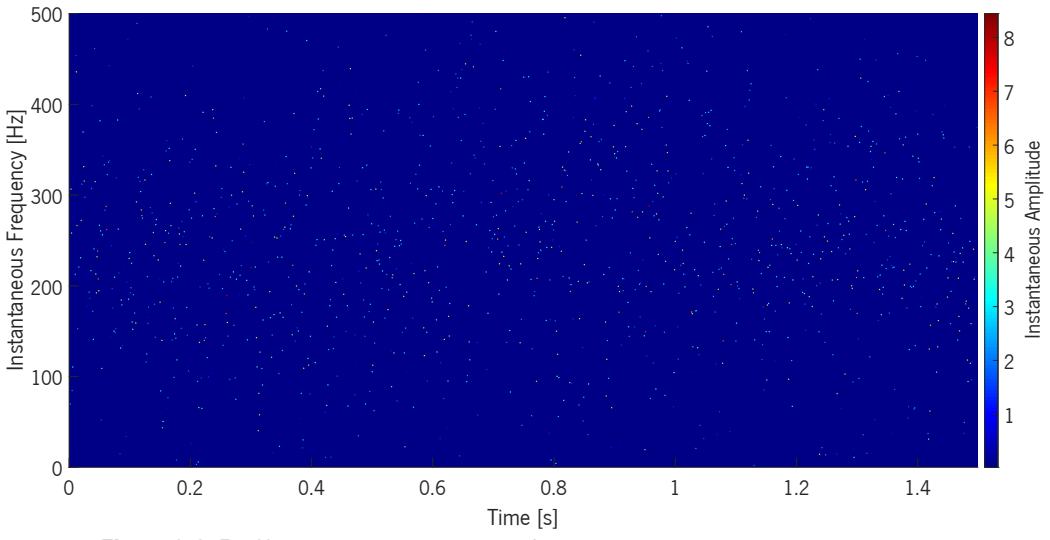


Figure 2.6: Flat Hilbert spectrogram computed from a single broadband raw acceleration data.

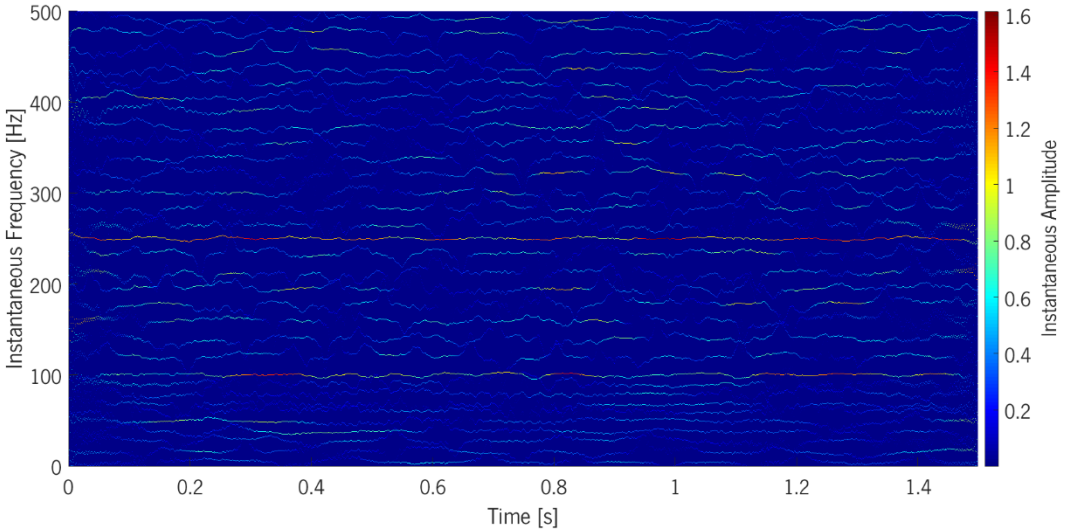


Figure 2.7: Hilbert spectrogram computed from decomposed acceleration data.

The spectrogram computed from the raw data cannot show the real frequency content of the signal, producing an almost flat response without any peaks in the colour scale of the amplitude, i.e. full blue background of the spectrogram. On the other hand, in the decomposed-data spectrogram, it is easier to observe the higher level of energy around the 250 Hz and the 100 Hz zone, where the sinusoidal data from the example are located.

In addition to the need for well-behaved pseudo-mono-component or narrow-band signals, the HT has some well-known limitations that can affect its performance as well as the computed outputs. Mainly, it is restricted by the Bedrosian and the Natter theorems (Nuttall and Bedrosian 1966; Boashash 1992a) and can lead to outliers in the results and even negative values of instantaneous frequencies in case of discontinuities or sudden changes in the input data amplitude. Further information on the application of HT to mechanical vibrations can be found in (Feldman 2011). Additionally, since HT is a core component of the algorithm developed within the present thesis, additional details on its operation and background theory are provided in Section 3.2.2 presenting the novel methodology.

Besides the aforementioned methods, several approaches have been developed for computing instantaneous components from time series, especially for machinery and electrical power condition monitoring and maintenance, and for the signal processing fields. For instance, discrete energy separation algorithms like the Teager-Kaiser operator (Teager and Teager 1990; Kaiser 1990) are extensively applied in speech recognition and audio analysis. Teager-Kaiser operator has a well-known limitation: it is strongly affected by uncorrelated noise existence in the analysed signal. The Taeger-Kaiser operator was designed specifically to compute results with a reduced number of samples, and

it can compute results with just three samples of data, which makes this algorithm extremely fast, but it is also the main reason for its high sensitivity to wideband noise, especially when it reaches energy levels close to or above the zero decibels (Kaiser 1990).

More direct approaches have also been developed, like the Zero-Crossing points-based algorithms. These algorithms analyse the number of zero-crossing points in the data in order to estimate an instantaneous frequency value. Due to the nature of the calculation, the resulting value is extended to the period of observation, thus, it corresponds to an approximation of the instantaneous values for each period (Boashash 1992b; Londoño, Neild, and Cooper 2015).

Other straight approaches are the Direct-Quadrature algorithms such as the Clarke-Park Transform (Paul C. Krause, Oleg Wasynczuk, and Scott D. Sudhoff 2002) that is intensively used to assess the instantaneous frequency of three-phase power systems. Resorting to similar approaches, other authors have developed alternative proposals for Direct-Quadrature methods, like applying a direct ninety-degrees-shift to the data stream and computing a pseudo-analytical instantaneous phase (Huang et al. 2009). Nevertheless, many of these algorithms remain sensitive to noise, particularly the algorithms based on cubic-spline envelopes, like the Normalised Hilbert Transform method (Huang et al. 2009), that performs recursive normalisations of the data to remove the influence of modulated amplitude during the computation of the instantaneous frequency. Other instantaneous frequency algorithms are based on the computation of spectral moments from frequency distributions that are based on the calculation of FFTs or PSDs, thus, the size of the outputs is conditioned to the chosen number of FFT lines in the computation of the requested spectrums.

The above stated means that these methods' outputs are useless in order to compute further statistics and probabilities analyses, unless the used FFT and PSD are computed with full resolution, by setting the number of FFT lines equal to the number of samples on the original data. However, computing full-resolution FFTs will produce a large increment of the computational burden. It is worth noting as well that, since the computation is based on Fourier's theory, the outputs are limited by the superposition principle making these algorithms not appropriate to analyse non-linear seismic data or time-varying systems. Nevertheless, all the methods previously described require pseudo-mono-component-narrow-band signals. Thus, in most practical applications, the decomposition of the data before the calculation of the instantaneous frequency remains mandatory and of high importance.

Wavelet Transform (WT) allows to perform multi-resolution time-frequency data analysis, being capable of detecting time-dependent features even in the presence of high levels of noise. WT has become by far the most widely used time-frequency algorithm for signal processing, data denoising,

and multiresolution TFA. The first approach to Wavelet was set up by Alfréd Haar in his doctoral thesis where he proposed a new base of functions, or a family of orthogonal functions, not yet known as Wavelets (Haar 1910).

Later that century, many other authors contributed to the development of full Wavelet theory, from Gabor´s *Theory of Communication* (Gabor 1946), through Morlet´s papers where he first used the name "*Wavelet*" and started applying the wavelet theory to the analysis of seismic data (Goupillaud, Grossmann, and Morlet 1984). Finally, in the '90s, Ingrid Daubechies set the full basis of Wavelet theory in her book *Ten Lectures on Wavelets* (Daubechies 1992).

Mathematically, the WT is an integral transform that represents a signal $x(t)$ in terms of a series of coefficients related to the convolution of the signal waveform with dilated and translated versions of a defined mother wavelet function $\psi(t)$.

A function $\psi(t)$ is a valid mother wavelet function if, and only if:

$$\int_{-\infty}^{\infty} \psi(t)\, dt = 0 \qquad \text{(Eq. 2.11)}$$

and,

$$\int_{-\infty}^{\infty} |\psi(t)|^2\, dt < \infty \qquad \text{(Eq. 2.12)}$$

The Continuous Wavelet Transform (CWT) is one of the most widely used methods for TFA. It has been widely used in signal processing, data denoising, seismic data analysis, and image processing, among other disciplines, offering a high-resolution time-frequency representation of signal spectrum components' evolution on time.

The CWT is mathematically defined as:

$$CWT\{x(t)\} \;=\; |a|^{-1/2} \int_{-\infty}^{\infty} x(t)\, \psi\left(\frac{t-b}{a}\right) dt \qquad \text{(Eq. 2.13)}$$

where a is the scale, b the position, and $\psi(t)$ the mother Wavelet function. If required, the original signal $x(t)$ can be fully reconstructed through the following inverse relation:

$$x(t) \;=\; {C_\psi}^{-1} \int_{-\infty}^{\infty} \int_{-\infty}^{\infty} \frac{1}{a^2} \langle x, \psi^{a,b} \rangle\, \psi^{a,b}\; da\, db \qquad \text{(Eq. 2.14)}$$

where,

$$\psi^{a,b}(x) = |a|^{-1/2}\ \psi\left(\frac{x-b}{a}\right) \quad \text{(Eq. 2.15)}$$

and,

$$C_\psi = 2\pi \int_{-\infty}^{\infty} |\psi^*(\omega)|^2\ |\omega|^{-1}\ d\omega \quad \text{(Eq. 2.16)}$$

A graphic representation similar to the previously described STFT spectrograms but generated by resorting to the computed CWT coefficients is formally known as a scalogram, which is related to the scaling of the frequency data produced by the scaling function. A CWT scalogram of the same example data previously used and computed using a *Bump* continuous mother wavelet can be observed in Figure 2.8, where it can be seen how the CWT distorts the lower frequencies of the spectrum, which can be noticed in the lower corners of Figure 2.8. Moreover, this distortion makes extremely difficult to identify the modal information of interest for the 50 Hz component, and even for the 250 Hz component due to the low resolution obtained for the lower frequencies.

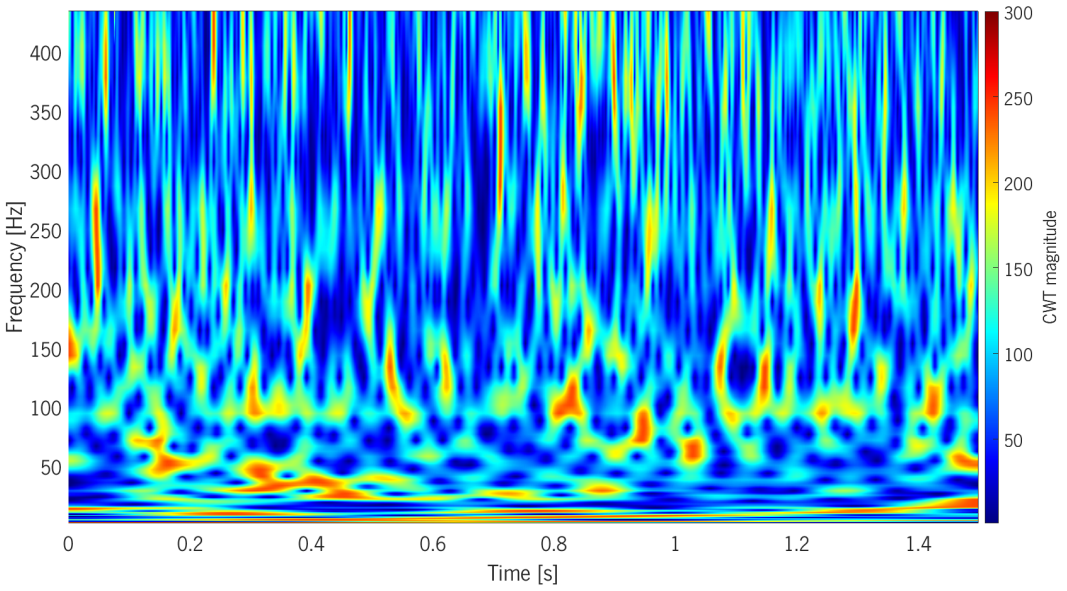


Figure 2.8: CWT scalogram computed using a *Bump* continuous wavelet.

Similarly to the FFT, which is the discrete equivalent of the continuous-time Fourier Transform, and despite the success of the CWT, the Discrete Wavelet Transform (DWT) is the most used and powerful tool for studying real data time-series and field measurements through wavelets analysis, In the DWT, the mother wavelet, the scaling function and the dilatation function are discretised into a set of compactly supported functions.

The DWT represents the discrete signal $x[n]$ as a time series of wavelet coefficients computed by convolving it with a pair of linear filters: a low-pass filter $g[n]$ as the discrete scale function, and a high pass filter $h[n]$ as the discrete wavelet function, where n is the discrete time-steps or samples of the digitalised data. The aforementioned filtering process generates two outputs in the form of a time series of wavelet coefficients: one known as the wavelet approximation coefficients, here denoted by $A_m[n]$ and related to the low-pass filter $g_m[n]$ outputs, and the other known as wavelet detail coefficients, denoted henceforth by $D_m[n]$ and related to the outputs computed by the high-pass filter $h_m[n]$, where m represents the level of the transform. It is worth noting that the DWT is an orthonormal transform, thus, if an orthogonal discrete mother wavelet function is employed, the computed subsequences $A_m[n]$ and $D_m[n]$ are orthogonal functions. If $a = a_0^m$ with $a_0 > 1$, $b = nb_0a_0^m$ with $b_0 > 0$, and assuming that ψ is real, then the DWT is mathematically computed as the inner product of function $x[n]$ with the corresponding scaled discrete wavelet:

$$W_\psi[n,m] = \langle x[n], \psi_{n,m} \rangle \qquad \text{(Eq. 2.17)}$$

where the scaled discrete wavelets are defined as follows:

$$\psi_{n,m}[s] = a_0^{-m/2}\, \psi(a_0^{-m}s - nb_0) \qquad \text{(Eq. 2.18)}$$

whereas s is the set of points that supports the discrete wavelet function.

As a reference, three examples of different mother wavelet functions are presented in Figure 2.9: a Morlet mother wavelet, commonly used to perform CWT analyses in Figure 2.9 (a), a discrete Daubechies 4 mother wavelet, commonly used for conducting DWT analyses and discrete data decompositions in Figure 2.9 (b), and a discrete Coiflets 4 mother wavelet, used mainly for DWT analyses and data decompositions in Figure 2.9 (c).

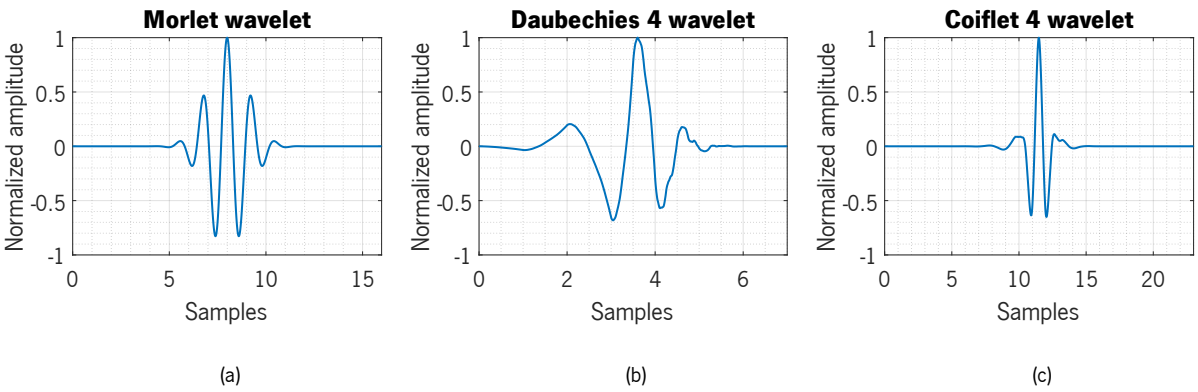


Figure 2.9: (a) Continuous Morlet wavelet, (b) discrete Daubechies 4 wavelet, (c) discrete Coiflets 4 wavelet.

2.5 Data decomposition algorithms

2.5.1 Parametrical Decompositions

The decomposition of a square matrix A into its so-called eigenvalues and eigenvectors is an extremely important concept in linear algebra for assessing linear time-invariant systems.

This type of decomposition is also known as "matrix diagonalisation", as it consists of the decomposition into the product of three matrices, one of them being diagonal.

Eigen-based decompositions are widely used in different mathematical disciplines and applications to decompose weighted matrices obtained from linear system responses. Any eigen decomposition is based on using the eigenvector-eigenvalue pairs as solutions of differential equations. If A is $n \times n$ matrix, then an eigenvector-eigenvalue pair is composed of a non-zero vector u and a scalar λ where:

$$Au = \lambda u \quad \text{(Eq. 2.19)}$$

then:

$$(A - \lambda \mathrm{I})\mathrm{u} = 0 \quad \text{(Eq. 2.20)}$$

and if Equation 2.20 has non-trivial solutions, then:

$$det(A - \lambda \mathrm{I}) = 0 \quad \text{(Eq. 2.21)}$$

Eigenvalues can be characterised in terms of the determinant and the trace of the matrix, then:

$$det(A) = \prod_{i=1}^{n} \lambda_i \quad \text{(Eq. 2.22)}$$

$$trace(A) = \sum_{i=1}^{n} \lambda_i \quad \text{(Eq. 2.23)}$$

The set of independent eigenvectors associated with the eigenvalues together with 0 forms a vector space called the eigenspace, hereby denoted by E_λ.

Let U be a square and invertible matrix, then A and $(U^{-1}AU)$ have the same eigenvalues. This leads to the Eigen Decomposition Theorem. Namely, let U be the matrix of eigenvectors of a given square matrix A and D the matrix with the corresponding eigenvalues on the diagonal.

Then, as long as U is a square and invertible matrix, A can be written as an eigen decomposition:

$$\mathrm{A} = \mathrm{UDU}^{-1} \quad \text{(Eq. 2.24)}$$

If A is symmetric, then the columns of U are orthogonal vectors. If U is not a square matrix, then U cannot have a matrix inverse and A does not have an associated eigen decomposition. Proofs of the theorem and further information regarding eigenvalues, eigenvectors and eigen decompositions can be found in (Gilbert Strang 2016; K. F. Riley, M. P. Hobson, and S. J. Bence 2006).

Any matrix A is orthogonally diagonalisable if there is an orthogonal matrix Q and diagonal matrix D that fulfil the following relationship:

$$A = QDQ^T \quad \text{(Eq. 2.25)}$$

and if A is an $n \times n$ symmetric matrix, then:

(1) The matrix A has n real eigenvalues.

(2) For all λ: $a_\lambda = g_\lambda$; where a_λ is the algebraic multiplicity of λ and g_λ is the geometric multiplicity.

(3) The eigenvectors are mutually orthogonal.

(4) Matrix A is orthogonally diagonalisable, with $D = diag(\lambda_1, \lambda_2, \ldots, \lambda_n)$.

The previous set of statements are known as the Spectral Theorem. According to this, if a matrix is real and symmetric, inside each eigenspace, there is an orthonormal basis of eigenvectors. According to the afore-presented statement (3), then if u_1 and u_2 are eigenvectors from the eigenvalues, λ_1, λ_2, then $u_1 \cdot u_2 = 0$, and:

$$\lambda_1 u_1 u_2 = (Au_1)^T u_2 = u_1^T A^T u_2 = u_1^T A u_2 = \lambda_2 u_1 u_2 \quad \text{(Eq. 2.26)}$$

then:

$$(\lambda_1 - \lambda_2) u_1 u_2 = 0 \quad \text{(Eq. 2.27)}$$

and since A is a diagonalizable matrix:

$$A = (u_1 u_2 u_3 \dots u_n)\begin{pmatrix} \lambda_1 & 0 & \cdots & 0 \\ 0 & \lambda_2 & \cdots & 0 \\ \vdots & \vdots & \ddots & \vdots \\ 0 & 0 & \cdots & \lambda_n \end{pmatrix}\begin{pmatrix} u_1^T \\ u_2^T \\ \vdots \\ u_n^T \end{pmatrix} \quad \text{(Eq. 2.28)}$$

$$A = (\lambda_1 u_1 \lambda_2 u_2 \lambda_3 u_3 \dots \lambda_n u_n)\begin{pmatrix} u_1^T \\ u_2^T \\ \vdots \\ u_n^T \end{pmatrix} \quad \text{(Eq. 2.29)}$$

$$A = (\lambda_1 u_1 u_1^T + \lambda_2 u_2 u_2^T + \lambda_3 u_3 u_3^T + \cdots \lambda_n u_n u_n^T) \quad \text{(Eq. 2.30)}$$

meaning that the matrix A can be calculated as a sum of n rank one matrices, where each one of these matrices is a projection matrix.

The Singular Value Decomposition (SVD) is a further generalisation of the aforementioned eigen decomposition in order to work with any $m \times n$ matrix. As in any eigen decomposition, the obtained singular values, and the corresponding singular vectors of a rectangular matrix A are, respectively, a scalar λ and a pair of vectors u and v that satisfy the relationships in equations 2.31 and 2.32.

$$Av = \lambda u \quad \text{(Eq. 2.31)}$$

$$A^H u = \lambda v \quad \text{(Eq. 2.32)}$$

where A^H is the Hermitian transpose of A. The singular vectors u and v are typically scaled to have a norm equal to unity. Also, if u and v are singular vectors of A, then $-u$ and $-v$ are singular vectors of A as well. Additionally, the singular values λ are always real and non-negative, even if the matrix A is a complex matrix. Collecting the singular values in a diagonal matrix Σ and the corresponding singular vectors forming the columns of two orthogonal matrices U and V, the following equation can be obtained:

$$AV = U\Sigma \quad \text{(Eq. 2.33)}$$

Then, and since U and V are unitary matrices, multiplying Equation 2.33 by V^H on the right side, yields the singular value decomposition equation:

$$A = \mathrm{U}\Sigma\mathrm{V}^H \quad \text{(Eq. 2.34)}$$

where the full singular value decomposition of an $m \times n$ matrix outcomes are a $n \times m$ matrix U, a $n \times m$ matrix Σ, and a $n \times n$ matrix V.

Further information about eigen decompositions and SVD can be found in (Michael D. Greenberg 2000; Gene H. Golub and Charles F. Van Loan 2013).

2.5.2 Nonparametric Decompositions

Several nonparametric time-frequency methods have been developed to investigate the time-dependency of modal properties. Most of these existing nonparametric decomposition algorithms were designed to assess output-only data. Algorithms that sift the data by extracting time series related to the original signal waveform commonly constitute the core of such methods.

For instance, the Hilbert-Huang Transform (HHT) makes use of the Empirical Mode Decomposition (EMD) to compute pseudo-SDOF subsequences known as Intrinsic Mode Function (IMF) (Huang et al. 1998).

The EMD identifies local extrema and computes means of upper and lower envelopes through cubic splines in order to apply an iterative sifting process that leads to identifying a set of IMFs. Each IMF must fulfil the mathematical relationship presented in Equation 2.35, which can be straightforwardly associated with the Cauchy convergence test (Bradley and Sandifer 2009).

According to the above, the sifting process for each IMF stops when SD_k is smaller than a pre-defined value. The identified IMF is then subtracted from the analysed data and the sifting process starts again with the remaining samples.

$$SD_k = \sum_{t=0}^{T} \frac{|h_{k-1}(t) - h_k(t)|^2}{h_{k-1}^2(t)} \qquad \text{(Eq. 2.35)}$$

It is important to notice that the EMD is not an orthonormal decomposition, thus, the computed IMFs may be linearly dependent functions (Peng, Tse, and Chu 2005; Huang and Wu 2008; Huang et al. 1998; Huang and Shen 2005).

Some of the new developments in TFA and data decomposition algorithms rely on the previously mentioned rock-solid Wavelet theory (Daubechies 1992). There exists a whole family of data decomposition algorithms based on the DWT, like the DWT itself, the Discrete Wavelet Packet Transform (DWPT), the Maximum Overlap Discrete Wavelet Transform (MODWT), and the Maximum Overlap Discrete Wavelet Packet Transform (MODWPT) (Walden and Cristan 1998), which is the decomposition method adopted by the proposed algorithm in the present research.

Most of these algorithms have been successfully applied in many fields of engineering, statistics, and data analysis as well, being part of many processing algorithms. Further information and analysis of the previously mentioned decomposition algorithms, to optimise the proposed methodology, can be found in Section 3.2.1.

An additional approach to data-driven wavelet analysis that aims to extract IMF-like components is the Wavelet Synchro Squeezed Transform (WSST) (Daubechies, Lu, and Wu 2011). WSST can operate both in the Fourier's and in wavelet domains and it works by first sharpening the spectrogram or wavelet scalogram through a frequency reassignment operator, then, ridge extraction techniques are employed to estimate ridges related to the instantaneous frequency behaviour. Finally, signal components are recovered by integrating the reassigned STFT or the reassigned wavelet coefficients in the vicinity of the corresponding ridges.

Other methods also use the capability of ridge extractions applied to modal analysis. For instance, some authors have proposed instantaneous frequency identification algorithms for time-varying structures based on the ridge extraction of continuous wavelet analysis (Dziedziech, Staszewski, and Uhl 2015; C. Wang et al. 2013; Iatsenko, McClintock, and Stefanovska 2016). Nevertheless, ridge extraction methods only employ single-channel spectrogram or scalogram data, usually with high-quality signal requirements resulting in low levels of noise robustness.

Another decomposition algorithm aiming to extract IMF-like components that also work in the frequency domain is the Empirical Wavelet Transform (EWT) (Gilles 2013). This relies on robust peak detection mechanisms and spectrum segmentation techniques to develop a wavelet filter bank for effective data decomposition, namely the Variational Mode Decomposition (VMD) (Dragomiretskiy and Zosso 2014), and the multichannel version, namely the Multivariate Variational Mode Decomposition (MVMD) (Rehman and Aftab 2019). The MVDM algorithm is used in some of the latest developments of time-dependent modal analysis in frequency domain through short-time like approaches (Liu et al. 2022). Both VMD and MVMD use adaptive Weiner filters to compute a set of modes that can properly reconstruct the system FRF.

2.6 Dynamic identification methods

As mentioned earlier, frequency domain-based methods make use of mathematical transforms to identify the modal parameters by assessing the spectral information of the measured signals. These types of algorithms are known for being straightforward methods with mid/low computational burdens. Notwithstanding the simplicity and well-known limitations of FFT (no time information, sensibility to

noise, unfeasibility for non-linear data, limited number of output samples), frequency domain methods have been successfully used to estimate modal properties of civil engineering structures (Oliveira and Navarro 2010; Hu, Wang, and Ji 2013; Valla et al. 2015). Indeed, Fourier's theory is the foundation of all frequency domain algorithms and they can be found on the main core of all the most used modal identification methods, including some of the oldest techniques, like the Circle-Fitting method (Kennedy and Pancu 1947) and the Peak-Peaking (PP) method (Bishop and Gladwell 1963; Bendat and Piersol 1980).

The PP method is one of the simplest frequency domain modal identification methods and it is based on the manual selection of resonant peaks on FRFs or PSDs, thus, the accuracy of the modal identification depends on the expertise of the operator and the quality of the obtained measurements. The PP method assumes that in a Multiple Degrees of Freedom (MDOF) system, the structural response can be represented as a sum of a series of SDOF components and that each well-defined peak in the spectrum is produced by one of these SDOF modal component (Anders Brandt 2023). Finally, for each selected peak the corresponding SDOF FRF can be calculated in the frequency domain through Equation 2.36, and the damping factor is calculated through the Half-Power Bandwidth Method (Papagiannopoulos and Hatzigeorgiou 2011).

$$H(\omega) = \frac{2Q\zeta_n\omega_n^2}{\omega_n^2 - \omega^2 + 2j\zeta_r\omega\omega_n} \quad \text{(Eq. 2.36)}$$

Frequency Domain Decomposition (FDD) is currently one of the most vastly used methods for modal identification from vibration measurements (Ventura 2001; Rune Brincker, Zhang, and Andersen 2000; 2001; Rune; Brincker, Ventura, and Andersen 2001). FDD algorithm uses an SVD applied to a CPSD matrix in order to identify the modal parameters by selecting peaks on the singular value curves in the frequency domain. Similar to PP, the method requires the manual selection of the resonant peaks, so the accuracy of the identification depends, once again, on the expertise of the operator.

After a peak is selected, the corresponding eigenvector is used for computing mode shapes. A further development of the method is the Enhanced Frequency Domain Decomposition (EFDD), which uses Impulse Response Functions (IRF) to identify the damping factor from the exponential decay on the slope of each analysed IRF. Later updates of the FDD method aim at the automatization of the selection process (Rodrigues and Brincker 2005; Rodrigues, Brincker, and Andersen 2004; Magalhães et al. 2010; Rune Brincker, Andersen, and Jacobsen 2007; Rune Brincker and Zhang 2009; Rune Brincker 2010).

Time-domain methods employ raw time series and do not require a space transformation to extract the modal parameters. Moreover, they demand little user interaction and present many advantages, including the possibility to estimate closely spaced modes, which are hardly distinguished by frequency domain methods. However, they are often intensive from a computational standpoint.

The Random Decrement Technique (RDT) is a reliable and simple method proposed in 1973 by *Henry Cole* (Cole, Henry A. 1968; 1973) for computing free decay IRF. Although this is not a modal estimation method itself, the RDT has been commonly used in combination with other estimators to compute the free decay required for the following modal properties estimation. The principle behind the method is that any raw measurements, like ambient vibrations, are contaminated with large quantities of noise and stochastic information masking the deterministic data. Therefore, the method averages selected sections of data with a specified time duration. The selection of a portion of data is activated every time this reaches a pre-defined threshold, so the number of averaged sections depends exclusively on the type of data and the total length of the sample. After enough sections are averaged, the stochastic data is discarded and only the deterministic information remains in the form of an IFR.

Similarly to RDT, the Natural Excitation Technique is another solution for generating well-behaved IFR from raw measured data rather than a modal identification method (James, Carne, and Lauffer 1995). The method makes use of cross-correlation functions to compute IRF from the analysed signal and needs low amounts of computation for generating reliable results.

As mentioned above, the generation of the IRF is commonly a preliminary step towards modal identification. The Ibrahim Time Domain method (ITD) is a well-established technique that uses the IRF to compute modal parameters (Ibrahim and Mikulcik 1973). In the case that the registered input data are FRFs, an inverse Fourier transform is used to go from the frequency domain to the time domain. The method was then further improved in 1977 by the same author (Ibrahim and Mikulcik 1977; Ibrahim 1977). Despite that the ITD identification technique was one of the first techniques formulated for multiple output modal analysis based on IRFs or general free decays, the method has not been intensively exploited since the technique was originally formulated for single input systems. This approach is well-known for suffering problems in the case of closely spaced modes. Indeed, later developments of the method include improvements for dealing with closely located modes and working with MIMO systems (Malekjafarian et al. 2012; Rune Brincker et al. 2019).

The Eigensystem Realization Algorithm (ERA) is a MIMO method, based on control theory, that makes use of the SVD of the Henkel matrices generated from raw measured data to set up a System State model (J.-N. Juang and Pappa 1985; J. N. Juang and Pappa 1986). A problem of the method is

that the results from the SVD can be affected by noise or non-linearities in the analysed data, thus the method provides the possibility of performing checks of the calculated modes, to distinguish between actual and spurious ones.

Stochastic Subspace Identification (SSI) algorithms are powerful time domain methods capable of estimating modal parameters directly from raw measured data. SSI can properly deal with closely spaced modal components and present strong immunity to signal noise. Several types of SSI methods have been proposed in the literature over the past decades, such as covariance-driven, covariance-variate, and data-driven. Despite the inherent differences, all these SSI methods can be generalised into a unified theory dependent on the weighting matrix selection before the parametrical decomposition. As ERA, SSI methods are based on control theory and are one of the most accurate and reliable currently used identification techniques for structural modal analysis. Further information about SSI algorithms can be found in (Peeters and de Roeck 2001; Döhler, Andersen, and Mevel 2012; 2017; Gres et al. 2017; van Overschee and de Moor 1996; Greś et al. 2021).

Statistics and probability-based methods make use of statistical models to simulate the system behaviour and estimate the modal properties. The Complex Exponential (CE) method (Spitznogle and Quazi 1969) is an MDOF indirect local SISO method. It is a time domain modal analysis method that explores the relationship between an IRF and its complex poles and residues through a complex exponential and an Auto-Regressive (AR) model. The method does not require initial estimates for the modal parameters and the only unknown is the number of modes to be considered in the analysis.

The Least Square Complex Exponential (LSCE) method is an extension of the CE method for working on global MISO assessment (Brown et al. 1979). The solution of this model leads to the establishment of a polynomial whose roots are the complex roots of the system (i.e. the natural frequencies and damping ratios). Having estimated the roots, the residues can be derived from an AR model for computing mode shapes. Polyreference Complex Exponential (PRCE) further improves the CE method and LSCE method to perform MIMO modal analyses (Vold et al. 1989). Indeed, PRCE is a generalized and automatic method which provides a more accurate modal representation and can properly work with closely spaced modes. One known disadvantage is the sensitivity of the method to the presence of non-linearities in the measured data.

The Auto-Regressive Moving-Average (ARMA) method is a SISO technique based on control theory. The method uses a two-polynomial approach, one for the AR analysis, and another for the Moving-Average (MA) analysis (Will Gersch 1970; Will Gersch and Sharpe 1973; W. Gersch 1974; 1975; W. Gersch and Liu 1976; W. Gersch and Martinelli 1979; W. Gersch and Brotherton 1982).

Statistical methods have been developed for time-varying dynamic identification as well. An ARMA-based modal identification method for performing dynamic analysis on time-varying systems called the Time-Varying Auto Regressive Moving Average model in Vector form method (TV-ARMAV), was developed by *Bertha* et al. in 2017 (Bertha and Golinval 2017). This method not only allows the computation of time-varying natural frequencies but also time-varying mode shapes. However, it is limited to work with linear systems where the ratio of variation is slow with respect to the period of vibration. For further information on statistical methods, including applications to civil engineering systems, the reader is referred to (Grenier 1983; Saito and Beck 2010; Gomez, Ulusoy, and Feng 2013; Gong, Sun, and Xie 2014; S.-D. Zhou et al. 2014).

High-resolution (HR) methods are known for detecting frequencies, especially closely-spaced ones, in signals with a low signal-to-noise ratio (high-level noise). It is worth noting that many of these methods were not originally designed for working on civil engineering or seismic engineering applications, but they have been already successfully tested in many cases.

Blind Source Separation (BSS) emerged in the '90s as a powerful signal processing tool for de-mixing audio sources from recordings (Cardoso 1998), commonly known as the "*Cocktail party problem"*, where the goal is to separate a certain number of outputs from unknown sources registered all together into an unknown mixture of data. The method makes use of correlations and decorrelations of the analysed data based on the assumption that the measured data is a linear combination of statistically independent sources (Cardoso 1998; Hyvärinen, Karhunen, and Oja 2001). Even though the original BSS proposal was not related to structural analysis, the method has been successfully applied to assess dynamic structural parameters and system identification through output-only data (Kerschen, Poncelet, and Golinval 2007; Poncelet et al. 2007). BSS presents some problems that hinder a straightforward application to real-world case studies. For instance, the method relies on Principal Component Analysis (PCA) and requires an estimation of the mass matrix. An alternative solution consists of adopting the Independent Component Analysis (ICA) which presents better capabilities for assessing structural vibrations, despite a larger computational burden.

Second-Order Blind Identification (SOBI) is a modified version of BSS that makes use of second-order statistics. Likewise the BSS, SOBI was not originally proposed for structural analysis, nonetheless, it was successfully applied to perform structural dynamic identification using output-only data (Kerschen, Poncelet, and Golinval 2007; Poncelet et al. 2007; Hazra et al. 2012; K. Yang, Yu, and Li 2013), even though presented some issues when dealing with too closely spaced modes (Belouchrani et al. 1997).

The Multiple Signal Classification algorithm (MUSIC) (Schmidt 1979) is another method that was originally designed as an HR audio analysis algorithm, but it has also been successfully used to estimate the natural frequencies of civil structures. MUSIC method can properly identify closely spaced modes, but the pseudo spectrum calculated by MUSIC cannot be used for estimating damping ratios because its amplitude has no physical meaning (X. Jiang and Adeli 2007; Amezquita-Sanchez et al. 2013; Osornio-Rios et al. 2012).

During the last decade, a large number of nonparametric TFA methods have been developed to investigate the time-dependency of dynamic systems, where many of these existing nonparametric algorithms were designed to assess output-only structural vibrations resorting exclusively to an empirical approach. It is worth noting that this output-only design makes these methods unsuitable for performing EMA. Nonetheless, they have been proven successful in the context of OMA and especially in any case where there is little or no knowledge of the system characteristics. The previously commented HHT (Huang et al. 1998), has been successfully exploited for modal identification for civil engineering purposes (Shi, Shan, and Lu 2012) and structural damage detection (Simon Carbajo et al. 2014; J. N. Yang et al. 2004). Nonetheless, the EMD adopted for the HHT is negatively affected by highly noise-contaminated data, which is common for OMA acceleration measurements. Recently, Wavelet analysis has been successfully applied to modal identification, exhibiting relevant advantages, as both linear and non-linear data can be analysed. Recent research has explored the potential of wavelets to assess time-varying entropy measurements for SHM purposes as well (Civera and Surace 2022). Further information and applications of interest can be found in (Ruzzene et al. 1997; Dai, Xue, and Wang 2014; Hormazábal, Masciotta, and Oliveira 2021).

2.7 Vibration-based damage identification methods

Damage identification is a subdiscipline of SHM. However, the overlapping between their goals is so strong that the SHM's ultimate purpose has been described as the implementation of damage identification strategies (Farrar and Worden 2012). Vibration-based damage identification methods, a crucial subset within the broader SHM discipline, leverage the analysis of dynamic responses to detect and characterise damage in structures, offering valuable insights into the structural integrity and performance. Indeed, damage induces stiffness reductions that, in turn, lead to a decrease in modal frequency values and an increment in damping factors. Furthermore, localised damage alters the mode shapes as well. These methods have particularly drawn the attention of the scholars as they are suitable for identifying both global and local damage.

The damage identification process can be summarised according to Rytter's hierarchy in five main goals of increasing complexity (Farrar and Worden 2007; Rytter 1993):

(1) Detection of existence.

(2) Localisation.

(3) Classification of the type.

(4) Quantification of the extent.

(5) Prognosis.

Most of the methods developed to identify global structural damage consist of a direct assessment of the changes in the modal frequencies induced by the decrease in the stiffness of the structure, mainly due to structural cracks (Cawley and Adams 1979; Y. Narkis 1992; Messina, Williams, and Contursi 1998; He and Zhu 2011; C. Surace and Bovsunovsky 2020; Jarosińska and Berczyński 2021). It is worth noting that these parameters are correlated through an inverse square relationship, thus, larger reductions of stiffness are needed to generate a significant change in the modal frequency values.

Further proposals assess changes and differences between structural dynamic parameters through frequency domain or modal spectral responses. In 2015, Masciotta presented a spectrum-driven method that uses second-order properties of structural vibrations and successfully applied it to masonry structures and modern bridges (Masciotta 2015; Masciotta, Ramos, et al. 2016; Masciotta et al. 2017). A limitation of the frequency-based damage identification methods is that they can reliably detect the presence of damage (first level of Rytter's hierarchy) but they can hardly provide a higher order identification, for instance locating or quantifying it.

Another viable solution for damage identification consists of the assessment of the evolution over time of the displacement mode shapes and their higher derivatives. Indeed, the mode shapes determined through experimental or OMA repeated over time can be compared in order to establish discrepancies and similarities between them. Some of the most common sources of measured discrepancies are due to changing stiffness conditions related to structural damage, due to changes in the dynamic loads, or due changes in environmental conditions, etc.

Among the methods for shape comparison, the Modal Assurance Criterion (MAC) is by far the most used. MAC is designed to provide a measure of consistency (degree of linearity) between vectors, i.e. mode shapes or modal vectors (Allemang and Brown 1982; Greś, Döhler, and Mevel 2021).

MAC is mathematically defined as follows:

$$MAC_n = \frac{\left|\{\boldsymbol{\phi}_{u_n}\}^T\{\boldsymbol{\phi}_{d_n}\}^*\right|^2}{\left(\{\boldsymbol{\phi}_{u_n}\}^T\{\boldsymbol{\phi}_{u_n}\}^*\right)\left(\{\boldsymbol{\phi}_{d_n}\}^T\{\boldsymbol{\phi}_{d_n}\}^*\right)} \quad \text{(Eq. 2.37)}$$

where: $\boldsymbol{\phi}_{u_n}$: Undamaged displacement mode shape for mode n.

$\boldsymbol{\phi}_{d_n}$: Damaged displacement mode shape for mode n.

$\{\boldsymbol{\phi}_{u_n}\}^T$: Transposed undamaged displacement mode shape for mode n.

$\{\boldsymbol{\phi}_{d_n}\}^T$: Transposed damaged displacement mode shape for mode n.

$\{\boldsymbol{\phi}_{u_n}\}^*$: Complex conjugate of the undamaged displacement mode shape for mode n.

$\{\boldsymbol{\phi}_{d_n}\}^*$: Complex conjugate of the damaged displacement mode shape for mode n.

The use of MAC as damage sensitive feature requires the comparison of the actual mode shapes with the reference undamaged ones. A computed MAC value equal to 1 means an absolute similarity between the reference and the current mode shapes, thus no damage is detected. The lower this value becomes, the worse the mode shapes correlation is, likely due to a relevant damage condition. It is worth noting that, like in any experimental procedure, the estimation of the mode shapes is indeed affected by sources of uncertainty and error in the measurement and processing of the data likely leading to a reduction in the MAC irrespective of the occurrence of damage.

The Modal Scale Factor (MSF) is another method used for comparing mode shapes originated from different sources, by using a least-squares difference to project and scale a modal vector against a reference mode shape, i.e. numerically computed mode shapes from finite element (FE) analyses can be compared against mode shapes obtained from field testing, or several sets of experimental mode shapes from different measurements can be compared between them.

MSF can also be exploited to generate missing nodes when a pair of modal vectors are deemed consistent or similar and some DOFs cannot be measured, or in case some channels data are damaged or missing. To this end, a reference mode shape can be exploited in conjunction with the MSF to complete the missing data in other experimentally obtained mode shapes. By resorting to the same definitions of undamaged and damaged mode shapes previously used on Equation 2.37, the MSF is mathematically defined as follows:

$$MSF_n = \frac{\{\boldsymbol{\phi}_{u_n}\}^T \{\boldsymbol{\phi}_{d_n}\}^*}{\{\boldsymbol{\phi}_{d_n}\}^T \{\boldsymbol{\phi}_{d_n}\}^*} \quad \text{(Eq. 2.38)}$$

The Coordinate Modal Assurance Criterion (COMAC) is an extension of the MAC developed by Lieven and Ewins (Lieven and Ewins 1988), to assess the change in the response at each measured coordinate. As for the previous metrics, the computation of COMAC requires the comparison of mode shapes from two different structural stages. COMAC can identify which degree of freedom contributes more to a low correspondence between the same mode shape at different instants. COMAC is computed through the following expression:

$$COMAC_j = 1 - \frac{\left(\sum_{n=1}^{N} \left|\{\boldsymbol{\phi}_{u_{n,j}}\}\{\boldsymbol{\phi}_{d_{n,j}}\}\right|\right)^2}{\sum_{n=1}^{N} \left|\{\boldsymbol{\phi}_{u_{n,j}}\}\right|^2 \sum_{n=1}^{N} \left|\{\boldsymbol{\phi}_{d_{n,j}}\}\right|^2} \quad \text{(Eq. 2.39)}$$

where j is the coordinate, or number of the node.

COMAC is frequently used together with MAC. First, the mode shapes from the two stages are matched using MAC, and then, after establishing the set of the nodes and coordinates to be correlated, the COMAC is used to identify the locations where the differences are greater (Catbas et al. 1998).

Due to their widespread application, improved versions of MAC and COMAC have been developed over time, for instance, the COMAC-S criterion which relies on a scaling of the second set of mode shapes to minimise the quadratic norm of the difference between the two compared structural conditions (D. J. Ewins 2009; Allemang and Brown 1982; Catbas et al. 1998; Schwarz and Richardson 2003), or the Enhanced Coordinate Modal Assurance Criterion, which in addition to mode shape normalisation investigates phase consistency between each mode pair using the MSF (I. Hunt 1992).

Other methods assess the correlation between damaged and undamaged mode shape second derivatives or mode shape curvatures. Mode shape curvatures have been demonstrated to be more sensitive to damage and can accurately conduct damage localisation.

These second derivatives are generally calculated numerically through forward-difference approximation and backwards-difference approximation for the extreme nodes and central-difference approximation for any node located elsewhere. This numerical approximation likely induces errors in the estimation of the mode curvature, that are greater if a reduced number of nodes is used. Thus, this approach works better if mode shapes are smoothed through curve-fitting (Wahab and Roeck 1999).

Many curvature-based methods have been proposed and tested, such as the Mode Shape Curvature Method which computes an absolute difference between damaged and undamaged modal curvatures (Equation 2.40) (Pandey, Biswas, and Samman 1991).

$$\Delta\boldsymbol{\phi}''_{\boldsymbol{n}} = \sum_{n=1}^{N} \left| \boldsymbol{\phi}''_{u_n} - \boldsymbol{\phi}''_{d_n} \right| \quad \text{(Eq. 2.40)}$$

where: $\boldsymbol{\phi}''_{u_n}$: Undamaged curvature for modal shape n.

$\boldsymbol{\phi}''_{d_n}$: Damaged curvature for modal shape n.

Some of these methods have been tested over real case studies. Wahab and De Roeck, for instance, successfully applied the Curvature Damage Factor method (Equation 2.41) to the Z24 bridge located on the A1 highway between the cities of Bern and Zurich, in Switzerland (Wahab and Roeck 1999).

$$CDF = \frac{1}{N} \sum_{n=1}^{N} \left| \boldsymbol{\phi}''_{u_n} - \boldsymbol{\phi}''_{d_n} \right| \quad \text{(Eq. 2.41)}$$

Unlike frequency-based methods, mode-shape-based ones are more sensitive to changes in higher modes, due to their local nature. However, the well-known limitations in the estimation of such modes, due to the energy required to excite them, and the need for more sensors to correctly interpret their shapes may hinder their use for damage identification purposes.

To this end, promising strategies for damage identification have focused on changes in the flexibility matrix, namely the inverse of the static stiffness matrix. The flexibility matrix is estimated from mass-normalised mode shapes and frequencies. This approach has been demonstrated to be more sensitive to damage-induced changes and few lower modes can be sufficient for a reliable detection and localisation of the structural damage.

Examples of the aforementioned approach are the Change in the Flexibility Matrix method (equations 2.42 and 2.43) (Pandey and Biswas 1994), the Uniform Load Surface method with its variations (Z. Zhang and Aktan 1998; Sung, Jung, and Jung 2013; Yan et al. 2019), or further developments assessing changes on the flexibly matrix, together with natural frequencies and other modal parameters (L. Wang et al. 2022).

$$F = \sum_{n=1}^{N} \frac{1}{\omega_j^2} \{\boldsymbol{\phi}_n\}\{\boldsymbol{\phi}_n\}^T \quad \text{(Eq. 2.42)}$$

$$\boldsymbol{\beta} = diag\{F^d - F^u\} \quad \text{(Eq. 2.43)}$$

Non-modal estimation methods have also been developed. One of the first damage detection proposals using wavelet transforms exploited the capability of the transform to detect sudden changes in analysed signals and was used to assess a numerically modelled cracked beam (Cecilia Surace and Ruotolo 1994). CWT was also employed for detecting and localising damage in beams (Douka, Loutridis, and Trochidis 2003). A further approach by the same authors used CWT to assess the fundamental mode of a double-cracked beam for estimating the localisation and depth of the damage (Loutridis, Douka, and Trochidis 2004). The CWT was also used for damage identification on a plate with numerically simulated data and properly correlated the peaks of the wavelet coefficients with the damage locations (Chang and Chen 2004). Further research used the same idea to assess mode shapes for detecting damage on plates (Fan and Qiao 2009). A deep analysis of wavelet transform is presented in (Ovanesova and Suárez 2004), where the capabilities for damage detection in frame structures of the different types of wavelets are assessed and CWT and DWT are used. A complete review of different time-frequency techniques and wavelet transform for damage detection with output-only data is presented in (Nagarajaiah and Basu 2010).

HHT has also been applied to damage detection. A method based on EMD was developed to detect the presence of peaks in IMFs computed from acceleration data and the instants of sudden changes in stiffness (J. N. Yang et al. 2003). A second method was also proposed in the same paper, based on the prior and using an additional step, namely the application of HHT to finally detect the modal frequencies and damping factor. A further enhancement consisted of the automatization of the process through an Energy-based Frequency Weighted Average algorithm applied to the most significant IMFs in order to extract the involved frequencies (Simon Carbajo et al. 2014).

Machine Learning Algorithms have also been successfully used for deep analysis of vibration data to conduct structural damage identification. These methods are commonly used to identify patterns and reliable behavioural models to promptly detect any deviation from the expected structural response in newly acquired data. They allow to deal with and rely on big data flows produced by the monitoring systems, upon the extraction of damage-sensitive features, e.g. natural frequencies, spectrums, mode shapes or their derivatives as previously described. More recent approaches are

based on the emulation of biological functions or natural processes, in the form of bio-inspired algorithms that can potentially outperform conventional strategies. Indeed, biomimetics is commonly used to address nature-inspired algorithm designs (Vincent et al. 2006; Bhushan 2009). Inspired by the functioning of the central nervous system, in the early 1940s Artificial Neural Networks (ANNs) were developed and implemented in computer software as an attempt to formulate mathematical representations of the basic physiology of an interconnected mesh of neurons (Gupta, Jin, and Homma 2003). Many versions of ANNs have been developed and successfully applied to various tasks related to damage identification (Chun, Yamashita, and Furukawa 2015), such as Fuzzy Neural Networks (Wen et al. 2007; S. F. Jiang, Zhang, and Zhang 2011) Probabilistic Neural Networks (Li 2011; X. T. Zhou, Ni, and Zhang 2014; S.-F. Jiang, Zhang, and Koh 2006), Convolution Neural Networks (Avci et al. 2017; Abdeljaber et al. 2017; 2018), Back-Propagation Neural Network (Fang, Luo, and Tang 2005) among others.

Alternative approaches for classification have been inspired by the immune system. Among them, the Negative Selection Algorithm (NSA) was developed to address intrusion detection in computer systems (Forrest et al. 1994; Gonzalez, Dasgupta, and Kozma 2002). From then on, several versions have been developed to tackle the shortcomings that emerged in real-valued representation. NSA proved to be a valuable methodology to address anomaly detection in several contexts. An application to SHM for damage detection purposes was proposed in (Barontini et al. 2019; Barontini 2021).

2.8 Chapter conclusions and final remarks

The present chapter has provided a systematisation of the existing studies carried out in the field of modal identification and has analysed their relevance and possible application to SHM and early damage identification. The comprehensive literature review conducted allowed to point out a set of significant shortcomings as well as promising solutions to address them. In particular, the following conclusions, relevant to the present thesis work, can be drawn.

OMA is a reliable and non-invasive strategy to perform dynamic identification on any structure. Moreover, many times OMA is the only suitable approach as it minimises the interference with normal operations, the need for previous information regarding the structure's main features and the harm to the system.

Nonetheless, OMA algorithms need to properly deal with data presenting not optimal quality. Indeed, in the civil engineering field, structural modal identification resorting to ambient vibration tests under operational conditions could face many unexpected situations. In particular, available sources

of excitation commonly allow to explore the lower part of the frequency spectrum only. Additionally, it is common to obtain highly noise-contaminated signals, multiple unexpected high-transient events and very low amplitude structural responses to ambient vibrations.

Due to these issues, widespread algorithms for dynamic identification suitable for OMA often require very long acquisitions, several times the duration of the minimum period of interest or performing various measurements under similar controlled conditions. This is, for instance, the case of the CPSD matrices used in the EFDD method or the Henkel matrices used in ERA and SSI-based algorithms which require a vast amount of data in order to reduce the noise influence and to properly detect the presence of modes (Pourgholi et al. 2023; Carpine, Ientile, and Argoul 2023).

Moreover, these traditional methods assume that the assessed structures present linear responses to the inputs and often rely on parametric data decompositions applied to a weighted matrix, such as Eigenvalue and SVD decompositions. As these parametric decompositions make use of Fourier's series, henceforth, they are limited to the linear-elastic range of structural measurements and are not capable of performing dynamic identification in the presence of non-periodic and non-linear structural responses.

Furthermore, these methods fail to provide time-dependent results, meaning that each acquisition constitutes a single identification of the dynamic behaviour. Therefore, they cannot assess and track the evolution of the structural response due to quick changes in stiffness conditions (e.g. during and after a strong seismic event), if not by conducting recursive or sequential analyses.

These conclusions highlight the need for new dynamic identification methods and algorithms able to process signals affected by non-linear and non-stationary processes as well as relevant noise contamination and to track the time dependency of modal properties with reduced computational effort for real-time applications (Ubertini, Gentile, and Materazzi 2013; Masciotta 2015; Masciotta et al. 2017; Masciotta, Ramos, et al. 2016; Giordano et al. 2022).

3 THE EMILIA ALGORITHM

3.1 Introduction

The present chapter is devoted to a thorough presentation of the Enhanced Modal Identification for Long-term Integrity Assessment algorithm (EMILIA), including a description and testing of its main components. This novel time-dependent estimator makes use of a nonparametric time-domain data decomposition algorithm capable of analysing stationary and non-stationary scenarios as well as linear and non-linear structural data measured under any condition to perform output-only dynamic identification. The EMILIA algorithm design, coding, and development is based on three main stages:

(1) Wavelet time-domain discrete data decomposition.

(2) Hilbert transform TFA.

(3) Statistical and conditional probability analyses of previous outputs.

The main outcomes are instantaneous frequencies, instantaneous amplitude, and instantaneous displacements, together with a set of estimated statistics. To support a straightforward presentation of the method, simulated data from an undamped SDOF model with a one-kilogram mass and stiffness of $64\pi^2$ N/m (see Figure 3.1) and with the addition of normally distributed noise contamination is used throughout this chapter for practical examples ensuring the explanation and justification of the final components of EMILIA.

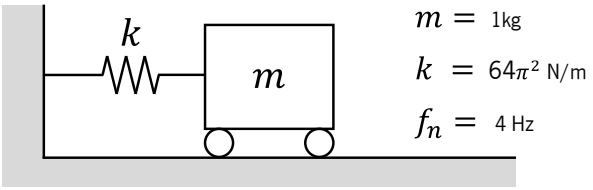


Figure 3.1: Undamped SDOF model.

The three stages and the main outcomes presented in Figure 3.2, are extensively detailed in the following sections, providing a comprehensive description and analysis of the adopted algorithms, and also performing benchmarking tests and comparisons against alternative methods.

To accomplish the aforementioned objectives, in the first part of the current chapter, the EMILIA algorithm is exhaustively addressed by recalling and expanding on further the theoretical framework outlined in Chapter 2, with output examples presented by resorting to the aforementioned undamped SDOF simulated data. In the second part of the chapter, a benchmarking test comparing different data decomposition algorithms is presented in order to justify the selection of wavelet analysis as the tool for performing the critical time-domain data decomposition.

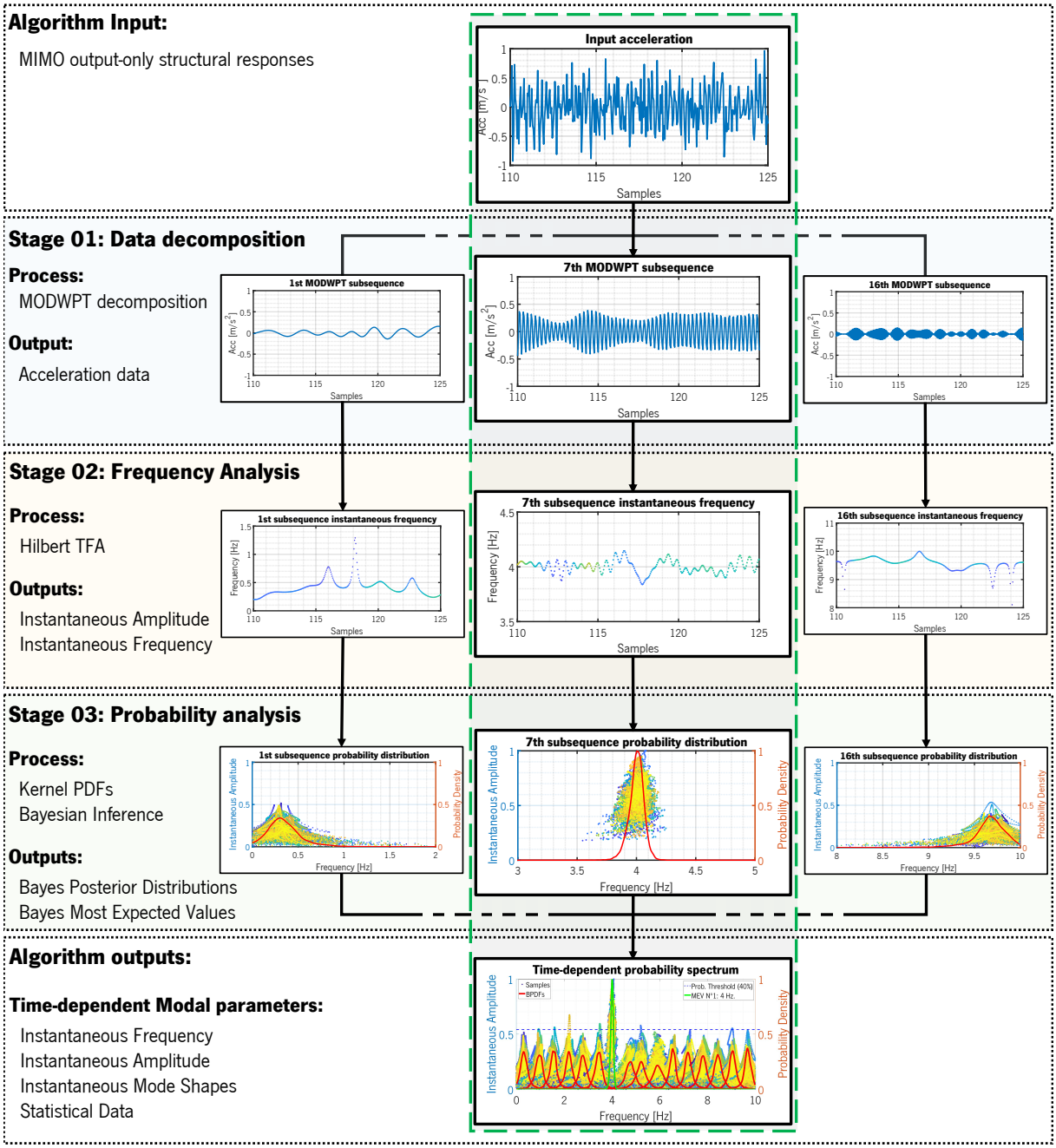


Figure 3.2: EMILIA algorithm workflow applied to the case study of Figure 3.1 processed with a four-level MODWPT decomposition. For the sake of brevity, only the first, the seventh, and the sixteenth subsequences are presented.

3.2 The EMILIA Algorithm

3.2.1 Stage 01: Data decomposition

As previously mentioned in Section 2.4, wavelet analysis is built on the convolution of a chosen mother wavelet function with the time series to examine, thus, in any wavelet-based analysis the assessment of the data comes from the evaluation of the area computed between functions, rather than envelope interpolations, curve fittings, or any other function modelling. This type of inner-function-

processing leads to a great resolution in time and to a robust identification against noise-contaminated signals and makes this type of analysis sensible to sudden changes in the data as well.

Figure 3.3 shows a normalised *Morlet* mother wavelet function (red coloured line) in five different states of dilatation, used to decompose the normalised accelerations from the undamped SDOF example data (blue coloured line).

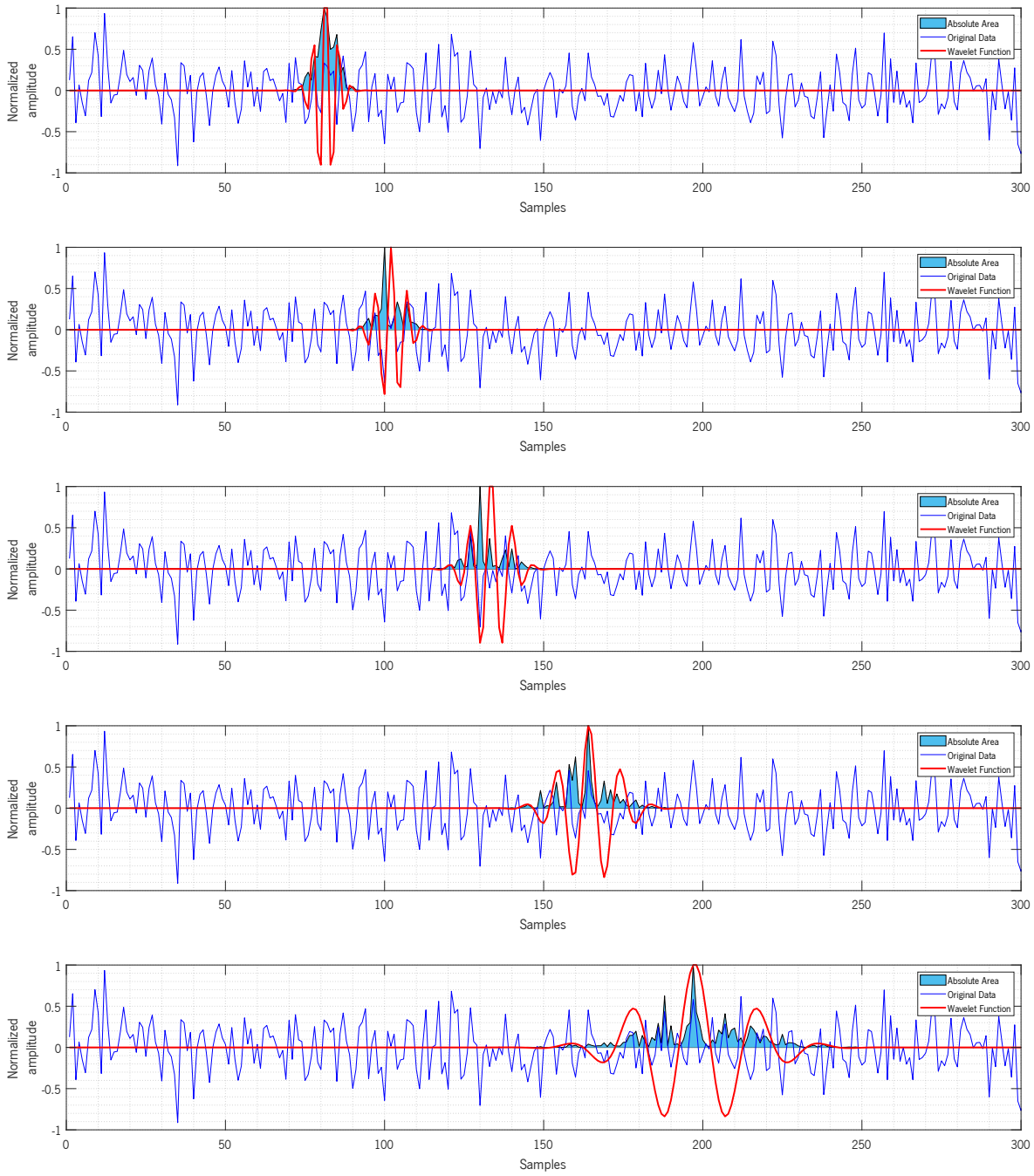


Figure 3.3: Example of the convolution process of continuous Wavelet analysis. The plots show Morlet wavelets with different dilatations (red colour), plotted against the normalized SDOF example data (blue colour). The light blue colour highlights the absolute area between the two functions.

The figure intends to visually resemble a continuous-time convolution process. For the sake of a better and more detailed visualisation of the inner process, only 300 samples of the data are presented. The convolution-based approach of the wavelet analysis explores the behaviour of the signal and identifies sudden or even instantaneous changes, being able to properly extract and represent the time-evolution of non-linear time-variant data. Despite that in the figure it is evident that wavelet analysis is affected by the chosen mother wavelet function, this dependency can be leveraged to select the mother wavelet based on the aim of the decomposition and the specific characteristics of the data. For instance, a wavelet function with many zero-crossing instants, formally known as vanishing moments, may be used to properly identify periodic information and reject sudden changes or noise in the data. On the other hand, if it is intended to detect sudden changes in the data, for example, to perform quick damage identification during or after seismic events, a mother wavelet function with fewer vanishing moments may be the most appropriate one to resort to.

The data decomposition stage of the EMILIA algorithm relies on the MODWPT algorithm to compute 2^m subsequences from each channel of the input data, where m is the level of the wavelet decomposition. Recalling what mentioned in Section 2.4, any DWT-based decomposition algorithm represents a discrete signal $x[n]$ as a set of m $D_m[n]$ and one single $A_m[n]$ time series (Figure 3.4), computed by repeating iteratively the convolution of $x[n]$ with a family of linear filters – low pass filters $g_m[n]$ as the scale functions and high-pass filters $h_m[n]$ as the wavelet functions – until reaching a certain level m:

$$A_m[n] = (x * g)_m[t,n] = \sum_{n=1}^{N} A_{m-1}[n]\, g_m[t-n] \qquad \text{(Eq. 3.1)}$$

$$D_m[n] = (x * h)_m[t,n] = \sum_{n=1}^{N} D_{m-1}[n]\, h_m[t-n] \qquad \text{(Eq. 3.2)}$$

where N are the number of discrete time steps or samples of the digitalised data. As aforementioned, since the DWT is an orthonormal transform, if an orthogonal discrete mother wavelet function is employed the computed subsequences $A_m[n]$ and $D_m[n]$ are orthogonal functions as well.

According to Nyquist-Shannon criteria, the original number of samples becomes redundant (Nyquist 1928; Shannon 1949), thus a decimation process of $A_m[n]$ and $D_m[n]$ is performed after every level of decomposition and the half of the frequency spectrum is discarded as well, so that each

new $A_{m+1}[n]$ and $D_{m+1}[n]$ has half the samples of its immediate preceding sequence. A direct consequence of the decimation process is the loss of resolution in the low-frequency zone of the spectrum, and additionally, this decimation process restricts the maximum achievable level of decompositions M as a function of the number of samples N in $x[t]$, according to the expression $M = log_2(N)$. It is worth noting that the sample size N must be an integer multiple of 2^m.

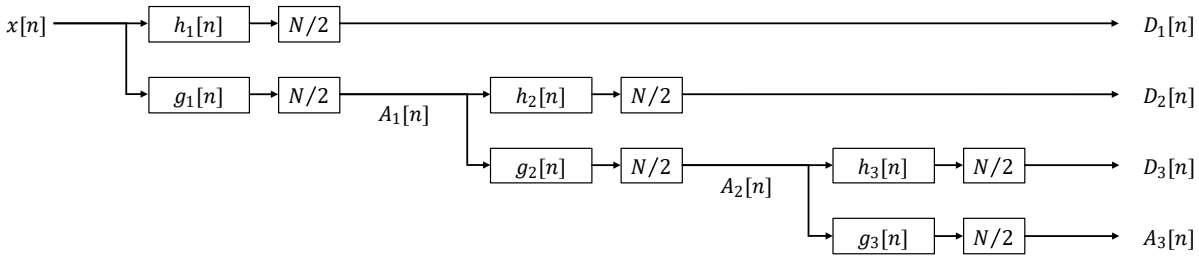


Figure 3.4: Schematic representation of a three-level DWT decomposition.

Furthermore, the iterative halving of the number of wavelet and scaling coefficients reduces the ability to carry out direct statistical and probability analyses along the coefficients of different levels.

Lastly, in the DWT the discrete wavelet and scaling coefficients are not circularly-shift equivariant, namely circularly shifting the time series by some amount will not circularly shift the DWT wavelet and scaling coefficients by the same amount.

The DWPT is a generalisation of the DWT in which at a certain level m of the transform, the frequency spectrum is divided into 2^m equal-width segments. The m-level coefficients are obtained by filtering the prior-level approximation coefficients with the corresponding discrete high-pass and low-pass filters.

Similar to the DWT, in the DWPT there is a decimation process after each level of decomposition. thus, increasing the decomposition level increases the frequency resolution but, once starting with a time series of length N, at level m there will be only $N/2m$ DWPT coefficients for each spectrum segment.

The MODWT algorithm shows a significant advantage concerning DWPT-based methods and is that an undecimated decomposition iterative process is performed. In this case, the filters $h_m[n]$ and $g_m[n]$ need to be re-scaled to conserve energy, then, the new high-pass filter is defined as:

$$\tilde{h}_m[n] = \frac{h_m[n]}{\sqrt{2}} \qquad \text{(Eq. 3.3)}$$

and the new low-pass filter is defined as:

$$\tilde{g}_m[n] = \frac{g_m[n]}{\sqrt{2}} \quad \text{(Eq. 3.4)}$$

The MODWT algorithm generates the wavelet coefficients and the scaling coefficients using these new filters with non-zero coefficients divided by $\sqrt{2}$. The MODWT coefficients computed at any level m are associated with the same nominal frequency band as for the DWT decomposition of the same level, but N coefficients are guaranteed at any level of the decomposition.

The data decomposition through the MODWPT algorithm (Walden and Cristan 1998) hereby adopted by the EMILIA algorithm is based on the DWPT algorithm, meaning that at a certain level m of the transform the frequency spectrum is divided into 2^m equal-width segments, and being a MODWT-based method as well, a non-decimated decomposition is conducted, therefore, there are no losses of resolution on the lower part of the frequency spectrum and, additionally, all the $W_m[n]$ subsequences computed after each decomposition level have the same number of samples as the original stream of data, which means that the decomposition outcomes can be used to perform further statistics or probability analyses.

For an orthogonal base of discrete wavelet functions, formally known as *wavelet family*, the low-pass filters can be defined as $\{g_{m.n}: n = 0, \dots, N-1\}$, and the high-pass filters can be defined as $\{h_{m,n}: n = 0, \dots, N-1\}$, and, as they are quadrature mirror filters, then:

$$h_{m,n} = (-1)^n \, g_{N-n-1} \quad \text{(Eq. 3.5)}$$

$$g_{m,n} = (-1)^n \, h_{N-n-1} \quad \text{(Eq. 3.6)}$$

thus,

$$\tilde{h}_{m,n} = \frac{h_{m,n}}{\sqrt{2}} \quad \text{(Eq. 3.7)}$$

$$\tilde{g}_{m,n} = \frac{g_{m,n}}{\sqrt{2}} \quad \text{(Eq. 3.8)}$$

then, by applying FFT, the transfer function of the low pass and high pass filters are presented in equations 3.9 and 3.10 respectively.

$$\tilde{H}_m(f) = \frac{1}{\sqrt{2}} \sum_{n=0}^{N-1} h_{m,n}\ e^{-2\pi\, j\, f\, n} \qquad \text{(Eq. 3.9)}$$

$$\tilde{G}_m(f) = \frac{1}{\sqrt{2}} \sum_{n=0}^{N-1} g_{m,n}\ e^{-2\pi\, j\, f\, n} \qquad \text{(Eq. 3.10)}$$

As previously mentioned, at the final level of the decomposition process the corresponding frequency spectrum is separated into 2^m equal-width segments, where each segment length can be expressed in terms of the sampling frequency through the expression $(f_s/2)/2^m$ Hz. A schematic representation of a three-level MODWPT decomposition can be observed in Figure 3.5.

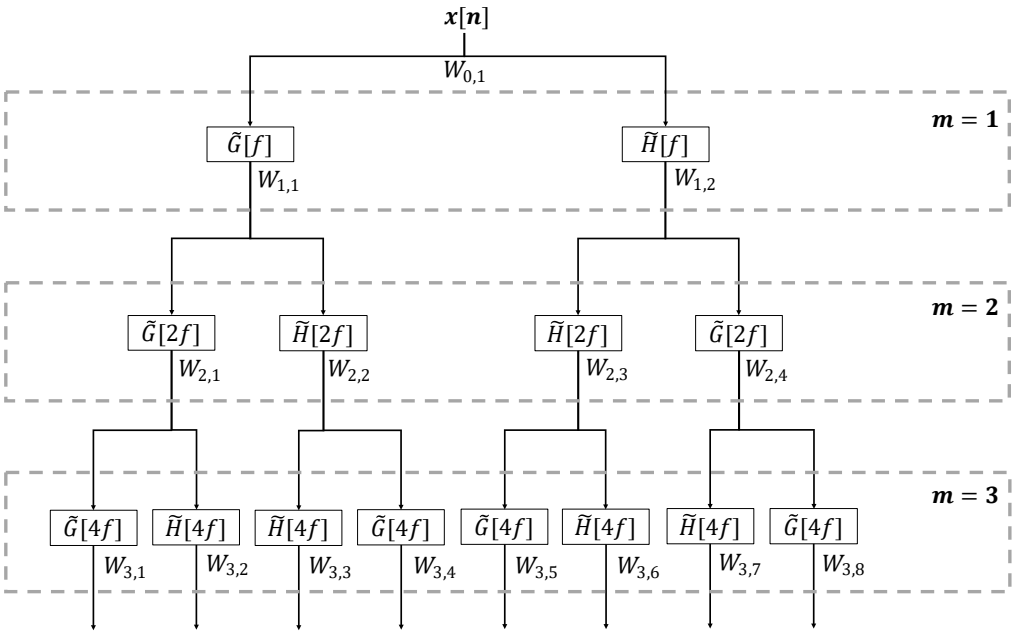


Figure 3.5: Schematic representation of a three-level MODWPT decomposition.

This first stage of the EMILIA algorithm has a $O(2m)$ time complexity according to the selected level of decomposition and the computed outcomes are two matrixes, one allocating the acceleration data and the other one allocating the displacement data. Both matrices have a space complexity equal to $[Ch, N, 2^m]$, where Ch is the number of channels.

For any analysis, the initial level of decomposition can be set according to the Nyquist frequency. For instance, if the data from the SDOF example are sampled at $f_s = 20$ Hz, the Nyquist frequency gives a total span of 10 Hz. By selecting a four-level decomposition, 2^4 subsequences are computed out from the wavelet decomposition, enough to fully cover the frequency range with at least one subsequence per each $(20\ /\ 2)\ /\ 2^4 = 0.625$ Hz spectrum segment. An unavoidable outcome of

splitting the frequency spectrum in equally spaced ranges, each one of $(f_s \ / \ 2) \ / \ 2^m$ Hz, is that some closely spaced modes may fall into a single range of the decomposition. In this case, the computed component would hold more than one frequency content. Thus, a relevant future enhancement of the algorithm consists in the optimisation of the trade-off between a sufficiently reduced span required to successfully isolate single modes and a larger span to prevent chopping the lower modes between different components or spectrum sections, without increasing excessively the computational burden that is significantly affected by the decomposition level.

Regarding the discrete wavelet function, an orthogonal mother wavelet with the highest possible number of vanishing moments is recommended to improve the modal identification. A mother wavelet function has p vanishing moments if, and only if, the wavelet scaling function can generate polynomials up to a degree $p - 1$, meaning that the scaling function alone can be used to represent such functions. Increasing the vanishing moments allows the scaling function to represent more complex functions while reducing the vanishing moments limits the wavelet capability to extract periodicities or polynomial behaviour in a signal. The vanishing moment is a criterion regarding the rate at which a certain function decays towards infinity, and it is closely related to the support required by a certain wavelet function. In continuous time, a wavelet function $\psi(t)$ will have p vanishing moments according to the following expression:

$$\int_{-\infty}^{\infty} t^k \psi(t) \, dt = 0 \qquad \text{(Eq. 3.11)}$$

for $0 \leq k < p$, where k is the rate of decay into infinity.

The size of the required support for the wavelet $\psi(t)$ is then related to the p vanishing moments. In the case of the Daubechies mother wavelets utilized in this thesis, the required support is equal to $2p$, but it is stressed that the previous is not a rule-of-thumb for wavelet design, and it only applies to the Daubechies wavelet family. For instance, the Coiflets family of wavelet functions requires a support of $6p$.

The size of the support can be understood as the size of the filter related to a corresponding mother wavelet, which can be further comprehended as the number of samples required by the filters.

For instance, Figure 3.6 presents the scaling function, the mother wavelet function, the low-pass and high-pass analysis filters used for data decomposition, and the low-pass and high-pass synthesis filters used for signal reconstruction from the Daubechies 8 mother wavelet, whilst Figure 3.7 shows the same functions and filter information but related to the Daubechies 20 wavelet function.

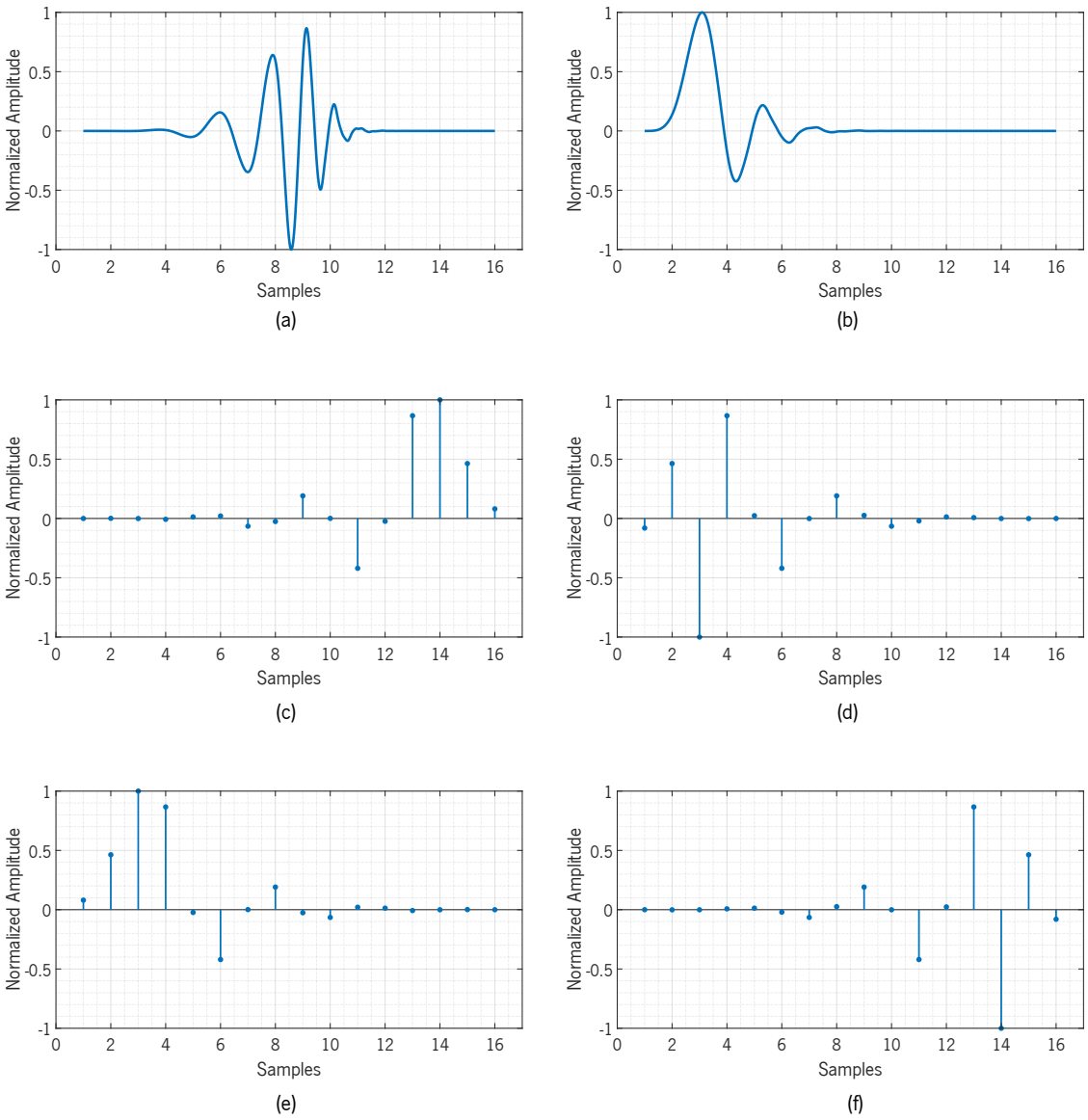


Figure 3.6: A Daubechies 8 scaling function (a) and its corresponding Daubechies 8 mother wavelet function (b), with its corresponding low-pass (c) and high-pass (d) analysis filters (decomposition algorithm), and the pair of low-pass (f) and high-pass (g) synthesis filters (for the reconstruction of the data).

In the second set of plots, it emerges that the Daubechies 20 mother wavelet and the scaling function offer considerably more zero-crossing points that will lead to an improved capability of assessing more complex and highly periodic data, against the capabilities that can be expected from a function with fewer zero-crossing points like the Daubechies 8 mother wavelet and scaling functions.

According to all the previously exposed, a Daubechies 45 mother wavelet function is the default solution exploited in the applications discussed in Chapter 4 and in Chapter 5 to analyse ambient vibration records. This ensures a robust modal identification when a linear and non-variational behaviour of the modal parameters is expected, by focusing the search on strongly periodic and continuous information and overlooking random transients and stochastic components of the signal.

The same solution is adopted also to process non-linear data under seismic excitation, due to the capabilities of this wavelet to deal with sudden events and stochastic data, rejecting the influence of noise and unexpected events.

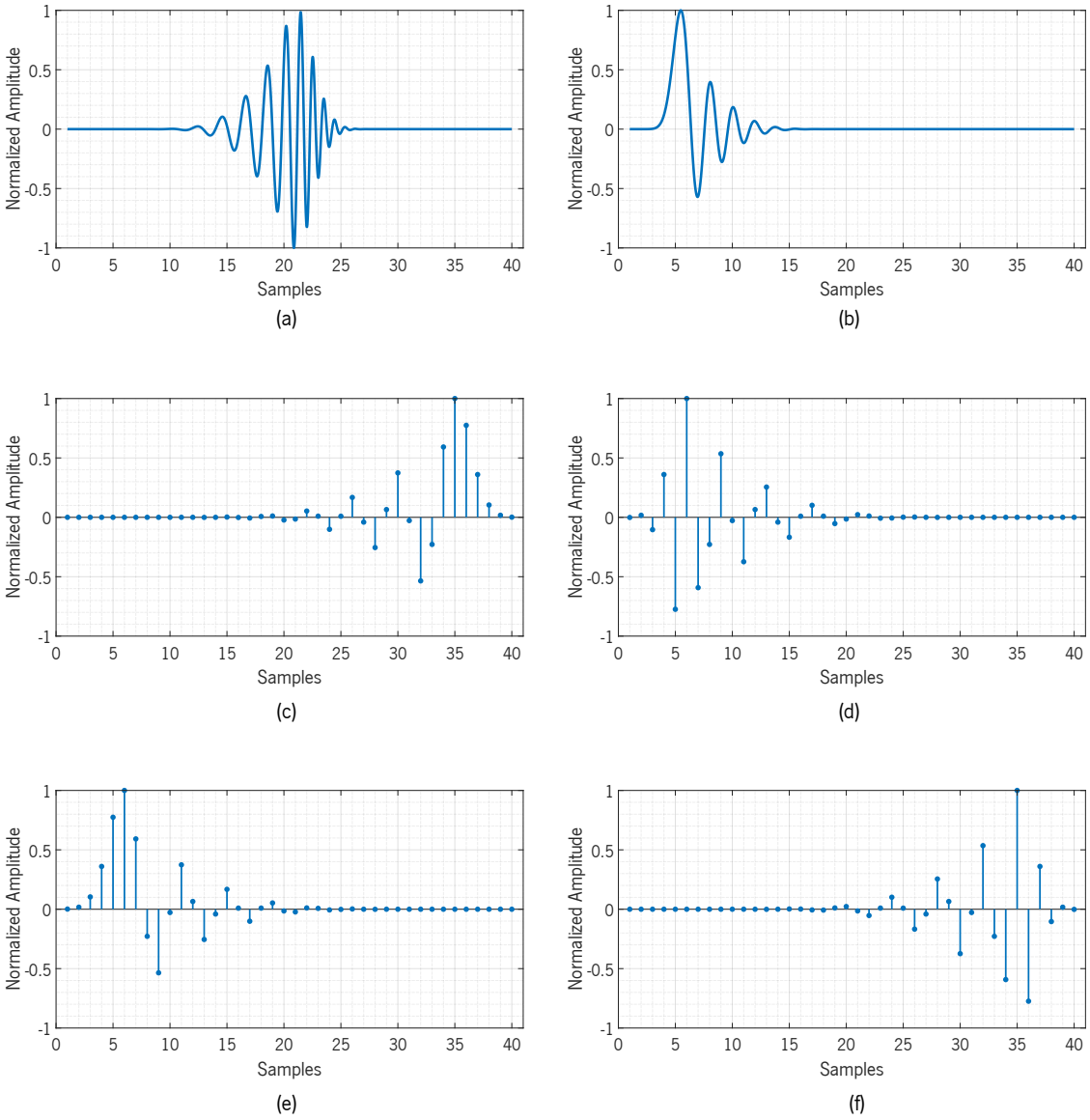


Figure 3.7: A Daubechies 20 scaling function (a) and the Daubechies 20 mother wavelet function (b), with its corresponding low-pass (c) and high-pass (d) analysis filters (decomposition algorithm), and the pair of low-pass (f) and high-pass (g) synthesis filters (for the reconstruction of the data).

The flowchart presented in Figure 3.8 displays some of the outcomes obtained after processing the undamped SDOF model data through a four-level MODWPT decomposition and using the previously mentioned Daubechies mother wavelet with 45 vanishing moments, resulting in a set of 16 acceleration subsequences. For the sake of brevity, only the first, seventh and sixteenth subsequences are shown. By direct comparison of the computed waveforms, it can be noticed that higher-level subsequences present shorter periods, thus belonging to higher frequency results than lower-level

subsequences that present larger periods. For Instance, the first subsequence at the bottom left and the last subsequence at the bottom right, are examples of lower and higher frequency information respectively, while the seventh subsequence in the middle, actually contains the modal information of interest, as it is determined in the subsequent steps of the analysis.

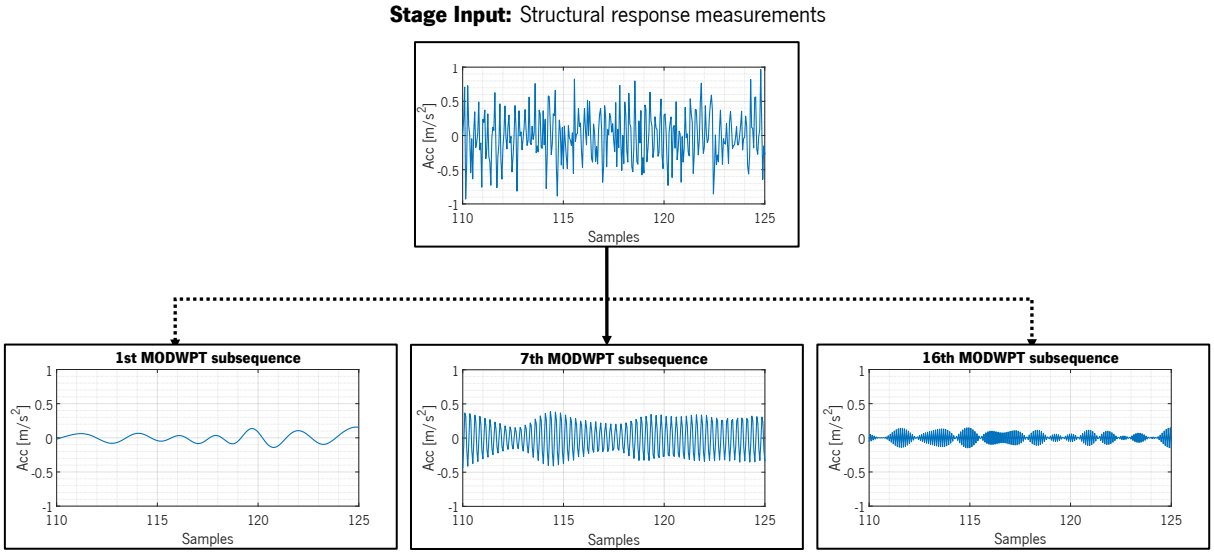


Figure 3.8: EMILIA algorithm first stage workflow: 1st (left), 7th (middle), and 16th (right) subsequences.

3.2.2 Stage 02: Time and frequency domain analysis

In the second stage of the proposed method, the Hilbert transform is exploited to compute an analytical signal from each one of the $W_m[n]$ subsequences produced by the MODWPT decomposition and obtain therefrom the corresponding instantaneous amplitude and instantaneous frequency data (Kijewski-Correa and Kareem 2006; Feldman 2011).

The Signal-to-Noise Ratio (SNR) is a mathematical resource commonly used in signal processing and data analysis to measure and quantify the amount of a desired signal against the background noise existing in the data. Theoretically, SNR is defined as the ratio of signal power to noise power, where an SNR value greater than 0 dB indicates that a higher amount of signal than uncorrelated noise can be found in the analysed data (Equation 3.12). A high level of SNR means that the signal is clear and easy to detect, while a low level of SNR means that the signal is deeply hidden in uncorrelated noise and may be difficult to separate or detect the desired data.

$$SNR = 10\log_{10}\left[\left(\frac{A_{data}}{A_{noise}}\right)^2\right] \quad \text{(Eq. 3.12)}$$

In order to explain the importance of the data decomposition prior to the Hilbert TFA, Figure 3.9 shows the SNR computed from the example SDOF full data directly, whilst Figure 3.10 shows the SNR computed from the seventh subsequence produced by the four-level Wavelet decomposition. In the first figure, the fundamental frequency is visible at 4 Hz (blue line) but it is rather covered by the broadband white noise in orange colour. The computed SNR level is -2.81 decibels, confirming the large amount of noise contamination that can be found in the raw data. In the second figure, as upon decomposition the modal data is isolated in a $(f_s \ / \ 2) \ / \ 2^m$ spectrum segment, the improvement in the quality is evident. This is reflected in a better SNR, equal to 9.57 decibels, meaning that the modal data emerges over the noise.

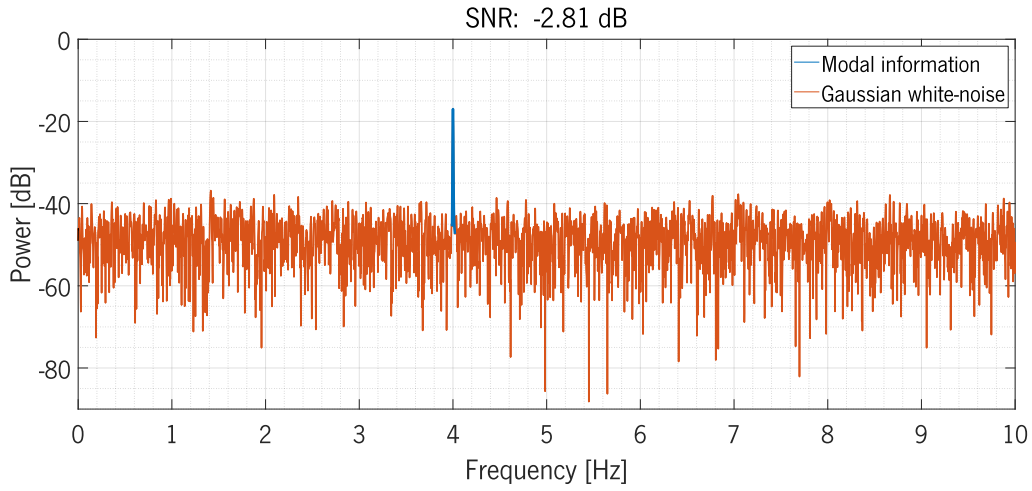


Figure 3.9: SNR from the example SDOF raw data. The natural frequency of 4 Hz is highlighted in blue against the background noise presented here in orange colour.

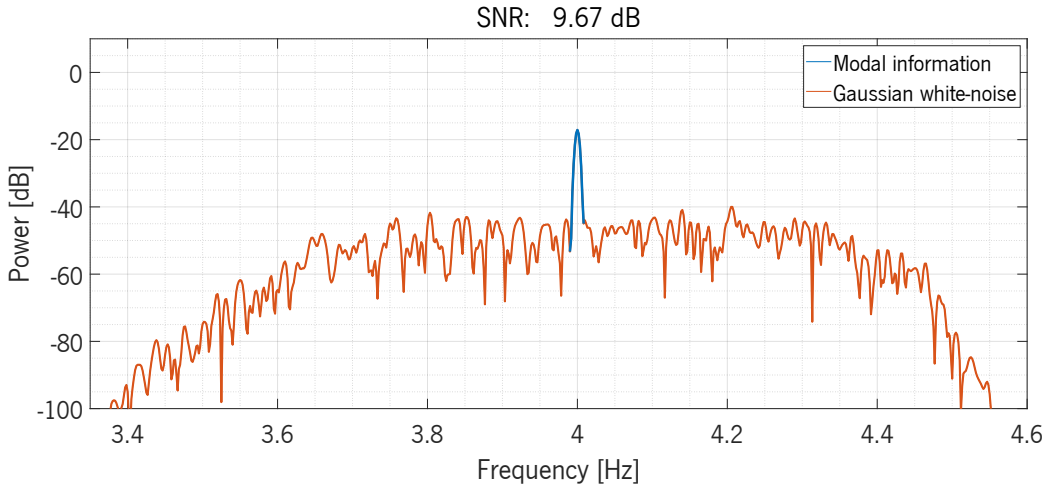


Figure 3.10: SNR computed from the seventh MODWPT subsequence. The natural frequency of 4 Hz is highlighted in blue against the background noise presented here in orange colour.

The MODWPT data decomposition previous to the TFA stage ensures an enhanced application of the HT by effectively reducing stochastic data and noise contamination. Indeed, the MODWPT outputs are pseudo-mono-frequential component signals, therefore perfect candidates for Hilbert analysis, resulting in well-behaved instantaneous frequency functions.

The analytical signals of each one of the MODWPT outputs computed by the Hilbert transform are noted onward as AS_m. Recalling Section 2.4, all the resulting AS_m are a complex-pair representation of each $W_m[n]$ pseudo-mono-component subsequence, with the imaginary part being the HT of the original $W_m[n]$.

Therefore, the Hilbert transform and the AS_m of each $W_m[n]$ subsequence are computed through equations 3.13 and 3.14 respectively.

$$HT\{W_m[n]\} = W_m[n] * g[n] \quad \text{(Eq. 3.13)}$$

$$AS_m[n] = W_m[n] + iHT\{W_m[n]\} \quad \text{(Eq. 3.14)}$$

By applying the modulus operation, the instantaneous amplitude A_{inst_m} is calculated as:

$$A_{inst_m}[n] = |AS_m[n]| = \sqrt{W_m[n]^2 + (HT\{W_m[n]\})^2} \quad \text{(Eq. 3.15)}$$

Finally, evaluating the time derivative of the analytical signal´s complex angle θ_{inst_m}, the instantaneous frequency ω_{inst_m} of each MODWPT output is obtained (equations 3.16 and 3.17). It is worth noting that according to Equation 3.17 the instantaneous frequency is a time-dependent parameter.

$$\theta_{inst_m}[n] = arctg\left(\frac{HT\{W_m[n]\}}{W_m[n]}\right) \quad \text{(Eq. 3.16)}$$

$$\omega_{inst_m}[n] = \theta'_{inst_m}[n] \quad \text{(Eq. 3.17)}$$

The algorithm's instantaneous amplitude output has a space complexity of $[Ch, N, 2^m]$ and the instantaneous frequency outputs have a space complexity of $[Ch, N - dX_N, 2^m]$, where dX_N is the number of samples used to compute the derivation of the phase angle.

As previously mentioned in Section 2.4, the Hilbert transform is not the only method developed to compute instantaneous outputs, as many other approaches have been successfully used in different areas of physics and engineering. However, upon a comprehensive pilot test, it has been considered the best-suited method for the specific purposes of the EMILIA algorithm.

For the sake of brevity, hereafter, a simple comparison is reported to discuss the main disadvantages of some of the alternative methods presented in Section 2.4. To this end, the acceleration data from the seventh subsequence of the MODWPT decomposition is used, and the graphic outcomes are presented in Figure 3.11. Additionally, in Table 3.1 are presented instantaneous frequency statistics computed from the same methods and results presented in the previously mentioned figure.

Table 3.1: Instantaneous frequency statistics computed through the methods in Figure 3.11.

Method	Mean	Variance	Min	Max	Kurtosis	Output Samples
Tieger-Kaiser	0.0555	0.0006	0.00	0.17	3.49	11998
Spectral moments	4.0057	0.0006	3.93	4.07	2.95	258
Zero-crossing	3.9895	0.0200	3.50	4.50	12.32	11990
Direct-Quadrature	3.9998	0.0161	1.83	4.33	9.45	11999
Adaptive Filtering	3.9992	0.0153	-6.03	4.29	3580.60	11996
Hilbert Transform	4.0000	0.0039	3.55	4.25	4.95	11999

According to the results that can be observed in Figure 3.11 (b) and the statistics computed from the instantaneous frequency data and presented above in Table 3.1, the Tieger-Kaiser operator fails to assess the example data, not being able to produce proper results mainly due to the noise content. Indeed, this confirms the main drawback of Tieger-Kaiser operators, namely their extreme sensitivity to stochastic data and sudden changes in the signal.

The same table shows the main drawback of the algorithms based on the computation of spectral moments from frequency distributions. As mentioned in Section 2.4, the output length of these methods is conditioned by the chosen number of FFT lines for the computation of the FFT or the PSD spectrums, producing a much smaller size of the output samples when compared with other methods.

Regarding the accuracy of these methods, however, the smooth output that can be seen in Figure 3.11 (c) and the statistics presented in Table 3.1 shows a sound identification with low variance of the 4 Hz natural frequency, which, combined with the low computational requirements, makes them a valid choice in the case of linear data where the main objective is to solely identify static frequency components with no further statistics or probability analyses to conduct.

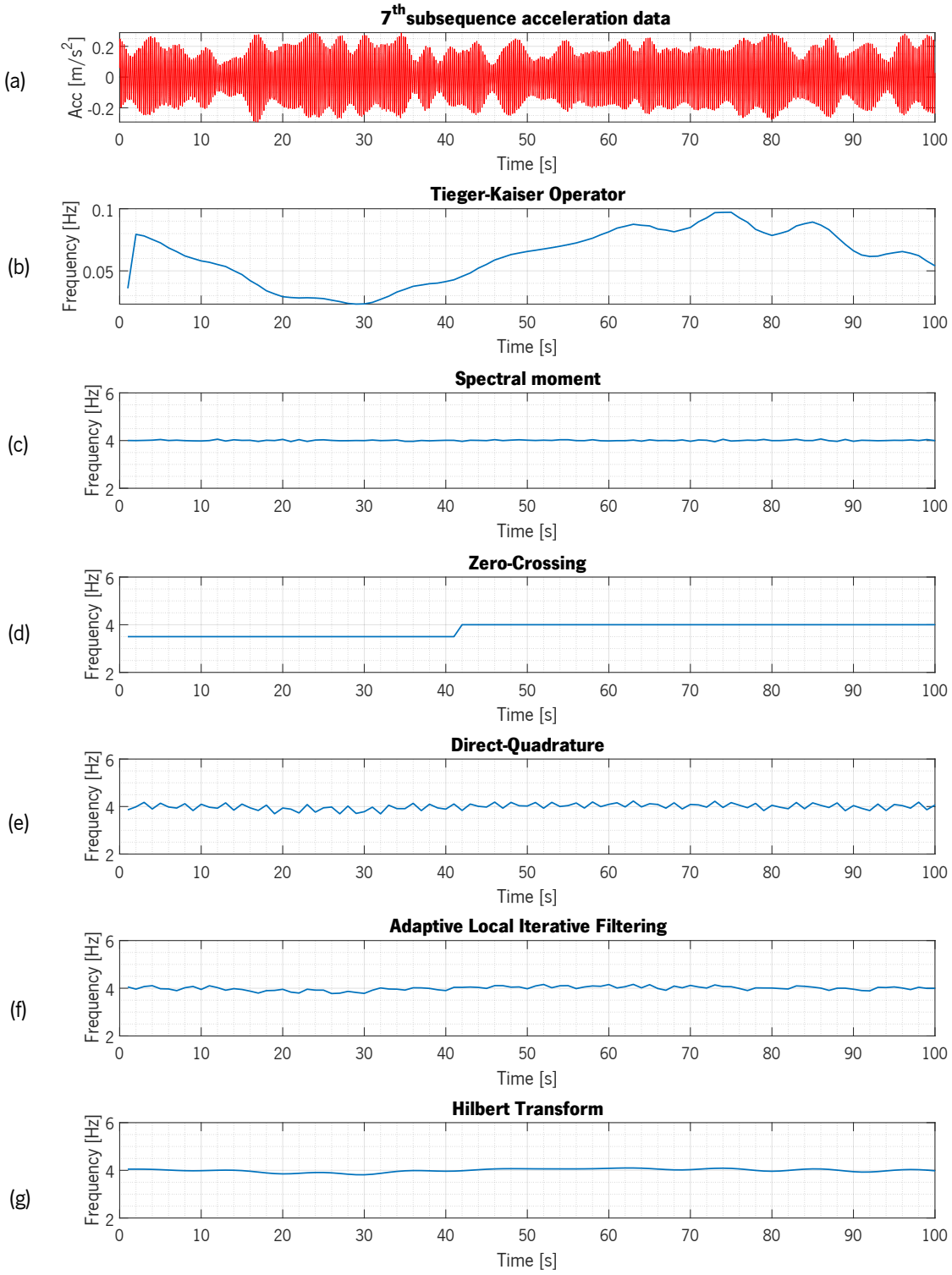


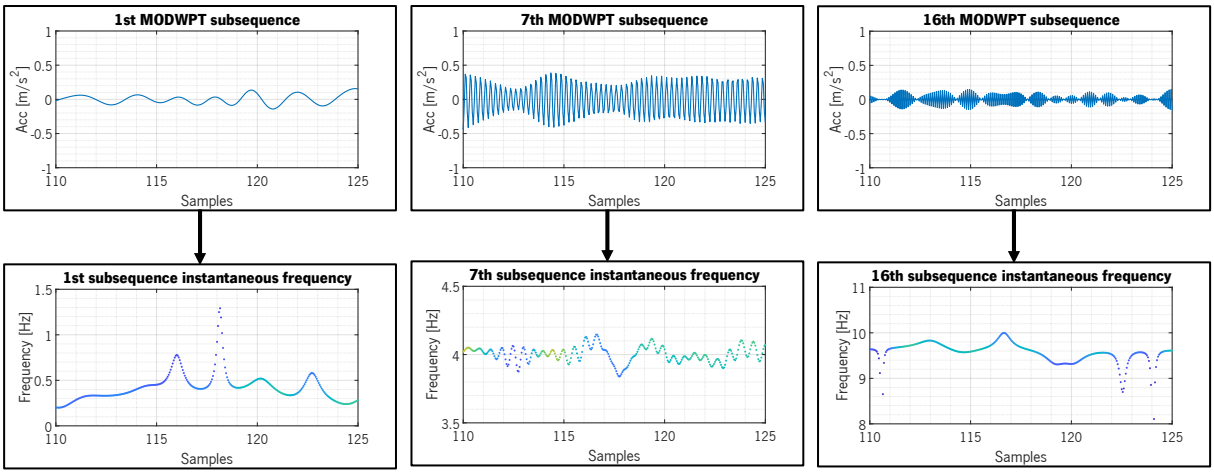
Figure 3.11: Comparison between different approaches for computing instantaneous frequency. At the top of the image, the original data is in red colour.

In Figure 3.11 (d), an estimation of instantaneous frequency computed through a zero-crossing approach can be observed. This algorithm calculates the instantaneous frequency within a certain amount of time by counting the zero-crossing events. Thus, the zero-crossing method outputs are comparable to a time-windowed approximation of the instantaneous frequency. Despite the previous, in Table 3.1, the method displays a fairly good estimation performance.

The results of the Direct-Quadrature approach are shown in Figure 3.11 (e), where the method shows an acceptable performance, as demonstrated by both the plot in Figure 3.11 and the statistics reported in Table 3.1 as well. In Figure 3.11 (d), the instantaneous frequencies calculated through the Adaptive Local Iterative Filter algorithm are presented. The version of the algorithm hereby implemented is the one described in (Cicone, Liu, and Zhou 2014). Like the Direct-Quadrature method, the adaptive Local Iterative Filter algorithm offers a sound identification of the desired frequency information and presents good statistical results as well. However, both the Direct-Quadrature and the Adaptive Local Iterative Filter methods produced several outliers among the minimum values obtained. This was especially evident for the Adaptive Local Iterative Filter method that computed negative frequency values, even while using linear non-variant data.

The instantaneous frequency outputs computed with the Hilbert Transform can be observed in Figure 3.11 (g). The outputs and the related statistics confirm the smoothness and the precision of the identification of the modal data. Indeed, this method shows the highest accuracy and one of the lowest variances among all the tested algorithms. Additional advantages of the Hilbert transform consist in its low computational requirements, robust formulation, and wide-spread adoption, which makes it available in almost any mathematical suite. Due to these reasons and upon a wider comparison of the alternative methods, with similar results to the ones here discussed, the Hilbert transform has been chosen as the most suitable component of the EMILIA algorithm to perform the computation of the instantaneous frequency. Figure 3.12 reports the outcomes of the second stage of the EMILIA algorithm for the same three subsequences previously presented in Figure 3.8.

Stage Input: Pseudo-SDOF acceleration subsequences (from previous stage)



Stage Output: Instantaneous Frequency and Instantaneous Amplitude data

Figure 3.12: Examples of instantaneous amplitude and frequency data computed from the first, seventh and sixteenth subsequences.

The three Hilbert spectrograms at the bottom of Figure 3.12 presents the instantaneous frequency data plotted against the time-steps over a white background, with the instantaneous amplitude information coded according to a colour scale, where deep-blue colour means a lower signal amplitude, whilst the yellow colour identifies higher amplitude values.

This type of graphic representation allows clear, easy, and informative visualisation of the instantaneous frequencies and their evolution over time within the acquisition.

3.2.3 Stage 03: Probability analysis

As mentioned earlier, the Hilbert transform of a multi-component signal can provide chaotic results with broadband instantaneous frequency values, which is a common outcome in the presence of noise contamination in the analysed data.

Furthermore, when working with non-linear data, and especially in the presence of sudden changes, the Hilbert transform likely produces outlier instantaneous frequency samples, including negative values due to the derivation of complex pairs.

As for the proposed EMILIA algorithm, the main goal is to perform modal analyses of potentially complex structures resorting to strong motion data recorded through multichannel acquisitions during seismic events, which are likely to induce non-linearities in the structural response and sudden changes in the amplitude and frequency content of the acceleration data, meaning that many outliers and stochastic outcomes are expected to be obtained from the Hilbert transform.

Therefore, additional tools for post-processing the raw instantaneous outputs are required in order to improve the dynamic identification and ultimately produce a single value of the frequency, estimated with higher reliability. It is worth noting that this static single value, per each acquisition, is a complementary outcome to the dynamic instantaneous values and not the only result produced, as in the case of traditional modal identification methods.

Therefore, in the third and final stage of the proposal, Probability Density Functions (PDF) of the instantaneous frequency data are computed and Bayesian inference is applied to estimate the final outputs using the total amount of instantaneous frequency samples available from all the channels of interest for this purpose.

Table 3.2 presents the computed variance (σ^2) and the maximum probability density of the instantaneous frequency values for the subsequences of the example SDOF previously presented in Figure 3.12. The seventh subsequence presents a lower variance and a higher maximum probability than the other two outputs, indicating a significant periodicity of the analysed data.

Table 3.2: Maximum probability density and variance from the first, seventh, and last subsequences.

Subsequence	Maximum Probability Density	σ^2
1	2.435	0.127
7	7.160	0.004
16	2.659	24.697

In order to obtain singleton natural frequency values, the Bayesian inference is adopted within the EMILIA algorithm as a robust method of statistical inference in which the computed probability distributions for any hypothesis (channel) are updated upon the availability of more observations (other channels) (Bayes 1763; Gelman et al. 2013). Bayes theorem is defined as:

$$P(H|O) = \frac{P(O|H)\ P(H)}{P(O)} \quad \text{(Eq. 3.18)}$$

where O is the new set of observations, H is the hypothesis whose probability may be affected by the new observations O, $P(H)$ is the estimate of the probability of the hypothesis previous to the new observations O, $P(H|O)$ is the updated probability of H given O, $P(O|H)$, also called likelihood, is the probability of observing O given H, and $P(O)$ is the marginal likelihood.

Computing any PDF requires the definition of an expected probability distribution to perform a parametric data fit. Normal parametric (Gaussian) distributions are commonly chosen, nonetheless, they are not always a good fit for the probability distributions that can be found in instantaneous frequency information of structural modes. Indeed, the latter often present resonant peaks with high amplitude and narrow bandwidth, hardly fitted by a Gaussian distribution.

To overcome this issue, Kernel distributions are here preferred. A Kernel distribution is a nonparametric representation of the probability distribution of a random variable, and it is defined by a smoothing function and especially by a bandwidth value that controls the smoothness of the resulting density curve. For any real values of x, the kernel density estimator is defined as follows:

$$\hat{f}_h(x) = \frac{1}{Nh}\sum_{n=1}^{N} K\left(\frac{x - x_n}{h}\right) \quad \text{(Eq. 3.19)}$$

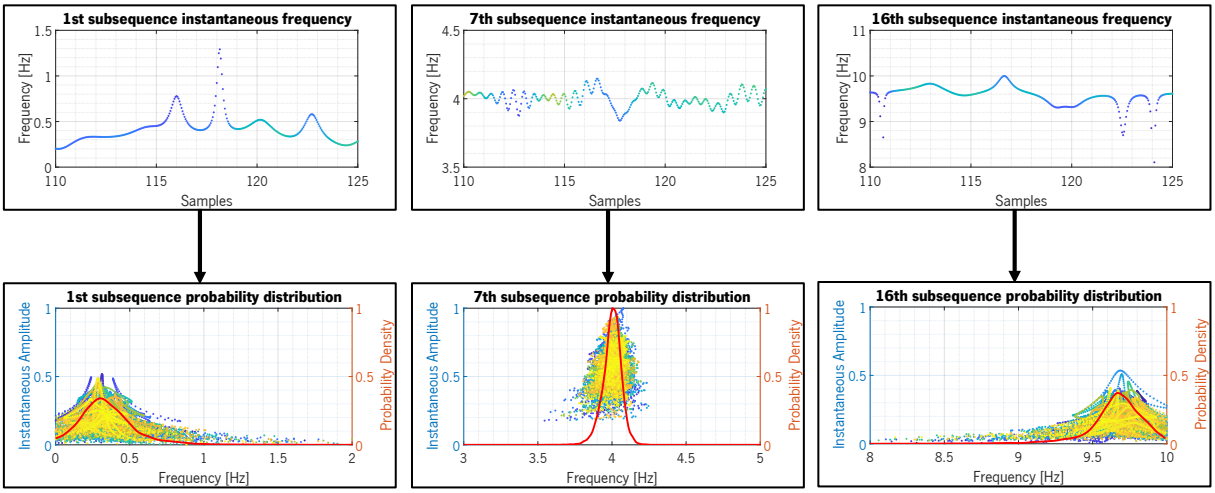
where h is the bandwidth, whereas N is the number of random samples $x_1, x_2, \dots, x_N$ from an unknown distribution and $K(\cdot)$ is the kernel smoothing function that defines the shape of the curve used to generate the computed probability distribution. Further information about Kernel distribution can be found in (Bowman and Azzalini 2000).

Therefore, at the beginning of the third stage of the EMILIA algorithm, Kernel distribution Probability Density Functions (KPDF) are computed for each one of the instantaneous frequency series. Afterwards, the Bayes theorem is applied to calculate Bayes Probability Density functions (BPDF) and the singleton frequency outputs f_{MEV} through Bayesian Most Expected Value (MEV).

At the bottom of Figure 3.13 it can be seen time-dependent probability spectrums computed from the instantaneous frequency samples obtained from the analytical signals of the first, the seventh and the last subsequences of the undamped SDOF example.

In the three spectrums, time information is coded as a colour scale where the older instantaneous frequency samples are presented in blue colour, the green-coloured samples belong to the middle of the analysis, whereas the yellow colour is used for the newest ones. For the sake of better visualisation of the spectrum thumbnails, the colour scales are not presented in Figure 3.13.

Stage Input: Instantaneous Frequency and Instantaneous Amplitude data (from previous stage)



Stage Output: Kernel PDF, Bayes PDF, and Bayes MEV

Figure 3.13: Time-dependent probability spectrums computed from the first, seventh and last subsequences obtained from the example SDOF data.

Figure 3.14 shows an example of a time-dependent probability spectrum computed using simultaneously the data from all the 16 output subsequences. In this graphic representation, it is possible to merge the instantaneous frequency and the instantaneous amplitude information and their evolution on time. Additionally, the probability results per channel and the BPDF per output are reported as well. Even though the resolution of time information presented as a colour scale is lower than the one that can be achieved in the Hilbert spectrogram time-axis, the time-dependent probability spectrum combines in a single item all the outputs from the proposed algorithm.

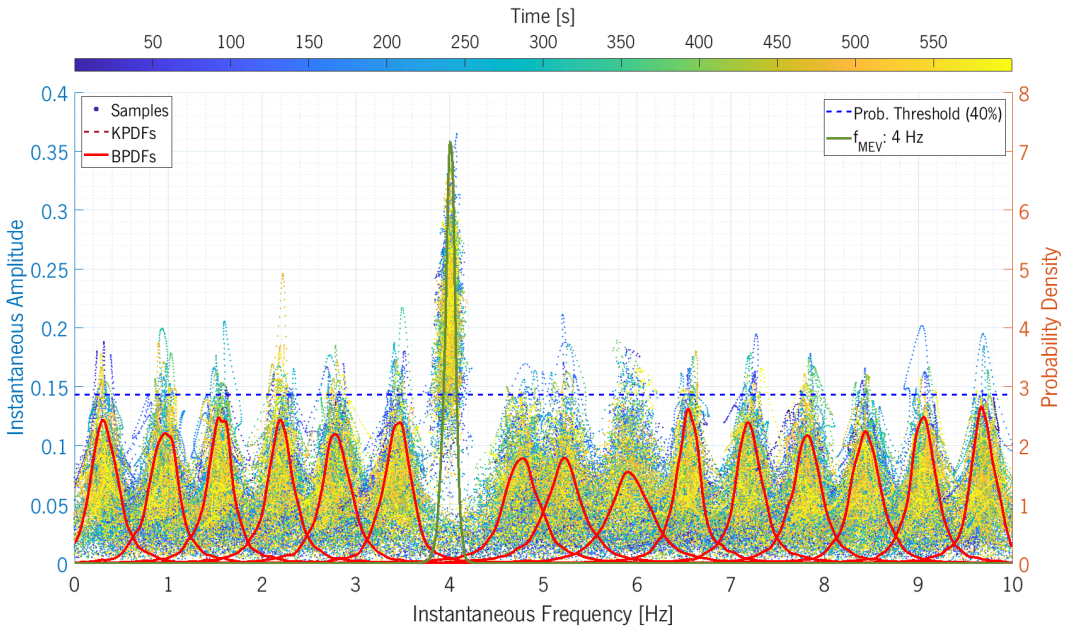


Figure 3.14: Complete time-dependent probability spectrum computed by the EMILIA algorithm from the SDOF example data.

In the figure, the computed ω_{inst_m} data are presented in the form of a scatter plot against their related A_{inst_m}, and each sample is coloured according to a scale that allows for identifying the time instant within the total duration of the acquisition. BPDFs are shown distinguishing with a continuous green line the identified modal information. For instance, the BPDF obtained from the seventh subsequence presents a clear peak at 4 Hz, showing a considerably higher probability than the other subsequences whose BPDFs are coloured in red. The EMILIA algorithm correctly identifies the modal information by labelling the subsequences with lower probability distributions (red lines) as spurious modes, likely due to noise and random events. As per the author's experience, for identification of structural modes based solely on the probability results while assessing linear data obtained ambient vibration measurements, a probability threshold equal to ten times the decomposition level is recommended. For illustration, in the example of Figure 3.14, the threshold is set to 40%, since four decomposition levels are adopted.

Worth noting that for pointwise analyses, as in the example, the computed KPDFs and BPDFs coincide. However, in the case of a multichannel analysis, the differences between the computed KPDFs and the final BPDFs are relevant.

The final algorithm outputs are time-dependent functions carrying information about the instantaneous frequency, the instantaneous amplitude and the instantaneous displacement shapes associated with the monitored structure. The instantaneous displacement mode shapes are determined through direct trapezoidal integration of the raw acceleration MODWPT subsequences

computed during the first stage. All the computed instantaneous outputs can directly be further analysed or processed, i.e. for computing instantaneous mode shapes derivatives.

For the sake of clarity, it is noted that the algorithm space complexity for the Instantaneous Displacement (Φ_{inst_m}) data is $[Ch, N, 2^m]$, and as previously mentioned, the space complexity for the ω_{inst_m} data is $[Ch, N - dX_n, 2^m]$ and for the A_{inst_m} data is $[Ch, N, 2^m]$.

3.3 Decomposition algorithms benchmarking test

Recalling Section 2.2, dynamic identification methods and data decomposition algorithms can be classified based on the domain where they perform the data decomposition.

In most of the frequency-domain data decomposition algorithms, the identification of the information of interest is conducted upon assuming stationary modes properly distributed along the frequency spectrum (not too closely located, nor coupled), often requiring a normal-like distribution of data with lower kurtosis and small damping (<5%). The reliability of these methods is commonly affected by noise contamination, non-linearities and high transient events induced by sudden changes in the analysed data.

The previous is mainly a consequence of the use of Fourier's series as solutions of the motion differential equation. Indeed, most of the frequency-domain data decomposition algorithms are based on Fourier´s theory by resorting to FFTs or PSDs of the analysed data to build weighted matrices that are then decomposed through SVD, where all the previously mentioned processes and tools are well known to share the restrictions imposed by the superposition principle.

On the other hand, time-domain-based data decomposition algorithms do not rely on PSD or FFT, thus, are less affected by the noise contamination that can be found in ambient vibrations structural measurements and, even more important, they are less affected by non-linearities or sudden changes in the analysed data. Nonetheless, they still suffer similar limitations as in the core of many of these methods the SVD remains the preferred approach for the decomposition.

Hereafter, the performance of the MODWPT decomposition algorithm is compared with two time-domain decomposition and three frequency-domain decomposition algorithms, to test the suitability of this method for the decomposition stage of the EMILIA algorithm. To this end, the same data from the undamped SDOF example previously displayed in Figure 3.1 is used and, upon decomposition, the instantaneous frequencies are computed by resorting to Hilbert transform TFA. For a further comparison between decomposition algorithms for SHM intents, the reader is referred to (Civera and Surace 2021).

In figures 3.15, 3.16, and 3.17 it can be observed the Hilbert spectrograms computed resorting to three frequency-domain data decomposition algorithms, namely the HVD, the EWT and the VMD. Among these three approaches the results provided by VMD present a better performance, seconded by the EWT algorithm, as it allows easy identification of the natural frequency even through simple visual inspection of the resulting spectrogram, which can be noticed on the high-intensity data around 4 Hz in Figure 3.17, whilst in the HVD and the EWT computed spectrograms a larger scatter emerges.

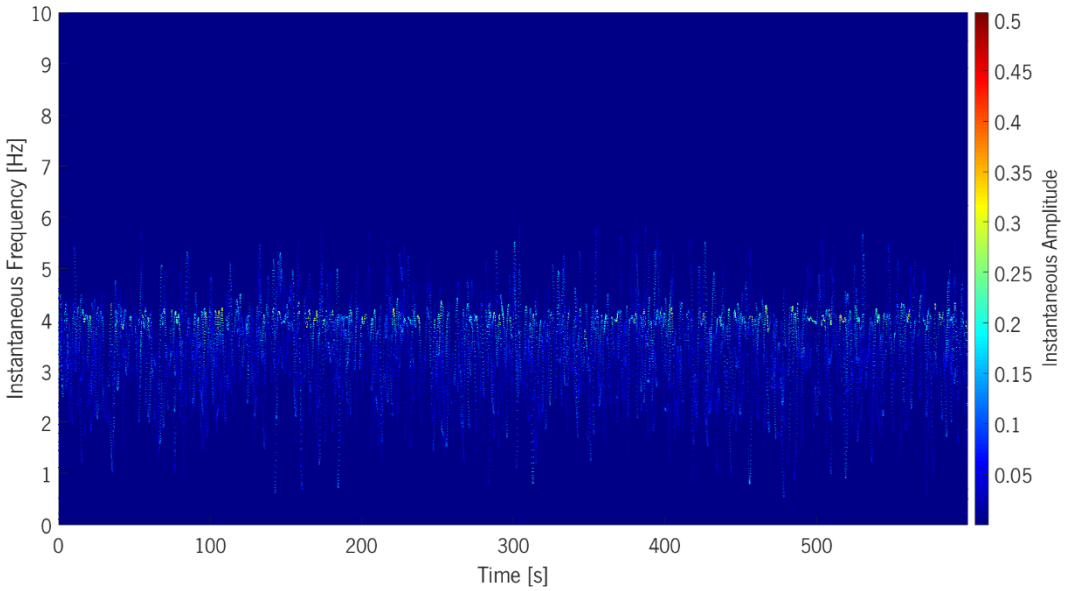


Figure 3.15: Hilbert spectrogram computed using the HVD decomposition algorithm.

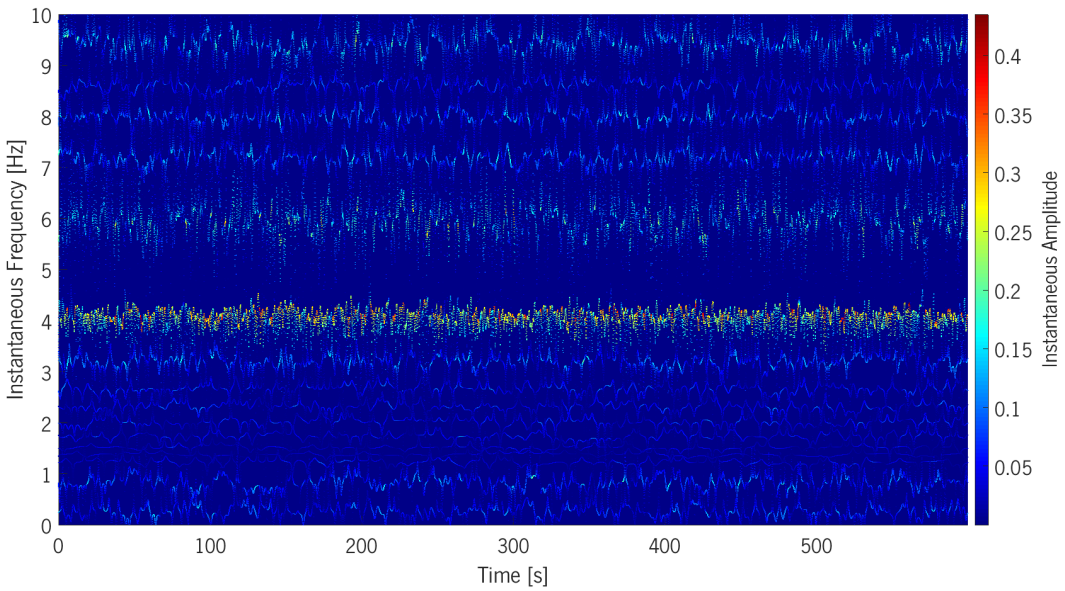


Figure 3.16: Hilbert spectrogram computed using the EWT decomposition algorithm.

In particular, the HVD algorithm in Figure 3.15 presents low resolution on the computed outputs with extremely high variance. The method computes nearly the same aliased results along the different subsequences, resulting in the overlapping instantaneous frequency samples, as presented in the figure and reflected in the coloured samples scattered around the 4 Hz zone.

The VMD algorithm, instead, appropriately processes the whole frequency spectrum, properly dealing with the high noise contamination that can be found in the data and producing different outputs well-spaced along the Y axis of Figure 3.17. However, these outputs are not even distributed along the frequency spectrum, showing wider spans and variance for increasing frequency content.

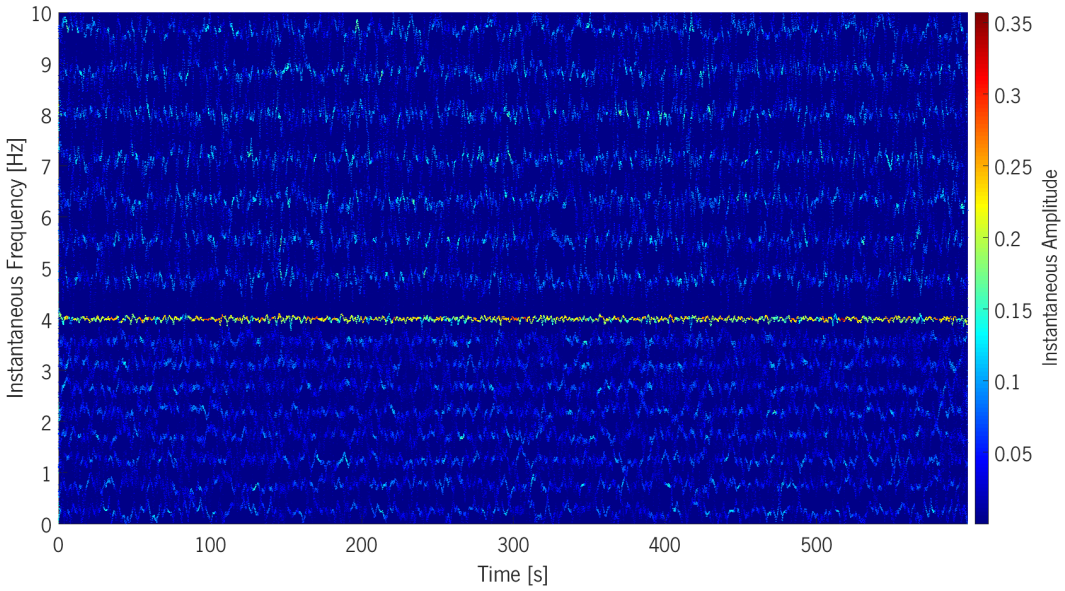


Figure 3.17: Hilbert spectrogram computed using the VMD decomposition algorithm.

In figures 3.18, 3.19, and 3.20 the Hilbert spectrograms computed based on the EMD, MODWT, and MODWPT time-domain decomposition methods are presented.

The EMD decomposition algorithm, which used in conjunction with the Hilbert transform is known as the Hilbert-Huang transform (Huang and Shen 2005), is not capable of providing a proper identification process for the simulated acceleration data, mainly due to the amount of noise contamination, therefore, it computes several spurious modes with high variance in addition to various aliased low-frequency modes. This is reflected in the utterly flat Hilbert spectrogram with highly scattered instantaneous frequency samples presented in Figure 3.18.

Furthermore, the simple visual inspection of the graphic outcome does not allow the identification of the modal frequency content, showing even more dispersed instantaneous samples than the outputs computed by the HVD method previously presented in Figure 3.15. Indeed, both HVD and EMD decomposition algorithms presented the worst performances, with the second producing

almost flat spectrograms with negligible peaks or defined high-energy zones that can be straightforwardly identified as modal information. Compared with the previously discussed EMD, the MODWT (Figure 3.19) and the MODWPT (Figure 3.20) decomposition algorithms offer better outputs allowing to identify the modal information located in the 4 Hz zone.

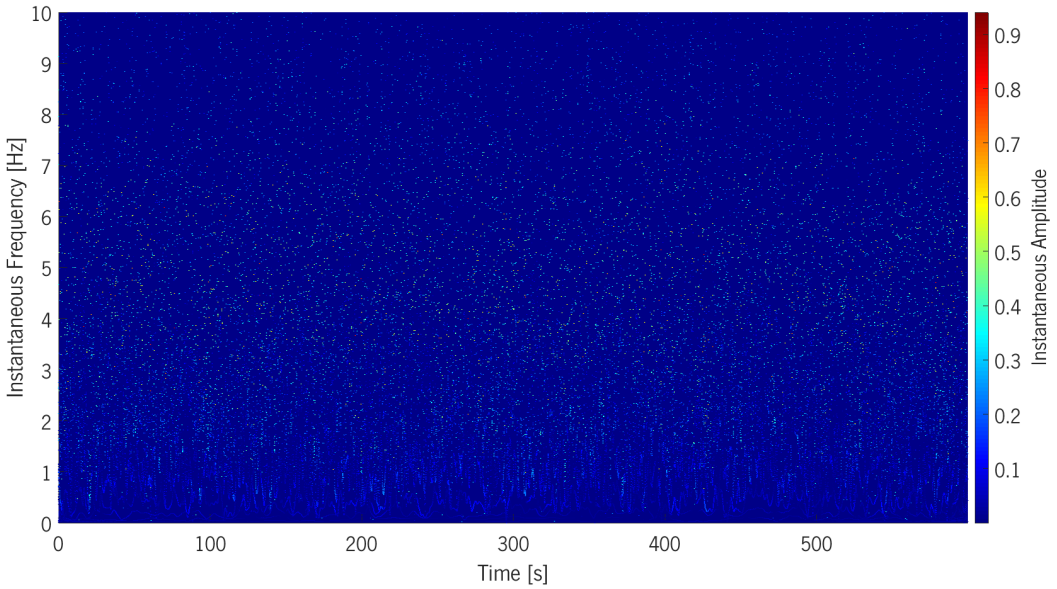


Figure 3.18: Hilbert spectrogram computed using the EMD decomposition algorithm.

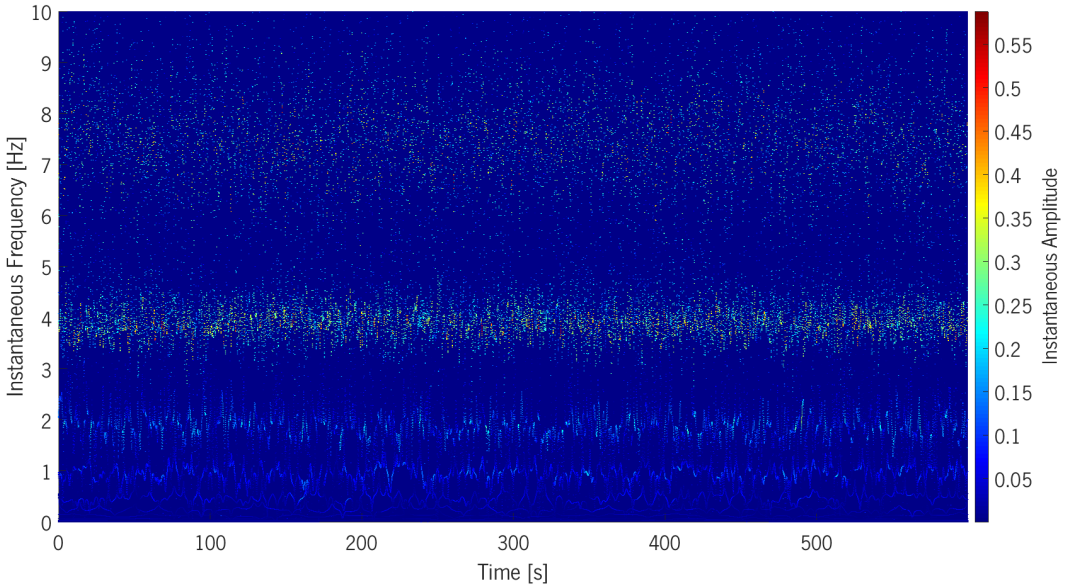


Figure 3.19: Hilbert spectrogram computed using the MODWT decomposition algorithm.

However, in Figure 3.19. it can be observed that the MODWT leads to the identification of several spurious modes and a poor frequency resolution, especially in the higher frequency range, offering a larger variance of the instantaneous frequency samples around the 4 Hz zone. This lower performance

is especially evident when compared with the outputs computed by the VMD and the MODWPT algorithms in Figure 3.17 and Figure 3.20 respectively. Additionally, it can be observed that the computed outputs are not equally distributed along the whole frequency axis, presenting wider spans for higher frequency results and higher variance in the plotted samples.

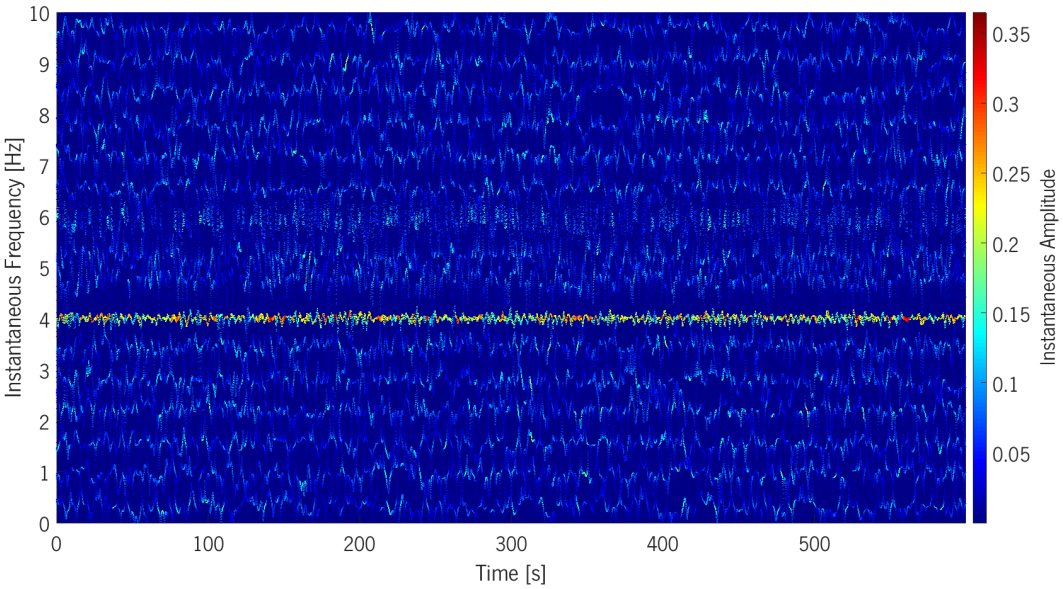


Figure 3.20: Hilbert spectrogram computed using the MODWPT decomposition algorithm.

Instead, the Hilbert spectrogram computed with the MODWPT decomposition and presented in Figure 3.20 shows an improvement of the computed outputs distribution along the frequency axis with a significantly superior resolution than the other tested wavelet based decomposition algorithms (EWT in Figure 3.16, and MODWT in Figure 3.19). Additionally, the MODWPT properly splits the spectrum into equally spaced $(f_s \ / \ 2) \ / \ 2^m$ frequency spans, allowing to entirely cover the frequency spectrum of interest with segments of previously known length, properly targeting the desired modal information. Finally, the accuracy of the results itself is enhanced.

Only the VMD algorithm is able to produce a similar performance of the identification, even obtaining a lower variance in the computed output holding the modal information. This performance makes the VMD algorithm an interesting candidate for designing dynamic identification algorithms when combined with the Hilbert transform TFA.

The outcomes presented in the Hilbert spectrograms are largely confirmed by the statistics of the distinct identifications, reported in Table 3.3 for the three frequency-domain decomposition algorithms. Here, the outcomes are reported in terms of mean and variance computed from the instantaneous frequency samples obtained through Hilbert transform TFA of each generated subsequence.

The HVD method computes only seven subsequences against the 16 outputs generated by EWT and VMD. This is because both EWT and VMD allow the selection of the number of fixed outputs, while the HVD algorithm does not allow it. Furthermore, HVD identifies almost the same instantaneous frequency mean along all the seven outputs but misses the correct natural frequency value along all of them.

Table 3.3: Frequency-domain decomposition algorithms instantaneous frequency output statistics.

Output	HVD		EWT		VMD	
	Mean [Hz]	σ^2	Mean [Hz]	σ^2	Mean [Hz]	σ^2
1	3.50	0.542	0.26	0.099	0.24	0.086
2	3.37	0.775	0.82	0.103	0.76	0.123
3	3.33	0.878	1.23	0.014	1.25	0.080
4	3.32	0.951	1.38	0.010	1.73	0.071
5	3.32	1.000	1.51	0.022	2.20	0.078
6	3.30	0.983	1.73	0.020	2.67	0.087
7	3.32	1.089	2.01	0.036	3.12	0.119
8	—	—	2.32	0.029	3.56	0.113
9	—	—	2.67	0.052	4.00	0.002
10	—	—	3.19	0.180	4.77	0.228
11	—	—	4.01	0.129	5.55	0.314
12	—	—	5.90	1.360	6.30	0.472
13	—	—	7.15	0.511	7.09	0.597
14	—	—	7.94	0.994	7.95	1.162
15	—	—	8.56	0.723	8.67	2.761
16	—	—	8.08	22.412	8.31	23.143

On the other hand, the means of the outputs from the EWT and the VMD algorithms confirm their effective selection of the filter banks to adequately investigate the full spectrum, from 0 Hz until the Nyquist frequency. Furthermore, both methods yield a correct identification of the modal information: the EWT algorithm on the eleventh output, whereas the VMD algorithm on the ninth output. Worth remarking that the VMD decomposition algorithm additionally presents the lower computed variance among the instantaneous frequency results.

Like the previous table, Table 3.4 shows the same statistics but computed for the three time-domain decomposition algorithms. Similar to the HVD algorithm, the EMD and the MODWT algorithms identify fewer components than the MODWPT algorithm. This is due to the presence in the EMD and the MODWT of criteria to stop the decomposition process according to the remaining data. The MODWPT algorithm, instead, allows to preset the number of computed outputs.

The results presented in the table for the EMD decomposition algorithm include several spurious modes in the lower range of the frequency spectrum, which are mainly due to the noise content in the example data. The influence of noise contamination likely produces seven computed IMFs, out of the total ten, that are just frequency-octave outputs, which is a typical output of the EMD decomposition in response to high levels of stochastic data (Huang 2014).

Furthermore, it can be noticed how the computed variance is increasing along the obtained outputs, with the tenth IMF presenting an enormous variance, and being the one holding the actual modal information this finally leads to the null possibility of a straightforward visual identification of the data presented in Figure 3.18. Similarly, according to their computed instantaneous frequency mean and variance, the first ten outputs of the MODWT are merely related to the stochastic content of the data. On the other hand, the outputs obtained by the MODWPT algorithm are evenly spaced according to the $(f_s \,/\, 2) \,/\, 2^m$ spectrum resolution, meaning that the computed outputs are properly distributed along the whole spectrum, simplifying targeting the modal information of interest inside each range.

Table 3.4: Time-domain decomposition algorithms instantaneous frequency output statistics.

Output	EMD		MODWT		MODWPT	
	Mean [Hz]	$\boldsymbol{\sigma^2}$	Mean [Hz]	$\boldsymbol{\sigma^2}$	Mean [Hz]	$\boldsymbol{\sigma^2}$
1	0.002	0.000	0.000	0.000	0.33	0.127
2	0.006	0.000	0.002	0.000	0.96	0.142
3	0.016	0.001	0.003	0.000	1.55	0.174
4	0.036	0.001	0.007	0.000	2.19	0.179
5	0.078	0.003	0.015	0.000	2.78	0.235
6	0.190	0.009	0.028	0.000	3.44	0.164
7	0.430	0.060	0.055	0.002	4.00	0.004
8	1.025	0.308	0.123	0.002	4.75	0.324
9	2.458	1.581	0.238	0.007	5.19	0.458
10	4.171	19.827	0.462	0.045	5.89	0.689
11	–	–	0.957	0.142	6.52	0.410
12	–	–	1.875	0.566	7.17	0.499
13	–	–	3.960	0.452	7.77	0.691
14	–	–	5.883	19.397	8.37	1.107
15	–	–	–	–	8.85	3.387
16	–	–	–	–	8.27	24.679

A final comparison among the alternative decomposition algorithms is carried out by resorting to the statistical analysis of the instantaneous frequency samples computed from the subsequence holding the modal information, whose statistics are reported in Table 3.5.

This result corroborates the previously presented ones, leading to the conclusion that the VMD frequency-domain decomposition algorithm and the MODWPT time-domain decomposition algorithm are the data decompositions leading to the best performances.

Table 3.5: Instantaneous frequency statistics computed resorting to the different decomposition algorithms applied to the time series containing the modal information.

Algorithm	Frequency Domain			Time Domain		
	HVD	EWT	VMD	EMD	MODWT	MODWPT
Outputs	7	16	16	10	14	16
Variance [Hz]	0.542	0.129	0.002	19.827	0.452	0.004
Mean [Hz]	3.50	4.01	4.00	4.171	3.960	4.00

However, the VMD, being a frequency-domain decomposition algorithm, is restricted by the limitations of Fourier analysis. This means that the VMD could be an effective alternative only when monitored data can be assumed as linear, time-invariant, and stationary. Therefore, to boost the suitability of EMILIA for a wide range of possible applications in the civil engineering field, the MODWPT is preferred for the decomposition stage of the algorithm, since it only requires that the signals are causal (Walden and Cristan 1998), being the amount of data produced due to the undecimated process the sole hindrance identified, which can be a burden for any CPU with low memory resources.

3.4 Chapter conclusions and final remarks

In the present chapter, the EMILIA algorithm framework and workflow have been presented and discussed. The selection of its main components and mathematical tools have been justified through benchmarking tests against other similar scientific tools available, highlighting the advantages and disadvantages of each method, especially in view of applications to dynamic identification in the civil engineering field. From the computed outcomes, it is demonstrated that the combination of the MODWPT time-domain discrete wavelet decomposition and the following TFA resorting to the Hilbert transform produces an effective mean for decomposing, processing, and identifying modal properties from non-linear structural and seismic data allowing to explore into the evolution of the structural response and behaviour to any input over time during the same acquisition. Moreover, the results presented in this chapter show that the MODWPT decomposition can appropriately work with highly noise-contaminated data and also can detect multiple modal components, processing several channels at the same time, meaning that the MODWPT algorithm can indeed separate the acceleration data obtained from MIMO ambient vibration measurements and earthquake recordings into a set of time-

dependent subsequences. The convolution process that can be found at the core of any wavelet analysis is the key to explaining why this approach shows extreme robustness against stochastic data, making it a rock-solid tool to deal with high noise-contaminated measurements. The possibility of a tailored selection of the mother wavelet allows to define the level of sensitivity to changes and differences in the measured accelerations, adapting to the response expected due to strong seismic excitations as well as low ambient vibration.

As highlighted in Section 2.4, broadband signals are not good candidates for applying Hilbert transform analysis, and as ambient and seismic structural vibration measurements have the deterministic information well-hidden between stochastic data, the MODWPT decomposition is of critical importance to successfully apply the Hilbert transform and compute well-behaved time-dependent instantaneous frequency and instantaneous amplitude functions from the generated pseudo-SDOF subsequences. As discussed in Section 2.4 as well, the Hilbert transform can compute many outlier samples and even negative values in the presence of almost instantaneous changes in the data, which is mainly produced by the derivation process applied to the complex angle of the analytical signals, angle that can show big variations between samples when dealing with non-periodic, non-static and non-linear data.

Therefore, to further enhance the identification minimising the influence of possible outliers computed by the Hilbert transform, a final stage of EMILIA is conducted by means of probability analysis and relying on nonparametric distributions, namely the Kernel probability density estimator. This nonparametric distribution estimator is used to fit the instantaneous frequency data produced in each computed subsequence. These outputs are then processed through Bayesian inference to obtain the final singleton results for the identified modal frequencies. This probabilistic outcome is supported by the MODWPT capability of performing full-resolution analysis in any section of the frequency spectrum, including the lower-frequency range that is of particular interest in structural modal identification. Indeed, the undecimated decomposition process of the MODWPT algorithm is of high importance in order to prevent resolution losses in the lower part of the frequency spectrum, no matter of the requested decomposition level.

All the aforementioned mathematical tools provide the EMILIA algorithm with the required capabilities to properly deal with linear or non-linear structural responses and with noise-contaminated acceleration data, being also able to compute the desired time-dependent modal outputs, i.e. the instantaneous amplitude, the instantaneous natural frequencies, and in the case of a multichannel setup, the instantaneous mode shapes, as well as robust single individual values for each acquisition.

4 TEST AND VALIDATION OF THE EMILIA ALGORITHM

4.1 Introduction

Safeguarding an adequate operational level of civil engineering structures and infrastructures through maintenance is essential for modern countries to support life quality, public health, security, and economic growth. This can significantly benefit from preventive strategies and periodic assessments aimed at ensuring not only a satisfactory performance during the structure's lifespan but also at optimising the activities needed for diagnosis and repair after natural or man-made disasters (Kim and Frangopol 2011; Hughes et al. 2021).

SHM is an active field of research concerned with the development and implementation of automatic non-invasive techniques devoted to the condition assessment of structures and infrastructures. Based on different types of data collected from different kinds of sensors attached to or embedded into the structures, SHM systems offer nearly real-time information regarding structural integrity (Vistasp M. Karbhari and Farhad Ansari 2009; Masciotta, Roque, et al. 2016; Limongelli and Çelebi 2019). However, the extraction of consistent metrics requires a preliminary application of appropriate signal processing, statistical classification and probability analyses to transform large, unstructured, and multi-type measured data into meaningful and accurate descriptions of the structure's health status.

As emerged from the review of the current state of the art (Chapter 2), output-only modal analysis based on AVT methodologies is the most viable solution to inform damage identification for many civil engineering systems (C. Zhang et al. 2022; Das, Saha, and Patro 2016; Ubertini, Comanducci, and Cavalagli 2016). Indeed, this strategy allows to obtain an accurate estimate of parameters like modal frequencies, damping ratios and mode shapes from the sole knowledge of output acceleration measurements and these parameters, in turn, present a significant sensitivity to damage outbreak and evolution (Rune Brincker 2014; Maia 1988; L.F. Ramos et al. 2010; Rainieri and Fabbrocino 2014). However, well-established methods for modal identification are not able to capture the variation of the modal properties during single acquisitions, hence they cannot adequately process non-linearities or non-stationarity in the signals.

In the present chapter, the capability of the novel EMILIA algorithm to properly carry out the dynamic identification of a structure is tested by considering both time-invariant and time-variant simulated processes. To this end, the numerical model of a bridge in sound and damaged conditions is generated and simulated acceleration records are produced for validation purposes. The algorithm outputs are hereby tested and validated against the outputs obtained from well-established traditional

modal identification algorithms from proprietary software, namely the EFDD and the SSI dynamic identification methods. Upon completion of the validation stage, additional tests are carried out in the second part of the chapter to investigate the robustness and the sensitivity of the main algorithmic components of the EMILIA algorithm and define a recommended parameter setting. To this end, the same numerical case study is used to generate the needed datasets.

It is stressed that most of the outcomes of the present chapter have been already published in (Hormazábal et al. 2023).

4.2 Case study I: 2D bridge model

4.2.1 Model description, eigenvalue analysis and simulated monitoring

The EMILIA algorithm is hereby tested and validated against the monitoring data of a three-span bridge simulated on a proprietary FE analysis software (DIANA FEA B.V. 2021). The bridge, modelled in a 2D environment, features a 0.5 m thick deck supported by two square piers of 1.0 m edge and 4.5 m height, with a main span of 30 m length and two lateral spans of 14 m each (58 m of total length). To simulate the interaction with the soil beneath piers and abutments, simple monoaxial springs are used as boundary conditions in both horizontal and vertical directions. Such a structure is conceived with the intent of guaranteeing a simple yet refined baseline model to address the instantaneous dynamic identification problem without incurring into cumbersome behaviours. A schematic representation of the model is presented in Figure 4.1.

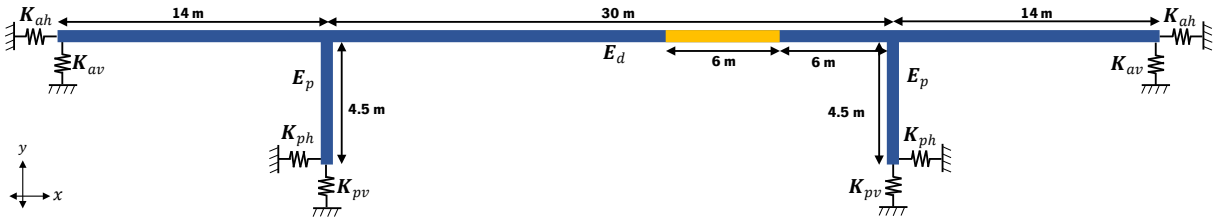


Figure 4.1: 2D bridge model schematic view. The damage location is highlighted in orange.

In the undamaged scenario (*ST00*), a linear-elastic isotropic homogeneous material with Young's modulus $E_d = 34000$ N/mm², Poisson's ratio $\nu_d = 0.2$ and mass density $\rho_d = 2950$ kg/m³ is adopted for the deck, and a linear-elastic isotropic homogeneous material with $E_p = 22000$ N/mm², $\nu_p = 0.2$ and $\rho_p = 2800$ kg/m³ is considered for the piers. Boundary spring elements located under the abutments have a stiffness equal to $K_{av} = 1.8\text{E+}08$ N/m (vertical) and $K_{ah} = 1.8\text{E+}08$ N/m

(horizontal), while boundary springs used under the piers feature a stiffness of K_{pv} = 1.8E+08 N/m (vertical) and K_{ph} = 2.1E+08 N/m (horizontal). Rayleigh damping mass factor is equal to 1.07520 1/s and the stiffness factor is equal to 0.000734350 s. As for the mesh discretisation, three-node two-dimensional beam elements of 0.25 m length with three degrees of freedom per node, two translational and one rotational, and a quadratic order displacement interpolation are adopted, resulting in a final model with 278 elements and 541 nodes.

To test the EMILIA effectiveness and accuracy, two configurations with asymmetric progressive damage scenarios in a single location are generated by applying to a selected zone of the deck (orange-coloured section of the main span in Figure 4.1) a stiffness reduction factor equal to 50% (*ST01*) and 75% (*ST02*) of the initial value, respectively.

An eigenvalue analysis of the bridge in the three scenarios (*ST00, ST01, ST02*) is carried out to identify the modal properties necessary to drive the selection of measurement points, sampling frequency and total duration of the acquisition window for the subsequent time history analyses. The first ten eigenvectors and the corresponding eigenvalues of *ST00* are presented in Figure 4.2. It is observed that the first, fourth, fifth, eighth and tenth eigenvectors are symmetrical vertical bending modes; the second, third, seventh, and ninth are asymmetrical vertical bending modes; whilst the sixth is a longitudinal mode.

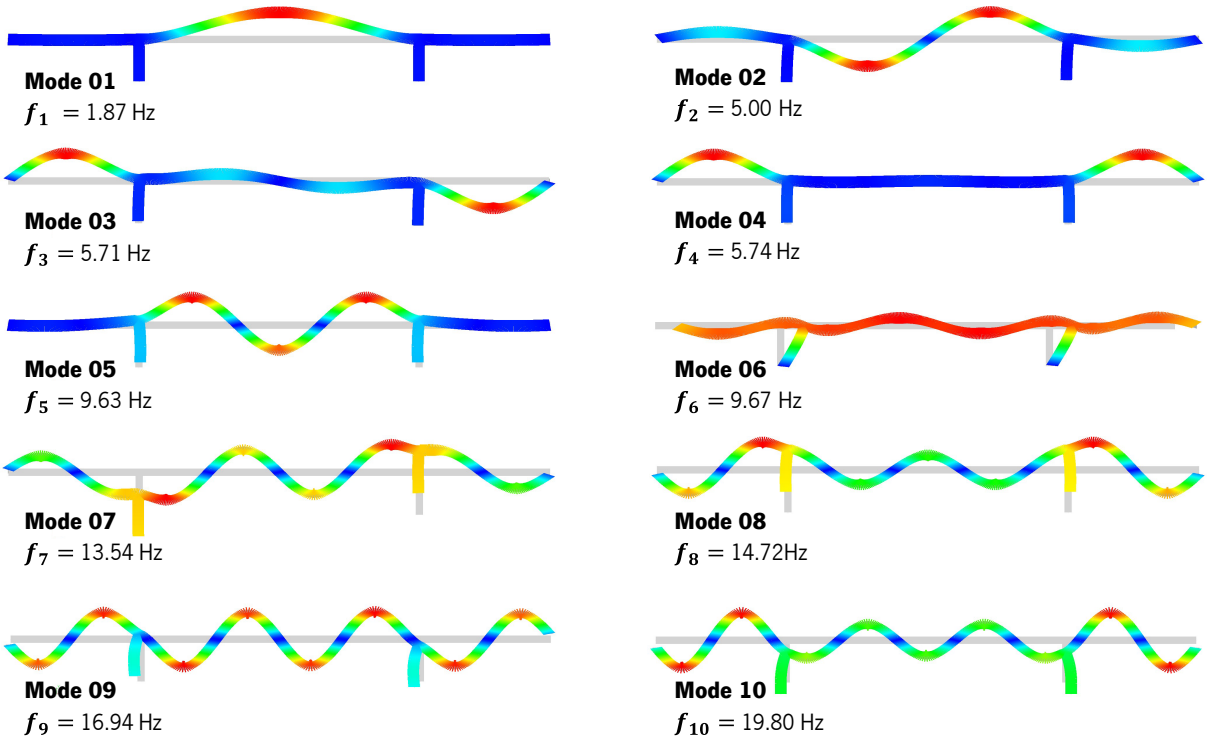


Figure 4.2: First ten eigenvectors and eigenvalues computed for the *ST00* stiffness configuration.

As expected, the number of inflexion points of the deflected bridge shapes progressively increases for higher-order frequencies except for the fourth mode, which is a local one involving exclusively the lateral spans. The percentage of effective mass participation computed for the same ten modes previously presented in Figure 4.2 is reported in Table 4.1.

It is noted that the modes that significantly contribute to the vibration response of the structure fall in the range of 1-10 Hz. Regarding scenarios *ST01* and *ST02*, the variations of the numerical frequencies for each mode are reported in Table 4.2. In global terms, the simulated structural damage mostly affects the first, second, fifth, and ninth modes of the bridge, which feature indeed the highest frequency differences over the three stiffness configurations.

Table 4.1: Eigenvalues and effective masses of the first ten numerical modes of the bridge.

Mode	f_n[Hz]	Horizontal		Vertical	
		Eff. Mass [%]	Σ. Eff. Mass [%]	Eff. Mass [%]	Σ. Eff. Mass [%]
1	1.87	0.00	0.00	27.73	27.73
2	5.00	0.91	0.91	0.00	27.73
3	5.71	0.56	1.47	0.00	27.73
4	5.74	0.00	1.47	34.67	62.40
5	9.63	0.00	1.47	13.33	75.73
6	9.67	91.24	92.71	0.00	75.73
7	13.54	0.14	92.85	0.00	75.73
8	14.72	0.00	92.85	13.69	89.41
9	16.94	2.14	94.99	0.00	89.41
10	19.80	0.00	94.99	7.13	96.54

Table 4.2: Eigenvalues of the bridge for the three stiffness configurations and percentage variation.

Mode	f_{ST00}[Hz]	f_{ST01}[Hz]	Δ_{00-01}[%]	f_{ST02}[Hz]	Δ_{00-02}[%]
1	1.87	1.81	-3.17	1.73	-7.68
2	5.00	4.57	-8.54	4.23	-15.35
3	5.71	5.70	-0.22	5.69	-0.34
4	5.74	5.74	0.01	5.74	-0.06
5	9.63	9.16	-4.85	8.48	-11.90
6	9.67	9.65	-0.23	9.62	-0.55
7	13.54	13.20	-2.53	12.66	-6.47
8	14.72	14.56	-1.09	14.39	-2.21
9	16.94	16.32	-3.69	15.64	-7.68
10	19.80	19.50	-1.52	19.17	-3.19

In order to simulate the monitoring of the system in each scenario, linear transient analyses are performed by applying ten-minute random vibrations in the form of bi-directional Gaussian white-noise excitations at 29 selected nodes: 19 distributed along the main deck and five over each pier. Different random input signals sampled at 0.01 seconds (100 Hz), with peak accelerations of 0.001 g, are considered for each node and direction.

Figure 4.3 shows at left the Gaussian white noise excitations applied to the node located in the middle of the central span of the bridge for the X axis and the Y axis, whilst at right it can be seen the simulated output accelerations computed for X and Y axes on the same node. In Figure 4.4 it can be observed a schematic plot of the 2D bridge showing, on top, the 29 input points where the excitation loading histories are applied (yellow colour dots), whilst at the bottom of the same figure are presented the 13 nodes where the simulated acceleration output data are collected (green colour dots).

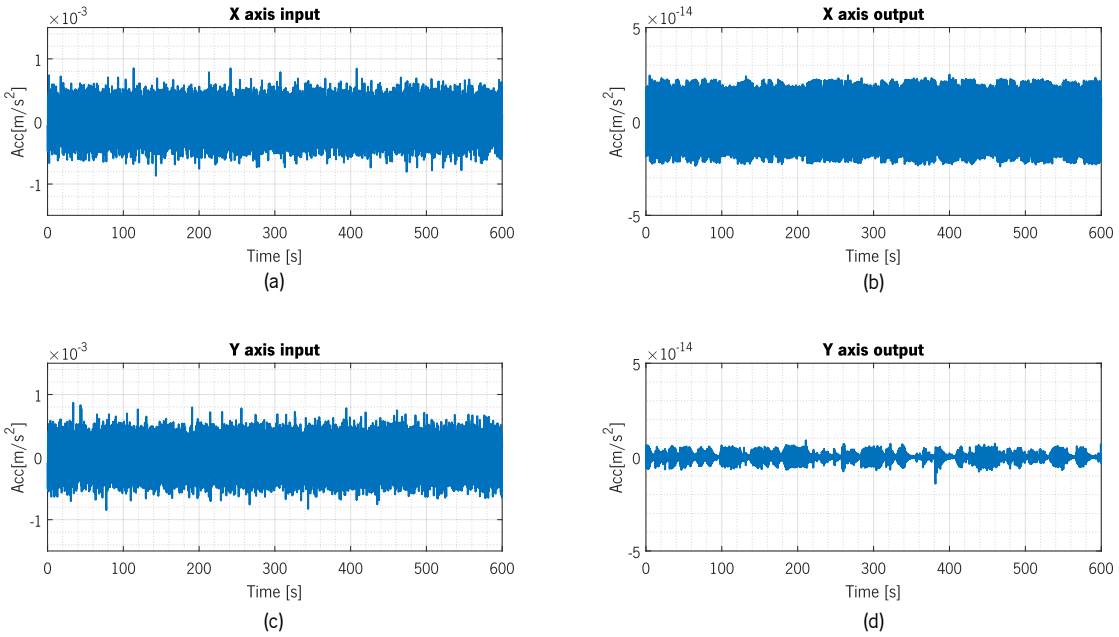


Figure 4.3: At left, white-noise inputs applied to X and Y axes of node N°15, located in the middle of the main span of the model. At right, the simulated output accelerations computed on the same node for X and Y axes.

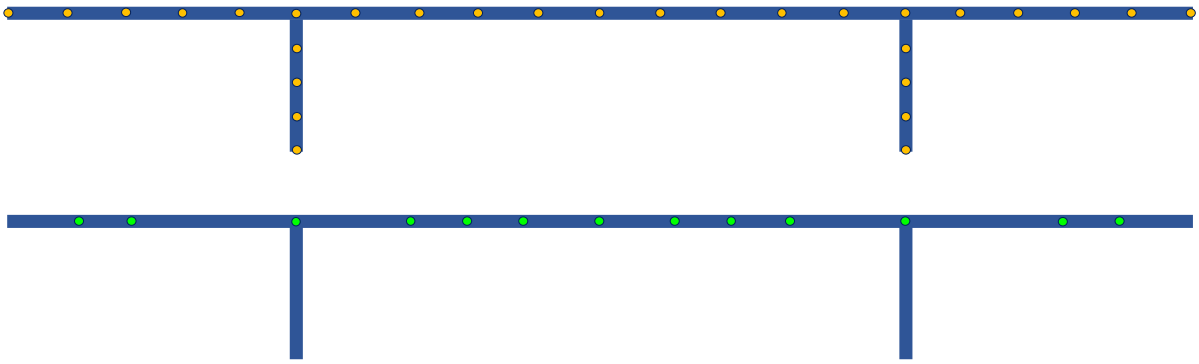


Figure 4.4: Distribution of the points selected for the application of random excitations (top, yellow dots). Deployment of the nodes selected for measuring the acceleration response (bottom, green dots).

All the FE transient analyses are performed resorting to the Hilbert-Hughes-Taylor method with $\alpha = -0.1, \gamma = 1/2(1-2\alpha), \beta = 1/4(1-\alpha)2$, resulting in a second-order accurate and unconditionally stable integration scheme.

Both the time variation of the excitation ($\Delta = 0.01$ s) and the shortest natural period of interest of the bridge ($T_6 = 0.103$ s) are considered to choose the best time step Δt for the analysis, thus resulting in a $\Delta t = 0.01$ s. The convergence criterion is based on the energy norm with a tolerance of 0.001.

Upon analysis, the nodal accelerations along X and Y are recorded at the thirteen different locations previously presented in Figure 4.4, which are selected according to the significance of the modal information carried by each node in the deformed shapes of interest for the structure (i.e., higher displacements in the eigenvectors). All simulated accelerations remains sampled at 100 Hz, thus resulting in 60,000 data points per channel.

4.2.2 Operational modal analysis and algorithm validation

Based on the simulated acceleration outputs, the dynamic characterisation of the bridge in the three stiffness configurations is carried out by making use of two modal estimators implemented in a proprietary modal analysis software (Structural Vibration Solutions A/S 2020), namely the EFDD modal analysis method and the SSI modal estimator with the extended Unweighted Principal Component algorithm (UPCX), as well as applying the EMILIA algorithm coded in a proprietary mathematical suite (The MathWorks Inc. 2021b; 2021a).

All the input datasets use the same sampling frequency of the transient analyses mentioned above, and no further signal processing techniques are applied.

The EMILIA algorithm utilises a six-level decomposition in order to generate a total of 64 subsequences, enough to cover the complete frequency span from 0 until the Nyquist frequency (50 Hz).

A Daubechies mother wavelet with 45 vanishing moments is employed, and the probability density functions are computed using the nonparametric Kernel distribution with a normal smoothing function and with a resolution of 1024 lines covering the whole spectrum from 0 to $f_s/2$ Hz.

According to the criteria mentioned in (Hormazábal et al. 2023) and Section 3.2.3, the probability threshold for modal identification is set to ten times the decomposition level, namely to 60%.

Regarding the traditional modal identification methods, the EFDD estimator presents a resolution of 1024 FFT lines with a 66% overlap for the spectral densities' estimations, whereas the SSI estimator adopts 100 state-space dimensions.

The natural frequency results computed by EFDD, SSI and EMILIA algorithms for the three stiffness scenarios are presented in Table 4.3, Table 4.4, and Table 4.5 along with the eigenvalue analysis results obtained from the FE model, here provided as comparative metrics to assess the estimator accuracy.

The percentage errors among numerical and simulated experimental frequencies highlight an excellent performance of the EMILIA algorithm in terms of frequency estimations, being in fairly good agreement with both the numerical target values and the results of the conventional output-only modal identification algorithms.

It is stressed that to perform an unbiased comparison and validation of the results, only the four modes successfully identified by all the modal estimators are further considered in this work. They are the first, second, third and sixth modes, hereafter referred as *Mode A*, *Mode B*, *Mode C*, and *Mode D*, respectively.

Table 4.3: Numerical vs experimental frequencies computed for the *ST00* scenario,

Mode	f_{eigen}[Hz]	f_{EFDD}[Hz]	Δ[%]	f_{SSI}[Hz]	Δ[%]	f_{EMILIA}[Hz]	Δ[%]
A	1.87	1.86	-0.53	1.87	0.00	1.86	-0.53
B	5.00	4.93	-1.40	4.93	-1.40	4.93	-1.40
C	5.71	5.62	-1.58	5.62	-1.58	5.63	-1.40
D	9.67	9.13	-5.58	9.14	-5.48	9.10	-5.89

Table 4.4: Numerical vs experimental frequencies computed for the *ST01* scenario.

Mode	f_{eigen}[Hz]	f_{EFDD}[Hz]	Δ[%]	f_{SSI}[Hz]	Δ[%]	f_{EMILIA}[Hz]	Δ[%]
A	1.81	1.81	0.00	1.81	0.00	1.81	0.00
B	4.57	4.52	-1.09	4.52	-1.09	4.49	-1.75
C	5.70	5.61	-1.58	5.62	-1.40	5.67	-0.53
D	9.65	9.39	-2.69	9.40	-2.59	9.38	-2.80

Table 4.5: Numerical vs experimental frequencies computed for the *ST02* scenario.

Mode	f_{eigen}[Hz]	f_{EFDD}[Hz]	Δ[%]	f_{SSI}[Hz]	Δ[%]	f_{EMILIA}[Hz]	Δ[%]
A	1.73	1.72	-0.58	1.72	-0.58	1.71	-1.16
B	4.23	4.19	-0.95	4.19	-0.95	4.20	-0.71
C	5.69	5.60	-1.58	5.60	-1.58	5.63	-1.05
D	9.62	9.35	-2.81	9.16	-4.78	9.47	-1.56

Figure 4.5 shows the time-dependent probability spectrum computed for the *ST00*. As all the vibration modes of interest are located within the frequency range of 0-10 Hz, only this part of the spectra is presented. As previously explained in Section 3.2.3, in this graphical output of the algorithm,

the instantaneous samples are reported as dots coloured according to a scale that is a function of the time instant. These instantaneous frequency samples are computed as a time derivative of the instantaneous complex phase, and as with any complex plot, they tend to show chaotic behaviour, especially in the presence of stochastic data or sudden changes in the analysed information. In the same plot, the KPDFs of the instantaneous frequency samples are reported as red dashed lines whereas the BPDFs are either red or green continuous lines.

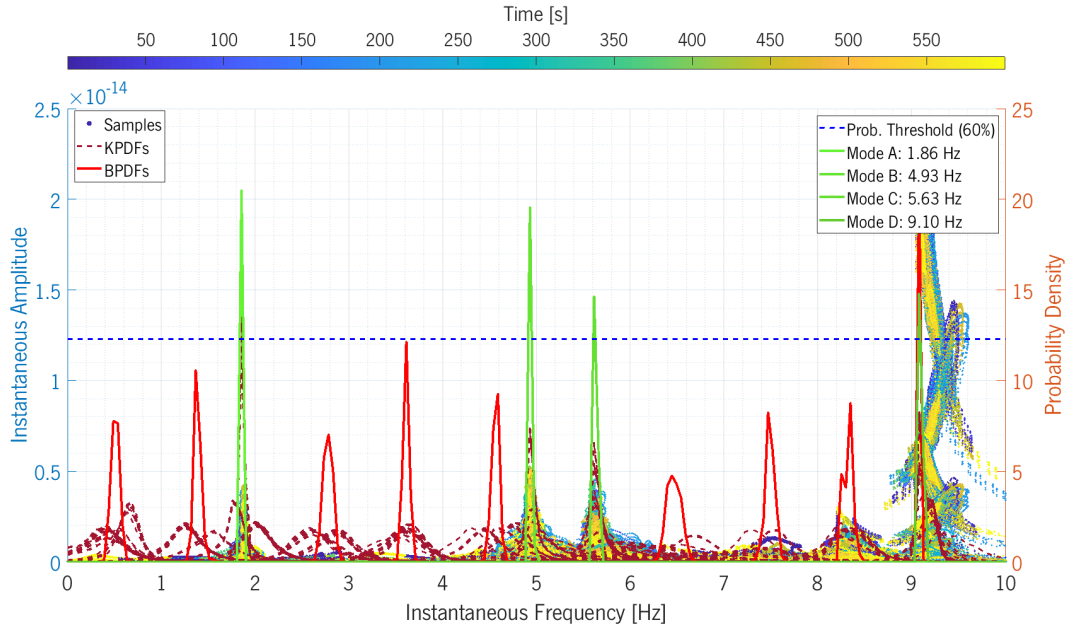


Figure 4.5: Time-dependent probability spectrum computed from *ST00* stiffness configuration using all available channels, with a Daubechies 45 mother wavelet function and a six-level MODWPT decomposition.

The green continuous lines highlight the BPDFs exceeding the thresholds corresponding to the four identified modes. Their matching f_{MEV} are reported in the legend. The red continuous lines, instead, show the distributions computed from spurious or rejected modes.

The differences in the probability peaks between the identified modes and the rejected ones, as well as between BPDFs and KPDFs (red dashed lines), highlight the remarkable improvement in the modal identification process gained by using Bayesian inference. Further analyses to support the hyperparameter and parameter setting for the Bayesian inference stage of EMILIA are presented in Section 4.3.2.

In Figure 4.6 and Figure 4.7, it can be observed the time-dependent probability spectrums computed from the *ST01* scenario and *ST02* scenario, respectively. Similar to Figure 4.5, as all the vibration modes of interest are located within the first 10 Hz of the spectrum, only this part of the data is presented.

Worth noting that for the sake of better visualisation of the computed probability distributions, a reduced amount of the instantaneous frequency samples are presented in the time-dependent probability spectrums presented in figures 4.5, 4.6, and 4.7, spectrums where only a 10% of the total amount of the instantaneous samples available from all the channels, and with f_{MEV} below 10 Hz can be seen.

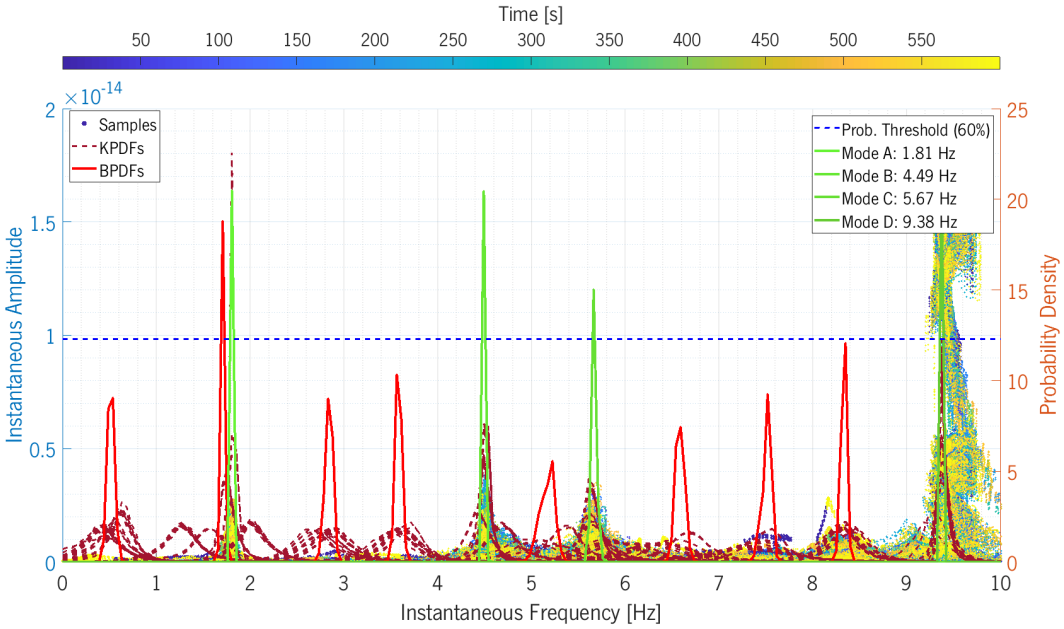


Figure 4.6: Time-dependent probability spectrum computed from *ST01* stiffness configuration using all available channels, with a Daubechies 45 mother wavelet function and a six-level MODWPT decomposition.

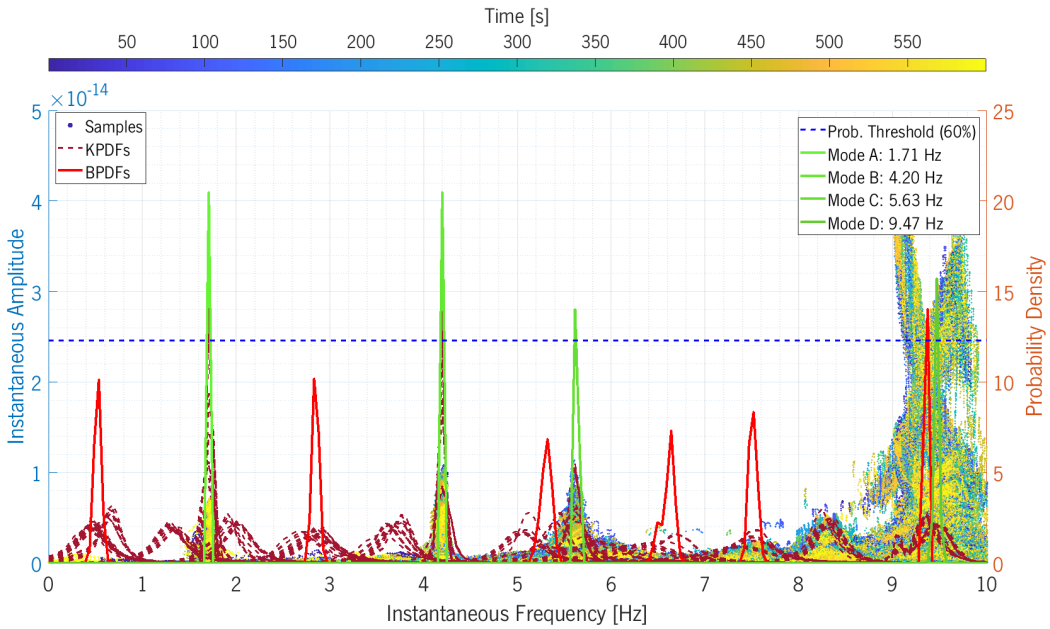


Figure 4.7: Time-dependent probability spectrum computed from *ST02* stiffness configuration using all available channels, with a Daubechies 45 mother wavelet function and a six-level MODWPT decomposition.

As previously mentioned in Section 3.4, one of the major strengths of the EMILIA algorithm lies in the possibility to compute time-dependent outputs for every single mode, yielding as many instantaneous natural frequencies and mode shapes as the number of time steps on the analysed data. This type of output is easy to handle concerning the instantaneous frequency, since all the samples can be presented at the same time in the form of a spectrogram. On the other hand, the visualisation of the instantaneous mode shapes outputs is not as straightforward.

A novel strategy was developed to allow a simple yet informative visualisation of the instantaneous mode shapes and the occurring changes concerning a predefined baseline reference within an acquisition. This strategy relies on the aforementioned MAC correlation (see Section 2.7) in order to compare each one of the instantaneous displacement mode shapes computed by the EMILIA algorithm, hereafter called dynamic values, against the corresponding reference mode shapes computed through the free-vibration eigenvalue analysis, and through the EFDD and SSI estimators as well, hereafter called static values as opposed to the instantaneous ones.

To explore the identification performance of the EMILIA algorithm, the outputs hereby presented come in the form of histograms describing the number of occurrences of the computed MAC values over the entire time window (60,000 data points).

For illustration, if no damage occurs during the acquisitions, instantaneous MAC values are expected to be equal to or greater than 0.9, implying a consistently correct identification of the undamaged mode shapes computed by EMILIA. However, if some kind of structural damage was induced during the acquisition, or if the compared instantaneous displacement shape information does not originate from the same mode, an output showing a histogram with a majority of low MAC results is expected.

For instance, Figure 4.8 shows a set of MAC tests computed resorting to *Mode B* from the *ST00* scenario, comparing the reference eigenvector, the mode shapes computed by the EFDD and SSI estimations, and a selected instantaneous mode shape computed by EMILIA. Additionally, in the three histograms that can be observed at the bottom of the same figure, it can be noticed that a big percentage of the MAC values computed from the EMILIA instantaneous mode shapes are located above the 0.9 MAC threshold, indicating a consistent identification along the set of tested instantaneous mode shapes of *Mode B* reference eigenvector, and of the EFDD and SSI mode shapes as well.

Worth noting that for the analyses performed by the EFDD, SSI and the EMILIA algorithms, the same simulated acceleration data is utilized for each example.

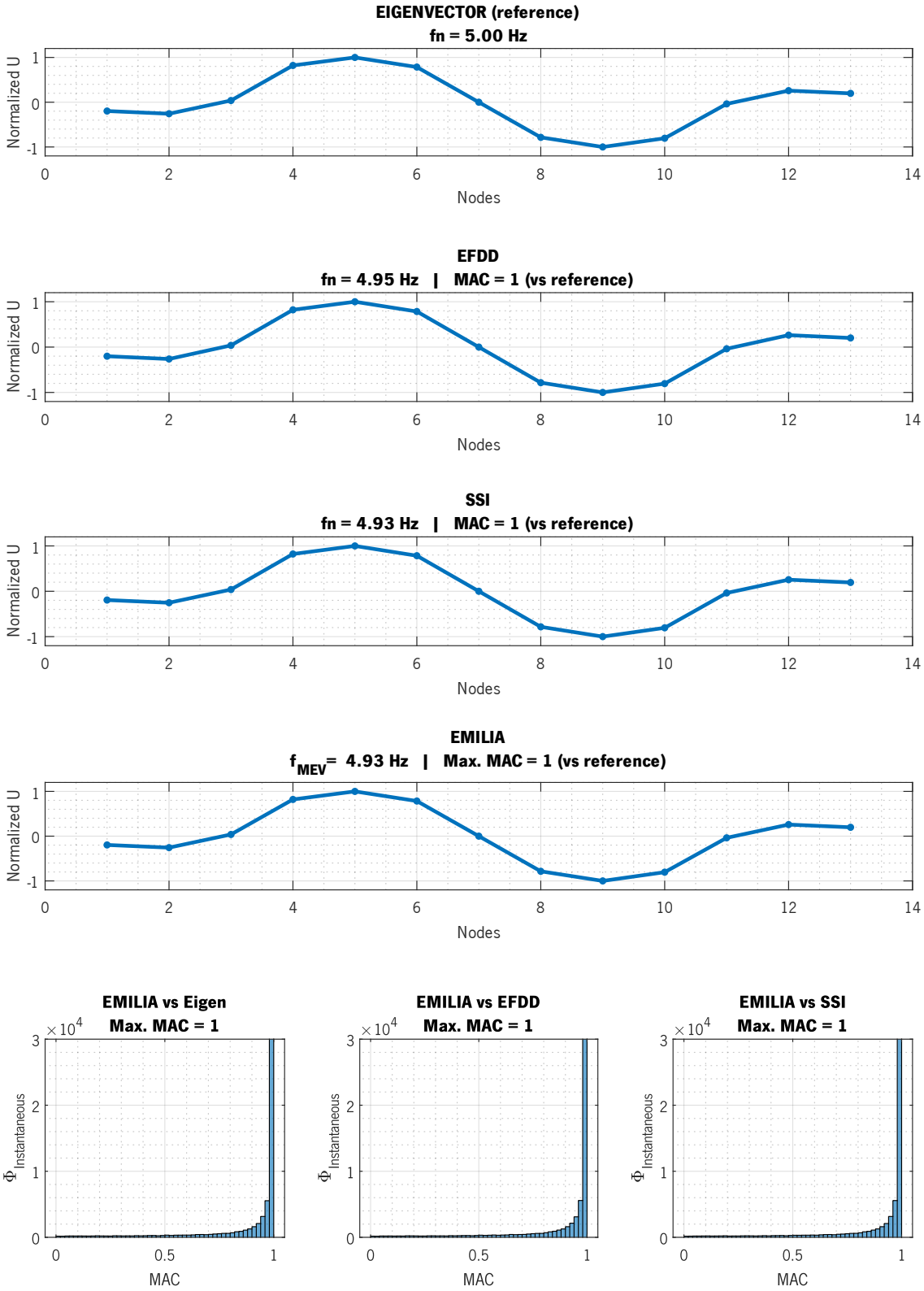


Figure 4.8: MAC test results for *Mode B* computed by EFDD, SSI and the EMILIA algorithms against the reference eigenvector.

On the other hand, Figure 4.9 shows a set of MAC tests computed resorting to the fifth original eigenvector in the *ST00* scenario against the mode shapes computed by the EFDD and the EMILIA algorithm.

It is worth noting that this mode was discarded from the original comparison (Table 4.3) since SSI failed at identifying it and EMILIA, as well, provided a poor quality of the identification (below threshold probability of the natural frequency).

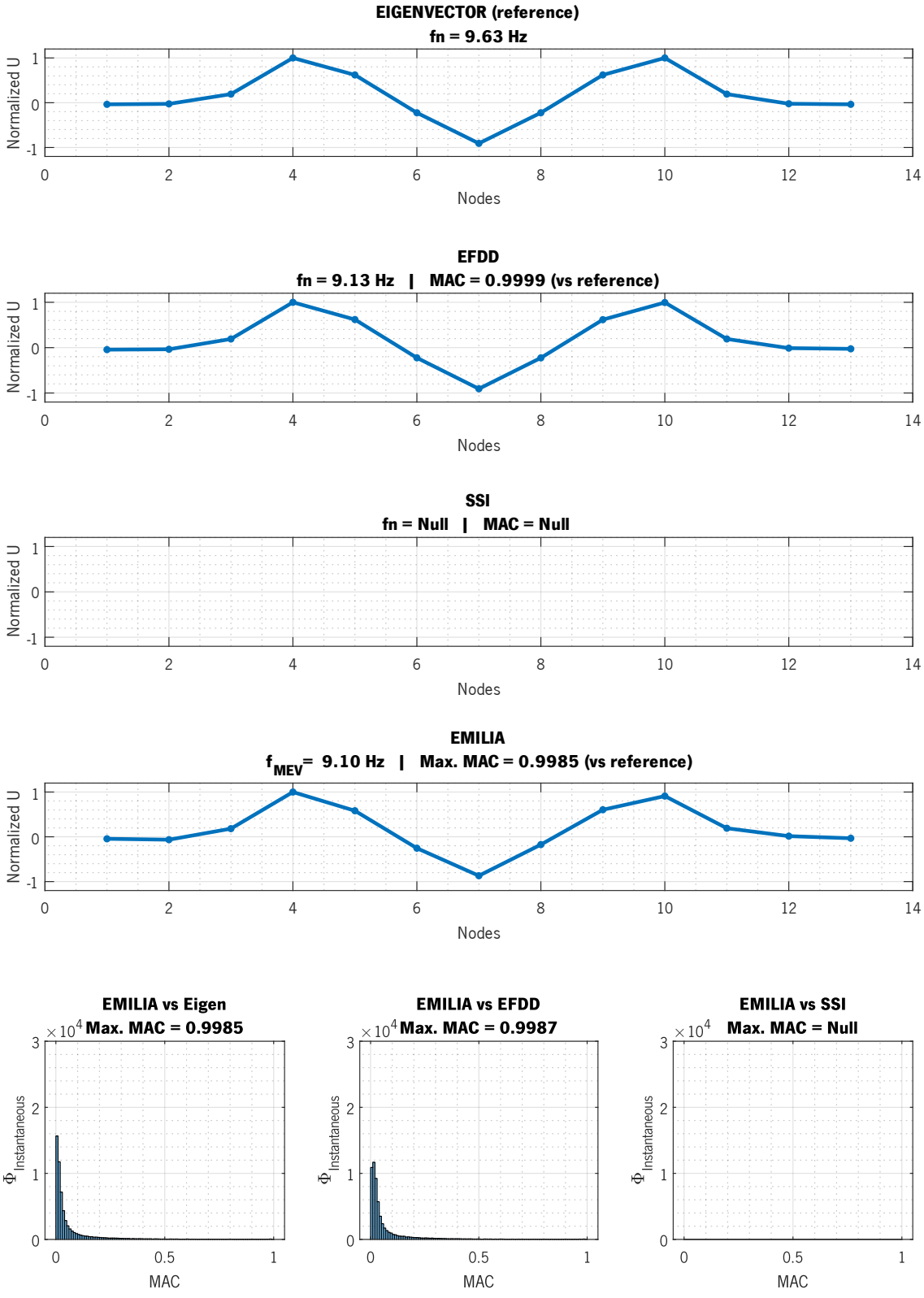


Figure 4.9: MAC test results for the fifth mode shape computed by EFDD, SSI and the EMILIA algorithms against the reference eigenvector (SSI information is not presented since this mode was not identified by that estimator).

Here, the MAC test confirms this poor result and suggests that the mode is discarded, as a significant trend of low MAC values, below 0.2, can be observed in the three histograms presented at the bottom of Figure 4.9. Even though a maximum MAC of 0.9985 is estimated by EMILIA during the acquisition, this is sparse and emerges for only a few seconds, while the correct mode shape is not consistently found within the instantaneous outputs computed by the algorithm. When assessing the complete output, in most of the recorded data, the shape of the fifth mode is coupled with and hidden by the shape of the sixth structural mode.

Regarding the modal data from the 2D bridge, Figure 4.10 and Figure 4.11 presents the instantaneous MAC histograms computed by the EMILIA algorithm in the *ST00* stiffness configuration and obtained from *Mode A* and *Mode B* mode shapes, and *Mode C* and *Mode D* respectively, measuring through this way the degree of consistency with the corresponding numerical reference eigenvectors (first column), mode shapes computed by EFDD estimator (second column), and SSI estimator (third column). For a better visualisation of the results, only the histogram bins above the 0.7 MAC value are presented, and by simple visual inspection, it can be concluded that most of the computed results present a very good consistency, with MAC values above 0.95.

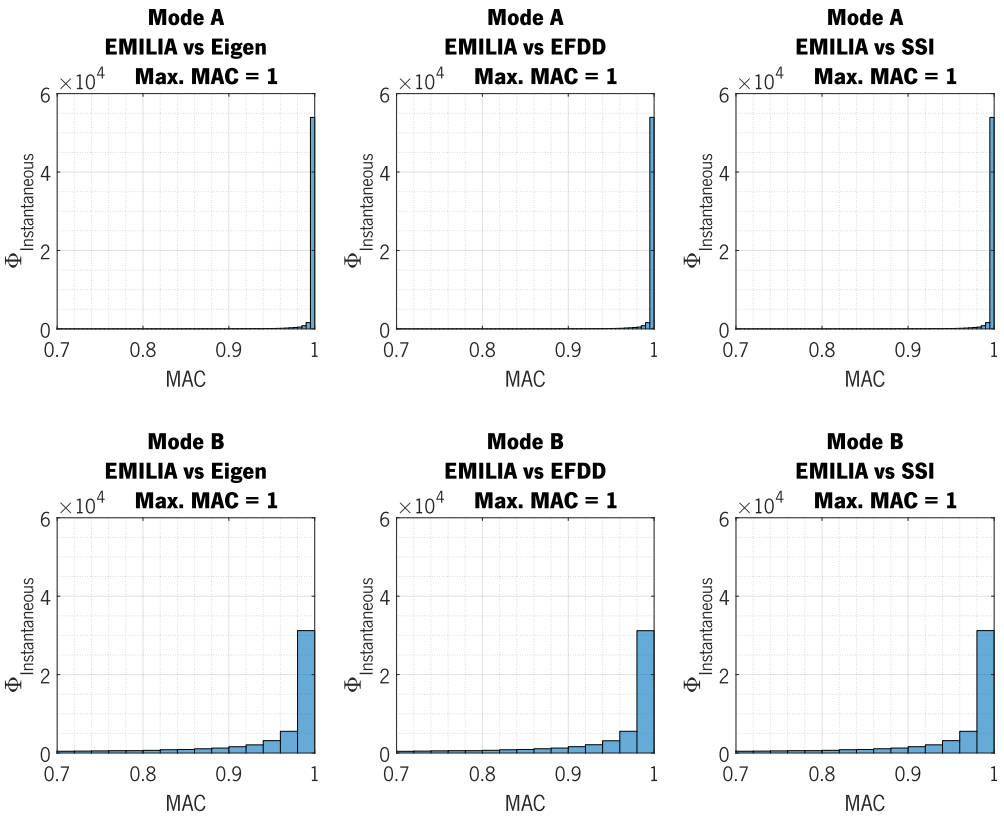


Figure 4.10: *Mode A* and *Mode B* dynamic MAC results of the EMILIA algorithm instantaneous mode shapes of the undamaged bridge against the static shapes from the other methods.

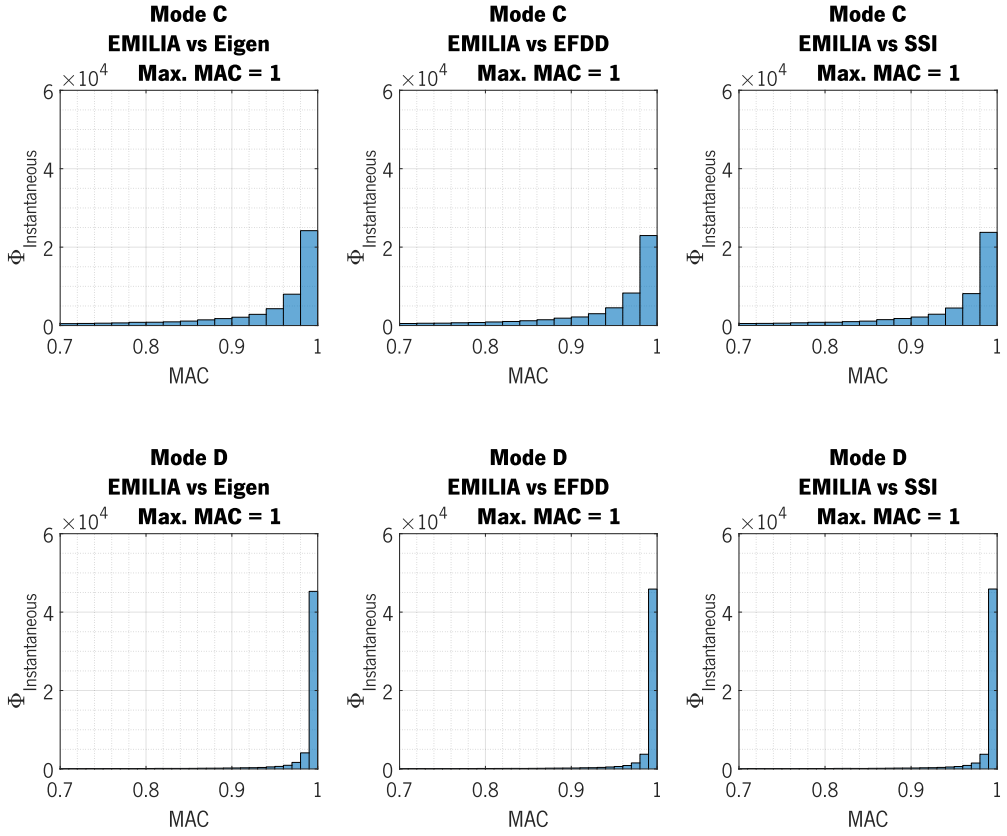


Figure 4.11: *Mode C* and *Mode D* dynamic MAC results of the EMILIA algorithm instantaneous mode shapes of the undamaged bridge against the static shapes from the other methods.

For the sake of completeness, Figure 4.12 gives a visual insight into selected instantaneous mode shapes estimated by the EMILIA algorithm and computed from the bridge in the *ST00* undamaged scenario for each one of the four modes under examination (f_A =1.86 Hz, f_B =4.93 Hz, f_C =5.63 Hz, and f_D =9.10 Hz), where the presented examples are selected by resorting to the instantaneous mode shape that computed the maximum MAC value (MAC = 1) against the reference eigenvector. At the right of the figure, it can be observed the MAC histograms computed from the entire number of instantaneous mode shapes (60,000).

Recalling the eigenvectors computing from the free-vibration analysis previously presented in Figure 4.2 in comparison with the ones in Figure 4.12, it can be appropriately noticed the great correlation existing between the reference eigenvectors and the instantaneous mode shapes computed by the EMILIA algorithm, hereby presented in the abovementioned figure.

Furthermore, as can be expected for any linear and non-varying structural response, the bins computed from the dynamic MAC values presented on the histograms at the right of Figure 4.12 are nearly permanently greater than 0.9 for all the four considered modes, being representative of the robustness of the EMILIA algorithm's time-dependent displacement outputs.

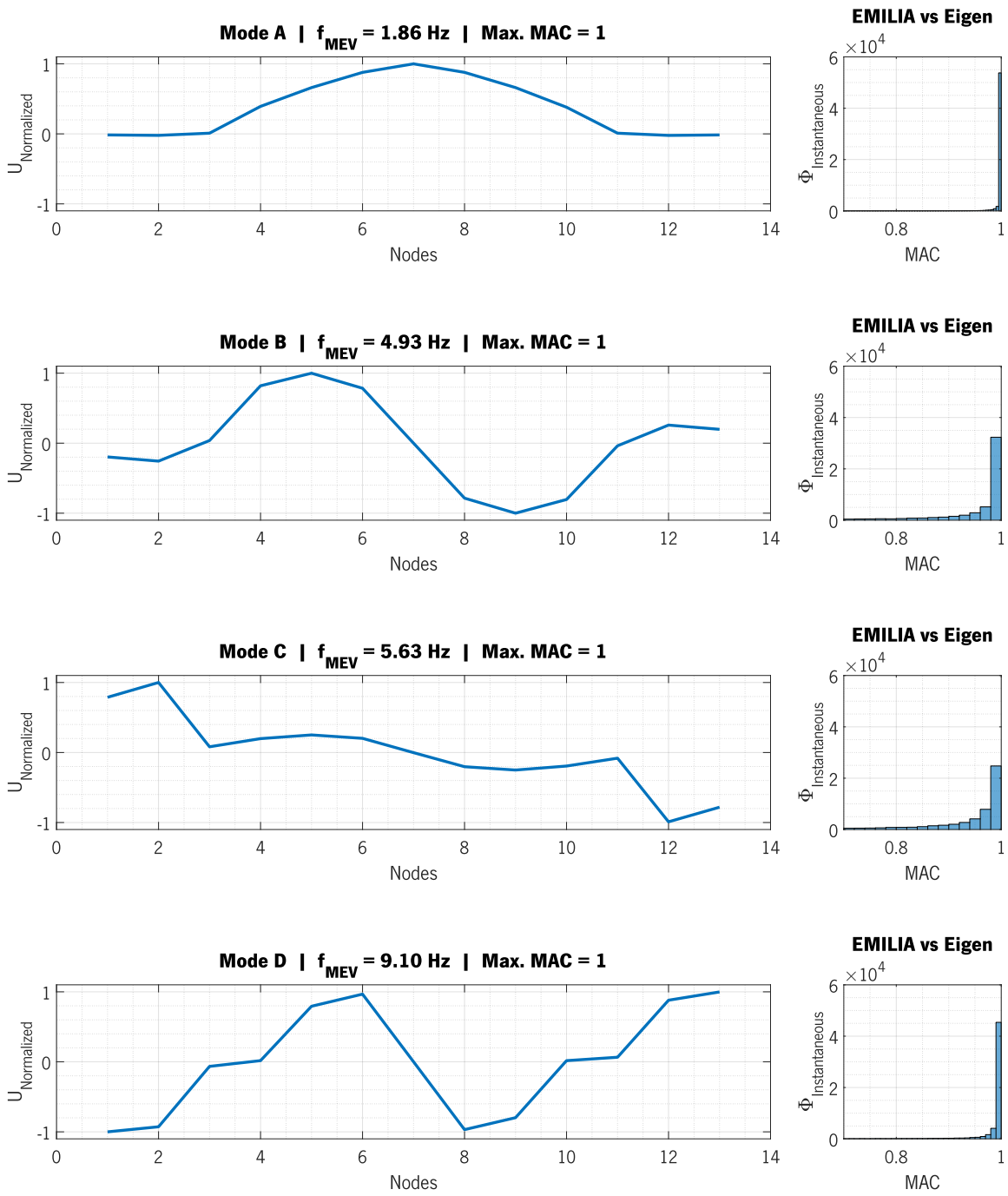


Figure 4.12: Mode shapes computed by the EMILIA algorithm for the *ST00* configuration and relative instantaneous MAC against the numerical eigenvectors.

4.2.3 Time-dependent dynamic identification

An additional data set is built by combining the three different stiffness scenarios into a single dataset in order to generate a unique 30-minute length acquisition of the 26 nodal responses (13 accelerations per direction, 180,000 data points per channel), suitable to be processed through the

EMILIA algorithm and to be exploited for a continuous time-dependent dynamic identification of a non-stationary time-variant process.

The resulting trend of the frequency values for the four modes of interest for the bridge across successive damage scenarios can be observed in Table 4.6.

Table 4.6: EMILIA f_{MEV} results and percentage difference amid the three stiffness configurations.

Mode	$f_{MEV\,ST00}$[Hz]	$f_{MEV\,ST01}$[Hz]	Δ_{00-01} [%]	$f_{MEV\,ST02}$[Hz]	Δ_{00-02} [%]
A	1.86	1.81	-2.69	1.71	-8.06
B	4.93	4.49	-8.92	4.20	-14.81
C	5.63	5.67	0.71	5.63	0.00
D	9.10	9.38	3.08	9.47	4.07

Figure 4.13 shows the time-dependent probability spectrum computed using the 30-minute-long data set. The colour scale on top of the plot allows tracking both the frequency and amplitude variations of the identified modes over time, instant-by-instant.

The EMILIA algorithm enables to follow the instantaneous frequency changes passing from the *ST00* sound condition (blue samples) to the *ST01* stiffness configuration (green samples) and, finally, to the *ST02* stiffness configuration (yellow samples).

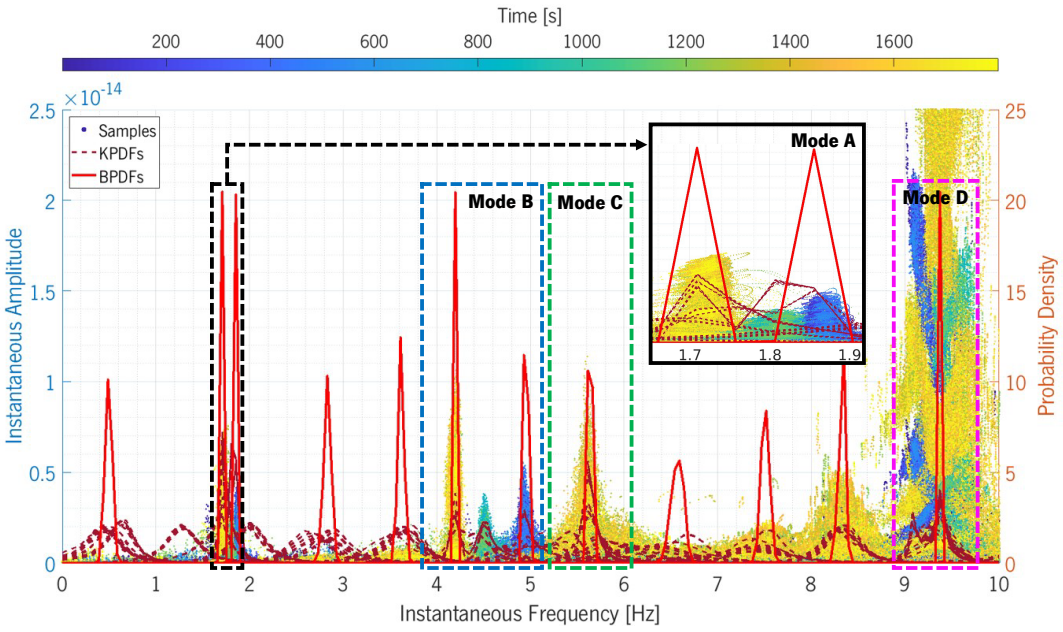


Figure 4.13: Time-dependent probability spectrum computed across all stiffness configurations. Close-up of *Mode A* dynamic variation of the instantaneous frequency values.

The close-up presented in Figure 4.13 provides a better insight into the changes in the instantaneous frequency values for *Mode A* and how EMILIA outcomes enable to follow this evolution over time, highlighting progressive frequency downshifts from $f_{MEV} = 1.86$ Hz (*ST00*, blue samples)

until $f_{MEV} = 1.71$ Hz (*ST02*, yellow samples). The blue line rectangle highlights the modal information concerning *Mode B*, whose instantaneous frequency values decrease from the initial $f_{MEV} = 4.93$ Hz, for the *ST00* scenario, until the $f_{MEV} = 4.20$ Hz in the *ST02* configuration. Analogously, the green line rectangle identifies the instantaneous frequency data from *Mode C*.

Unlike the first two modes, the third one does not undergo any visible sudden change in the instantaneous frequency values that remain almost constant at around 5.65 Hz throughout the acquisition window, irrespective of the new scenarios outbreak. Given the type of deflected shape featured by this mode, the insensitivity to mid-span damage was expected. A slight frequency increase is instead found for *Mode D*, highlighted in the same figure by the pink line rectangle. This mode, being longitudinal, was not expected to be significantly affected by the induced damage either.

The evolution of the system's condition is further assessed by analysing the instantaneous modal displacements. To this end, Figure 4.14 presents, for each scenario, the shapes of the first and second vibration modes tracked by the EMILIA algorithm, displayed in the configuration corresponding to a MAC value of 1 (numerical eigenvectors are used as reference metrics), together with the evolution of the instantaneous MAC values over the entire number of samples. Additionally, the best shapes showing a MAC value equal to 1 for the *ST01* and *ST02* scenarios are reported as well. The close inspection of the plots allows perceiving that the first two mode shapes experience only minor modifications upon the damage outbreak.

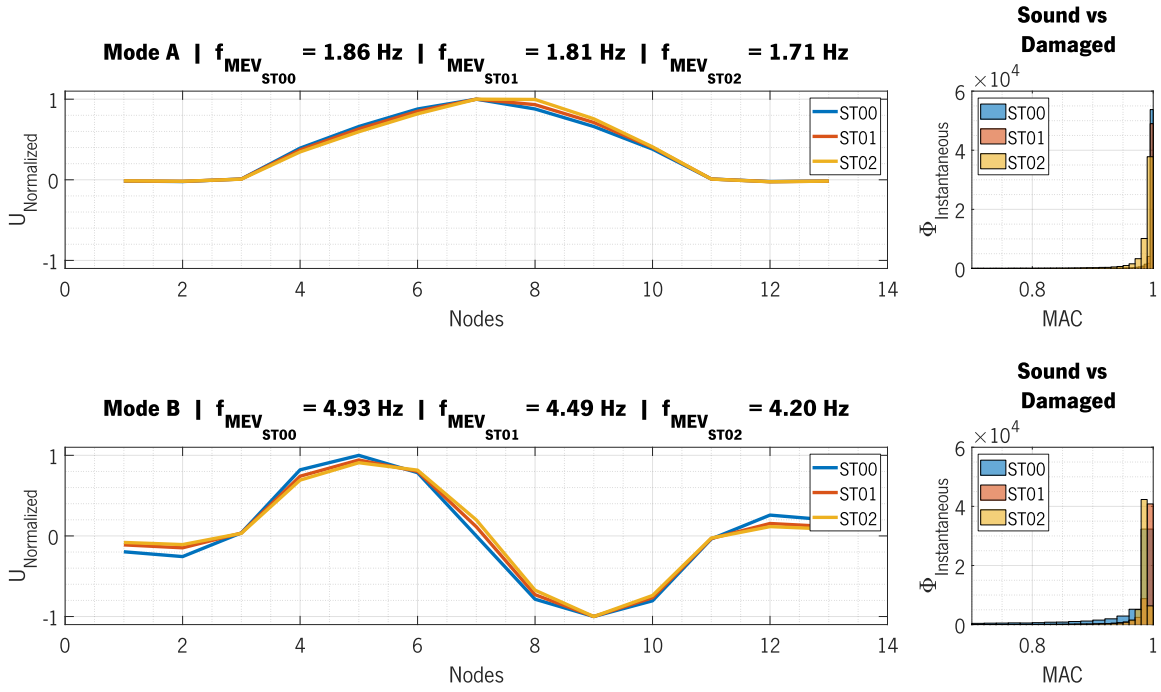


Figure 4.14: Evolution of *Mode A* and *Mode B* shapes and instantaneous MAC values with progressive damage.

By resorting to the same configuration as in Figure 4.14, in Figure 4.15 is presented the best shapes with a MAC value of 1 computed for the three different stiffness scenarios from *Mode C* and *Mode D* data, all together with the histograms computed from the instantaneous displacement mode shapes.

As damage is a local phenomenon, the deflected shapes associated with global low-frequency modes are always less affected by component-wise shifts. The higher the number of inflexion points of the mode, which typically increases for higher-order frequencies, the greater the coordinate-dependent variation due to the occurrence of damage (Masciotta and Pellegrini 2022).

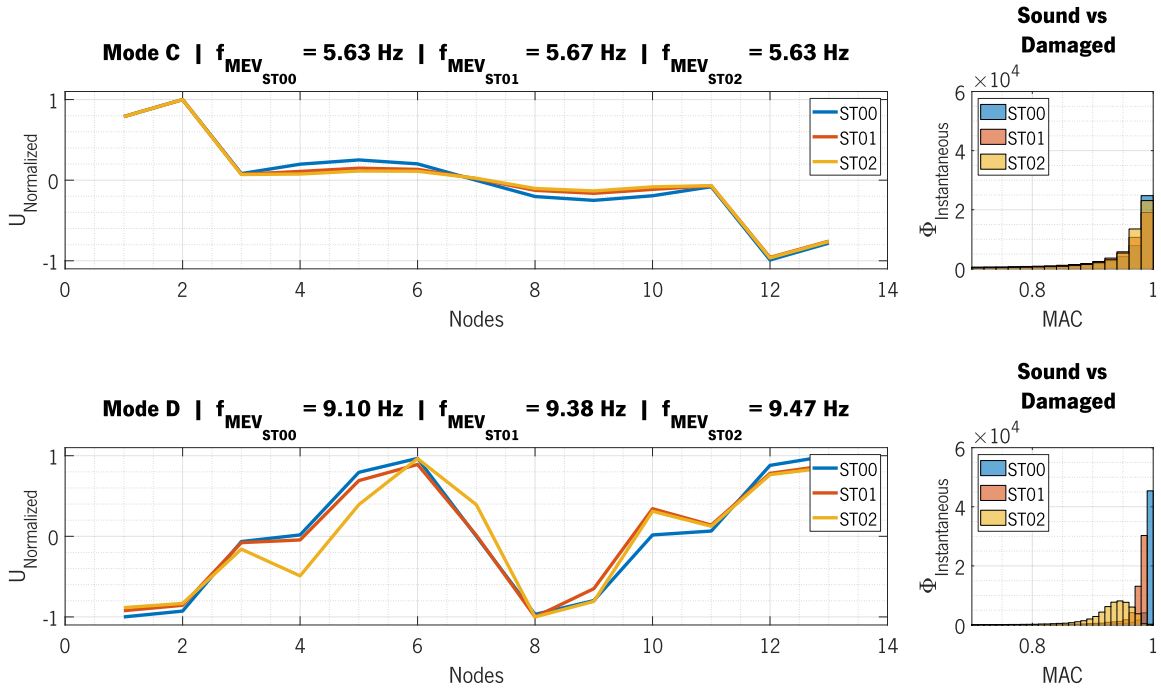


Figure 4.15: Evolution of *Mode C* and *Mode D* shapes and instantaneous MAC values with progressive damage.

To test the EMILIA capability of identifying damage-induced variations in the instantaneous mode shapes, a further MAC calculation is carried out considering the four free-vibration eigenvectors estimated from the bridge in undamaged condition (*ST00* scenario) as reference metrics. The obtained results are reported in Figure 4.16 as dynamic time-dependent MAC plots.

For the sake of cleanest and smoothest graphics, the plotted progressive MAC values computed between EMILIA instantaneous mode shapes and FE model reference eigenvector are computed within one-second time-window, as the maximum out of the 100 instantaneous MAC values estimated in each second (as per the sampling frequency).

After each damage onset, clear drops can be observed in *Mode D,* despite the lower sensitivity to damage of its natural frequency, and, to a minor extent, within *Mode A* and *Mode B*. At the same

time, the variance of the MAC values increases with damage across the different stiffness configurations, except for *Mode C*, whose MAC values remain almost constant throughout the observation time. This is mainly because of the highly localized characteristic of the modal shape from *Mode C*, that have the largest displacements located along the lateral spans of the bridge (third eigenvector in Figure 4.2, and top plot in Figure 4.15).

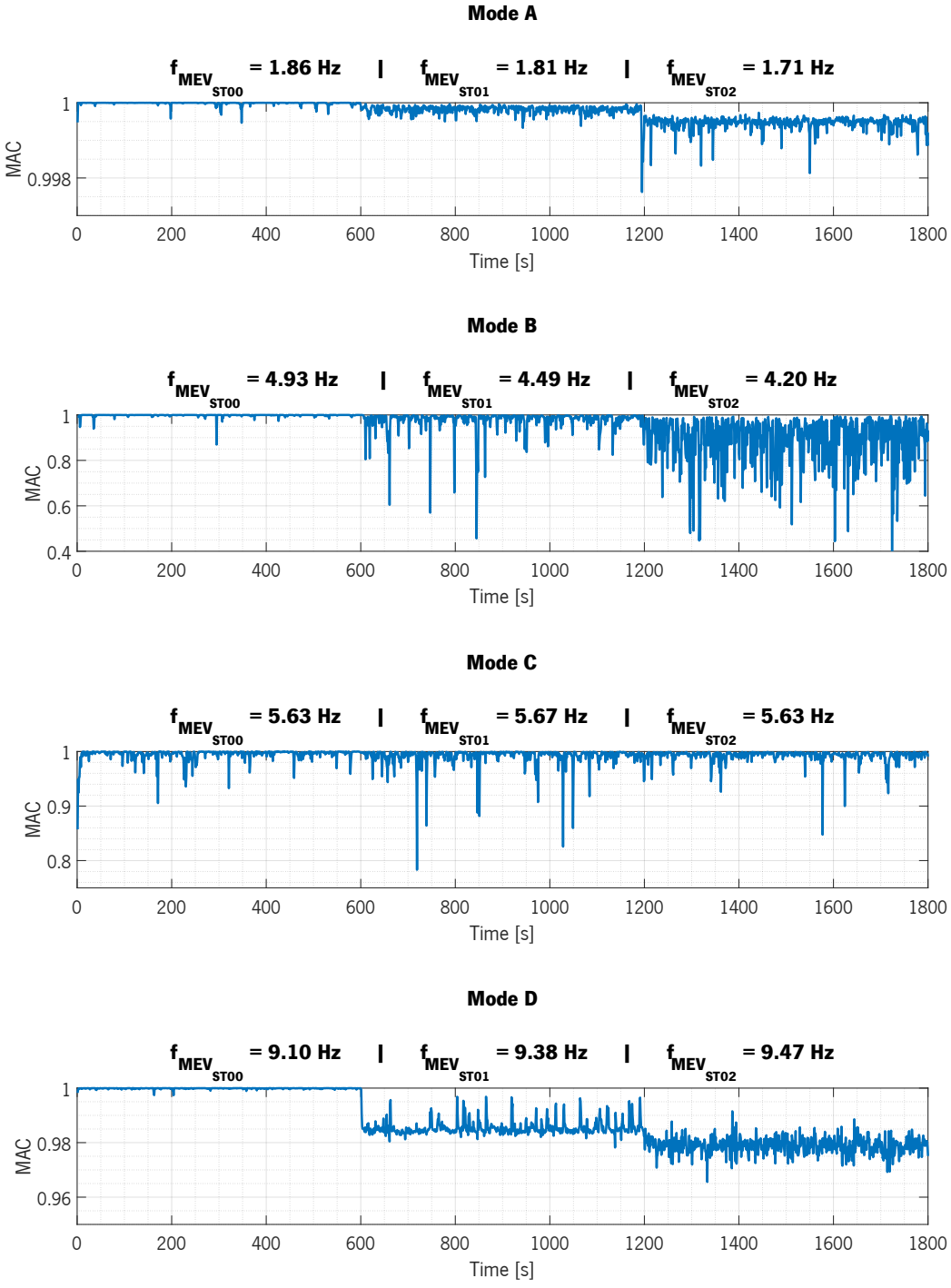


Figure 4.16: Time-dependent MAC results with progressive damage for the four modes of interest.

The same time-dependent information can be also plotted and assessed in the form of a traditional Hilbert spectrogram, aiming at identifying the precise time of occurrence of the sudden change in the system behaviour. For illustration, the Hilbert spectrogram associated with the instantaneous frequency data computed from the bridge's *Mode A* is presented in Figure 4.17. In the spectrogram, it is possible to visually locate with high accuracy when the instantaneous frequency values drop after each damage onset, at the 600 and 1200 seconds marks.

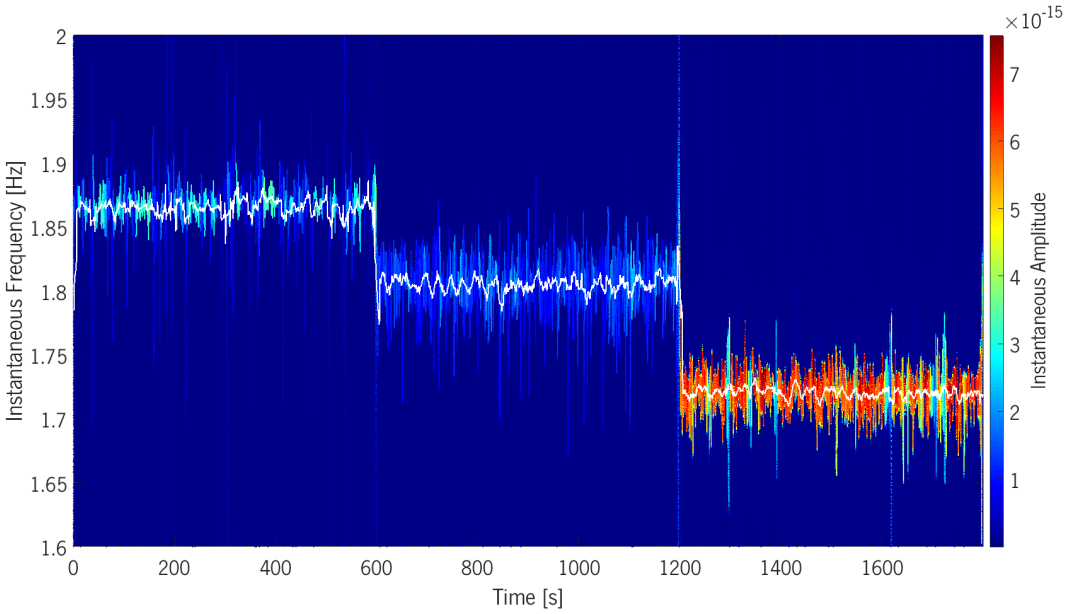


Figure 4.17: Hilbert spectrogram showing the first mode's instantaneous frequency evolution across the three stiffness configurations (white continuous line shows a moving average of the same data).

As previously mentioned in Section 3.2.3, the spectrogram X axis allows a clearer perception of the instantaneous natural frequency values evolution over time than the colour scale used on the time-dependent probability spectrums. On the other hand, the Hilbert spectrogram completely lacks information related to any of the probability analysis outcomes, namely the KPDFs and the BPDFs, stressing the importance of analysing both the graphical outputs of EMILIA for a better insight into the system behaviour.

4.3 Algorithm tests: parameters setting, robustness and sensitivity

Upon the extensive validation of the EMILIA algorithm on the numerical case study, including its comparison with exact solutions and well-established alternative estimators, an overview of parameter setting and recommended values for a wide range of applications in the civil engineering field is provided in the following sections.

However, before focusing on the parameter setting, a preliminary consideration addresses the robustness of the algorithm against processes like decimation or filtering of the data, rather common in the case of long-term monitoring and records performed with full sampling resolution.

Most used analog-to-digital converters that can be found in modern digital acquisition systems can easily sample data at rates above 48KHz with full bit depth. Considering that the most significant structural modal information is in the lower part of the frequency spectrum, using the maximum sampling frequency resolution will produce massive amounts of extra data to save and analyse, generating a huge computational burden with extremely time-consuming analyses. Due to the previous, many times a reduction in the amount of the total data to analyse is obtained by decimation or filtering the raw recordings in order to reduce the Nyquist frequency, and consequently, reduce the computational burden of the analyses.

The EMILIA algorithm can properly work with decimated data with no more effects than the ones strictly related to any decimation process (reduction of Nyquist frequency, high-frequency resolution loss, noise filtering, reduction of space and time complexity, etc). Indeed, the most evident effect of the decimation is the reduction of the Nyquist frequency and number of samples.

The above requires a reduction in the selected level of decomposition whenever the purpose is to keep the same frequency resolution of the analysis from the undecimated data, as further discussed in and in Section 4.3.2.

Data filtering is also a common practice in seismic records and structural measurements to eliminate non-desired data out of the frequency range of interest, that can be even lower than the Nyquist frequency, to cancel the drifting effect, or to contrast the increment of low-frequency noise after data integration. In any case, filtering of data is previous to the modal estimation, it is not required for the proper functioning of the EMILIA algorithm and does not affect its functioning or parameter setting.

4.3.1 Setting the decomposition level

The implementation of EMILIA requires an initial definition of the level of decomposition which should be case-specific. Therefore, at the beginning of any analysis process, checking the Nyquist frequency to know the spectrum length to cover is a good strategy for identifying the size and the number of frequency segments to produce.

It is worth noting that closely spaced and coupled modes may require an ad-hoc definition of the level of decomposition, beyond the preliminary recommended values hereafter indicated.

Based on the extensive pilot tests and applications carried out by the Author, for analyses based on a sampling frequency between 20 Hz and 50 Hz, a decomposition level between three and five can be assumed as a good starting point, because these selections will provide between eight and 32 subsequences to cover the frequency span of interest. In fact, according to the relation $(f_s/2)/2^m$, choosing for instance a four-level decomposition for analysing data sampled at 40 Hz produces 16 spectrum segments, each one with an equal span of 1.25 Hz.

When dealing with sampling frequencies between 50 Hz and 200 Hz, four to eight levels of decomposition are a good starting point, providing between 16 and 256 subsequences respectively. Choosing a six-level decomposition for data sampled at 100 Hz, as in the previously discussed application to the bridge data, produces 64 spectrum segments with an approximated length of 0.78 Hz for each one.

Undersetting the decomposition level would produce longer spectrum spans, thus affecting the accuracy of the identification and increasing the probabilities of mixing too closely located modes. However, oversetting the decomposition levels would produce a massive number of PDFs closely placed along the frequency spectrum, with an exponential increase in the computational burden. Moreover, extremely high decomposition levels produce a flattened probability spectrum, making more difficult the modal identification.

For the sake of testing the algorithm outcomes behaviour when varying the decomposition level, the analyses of the *ST00* dataset from the bridge model are here repeated considering two-, four-, six-, and eight-level decompositions, whilst all other parameters and settings remain the same.

Table 4.7 and Table 4.8 reports the outcomes from analyses resorting to a four-level MODWPT decomposition, and the results obtained from utilizing a two-level MODWPT decomposition.

By decreasing the number of decompositions below a certain level, the algorithm misses the identification of some modes, especially if they are closely spaced. For instance, the four-level decomposition produces only 16 subsequences, which are not enough to properly cover the 50 Hz frequency spectrum, thus, the algorithm output for the second mode is a mixture of the modes located inside the analysed frequency span (Table 4.7), showing considerably lower probabilities and higher variance than for the six-level decomposition results.

The overlapping of distinct modes within the subsequence is not only limited to the frequency output but also affects the instantaneous shapes. For example, Figure 4.18 shows one of the mode shapes obtained from the previously mentioned output, presenting at the mid-span the influence of the second mode, but on the side spans a shape closer to the third mode.

Table 4.7: *ST00* four-level Kernel results.

4 Level MODWPT decomposition			
Frequency Results			
Mode	f_{MEV}[Hz]	σ^2	Max BPDF
1	1.86	≈0.00	20.476
2	5.04	0.004	8.956
3	–	–	–
4	–	–	–
5	–	–	–
6	9.08	≈0.00	20.48
Elapsed Time			
Process/Stage		Ref. Time	Steps
Data decomposition		2.90 s	54
Hilbert TFA		2.69 s	443
Probability analysis		12.02 s	459
Bayes Inference		0.01 s	449
Mode Shapes		1.44 s	1682
Total elapsed time		19.11 s	19601

Table 4.8: *ST00* two-level Kernel results.

2 Level MODWPT decomposition			
Frequency Results			
Mode	f_{MEV}[Hz]	σ^2	Max BPDF
1	–	–	–
2	–	–	–
3	–	–	–
4	–	–	–
5	–	–	–
6	9.08	≈0.00	20.341
Elapsed Time			
Process/Stage		Ref. Time	Steps
Data decomposition		1.24 s	54
Hilbert TFA		0.69 s	131
Probability analysis		5.97 s	135
Bayes Inference		0.01 s	113
Mode Shapes		0.41 s	422
Total elapsed time		8.35 s	5016

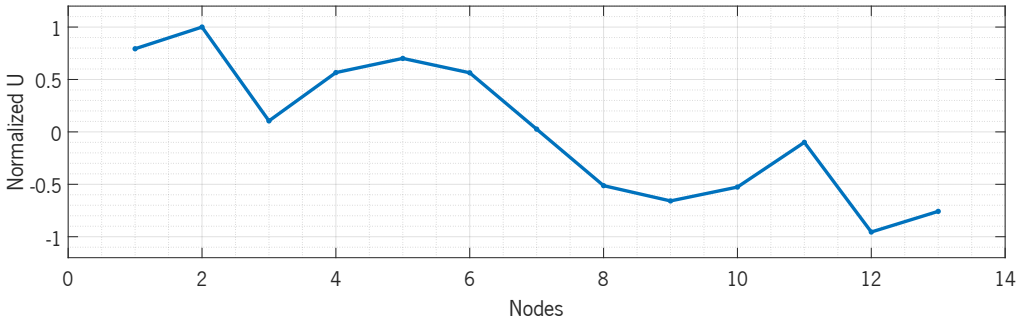


Figure 4.18: Second and third modal shapes mixed in the results of the four-level decomposition analysis from Table 4.7.

It is worth noting that the issue stressed in the above figure does not happen at all the instants along the acquisition. As the algorithm outputs are time-dependent calculations, the resulting shape of the coupled modes is continuously shifting depending on the influence of each modal component, which is similar to the aforementioned case between the rejected instantaneous mode shape from the fifth mode and previously presented in Figure 4.9, that is well hidden between the instantaneous shapes of the sixth mode.

On the other hand, Table 4.9 and Table 4.10 show the outcomes of the eight-level MODWPT decomposition and six-level MODWPT decomposition respectively. As previously mentioned, through the proposed default setting of a six-level decomposition analysis, 64 sub-sequences are obtained from the wavelet decomposition, ensuring a good identification of the first, second, third and sixth modes.

Table 4.9: *ST00* eight-level Kernel results.

8 Level MODWPT decomposition			
Frequency Results			
Mode	f_{MEV}[Hz]	σ^2	Max BPDF
1	1.86	≈0.0	20.48
2	4.93	≈0.0	20.48
3	5.62	≈0.0	20.48
4	–	–	–
5	–	–	–
6	9.23	≈0.0	20.48
Elapsed Time			
Process/Stage	Ref. Time	Steps	
Data decomposition	41.87 s	54	
Hilbert TFA	44.21 s	6683	
Probability analysis	111.13 s	6939	
Bayes Inference	0.10 s	7169	
Mode Shapes	22.84 s	26882	
Total elapsed time	220.20 s	311050	

Table 4.10: *ST00* six-level Kernel results.

6 Level MODWPT decomposition			
Frequency Results			
Mode	f_{MEV}[Hz]	σ^2	Max BPDF
1	1.86	≈0.0	20.48
2	4.93	≈0.0	19.55
3	5.63	≈0.0	14.65
4	–	–	–
5	–	–	–
6	9.10	≈0.0	14.80
Elapsed Time			
Process/Stage	Ref. Time	Steps	
Data decomposition	10.67 s	54	
Hilbert TFA	10.59 s	1691	
Probability analysis	33.01 s	1755	
Bayes Inference	0.03 s	1793	
Mode Shapes	6.06 s	6722	
Total elapsed time	60.39 s	77880	

By increasing the decomposition level to eight, the algorithm will compute 256 subsequences, which despite of providing a higher frequency resolution, in many practical applications does not actually improve the identification, since as aforementioned, the vast amount of KPDFs and BPDFs produced and placed too closely along the frequency spectrum flattens the computed probability results. The previous can be observed in Figure 4.19, in the time-dependent probability spectrum presented corresponding to the eight-level decomposition analysis presented above in Table 4.9.

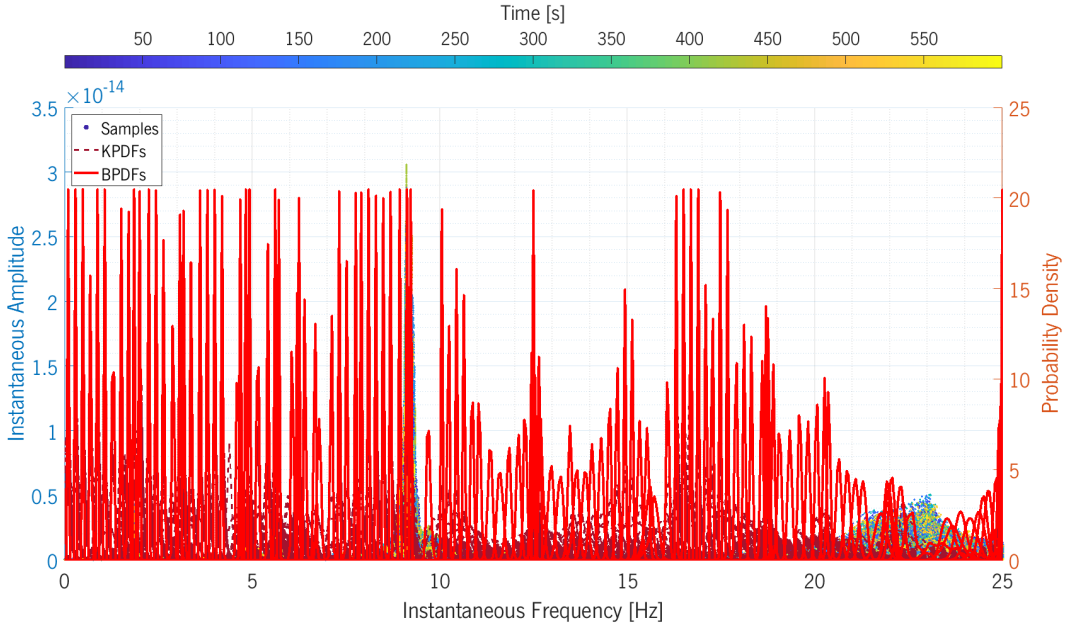


Figure 4.19: Time-dependent probability spectrum computed from the bridge in sound condition and resorting to an eight-level MODWPT decomposition. For better visualisation of the computed outputs, the spectrum is here presented until 25 Hz.

Therefore, a correct initial selection of the decomposition level is paramount and finding a good trade-off between resolution and computational burden may require an initial case-specific iterative test, by repeating identifications with different settings, before defining the values for long-term monitoring.

Moreover, further settings of the decomposition level can be carried out in the case that the modal information of interest is partially allocated between two adjacent segments, in which case, a reduction of the decomposition level can be an option to merge the previously separated modal information into a single spectrum segment.

It is worth mentioning that the EMILIA algorithm has a geometric $O(2m)$ time complexity related to the MODWPT decomposition level. Furthermore, the space complexity of the outputs is affected by the same geometric complexity as well.

The aforementioned statements can be visually assessed in Figure 4.20, where is presented the time complexity curve obtained from computing the same analysis repeatedly with an increasing decomposition level, ranging from one to ten levels.

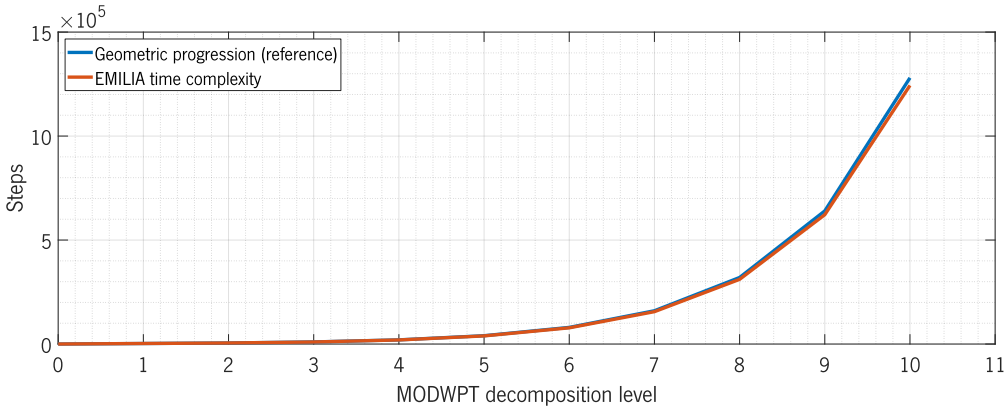


Figure 4.20: EMILIA algorithm time complexity computed by increasing decomposition levels.

4.3.2 Setting PDF distribution: Kernel vs Gauss and frequency resolution

As previously mentioned in Section 3.2.3, nonparametric Kernel probability distributions are preferred for computing the PDFs and providing the identification of the static frequencies for each acquisition, based on the dynamic instantaneous values. Hereafter, the bridge dataset is used to carry out a comparison between this default option of the EMILIA algorithm and a well-established parametric alternative, namely the Gaussian normal probability distribution.

For instance, Table 4.11 shows the results obtained from processing the *ST00* scenario data with a Kernel probability distribution, while Table 4.12 shows the results obtained by resorting to a Gaussian probability distribution.

Table 4.11: *ST00* six-level Kernel results.

6 Level MODWPT decomposition			
Frequency Results			
Mode	f_{MEV}[Hz]	σ^2	Max BPDF
1	1.86	≈0.0	20.48
2	4.93	≈0.0	19.55
3	5.63	≈0.0	14.65
4	—	—	—
5	—	—	—
6	9.10	≈0.0	14.80
Elapsed Time			
Process/Stage		Ref. Time	Steps
Data decomposition		10.67 s	54
Hilbert TFA		10.59 s	1691
Probability analysis		33.01 s	1755
Bayes Inference		0.03 s	1793
Mode Shapes		6.06 s	6722
Total elapsed time		60.39 s	77880

Table 4.12: *ST00* six-level Gauss results.

6 Level MODWPT decomposition			
Frequency Results			
Mode	f_{MEV}[Hz]	σ^2	Max BPDF
1	1.86	≈0.0	18.38
2	5.01	0.007	4.50
3	5.69	0.007	4.75
4	—	—	—
5	—	—	—
6	9.17	≈0.0	15.35
Elapsed Time			
Process/Stage		Ref. Time	Steps
Data decomposition		12.807 s	54
Hilbert TFA		14.475 s	1691
Probability analysis		5.784 s	1755
Bayes Inference		0.031 s	1793
Mode Shapes		9.139 s	6722
Total elapsed time		42.277 s	77880

Notwithstanding that the results memory allocation is the same, the Gauss computations were completed about 25% faster than the ones using a Kernel probability distribution, but the most significant differences can be observed in the maximum probability results of the Gauss-based analysis that are considerably lower than the results computed by resorting to the Kernel distribution.

Indeed, the Gauss-based analysis initially failed to identify the second, third, and sixth modes due to the lower probability peaks (Table 4.12), thus in the case of using Gauss as a probability distribution, a lower probability threshold had to be set.

The analysis is extended in Figure 4.21 to the complete EMILIA output spectrum. Here PDFs computed resorting to Kernel nonparametric probability distributions (red lines) are compared against PDFs computed using Gaussian normal probability distributions (blue lines), considering the 30-minute combined scenarios data set. As expected, the lower peaks of each PDF computed with the Gaussian distribution are considerably evident. Moreover, the estimation produced through Bayesian inference applied to the Gaussian PDFs presents a lower accuracy in terms of frequency values, which further deteriorates when assessing non-linear data.

Once the most adequate PDF is selected, and similar to the decomposition level, the frequency resolution of KPDFs and BPDFs is an inner parameter of the EMILIA algorithm which may affect its performance both in terms of accuracy and computational burden. Increasing the frequency resolution, indeed, generates better fits and smoothest distributions, likely increasing the accuracy of the

computed natural frequencies as well, but it also means a higher computational burden in terms of duration and time consumed.

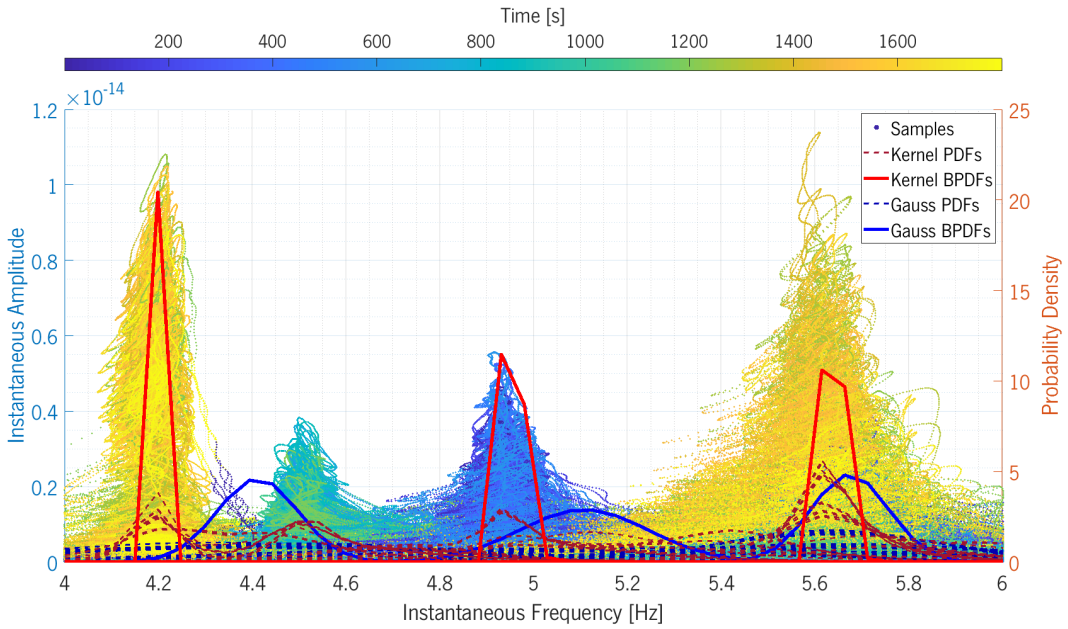


Figure 4.21: Time-dependent probability spectrum showing the probability analyses outputs computed by using a Gaussian parametric distribution (blue lines), and by using a Kernel nonparametric distribution (red lines).

Figure 4.22 shows on the left a time-dependent probability spectrum computed from the first mode instantaneous frequency data of the *ST00* scenario using a Kernel probability distribution with 1024 lines of resolution for all the KPDFs and the subsequent BPDFs and, on the right, the same spectrum but computed resorting to 10240 lines of resolution (ten-times the original resolution).
In this latter case, the distribution presents higher amplitude and narrower bandwidth, with an overall improved estimation performance, considering the exact frequency value of 1.87 Hz.

However, this almost negligible improvement in the accuracy of the result (0.53%) requires a considerable increment of the computational burden, both in the time needed to complete the analysis and in the size of the output files.

By investigating the sensitivity of the identification to the resolution through more simulations, it emerges that the f_{MEV} results converge to the best estimation at a resolution of 4069 lines, and they remain almost constant until 32768 lines of resolution (no further analyses with higher resolution were computed).

Therefore, commonly used resolutions of 512 to 2048 lines can be used as a good initial setting. For performing further and more complex studies, case-specific analyses might be carried out to optimise the parameter setting as needed.

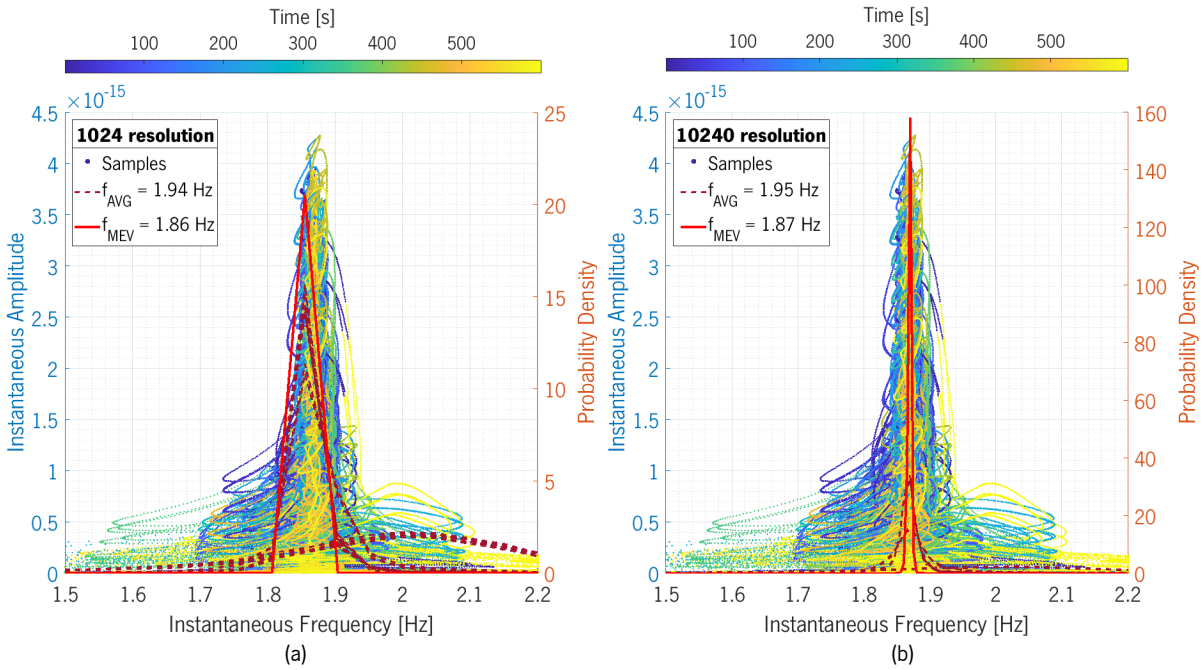


Figure 4.22: First mode Kernel PDFs and Bayesian PDFs computed using data from the *ST00* stiffness configuration. For the left plot, a resolution of 1024 FFT lines is used; whilst for the right plot, a resolution of 10240 FFT lines is used.

It is worth noting that Figure 4.22 allows also to explain the importance of the final Bayesian inference for the accuracy of the modal identification. By comparing the estimated frequency values reported in the legend, it is clear how the inference ($f_{MEV} = 1.86$ Hz) outperforms the simple average of all KPDFs' maximum probability frequency values ($f_{AVG} = 1.94$ Hz), considering that the target eigenvalue is equal to 1.87 Hz. This can be explained by observing the striped-red lines representing the KPDF distributions computed from the input channels, which depend on the local behaviour of each one of the instantaneous frequency outputs. For instance, higher probabilities are computed from nodes located at mid-span that present higher modal displacements in the first bending mode here investigated, while lower probability peaks are obtained at nodes located along the side spans. These latter KPDFs are also shifted over the frequency spectrum, concerning the former, leading to a lower accuracy of their mean. Bayesian inference, instead, weights the estimation by the computed distribution densities, therefore, higher peaks contribute more to the final BPDF.

4.4 Chapter conclusions and final remarks

In the present chapter, the proposed algorithm was tested and validated over the numerically simulated structural response of a three-span bridge under three different static stiffness conditions, where the latter was obtained by applying a progressive stiffness reduction factor to a selected area of the deck. A fourth case simulating varying stiffness conditions during a single acquisition was also built by joining the three previous ones altogether.

The validation of the results computed by the proposed algorithm was carried out by comparing the outputs against two well-known traditional modal estimators from proprietary modal analysis software (i.e. EFDD and SSI-UPCX). According to the obtained outputs and results, the EMILIA algorithm successfully identified the modal parameters of the system in its static undamaged and damaged conditions, producing a single set of natural frequencies for each acquisition and demonstrating performance comparable with the well-established alternative estimators. Moreover, the algorithm allowed identifying with high-reliability dynamic outputs, namely the instantaneous natural frequencies, and the instantaneous mode shapes, as proven by a newly developed strategy to visualise comparative results through instantaneous MAC values. These dynamic results cannot be achieved with the alternative dynamic identification algorithms, constituting a relevant advantage of EMILIA. This has allowed the processing of the non-linear data generated by combining in a single simulated acquisition the records from different structural conditions, successfully tracking the damage-induced shifts in the instantaneous outputs during the acquisition. This benchmark analysis confirmed the importance of the algorithm components combined within the three main stages of EMILIA, i.e. the MODWPT for the decomposition, the Hilbert transform for the instantaneous TFA, the Kernel nonparametric probability distribution employed to fit the instantaneous frequency data from each input, and the Bayesian inference for the final estimation of the static frequencies.

In the second part of the chapter, the dataset was exploited to conduct further tests aimed at validating the performance of these default components against valid alternatives as well as at defining a suggested setting for two main algorithm parameters, namely the MODWPT decomposition level and the PDF frequency resolution. The required level of decomposition is indeed a critical setting that can lead to a shortcoming of the current configuration of the algorithm, namely its potentially poor performance against closely spaced modes located inside the same $(f_s/2)/2^m$ frequency spectrum segment, especially in the case of modes with high complexity. In such a case, an increment of the chosen decomposition level of the MODWPT algorithm is a valid solution to reduce the span of the spectrum segments and properly isolate closely spaced modes, but at the cost of an increment in the computational burden. The suggested values presented in this chapter are a sufficiently robust initial setting for the parameters, however, they could require case-specific preliminary analyses for a tailored enhanced solution. For further insight into the outputs computed by the proposal, the complete outputs computed by the EMILIA algorithm for the 2D bridge case study, in means of the full probability analysis outputs, the time-dependent probability spectrums, and the Hilbert spectrograms can be found in the Annexe.

5 NON-LINEAR TIME-DEPENDENT DYNAMIC IDENTIFICATION

5.1 Introduction

Over the past decades, many researchers have tested the use of seismic excitations and earthquake records to perform dynamic identification of civil engineering structures for SHM and damage evaluation purposes (Quqa, Landi, and Diotallevi 2021; Limongelli and Çelebi 2019; Ebrahimian et al. 2018; Noël and Kerschen 2017). However, several complications can appear when resorting to strong seismic records due to the non-linear response of the structure and the unknown characteristics of the input in terms of energy and frequency content and its evolution during the event.

Furthermore, the structural responses to strong motion data are usually dominated by the first two bending modes, also known as the *whip effect*, which is especially relevant during massive seismic events (Housner 1963), and then remain in transitional state until the energy of the event is utterly dissipated. As previously mentioned, traditional parametric modal analysis algorithms limited by the superposition principle (Brincker 2014; Peeters and De Roeck 2001) are hardly capable of correctly identifying the structures in this condition.

One of the most underestimated consequences regarding the above statements is that the extensive database of seismic records currently available worldwide can hardly be used to perform dynamic identification for civil engineering purposes. To this end, to generate the capability of performing OMA with seismic records could be a powerful tool for assessing the actual conditions and performance of civil structures.

Therefore, upon the successful validation in the previous chapter of the EMILIA algorithm over a traditional linear modal analysis and time-dependent dynamic identification, hereafter the methodology is applied to non-stationary acceleration records, the goal being testing the proposal against two relevant case studies subjected to realistic damage scenarios.

The first case study consists of the FE model of an idealised masonry tower developed in proprietary FE software, to numerically simulate undamaged and damaged conditions induced by strong seismic base excitations. EMILIA is thus assessed against non-linear and high-transient data and employed to support time-dependent damage identification.

The second case study consists of a scaled shear-type steel structure measured in sound and damaged condition, in order to evaluate the capability of the proposed algorithm to process real structural responses resorting to short and potentially noisy trends of data. Non-linear OMA is conducted as well by utilising acceleration measurements performed while structural damage is manually induced in the structure.

5.2 Case study II: FE model of a masonry tower

5.2.1 Model description, eigenvalue analysis and simulated monitoring

For a more comprehensive validation of EMILIA against realistic seismic induced structural damage scenarios, an artificial case study was utilised. Simulated case studies allow the generation of relevant information for algorithm testing in a controlled way, circumventing the typical lack of such information from real-world cases. To this end, an idealized 3D double-leaf masonry tower was modelled on proprietary FE analysis software (DIANA FEA B.V. 2021).

The tower is 28 m high and features a square plan of 6 m x 6 m, with double-leaf masonry walls 0.6 m thick. Two timber floors are located at 10 m and 20 m, respectively. Floor slabs are directly connected to the timber beams inserted in the masonry wall thickness. The material properties adopted for the numerical model are reported in Table 5.1.

Table 5.1: FE material properties adopted for the numerical model.

Timber Properties		
Linear Properties		
Young´s modulus	10000	[N/mm²]
Poisson's ratio	0.35	
Mass density	428.28	[kg/m³]
Masonry Properties		
Linear Properties		
Young´s modulus	2200	[N/mm²]
Poisson's ratio	0.2	
Mass density	1400	[kg/m³]
Tensile behaviour		
Tensile curve	Exponential	
Tensile strength	0.18	[N/mm²]
Mode-I tensile fracture energy	10	[N/m]
Crack bandwidth specification	Rots	
Residual tensile strength	0.12	[N/m²]
Poisson's ratio reduction	Damage based	
Compressive behaviour		
Compression curve	Parabolic	
Compressive strength	3.7	[N/mm²]
Compressive fracture energy	5900	[N/m]

A linear behaviour is assumed for all timber elements, whereas non-linear properties are assigned to the masonry material. Particularly, the latter are set based on values retrieved from the literature, for instance in (Ramírez, Lourenço, and D'Amato 2019).

The interaction between the tower foundations and the soil is modelled as a boundary interface connection with Coulomb friction and a cohesion equal to 100 kN/m, inserted between the model base elements and the ground fixed supports.

The FE model comprises a total of 8467 quadratic/hexagonal elements with quadratic mesh order and linear inner element point interpolation. The maximum side length for any element is set at 0.5 m. A total-Lagrange geometrical formulation and a crack model based on total strain are used.

An initial free vibration eigenvalue analysis is conducted to identify the reference modal parameters for the tower in sound condition and inform the definition of the acquisition parameters required for the subsequent non-linear transient analyses as well as the positioning and number of output nodes for the simulated monitoring.

As for the eigenvalue and eigenvector results, the dynamic response of the masonry tower may be adequately described by the first six vibration modes, accounting for an accumulated participating mass in the frequency range of 1-12 Hz of about 85% in all three directions. The computed periods, frequencies, and shapes of these modes are presented in Figure 5.1, along with the relevant mass participation per mode.

The first two vibration modes of the tower are very close spaced with frequency values of 1.79 Hz and 1.82 Hz respectively, as expected due to the symmetry of the structure. Both modes present essentially translation components, the first one along the x direction and the second one along the y direction, and feature more than 60% of effective mass participation each. The third mode is the first torsional and has a natural frequency of 5.61 Hz and a 3% effective mass along the Y axis, producing a slight leaning of the eigenvector towards the main-entry wall.

The fourth and fifth modes are the second translational modes. Similarly to the first and second modes, they are closely spaced. The fourth mode has a natural frequency equal to 7.43 Hz, with an effective mass participation of 18.8%, whilst the fifth mode presents a natural frequency of 8.04 Hz with an effective mass participation of 20.7%. The sixth mode presents normal displacements along the Z direction, at a natural frequency of 11.11 Hz, and with an effective mass participation of 82.6%.

According to the above, from each corner of the tower, eight nodes equally spaced in height, every four meters, are selected to acquire the nodal acceleration response in X, Y and Z directions. All collected records are then used for output-only dynamic identification with the proposed algorithm.

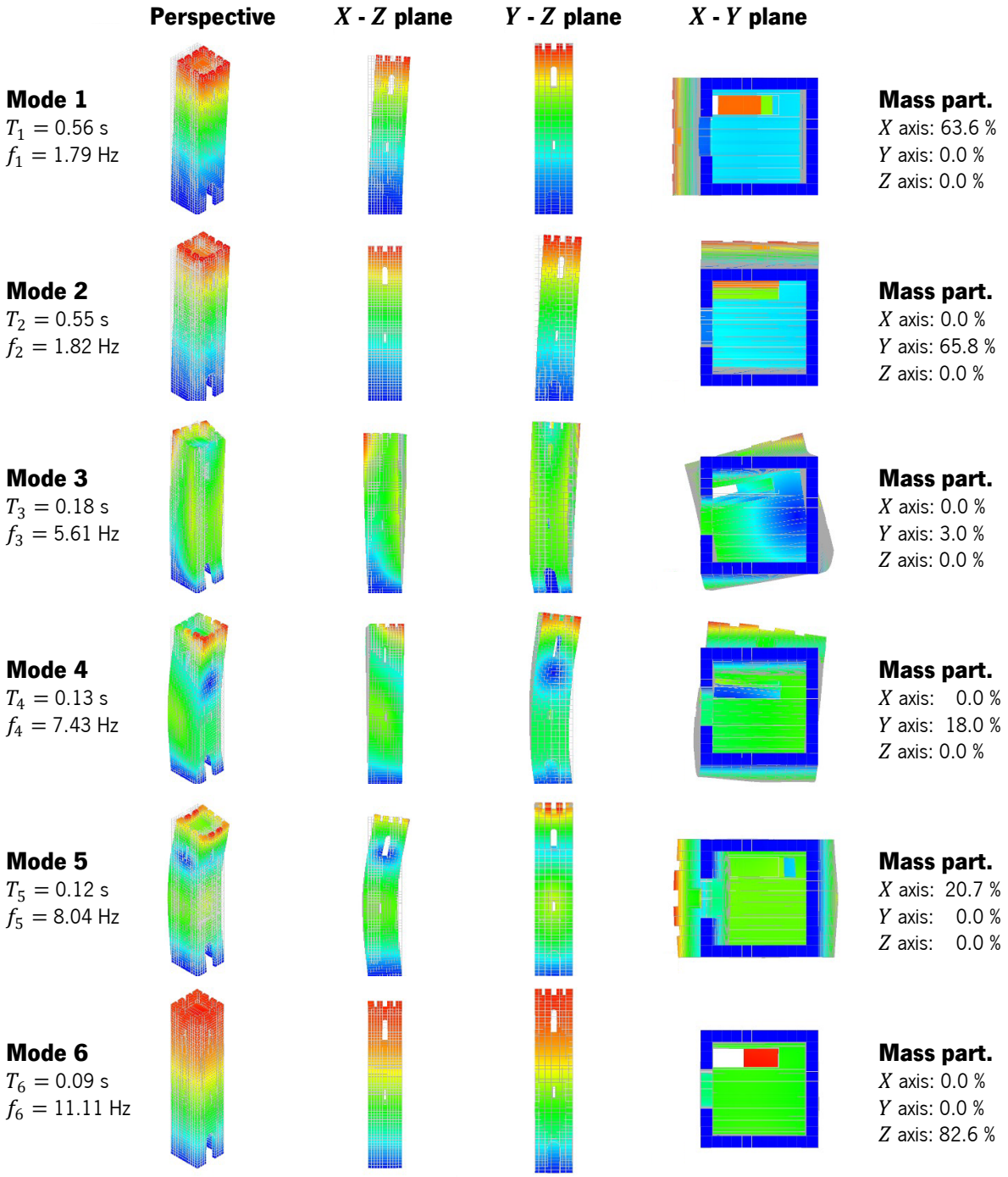


Figure 5.1: First six eigenvectors and eigenvalues of the masonry tower.

Based on the eigenvalue analysis, $T_6 = 0.09$ s and $f_6 = 11{,}11$ Hz are considered as the lowest period and corresponding highest frequency of interest for the structure. The highest period of interest allows setting the time steps as 0.01 seconds, to ensure a good resolution for the subsequent non-linear transient analyses under ambient vibrations. However, for the non-linear transient analyses with real earthquake excitations, a shorter time step, equal to 0.00125 seconds, is used to ensure the

convergence of each iteration due to the structural damage induced on the masonry tower by the seismic inputs.

A Non-Linear Time-History (NLTH) analysis is performed using real earthquake acceleration data applied as base excitation in all three directions. The ground motion selected for this purpose is the main shock of the L'Aquila earthquake (ITACA ID: IT-2009-0009) that occurred on April 6th, 2009, in the region of Abruzzo, Italy. The earthquake intensity map can be examined in Figure 5.2.

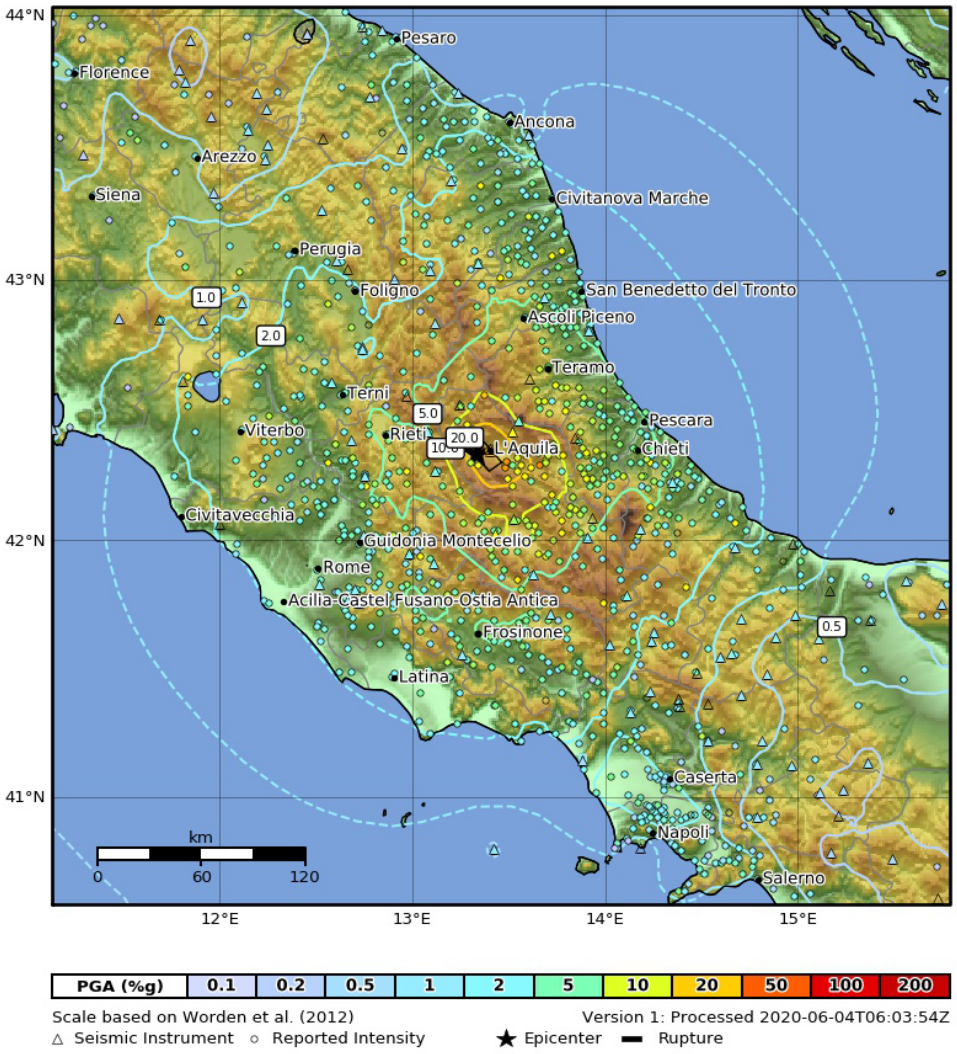


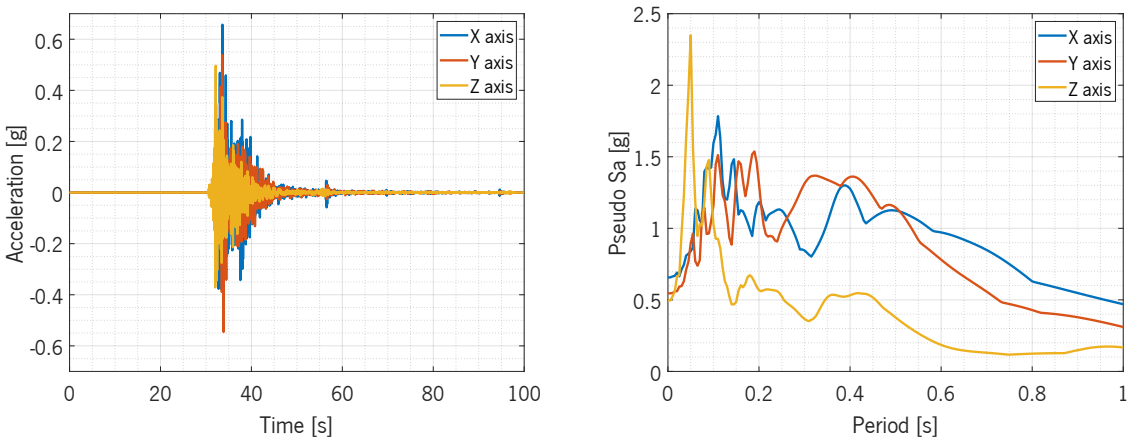
Figure 5.2: PGA map from 2009 L'Aquila 6.3 Mw main shock (Image courtesy of the U.S. Geological Survey).

The main shock occurred at 03:32 CEST (01:32 UTC) and was rated 5.9 on the Richter magnitude scale and 6.3 on the moment magnitude scale. The epicentre was at a depth of 8.3 km near the city of L'Aquila (INGV 2009b). The earthquake caused severe damage to L'Aquila and various towns in the surrounding areas, where many buildings and structures were destroyed or extensively damaged, leading to widespread displacement of residents. The earthquake also caused landslides and power outages, and several aftershocks occurred in the following days, more than thirty of which

had a Richter magnitude higher than 3.5. A summary of 2009 L'Aquila's earthquake main shock data and characteristics can be found in Table 5.2. The data selected as base excitation inputs for the NLTH analysis was recorded at the *L'Aquila V. Aterno Centro Valle* station, part of the *Rete Accelerometrica Nazionale* (RAN), located at 4.9 km from the earthquake epicentre (INGV 1997; 2009a). The recorded data are sampled at 0.005 seconds for a total duration of 100 seconds. Figure 5.3 shows the earthquake data accelerograms and the pseudo-acceleration spectrum.

Table 5.2: L'Aquila earthquake overall information.

Axis	T_s	HP [Hz]	LP [Hz]	PGA [cm/s²]	PGV [cm/s]	PGD [cm]	Arias Int. [cm/s]	Housner Int. [cm]
North	0.005	0.1	40	-535.20	-42.72	3.31	199.20	94.81
Normal	0.005	0.1	40	486.65	12.44	-2.45	94.18	41.79
East	0.005	0.1	40	644.25	-40.21	6.79	282.46	131.41



(a) (b)

Figure 5.3: (a) 2009 L'Aquila earthquake accelerogram, (b) pseudo-acceleration response spectrum.

To simulate the effect of sources of noise in the input, besides the acceleration records employed as base excitations, low-amplitude Gaussian white noise actions are applied to several points on each side and along the entire height of the structure using non-symmetrical patterns. The Hilbert-Hughes-Taylor transient time integration method with alpha equal to -0.1 and the secant iteration method are used for the NLTH analysis. The computed accelerations in X, Y, and Z directions for the 32 selected nodes located along the four edges of the tower are the requested data outputs. The computed data, originally with a 0.00125-second time-step, is decimated to finally generate simulated acceleration records with a sampling frequency equal to 100 Hz. Examples of the X, Y, and Z axes computed acceleration outputs in the four base-level and the four top-level nodes can be seen in Figure 5.4 and Figure 5.5, respectively.

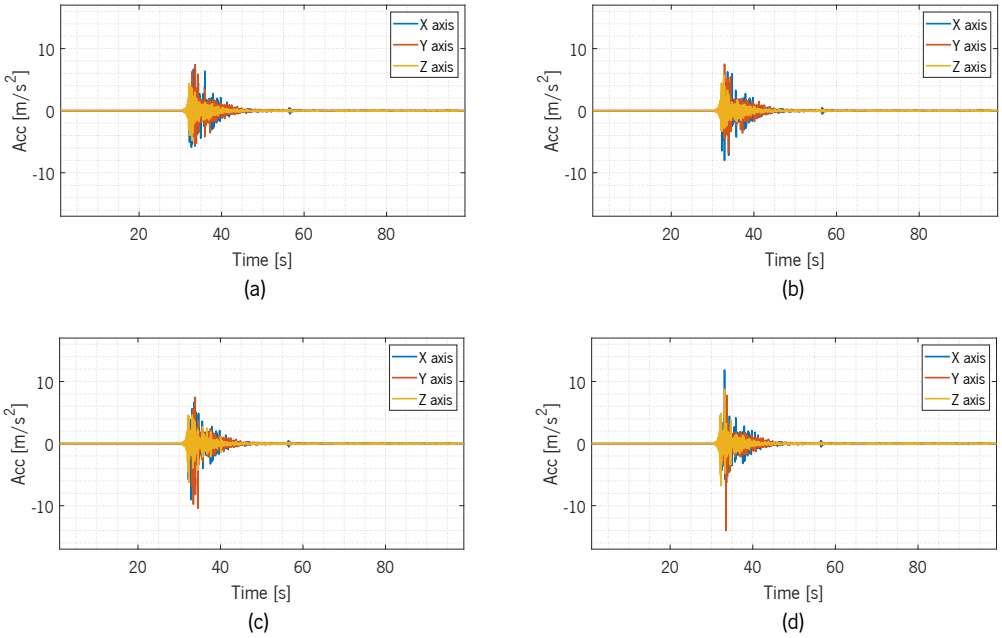


Figure 5.4: Computed acceleration outputs on the four base-level nodes. Plot (a) is from the north base node, plot (b) is from the east base node, plot (c) is from the south base node, and plot (d) is from the west base node.

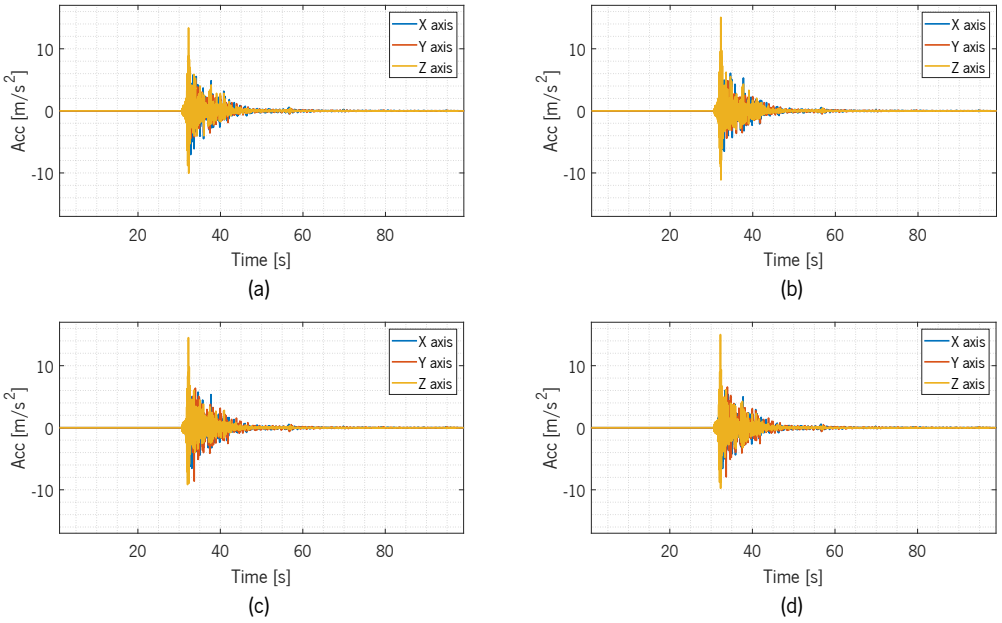


Figure 5.5: Computed acceleration outputs on the four top-level nodes. Plot (a) is from the north top node, plot (b) is from the east top node, plot (c) is from the south top node, and plot (d) is from the west top node.

The outcomes presented on above figures displays a high transient non-linear structural response activated along the whole height of the model by the seismic input. To localise the structural damage, principal strains and crack-width outputs are further investigated.

Through the computed results, the most affected area of the tower is identified above both upper corners of the main entry door. The four time steps characterised by the higher tensile strain in the

obtained results are reported in Table 5.3. All of them occur during the main shock of the earthquake. The highest strain observations are obtained for *Node 6453* at 34.5 seconds into the analysis, whilst for *Node 7965* at 35.73 seconds into the analysis. Figure 5.6 shows a detailed view of the tower with the two node locations and the computed principal strain results around the tower's main door.

Table 5.3: Identified time steps showing the higher principal strain results.

Ts	Time	Principal Strain	Node
3350	33.50	2.20E-04	6453
3388	33.88	2.12E-04	6453
3450	34.50	2.26E-04	6453
3573	35.73	2.26E-04	7965

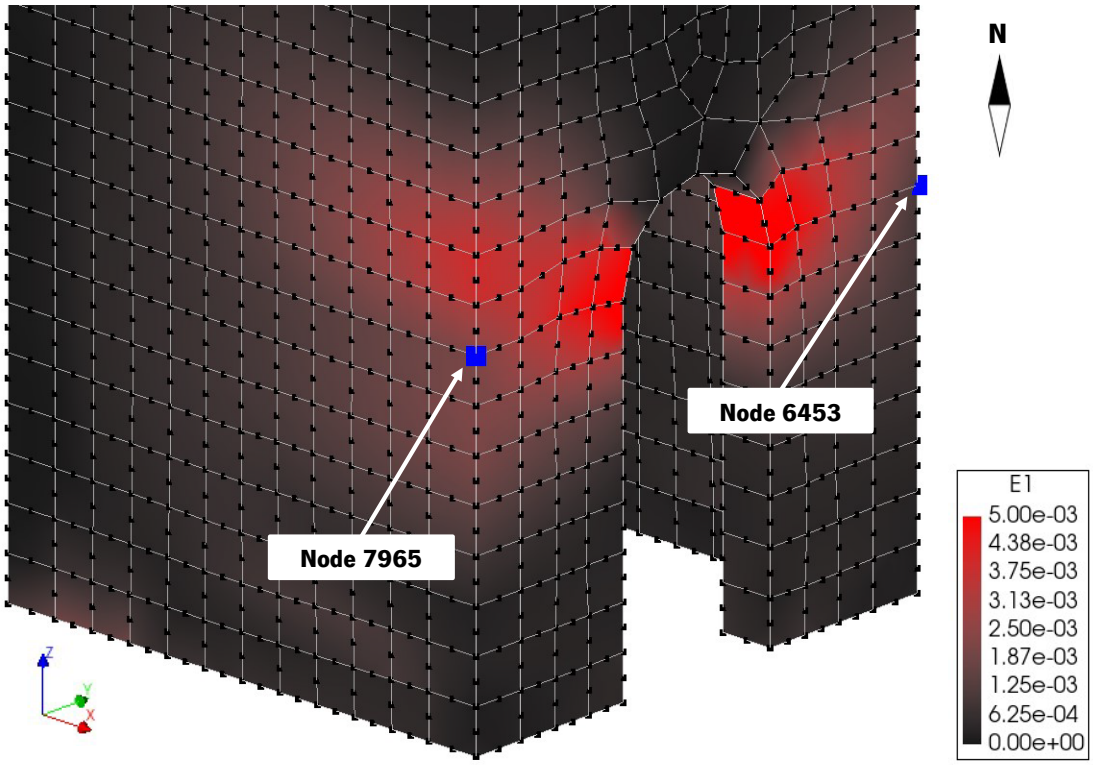


Figure 5.6: Principal-strain results computed in the upper side of the FE model's main door. The two blue nodes show the closest output nodes to the location of the induced damage.

Furthermore, the computed outcomes of NLTH analysis in terms of crack width confirm that the area with the most severe structural damage induced is located on the two sides of the main door, as can be observed in Figure 5.7. The time steps that present the higher crack-width results for both nodes are presented on Table 5.4. For the sake of simplicity and shortening the nomenclature of the writing, from this point onward, the two selected nodes are addressed as *Node A* (formerly *Node 7965*) and *Node B* (formerly *Node 6453*).

Table 5.4: Identified time steps with the biggest crack widths results.

Ts	Time	Crack width	Node
3356	33.56	1.41E-03	B (6453)
3573	35.73	1.38E-03	A (7965)

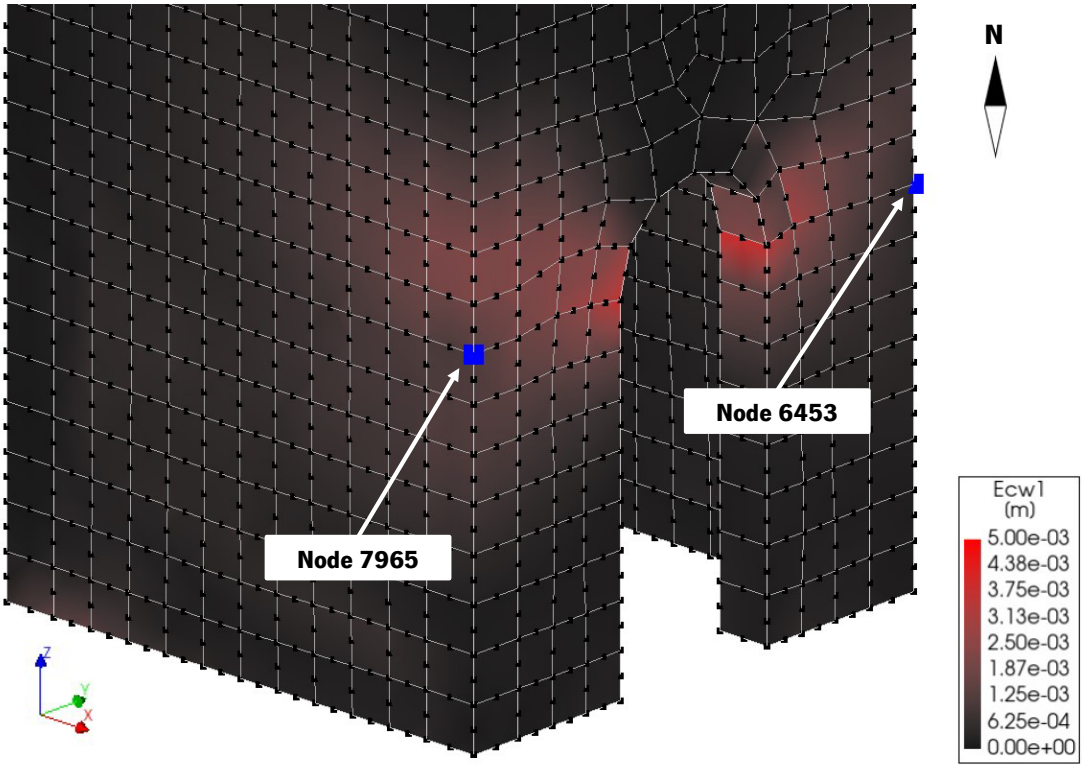


Figure 5.7: Crack-widths results computed at 35.73 seconds of the NLTH analysis.

5.2.2 Operational modal analysis

The preliminary OMA is performed resorting exclusively to the first 30 seconds of the simulated acceleration data, which is related to the structural responses before the earthquake's main shock, as can be noticed in figures 5.3, 5.4, and 5.5. Regarding the EMILIA algorithm settings, the same mother wavelet used for the OMA analyses that can be found in the previous chapters, namely a Daubechies 45 mother wavelet, is once again used. For this case, the pre-existing knowledge of the number of modes of interest is used as a reference for choosing the initial level of the discrete wavelet decomposition. Seventy-one eigenvectors with natural frequency values below the Nyquist frequency (50 Hz) were found through the FE eigenvalue analysis, thus, a six-level MODWPT decomposition was selected for applying the EMILIA algorithm in order to obtain 64 sub-sequences.

For this modal identification with short records, a strategy to improve the results of the probability analyses is defined by processing only the acceleration data from degrees of freedom expected to have

an effective participation in each mode, namely only the records along the X axis are used for the identification of the first mode, only the records along the Y axis are used for the identification of the second mode, both the records along X and Y axes are used for the identification of the third, the fourth and the fifth modes, and, finally, for the sixth mode, the records along the Z axis are used. It is worth noting that, for a real case study application, this strategy requires prior knowledge of the structure to assess, although, for simple structures, like masonry towers, expert judgment may easily support the selection of these degrees of freedom. The computed results of the first six identified vibration modes are summarised in Table 5.5 in terms of the f_{MEV} values computed from the instantaneous frequency samples of each decomposition output, and they are presented in comparison with the natural frequencies obtained from the FE eigenvalue analysis.

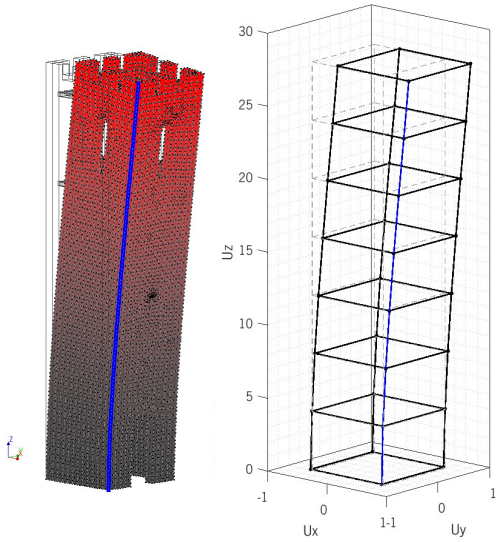
Table 5.5: EMILIA f_{MEV} results of the first six modes.

Mode	Period [s]	Eigenvalue [Hz]	EMILIA f_{MEV} [Hz]	Data set
1	0.56	1.79	1.88	X
2	0.55	1.82	1.90	Y
3	0.18	5.61	5.72	$X - Y$
4	0.13	7.43	7.48	$X - Y$
5	0.12	8.04	8.11	$X - Y$
6	0.09	11.11	10.70	Z

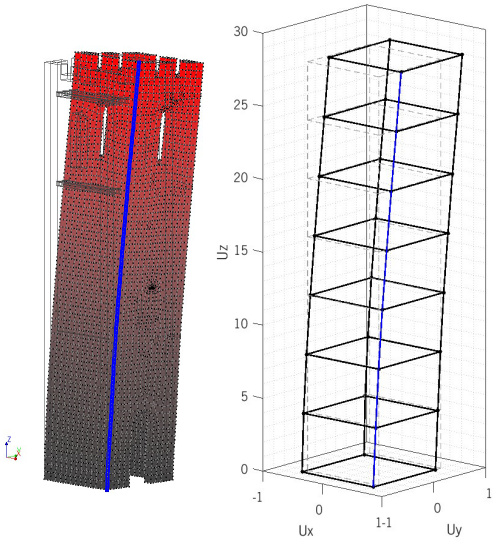
The results presented on the above table demonstrates that EMILIA was capable of identifying the intended modes with good accuracy. It is also important not to forget that the f_{MEV} values computed by the EMILIA algorithm are a statistical calculation to achieve a singleton result from the instantaneous frequency data, since the main characteristic of the algorithm lies in its capability of computing the instantaneous dynamic parameters as time-dependent functions.

As the sixth mode has almost all the effective mass participation in the vertical direction (see Figure 5.1), only the modes with higher horizontal displacements are considered onward for this case study. For instance, reference instantaneous displacement mode shapes of the first five modes with the correspondent eigenvector can be viewed in Figure 5.8.

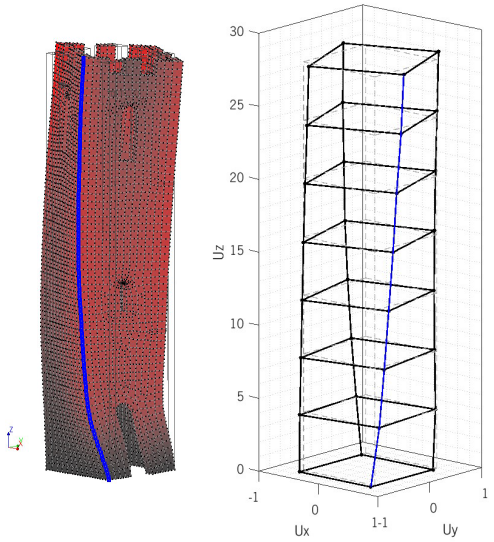
Following the preliminary OMA over ambient vibration in undamaged condition, the dynamic identification is carried out over the outputs of the strong seismic excitation. This high-transient action is expected to induce structural damage, which is likely to produce sudden variations in the modal parameters, namely instantaneous frequency values and mode shapes. As for the parameters of the EMILIA algorithm, they remain the same as those previously used in the ambient vibration analysis.



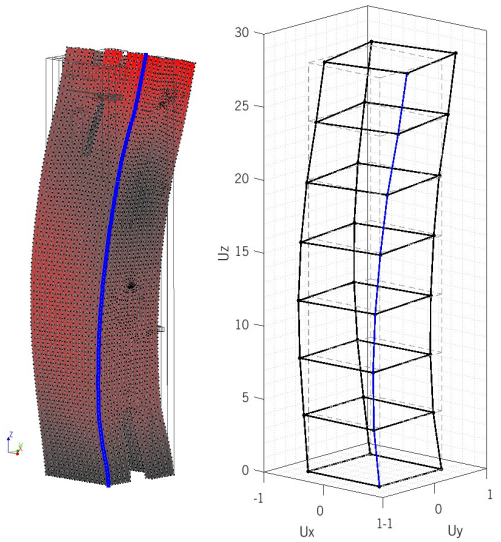
Mode 1: 1.88 Hz



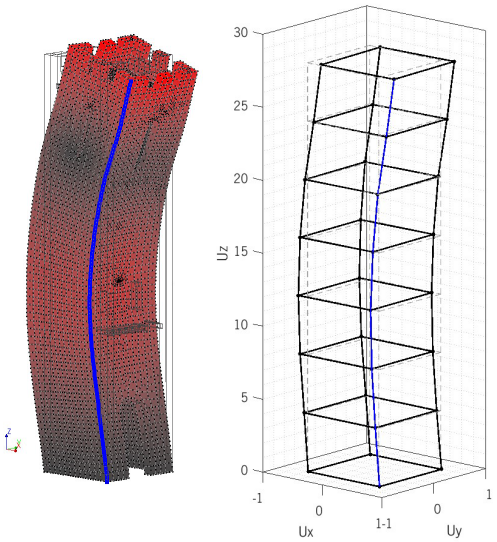
Mode 2: 1.90 Hz



Mode 3: 5.72 Hz



Mode 4: 7.48 Hz



Mode 5: 8.11 Hz

Figure 5.8: First five eigenvectors and corresponding examples of instantaneous mode shapes computed by the EMILIA algorithm. The blue colour lines highlight the south edge where *Node A* is located.

Figure 5.9 shows the Hilbert spectrogram computed resorting to the complete 100 seconds of the simulated acceleration data obtained from the X axis, whilst Figure 5.10 shows the Hilbert spectrogram computed from the same 100 seconds but resorting to the Y axis data.

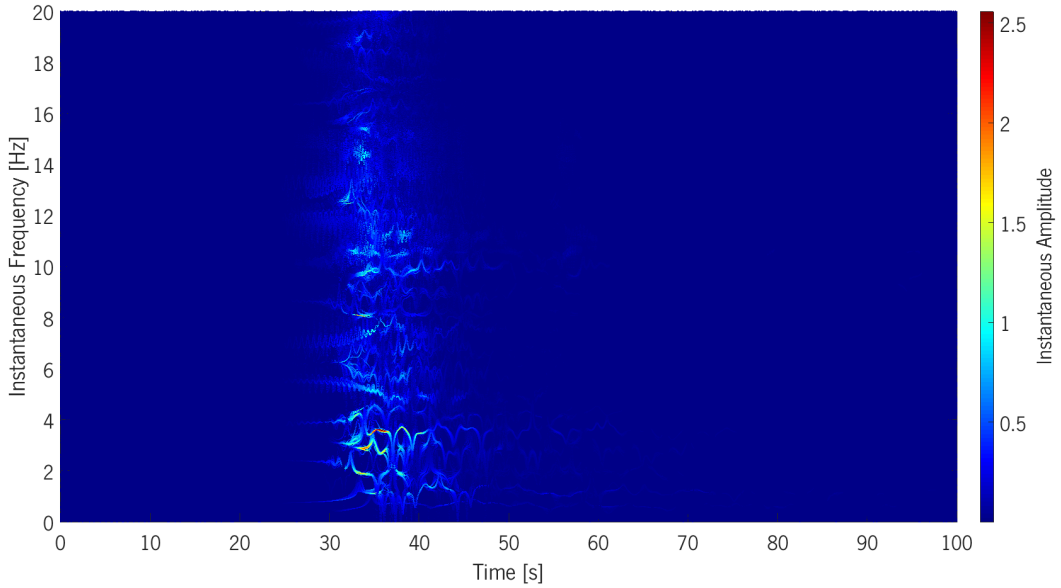


Figure 5.9: Hilbert spectrogram of the tower X axis responses to the L'Aquila earthquake's data.

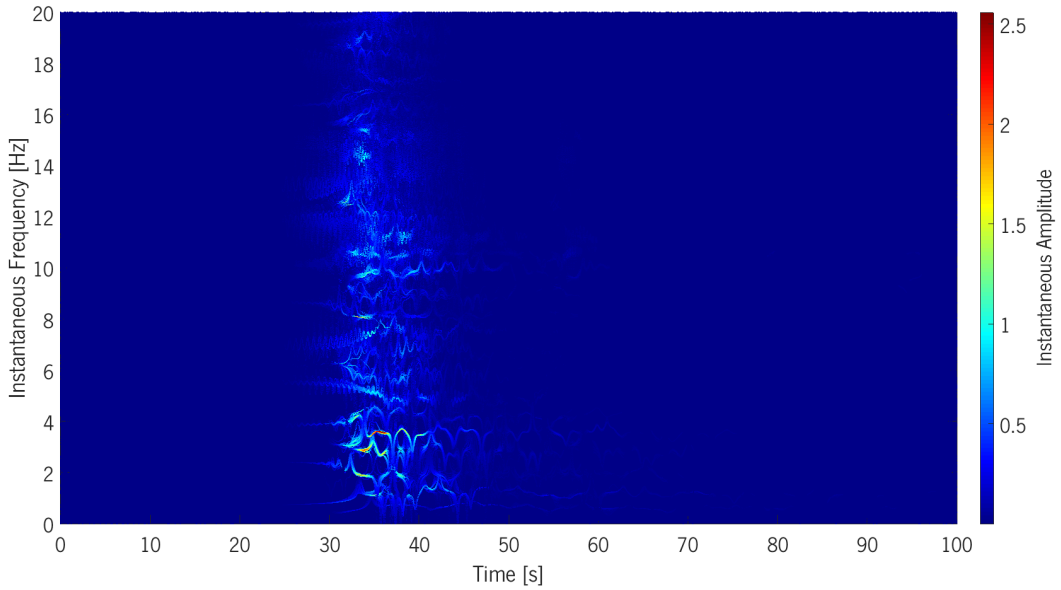


Figure 5.10: Hilbert spectrogram of the tower Y axis responses to the L'Aquila earthquake's strong data.

In both spectrograms, it can be noticed the high energy zone after the beginning of the seismic event, as highlighted by the colour scale of the instantaneous amplitude magnitude, between 30 and 40 seconds into the analysis, mostly concentrated in the range between 1 and 5 Hz, with another peak of energy around the 9 to 12 Hz range. This result is consistent with the seismic information previously reported in Figure 5.3, and the time step in which the highest principal strain and the largest crack-

width are recorded, namely 35.73 seconds. For example, Figure 5.11 reports instantaneous mode shapes computed at the 3573 time-step (black colour lines), corresponding to the maximum tensile principal strain record, whilst the edge holding *Node A* is highlighted in blue colour.

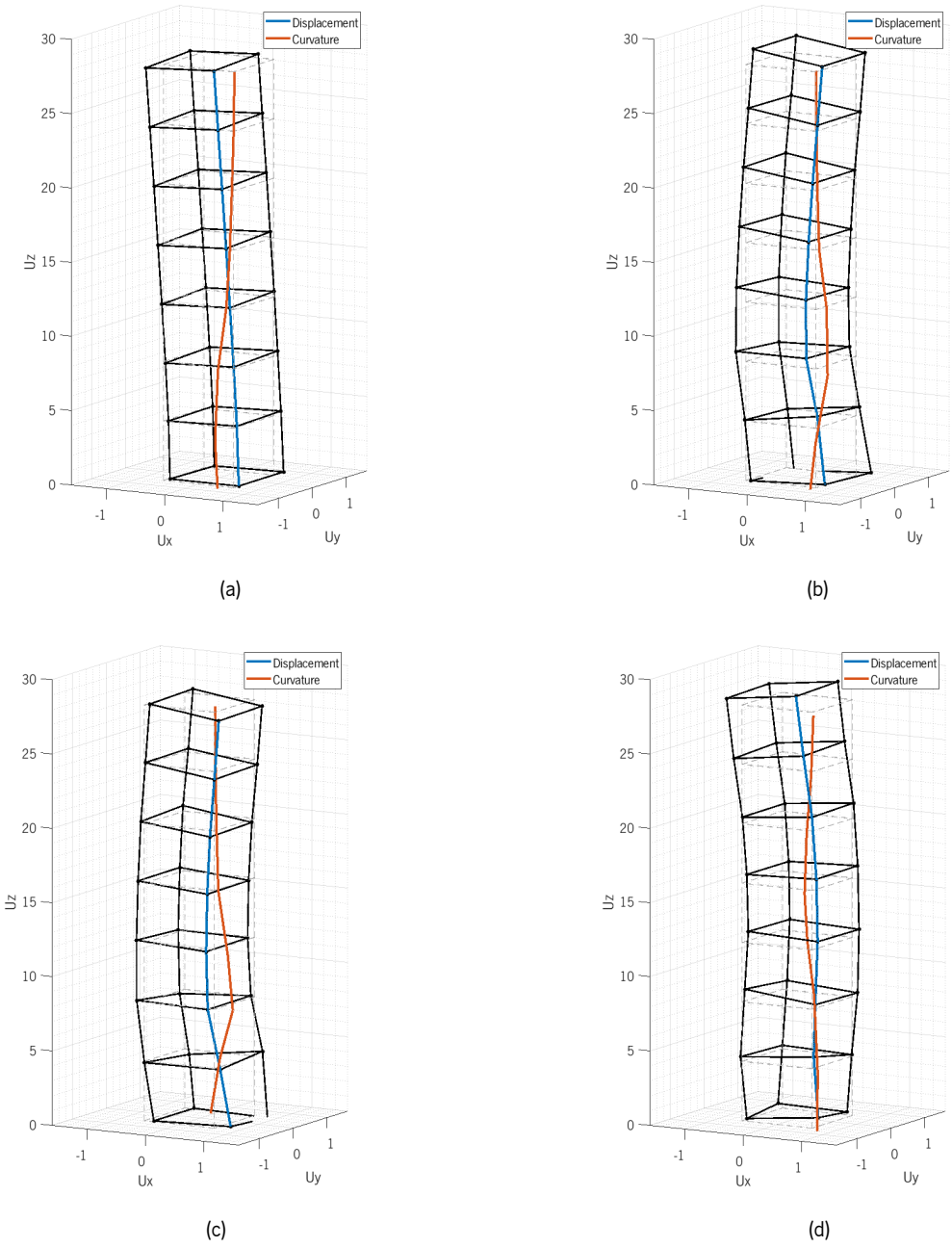


Figure 5.11: Displacement mode shapes computed for the 3573 time-step (T_s = 35.73 seconds): (a) Mode 2; (b) Mode 3; (c) Mode 4; (d) Mode 5. The blue line shows the displacements of the south edge. The orange line shows the modal curvatures for the same edge. Mode 1 is not considered due to the lower damage presented in Figure 5.12.

By taking a closer inspection of the nodes located on the base of the tower, especially in the instantaneous mode shapes at the bottom of the figure (Mode 4 and Mode 5), it can be observed that some sharp angles are formed by the excursion of the nodes located at 4 m and 8 m high of the

computed mode shapes, especially on the instantaneous curvatures computed for the fourth mode, which suggest that strong displacements were applied to the model at that specific time-step.

5.2.3 Time-Dependent Damage Identification

In order to validate the proposed algorithm for performing structural damage identification using non-linear high-transient data, time-dependent MAC analyses are conducted. The time-dependent MAC results computed for the first five modes are presented in figures 5.12, 5.13, 5.14, 5.15, and 5.16 as a light-blue-coloured line.

The plots are computed by comparing the instantaneous displacement mode shapes of the selected edge at each time step with the reference edge mode shape obtained through the eigenvalue analysis (see Figure 5.8 and Figure 5.11). Additionally, the second derivatives of the edge were treated as reference modal curvatures, and the time-dependent MAC was computed against the second derivatives of the corresponding instantaneous mode shapes, as indicated by the orange-coloured line. On top of the figures, it is reported the output from the channel that computed the maximum acceleration for the corresponding mode.

To compute smoother and neater functions, similar to the time-dependent MAC analyses presented in Section 4.2.3, only the highest MAC value within each one-second window of analysis (100 samples) is presented.

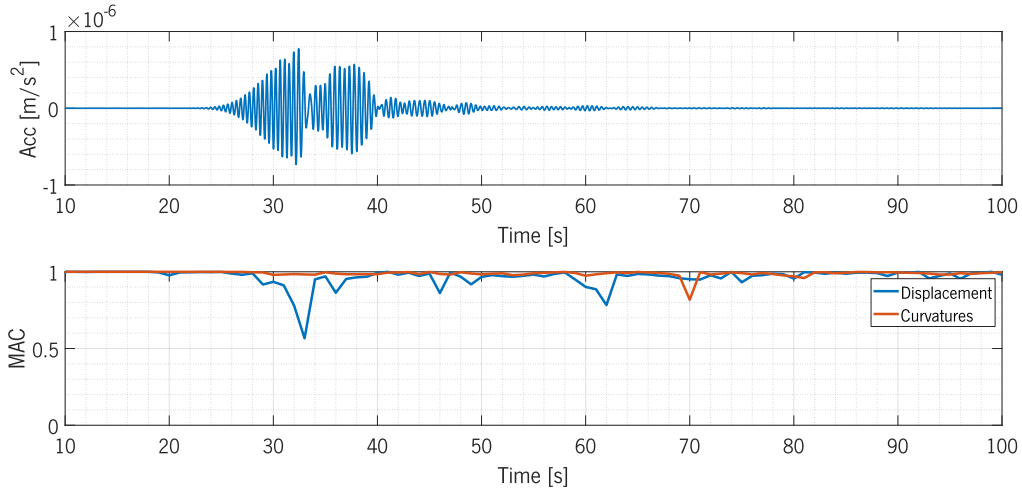


Figure 5.12: Mode 1 time-dependent MAC results.

The first mode appears to be mostly unaffected by the strong seismic excitations in terms of visible damage on the modal curvatures. However, the proposed algorithm is capable of detecting the main shock as a significant perturbation in the time-dependent displacement MAC results.

On the other hand, the results for the second mode (Figure 5.13) indicate that while the instantaneous displacement MAC results do not exhibit significant perturbations induced by the earthquake, the instantaneous curvature suffers significant variations during and after the main shock, likely a consequence of some degree of structural damage.

Figure 5.14 presents the time-dependent MAC results obtained for the third mode, which is the first torsional mode. The computed results show a significant reduction in the instantaneous MAC values computed after the onset of the seismic event, around the 30-second mark, for both the time-dependent displacement and curvatures MAC calculations.

Additionally, the divergence in the MAC results is not limited to the seismic event timeframe but continues after the end of the earthquake.

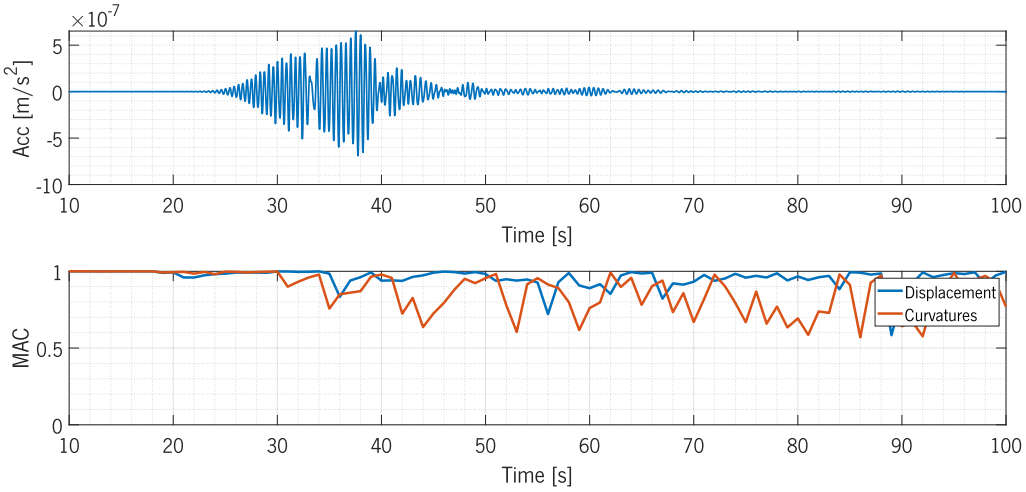


Figure 5.13: Mode 2 time-dependent MAC results.

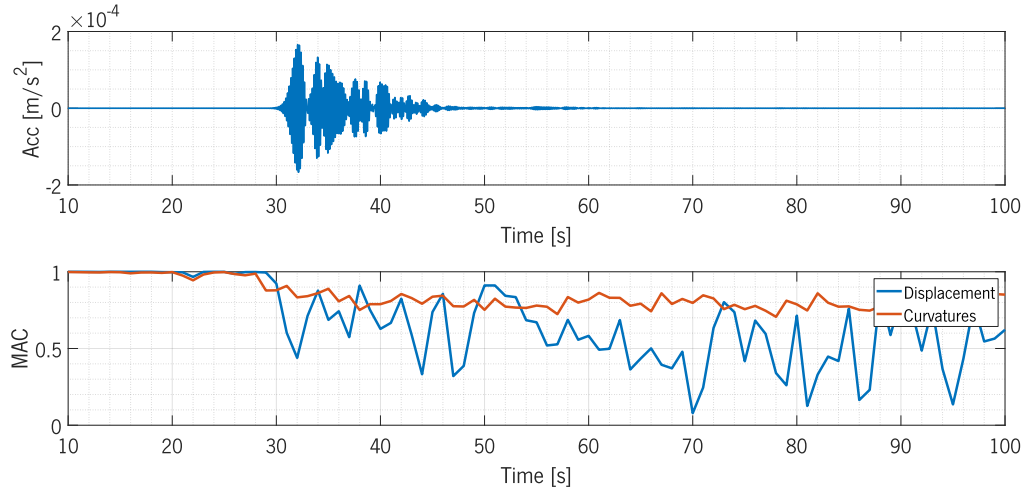


Figure 5.14: Mode 3 time-dependent MAC results.

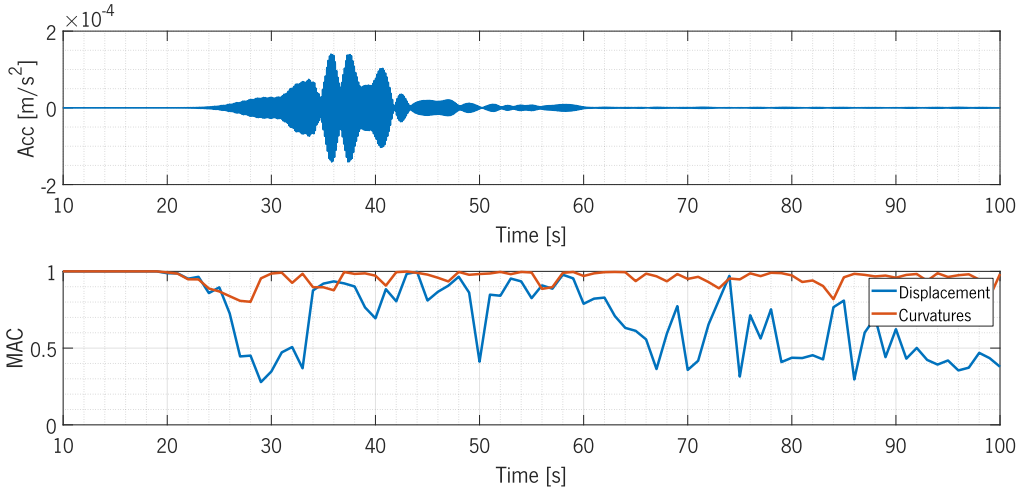


Figure 5.15: Mode 4 time-dependent MAC results.

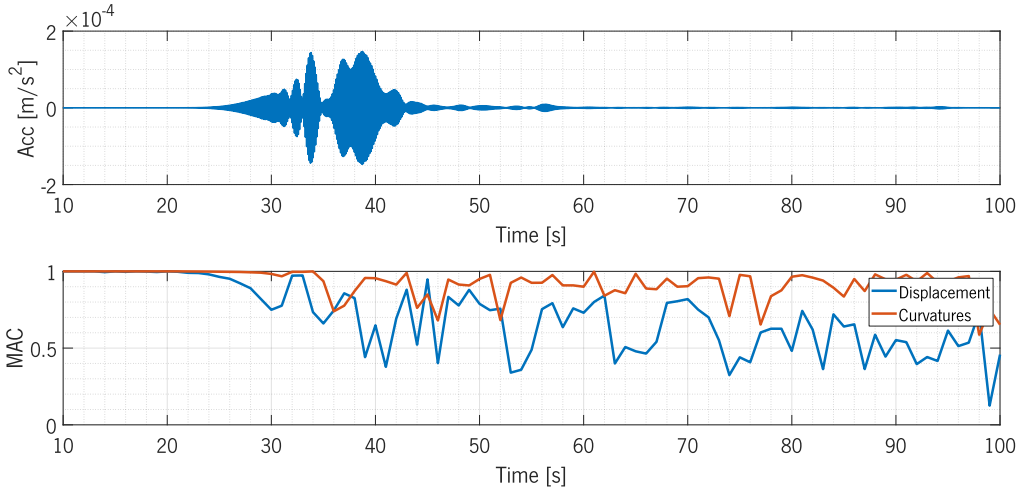


Figure 5.16: Mode 5 time-dependent MAC results.

A similar outcome can be observed for the fourth mode in Figure 5.15 and for the fifth mode in Figure 5.16. In the figures, both modes present instantaneous MAC computations with significant variations during and after the seismic event.

Recalling the mode shapes presented in figures 5.1, 5.8, and 5.11, the damage sensitivity of the second, third, fourth and fifth modes can be explained by the significant contribution of the most damaged area, above the door, to the shape, especially for the third and the fourth modes.

Figure 5.17 shows a pair of the fifth mode´s instantaneous shapes computed before the earthquake with the tower in sound condition (three plots on top), in comparison with another pair of instantaneous mode shapes computed after the earthquake main shock (three plots on the bottom). On the same plots, *Node A* is noted over each instantaneous mode shape with a blue dot, and the edge holding the transducers previously used for the MAC and results can be seen highlighted in green

colours for the shapes computed before the earthquake on top, and in red colours for the shapes computed after the earthquake on bottom. As a reference, the undeformed tower shape is plotted in dashed grey lines as well. It is worth noting that these two shapes were selected visually aiming to show the full displacement of the instantaneous shapes during each scenario.

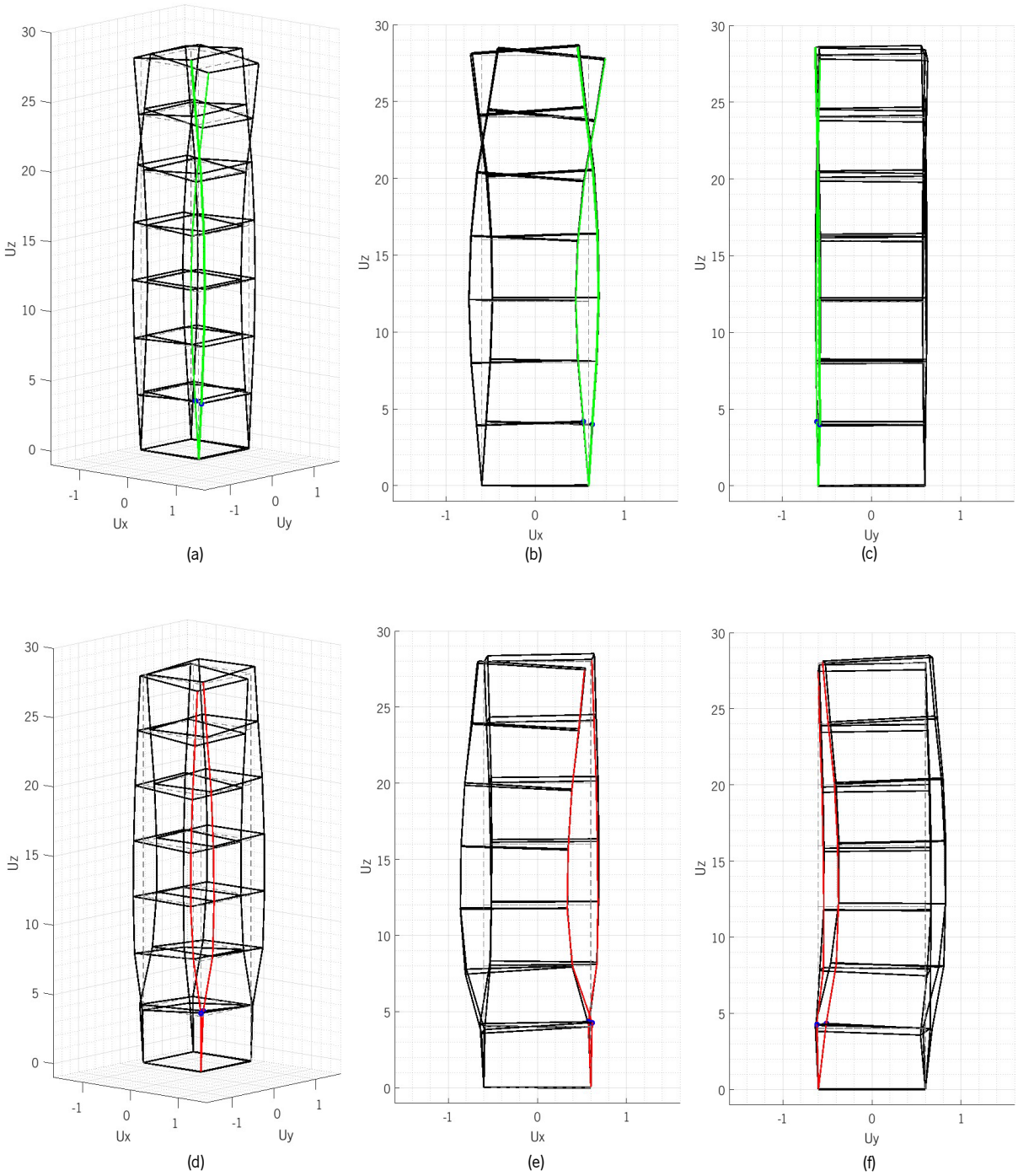


Figure 5.17: On top: (a) A perspective view, (b) an X-Z plane, (c) and Y-Z plane of a pair of selected fifth mode instantaneous mode shapes computed before the earthquake. On the bottom: (d) A perspective view, (e) an X-Z plane, (f) and Y-Z plane of a pair of selected fifth mode instantaneous mode shapes computed after the earthquake.

Regarding the shapes presented on top of the previous figure, the smooth displacements are in line with what can be expected for a second bending mode along the X axis.

On the other hand, the shapes presented at the bottom of Figure 5.17 show a significant change of curvature of the structure starting from the position of *Node A* and *Node B* at 4 m high, with smaller deviations of the instantaneous shapes at the simulated sensor located 8 m high.

The previous statements are especially notorious in the plot displaying the Y-direction view, at the bottom-right of the figure.

To ensure that the previous time-varying MAC results are solely produced by the non-linear response of the structure to the seismic strong motion and the consequent occurrence of damage, a linear-elastic time-history transient analysis is conducted. All the linear material characteristics and the analysis configurations used are the same as in the non-linear transient analyses. However, for this analysis the non-linear behaviour of the materials is neglected, as well as non-linear geometrical considerations are ignored.

In the middle of Figure 5.18 are reported the MAC results computed for the fifth mode shape resorting to the data from a linear-elastic analysis, whilst the outputs from the previously presented non-linear analysis computed from the same data are presented at the bottom of the figure.

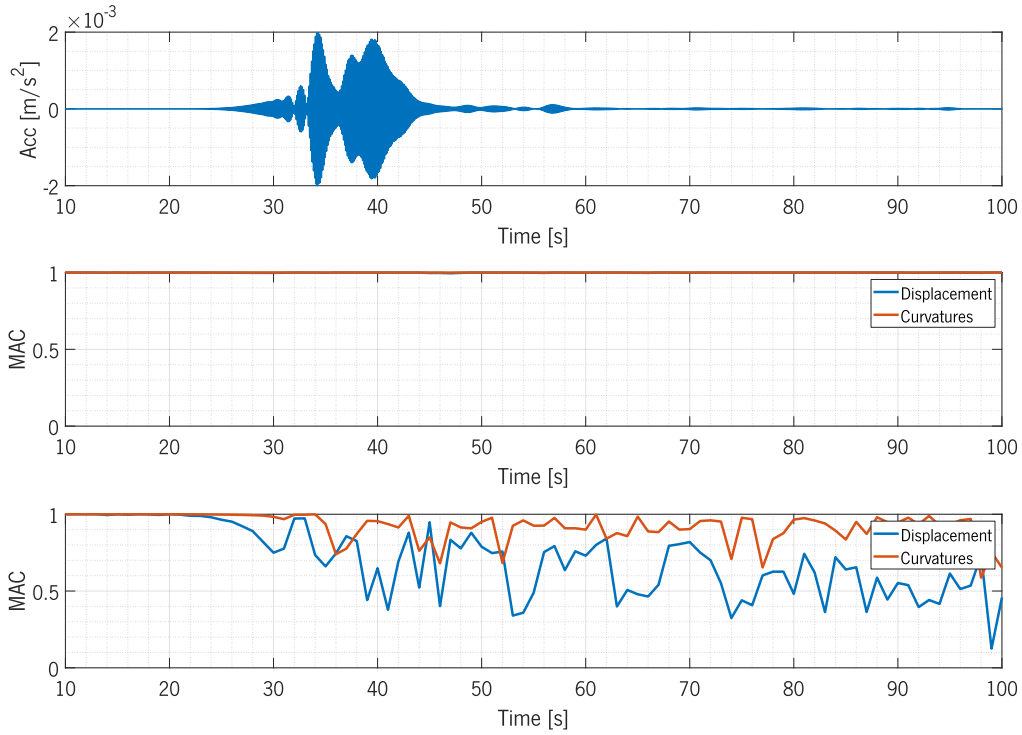


Figure 5.18: Fifth mode linear-elastic time-dependent MAC (middle) compared with the non-linear time-dependent MAC (bottom). A reference of the acceleration it can be seen at top.

The linear analysis is conducted using 0.01 seconds long time-steps, thus, the computed acceleration outputs are not decimated in order to obtain simulated acceleration records with a sampling frequency equal to 100 Hz, alike the non-linear data used in the previous analyses.

Similar to Figure 5.16, on top of the image a reference from the channel that exhibits the highest acceleration for the corresponding mode is reported. As anticipated, the time-varying MAC results computed from the linear-elastic analysis instantaneous mode shapes do not show any change in the evolution, and neither do the curvatures MAC values.

Quite the opposite, the time-dependent MAC results computed using the non-linear instantaneous mode shapes, show clear large fluctuations induced by the damage, whose effect remains active even after the earthquake's main shock.

This comparison suggests that indeed the temporary or permanent shifts in the instantaneous MAC values are due to the deterioration of the structural condition caused by the earthquake rather than to numerical errors.

5.3 Case study III: Laboratory test of a shear-type steel structure

The performance of the EMILIA algorithm is further tested against real structural acceleration measurements obtained from a steel shear-type scaled mock-up under ambient vibrations in laboratory environment. The experimental setup can be observed in Figure 5.19.

The model has a total height of 900 mm, with a 300 mm inter-storey height. Each floor is a 400 mm × 200 mm × 10 mm steel plate. The model columns are thin steel plates, 40 mm wide and 3 mm thick. Four columns are used per model storey. Two additional 50 mm long steel plates, welded at each corner of the floor plates, allow the connection with the columns. Each one is attached by two bolts at the top and two bolts at the bottom, located spaced 20 mm between them and at a distance of 10 mm under/over the floor plates. All the shear-type model columns and floor plates are assumed to be built from the same type of steel. No destructive testing of the model was conducted in order to obtain the material tensile and compressive strength.

Two sets of measurements are carried out under different stiffness configurations, simulating an initial sound condition, followed by structural damage induced between the second and the third storey on the location highlighted by the red square in Figure 5.19 (a). Each set of measurements consists of 32 records performed during daytime and 32 records performed during nighttime.

The abovementioned structural damage is simulated through the removal of two bolts located just below the second storey of the shear model. Detailed views of the model joints with the two bolts

removed can be seen in Figure 5.19 (c) and (d). Without the transducers and the supports attached, the shear model's total weight is 30.5 kg. The weight of each removed bolt with its corresponding nut and the two plain washers is equal to 3.58 g, reaching a combined weight of 7.16 g, which represents 0.023% of the total weight of the model, thus, the mass removed while inducing the structural damage is considered negligible in comparison with the total mass of the shear-type structure.



(a) (b) (c) (d)

Figure 5.19: (a) Full view of specimen and setup with area of stiffness reduction marked in red, (b) transducer detailed view, (c) external side view of the mode joints showing the removed bolts, (d) internal view of the column joints showing the removed bolts.

The structural response is recorded using three PCB 393B12 monoaxial accelerometers with a frequency range of 0.15–1000 Hz, a sensitivity of 10V/g, and a resolution of 8μg (Figure 5.19 (b)) connected to a four-channel NI 9234 analog-to-digital converter.

All records have an equal duration of ten minutes and were recorded sequentially during an eight hour span of time. Between each one of the 32 acquisitions performed during eight hour time window, the informatic system automatically save the ten minute data stream, thus, there is a time delay of a few seconds between records, and they cannot be treated as a single continuous acquisition.

The acceleration data was originally acquired with a sampling frequency of 52,000 Hz, to be later decimated until reaching a sampling frequency of 100 Hz.

Despite the induced stiffness reduction and the different starting times during the day and night of the measurements, all the acquisitions are conducted in the same laboratory installations, under rather similar environmental conditions, and resorting to the same sensors, cables, DAQ equipment, computer, and software.

The algorithm setting for all the analyses performed over this case study follows the default recommendations discussed in Chapter 4 and in (Hormazábal et al. 2023), namely six levels of decomposition with a Daubechies 45 mother wavelet and 1024 lines of resolution for the probability distributions.

The application of EMILIA to each one of the recorded datasets allows reliable and consistent identification of the two lowest bending modes, as demonstrated by the higher peaks of probability and the lower variance that can be identified along the different algorithm outputs, as well as by the examination of the instantaneous mode shapes.

As for the static identification in each acquisition, in Table 5.6 it can be observed the computed means of the f_{MEV} results from all the 32 daytime and 32 nighttime records in both stiffness scenarios. The standard deviation σ of each test is reported in the same table as well. The results in the table, in both stiffness scenarios, are characterised by a relevant consistency, regardless of the acquisition time.

Table 5.6: Natural frequency results mean and standard deviation computed from all test setups.

N°	Sound Day		Sound Night		Damaged Day		Damaged Night	
	f_{MEV} [Hz]	σ	f_{MEV} [Hz]	σ	f_{MEV} [Hz]	σ	f_{MEV} [Hz]	σ
1	4.82	0.010	4.82	0.004	4.68	0.018	4.65	0.009
2	13.92	0.009	13.91	0.003	13.71	0.006	13.68	0.005

Examples of the identified instantaneous displacement mode shapes for the first and the second modes are presented in Figure 5.20. Since only three degrees of freedom are instrumented, neither higher-order nor non-bending modes are further considered.

Hereafter, the analyses focus on the natural frequency results, and no further validation resorting to the mode shapes is conducted.

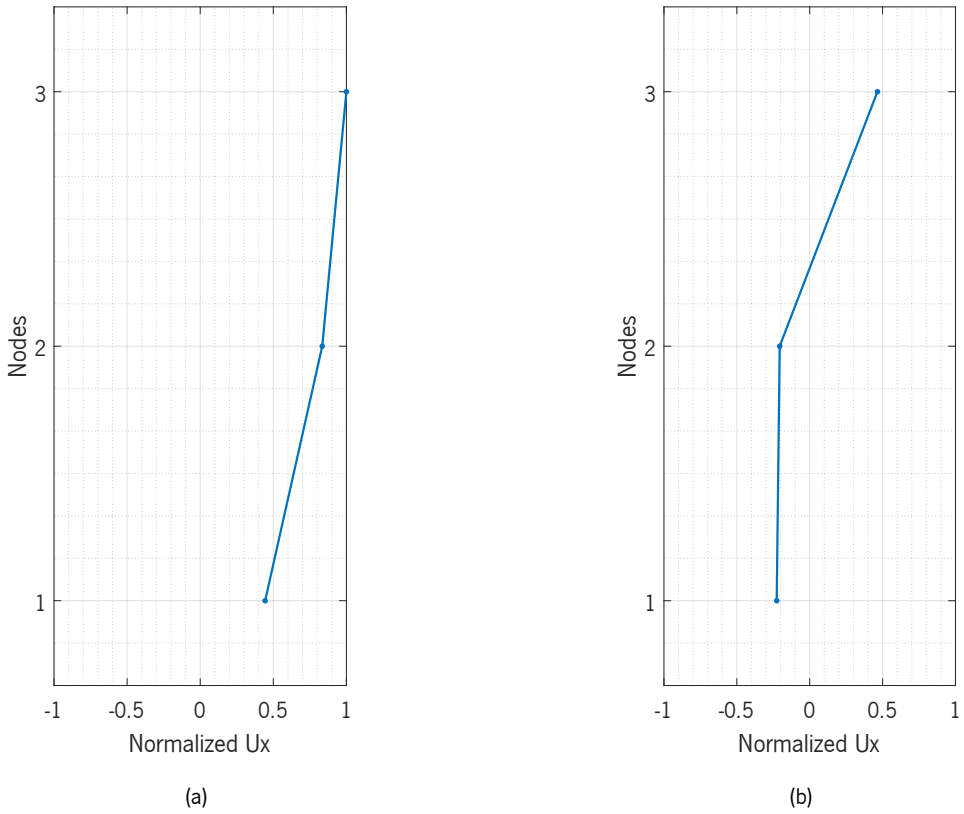


Figure 5.20: Examples from the shear model's instantaneous mode shapes: (a) first mode; (b) second mode.

For the sake of brevity, graphical outputs of EMILIA are hereby reported for one case only, being representative of all the 32 daytime and 32 nighttime analyses in sound condition.

To this end, Figure 5.21 shows a time-dependent probability spectrums computed using data of the shear structure in sound condition acquired during nighttime (16th record), whilst Figure 5.22 shows the Hilbert spectrogram obtained from the same data.

Both graphic outputs present evident peaks in the response, corresponding to the two natural frequencies, undoubtedly standing out when compared to the rest of the spectrum, and furthermore, the two high peaks visible in Figure 5.21 corresponds with the high amplitude instantaneous frequency samples that can be observed in Figure 5.22 around the same zone of the spectrum, and with the results previously presented in Table 5.6 as well.

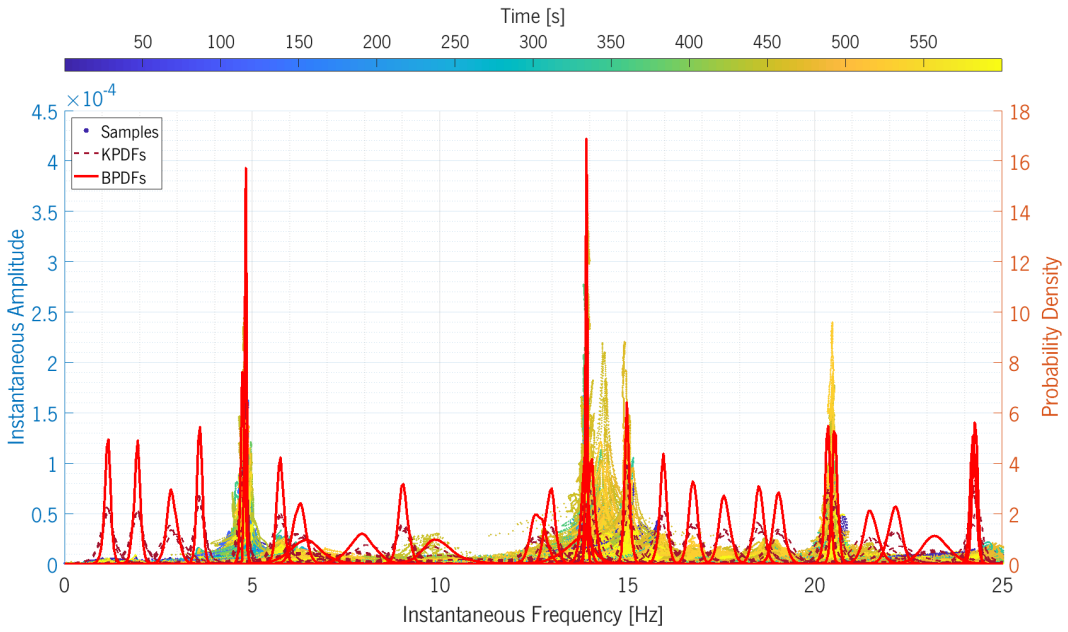


Figure 5.21: Time-dependent probability spectrums computed from the sound condition scenarios.

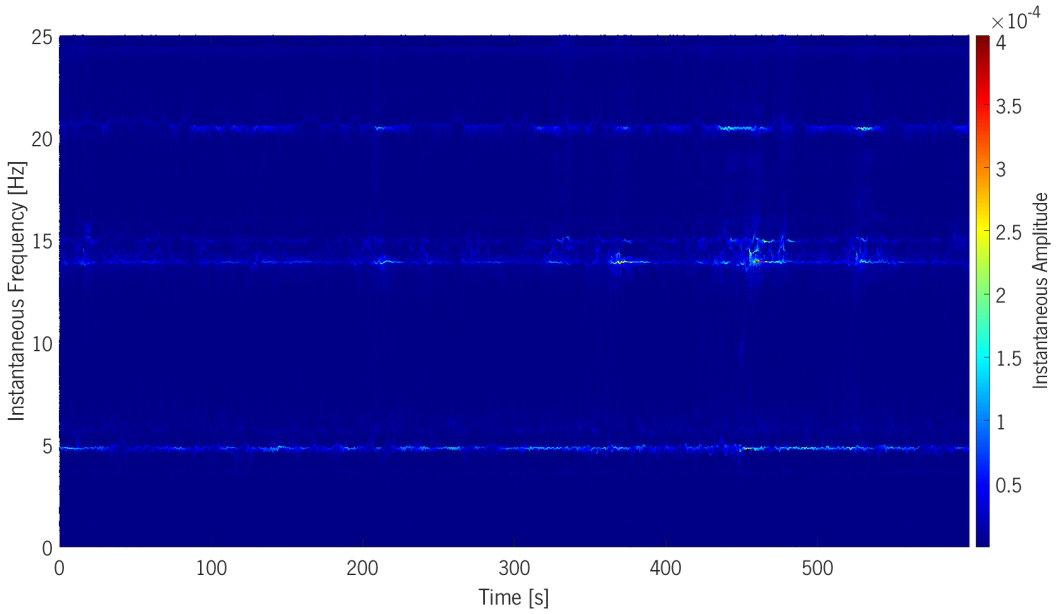


Figure 5.22: A six-Level Daubechies 45 MODWPT Hilbert spectrogram computed from the shear-structure in sound condition, same record processed in Figure 5.21.

The obtained f_{MEV} from all the 32 first subsequences and for all the 32 recordings conducted during daytime from the shear-model in sound condition are presented in Figure 5.23 along the left-Y-axis with stems coloured in light blue. On the right-Y-axis, the corresponding normalised probability densities are plotted as orange stems, while the black dots show the normalised standard deviation computed from the same f_{MEV} results. As a reference, at the bottom of the figure it can be found a frequency axis displaying the relation of the output subsequences with their location over the

related frequency spectrum. This innovative graphical output allows to combine all the identification tests to assess the consistency and reliability of the results.

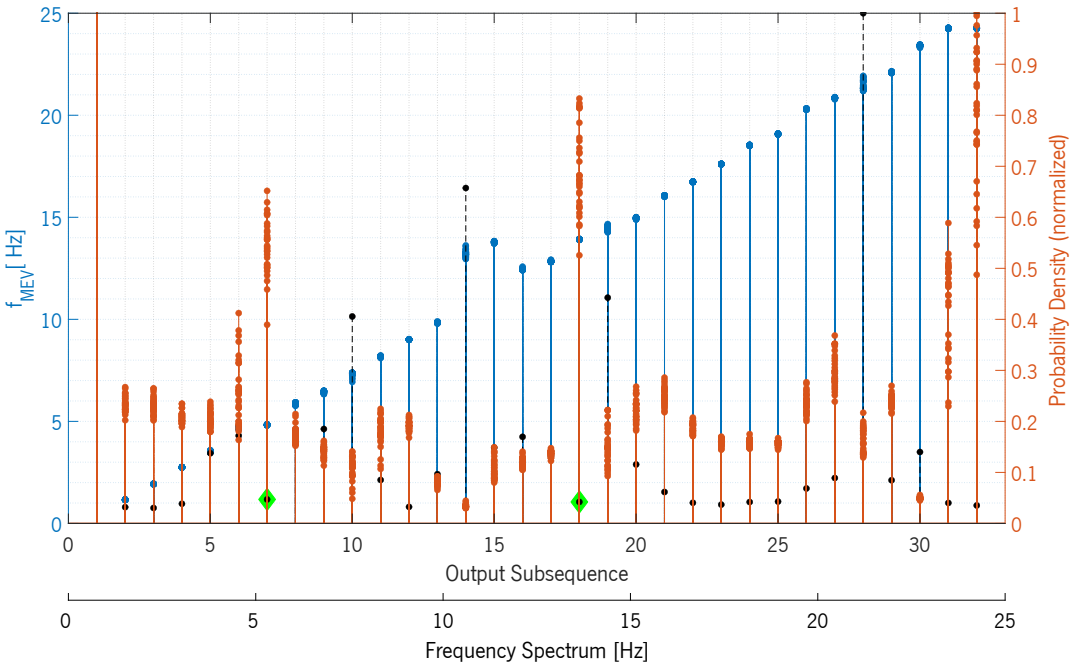


Figure 5.23: Bayes f_{MEV} results, standard deviation, and probability density, for all the 32 tests for the structure in sound condition and measured during daytime.

It is stressed that for the sake of better visualization of the outcomes, only the first half of the 64 subsequences is presented, In such outputs, a subsequence holding modal information is expected to present high values on the maximum probability density results (higher orange samples), with a noticeable consistency on the computed f_{MEV} values (blue dots displaying low scattering), which is reflected into a low value of the standard deviation (lower black dots). The standard deviation results for the 7th and the 18th subsequences (the 1st and the 2nd modes respectively), highlighted by means of a green diamond, are rather low when compared to other subsequences. Moreover, the normalised probability densities are consistently and significantly the highest.

Figures 5.24, 5.25, and 5.26 shows the same graphical output for the other three sets of acceleration measurements: the second set of the shear model in sound condition (recorded during the night), and the two sets with the structure in damaged condition. It is worth noting that in both nighttime outputs, the registered normalised f_{MEV} standard deviation is lower than during daytime, likely due to a lower extent of vibration input. In the damaged scenario (Figure 5.25 and Figure 5.26) the modal information of the first mode is found on the sixth subsequence due to the drop in the frequency values. This is also confirmed by the lower variance and higher probability density of the

sixth subsequence (marked with the green diamond) with respect to the seventh subsequence. The previously mentioned shift in the output is mostly related to the decomposition level selected and the natural frequency of the first mode. As a six-level decomposition is used and the Nyquist frequency is equal to 50 Hz, each spectrum segment has a span of 0.78125 Hz.

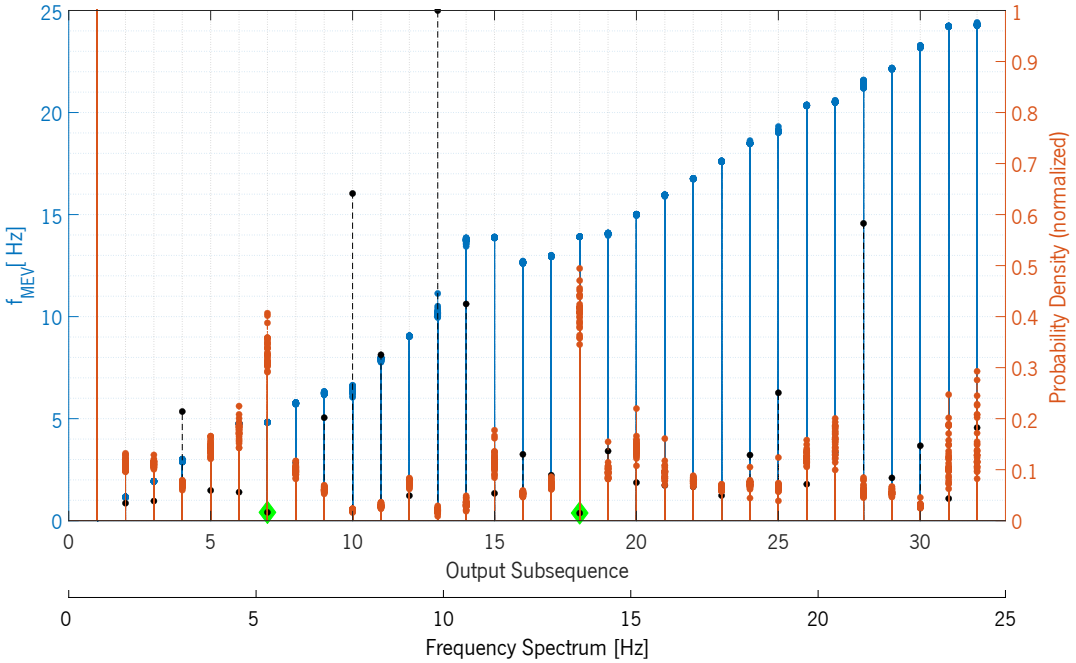


Figure 5.24: Bayes f_{MEV} results, standard deviation, and probability density, for all the 32 tests for the structure in sound condition and measured during nighttime.

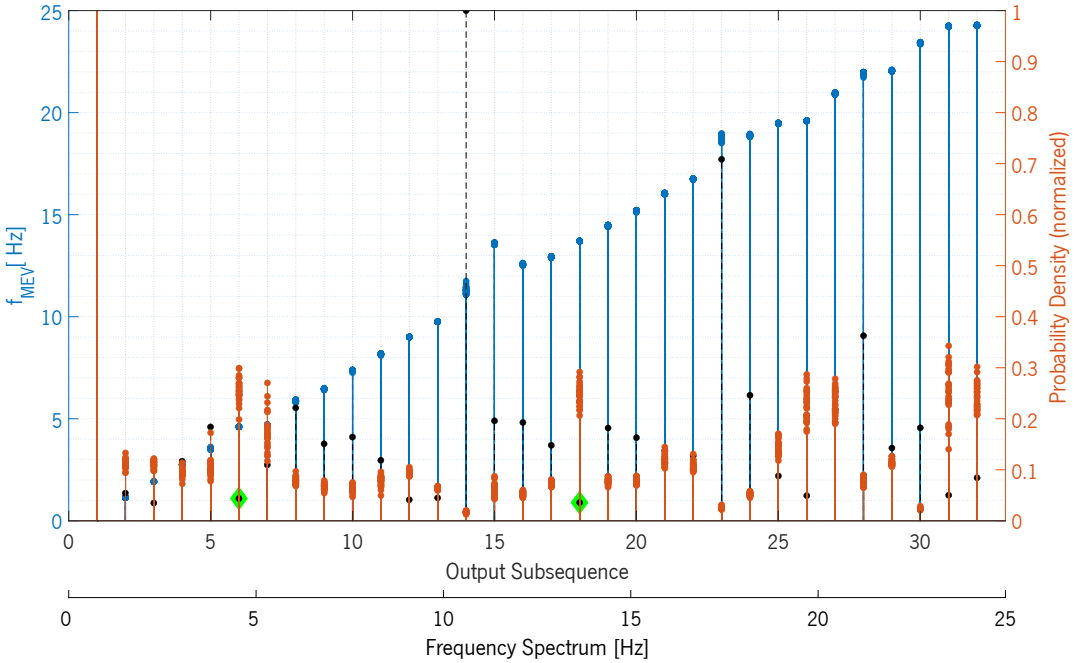


Figure 5.25: Bayes f_{MEV} results, standard deviation, and probability density, for all the 32 tests for the structure in damaged condition and measured during daytime.

With the previously specified spectrum segment, the border between the sixth and the seventh segment is then located at 4.68 Hz, almost in the same location as the first mode of the damaged configuration. On the other hand, in the second mode results it can be noticed that the modal data remains on the same subsequence (18th) for both undamaged and damaged scenarios. Using the same logic from the first mode, with 17 segments of approximately 0.78 Hz each, 13.28 Hz are reached, whilst, with 19 segments, 14.84 Hz are reached, meaning that the modal information of the second mode is utterly contained in the 18th segment of the spectrum.

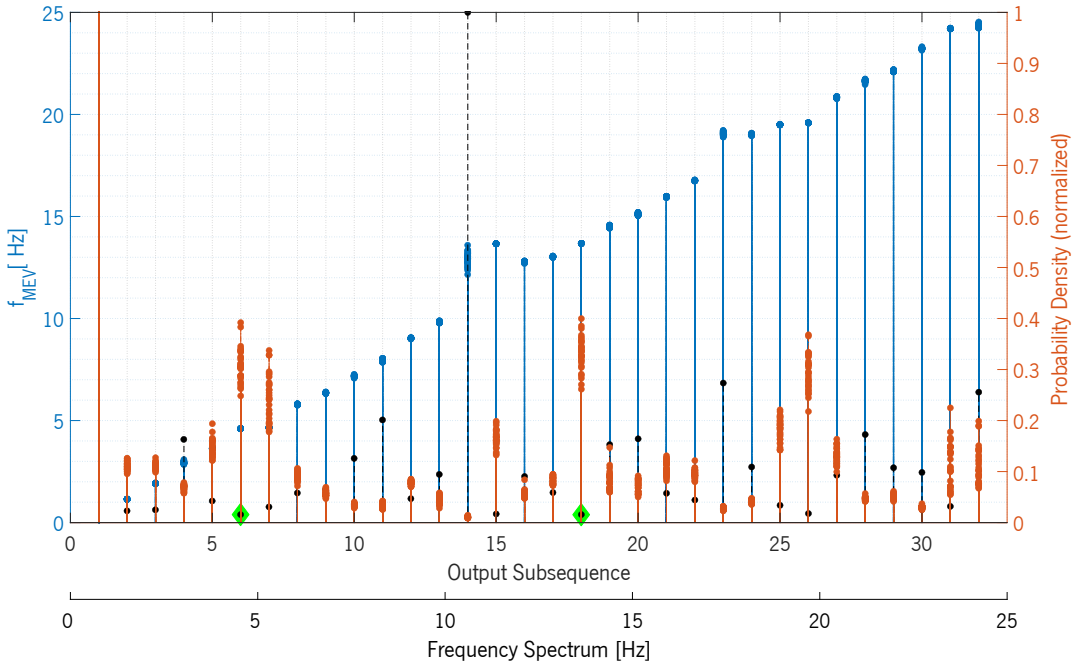


Figure 5.26: Bayes f_{MEV} results, standard deviation, and probability density, for all the 32 tests for the structure In damaged condition and measured during nighttime.

The algorithm consistency and steadiness of the computed results are further tested by considering reducing acquisition length. Algorithms that rely on a CPSD weighted matrix need a large amount of data to smooth the resulting CPSD and get rid of the stochastic content on the raw data (Carpine, Ientile, and Argoul 2023), while methods based on system identification need a large amount of data to compute the Hankel matrix as this affects the order of the matrix, hence, it limits the number of modes that can be identified and the quality of the identification (Pourgholi et al. 2023). On the other hand, a discrete mother wavelet function is a locally supported function that only needs a number of samples equal to two times its own length to fully support each one of the associated filters. This means that, for the Daubechies 45 mother wavelet function used in the present work, only one second of data could be enough to obtain an output. This allows to significantly reduce the length of the

acquisition, provided that a short record is sufficient to ensure a reliable identification. To this end, eight sets are built by randomly selecting data streams with a decreasing number of samples from each one of the 32 raw records of the structure in sound conditions measured during nighttime, meaning that there are no consecutive short recordings used for this test. Each one of the eight sets, thus, holds 32 data streams in a decreasing total number of samples, from the ten-minute length of the original acquisition until a five-second length record.

Table 5.7 and Table 5.8 show the first and second mode f_{MEV} means (in Hz), along with the standard deviation and variance from the eight data sets. The results demonstrate the EMILIA algorithm's capability of providing a robust and reliable identification even from reduced amounts of data. Figure 5.27 compares the f_{MEV} results in Hz and the corresponding variance for both bending modes computed from each data set. An increasing trend in the variance emerges when a reduction in the set's length is applied.

Table 5.7: First mode's statistics from different data lengths of the model in sound condition.

	10 min	5 min	2 min	1 min	30 sec	20 sec	10 sec	5 sec
Mean [Hz]	4.8214	4.8215	4.8212	4.8234	4.8224	4.8208	4.8327	4.8344
σ	0.0029	0.0035	0.0061	0.0106	0.0121	0.0157	0.0307	0.0563
σ^2	0.00001	0.00001	0.00004	0.00011	0.00015	0.00025	0.00094	0.00317

Table 5.8: Second mode's statistics from different data lengths for the model in sound condition.

	10 min	5 min	2 min	1 min	30 sec	20 sec	10 sec	5 sec
Mean [Hz]	13.9105	13.9105	13.9092	13.9059	13.9005	13.8957	13.89	13.8781
σ	0.0023	0.0033	0.0053	0.0091	0.0170	0.0220	0.0320	0.0687
σ^2	0.00001	0.00001	0.00003	0.00008	0.00029	0.00049	0.00102	0.00472

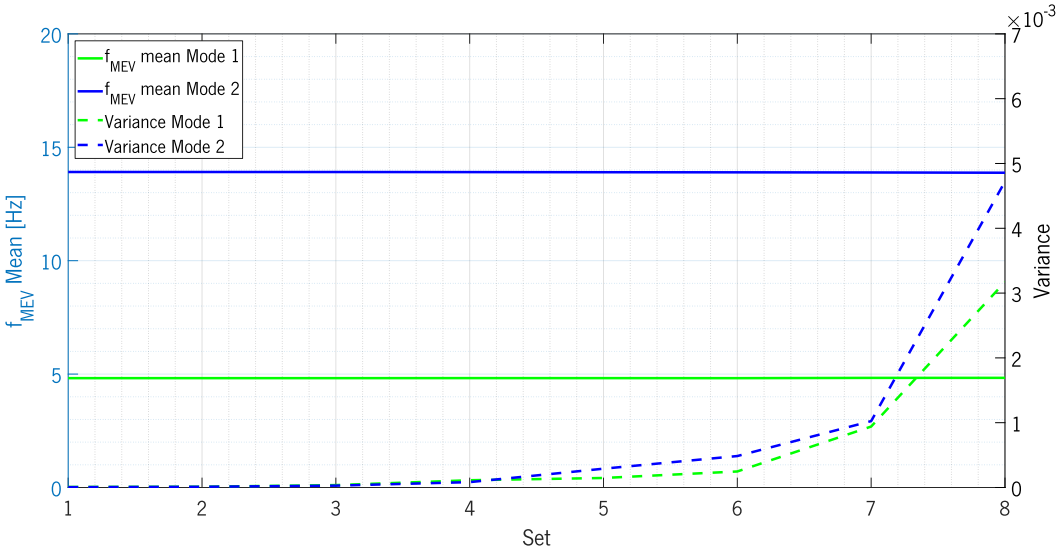


Figure 5.27: First and second modes f_{MEV} mean, standard deviation and variance for all the eight data sub-sets.

This is likely due to the reduced number of wavelet coefficients obtained from shorter records which affects any statistical output as well. For example, to analyse the samples obtained in five seconds of data at 100 samples per second, the Daubechies 45 mother wavelet produces 500 wavelet coefficients. However, this variability does not reflect a deterioration of the probability's estimation performance and the identified natural frequencies are sufficiently accurate for all the tested sets.

After performing the initial set of measurements in sound condition (32 during daytime and 32 during nighttime), a 20-minute acquisition is conducted in order to record the process of reducing the structural stiffness (Figure 5.19).

This is done ten minutes (600 seconds) into the test, in the middle of the acquisition, by removing the aforementioned two bolts (see Figure 5.19). The effect of this manual operation emerges clearly in the outputs of EMILIA, as shown in the three time-dependent probability spectrums presented in Figure 5.28.

In Figure 5.28 (a), the probability spectrum computed from non-linear response measurement is presented. Here, the high-energy samples are reported in turquoise according to the colour key of the instant of acquisition, meaning that they belong to the 600 seconds time zone. In the same figure, it is also possible to identify the downshift of the natural frequencies, which is especially notorious in the BPDFs enclosed in the striped-line boxes. On both nonparametric distributions, this is reflected in the occurrence of two closely spaced peaks around the 4.5-5.0 Hz and 13.5-14.0 Hz ranges.

For a better visualisation of these shifts, a detailed view of the isolated information of the first mode output is presented in Figure 5.28 (b), whilst a detailed view of the isolated data corresponding to the second mode is presented in Figure 5.28 (c).

Similar to the outputs presented in Figure 5.28, in the three Hilbert spectrograms that can be observed in Figure 5.29 is evident the high energy zone in the middle of the analysis just after the 600-second mark, and a drop in the computed instantaneous frequency results for the first and second modes it can be observed after the reduction of the system stiffness, as can be noticed in the detailed views presented in Figure 5.29 (b) and Figure 5.29 (c). Analogous shifts in the instantaneous frequencies can be seen in other regions of the spectrum in Figure 5.29 (a), like in the 20 Hz zone. This drop is likely due to other, non-identified modes of the structures affected by the induced damage and the corresponding reduction in the system stiffness.

Worth noting that both Figure 5.28 and Figure 5.29 are computed resorting to the same instantaneous output data.

It is stressed that, due to the significant difference in amplitude between the structural response to the ambient vibration and the effect of the manual actions on the specimen to induce the damage, the colour scale of the instantaneous amplitude for the three Hilbert spectrograms in Figure 5.29 is presented in logarithmic scale. Additionally, the white lines that can be seen in the three Hilbert spectrograms are moving averages computed from the instantaneous frequency samples by using a time window equal to 100 samples.

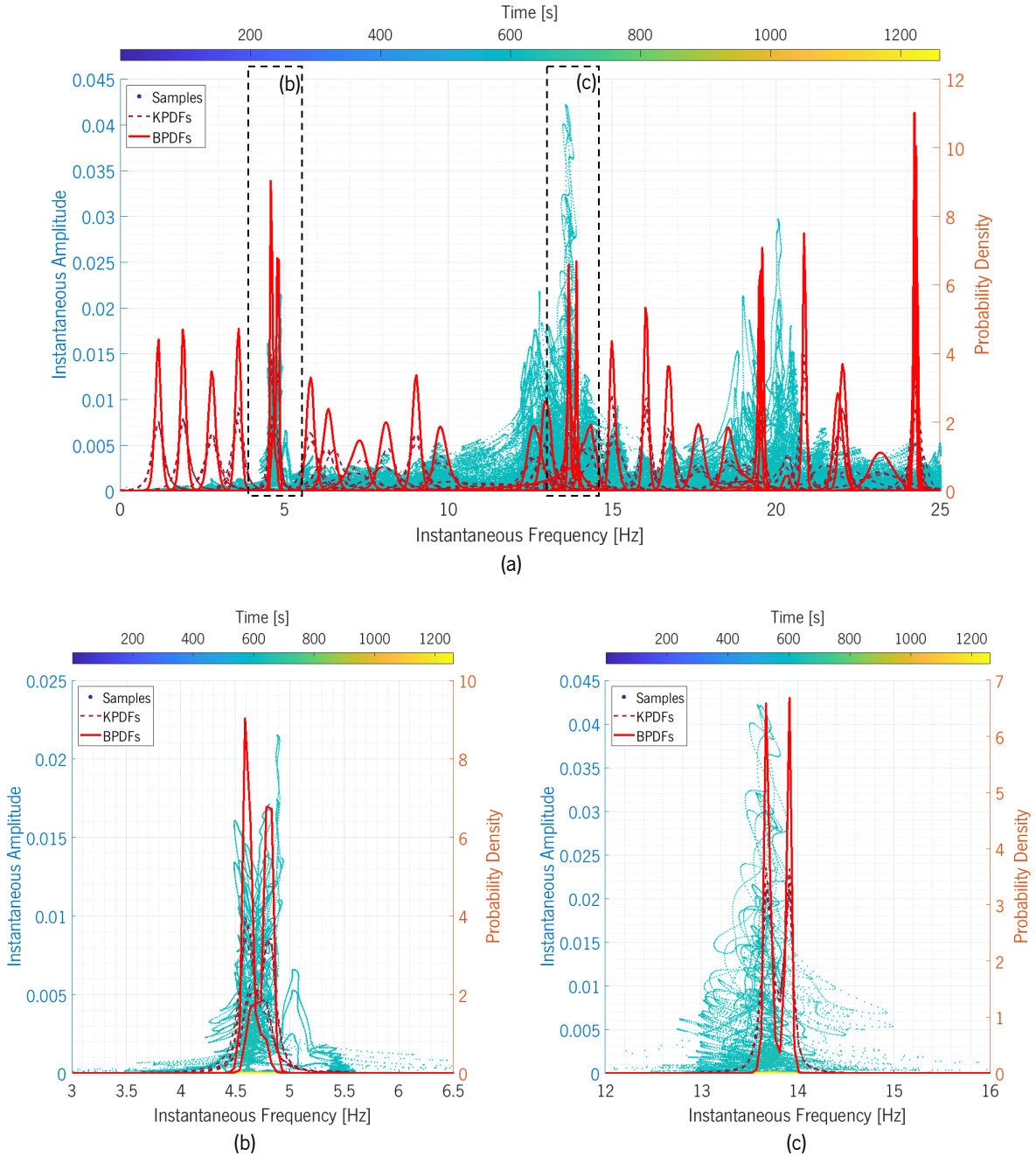


Figure 5.28: Time-dependent probability spectrums computed from the records containing the manual damaging procedure: (a) complete spectrum; (b) spectrum zoomed around first mode; (c) spectrum zoomed around second mode.

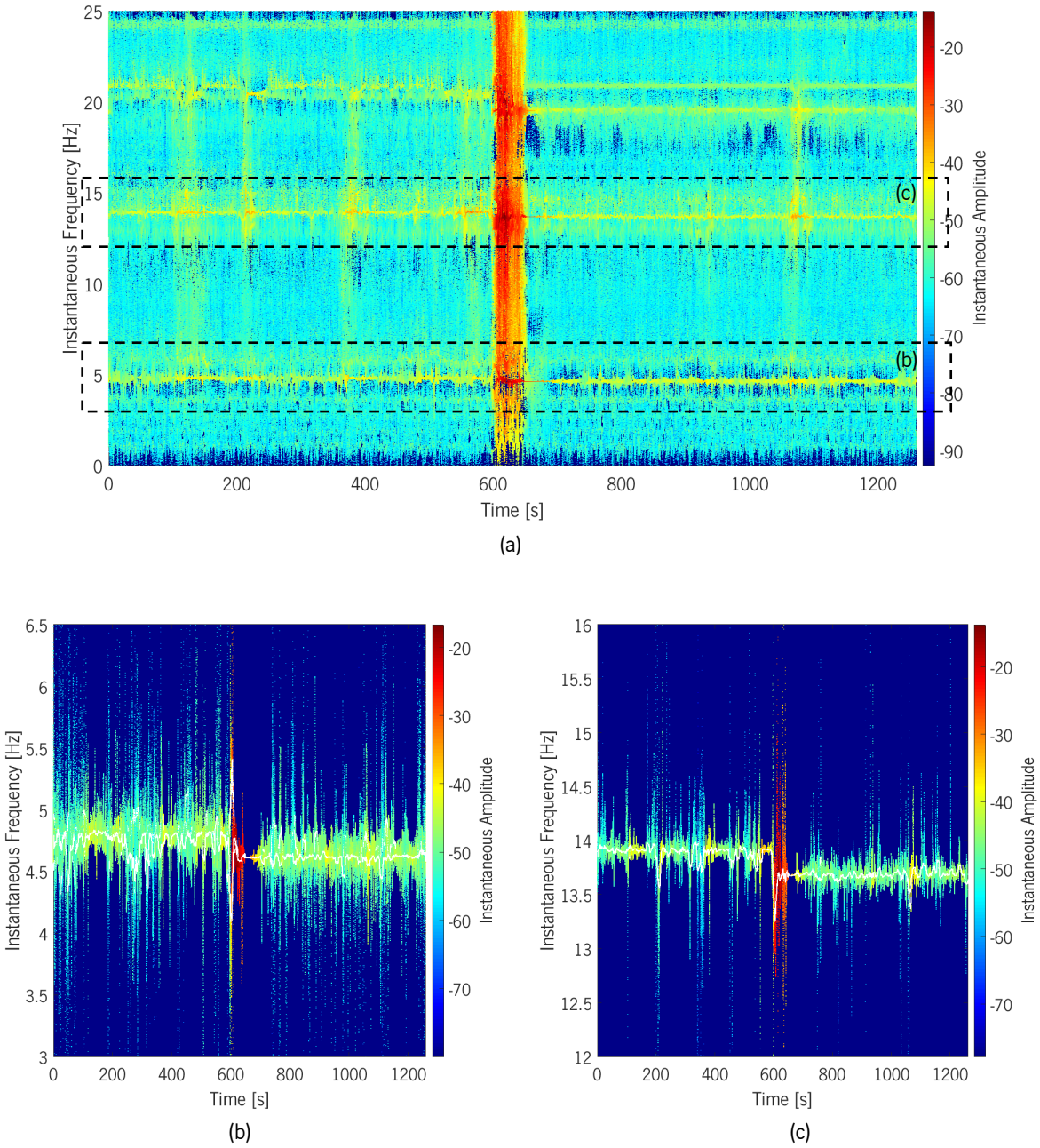


Figure 5.29: Hilbert spectrograms computed from the records containing the manual damaging procedure: (a) complete spectrogram; (b) spectrogram zoomed around first mode; (c) spectrogram zoomed around second mode.

5.4 Chapter Conclusions and final remarks

The present chapter analyses the capabilities of the EMILIA algorithm to conduct dynamic identification by processing linear and non-linear structural responses including to high transient seismic records. To this end, two case studies are presented, a FE model in order to compute simulated non-linear acceleration data, and a real case scenario used to acquire linear and non-linear structural acceleration measurements.

According to the previous, first the proposed algorithm was tested against the simulated monitoring data of an idealized masonry tower under non-stationary input excitations and progressive seismic-induced structural damage, resorting to acceleration data from the main shock of the 2009 L'Aquila earthquake.

Then, the algorithm performance was tested against real acquisitions of acceleration data, relying on the structural responses of a laboratory shear-type steel structure measured before, during and after manually introducing structural damage.

According to the examination of the outcomes obtained from the two case studies, EMILIA demonstrated to be capable of successfully processing non-linear structural responses and working with sudden changes in the analysed data, like the ones that can be found in structural responses due to strong motion seismic events.

Furthermore, the algorithm showed a great steadiness and consistency of the computed results, no matter the length of the assessed data. Indeed, the dynamic identification of the laboratory test was conducted by resorting to records of shorter length and repeated acquisitions during the day and nighttime under similar conditions. This positive result is a consequence of using a discrete wavelet decomposition like the MODWPT. Wavelet analysis does not require large records in order to deal with high levels of stochastic data, making it a rock-solid option for dealing with limited amounts of highly noise-contaminated data.

Moreover, EMILIA was used to inform the identification of structural damage through well-established vibration-based SHM techniques resorting to the instantaneous mode shapes data as time-dependent functions, and their higher derivatives, like the modal curvatures.

The mathematical tools selected for the proposed algorithm have shown a good sensitivity to changes in the dynamic behaviour, hence, the EMILIA algorithm can properly detect small and moderate damage, supporting the early warning and allowing to check the structural condition after an earthquake in almost real-time.

6 CONCLUSIONS

6.1 Thesis summary, main conclusions, and final remarks

The present research is focused on provide a non-destructive analysis tool to support the management of civil engineering structures. It aimed to facilitate online, real-time condition monitoring under ordinary operational conditions, as well as expedite damage assessment following strong motion seismic events.

For instance, the thesis main objective of this proposal was the developing, testing, and validating a novel nonparametric algorithm tailored for output-only dynamic identification. This algorithm is designed to process both stationary and time-variant, non-linear structural responses, enabling reliance on even short trends of data.

To achieve this objective, the thesis was structured into four main chapters, plus an introduction and conclusions, offering comprehensive information on the research findings and outcomes related to the proposed algorithm, as follows:

(1) In Chapter 1 is defined the motivation behind the research and the main and secondary objectives are presented.
(2) The current state of the field and the identified research gaps are then presented in Chapter 2.
(3) The design and workflow of the EMILIA algorithm are discussed in Chapter 3, including its main mathematical tools, methods, and key outcomes.
(4) Chapter 4 presents the testing and validating of the algorithm on a simulated structure exhibiting linear and nonlinear behaviour.
(5) In Chapter 5, the EMILIA algorithm is applied to two structures showing non-linear responses to non-stationary inputs, one simulated and one real measured in a laboratory environment. The algorithm is integrated into a vibration-based damage identification strategy as well.
(6) Finally, in Chapter 6 the main conclusions drawn from the research and the outlining of potential future research directions are discussed.

Along Chapter 4 and Chapter 5, three distinct case studies were adopted: (I) a 2D FE bridge model intentionally damaged by locally reducing its stiffness and subjected to stationary vibration inputs; (II) a 3D FE masonry tower model subject to seismic inputs causing damage to the structure; (III) a real shear-type steel structure tested in controlled laboratory conditions, with damage induced

manually by removing a pair of bolts. Table 6.1 presents a summary of the chapters and sections of the thesis covering the secondary objectives previously presented in Section 1.2. Additionally, the table indicates the specific case study utilised to address each of these topics.

Table 6.1: Thesis secondary objectives distribution summary.

Secondary Objective	Discussed in	Case(s) Study
Linear modal analysis	Chapter 4 *Section 4.2.2* Chapter 5 *Section 5.2.2* *Section 5.3*	I, II & III
Non-linear modal analysis	Chapter 4 *Section 4.2.3* Chapter 5 *Section 5.2.2* *Section 5.3*	I, II & III
Time-dependent dynamic identification	Chapter 4 *Section 4.2.3* Chapter 5 *Section 5.2.2* *Section 5.3*	I, II & III
Time-dependent damage identification	Chapter 4 *Section 4.2.3* Chapter 5 *Section 5.2.3* *Section 5.3*	I, II & III
Performing OMA with reduced data	Chapter 5 *Section 5.3*	II & III
Using strong motion seismic data for OMA	Chapter 5 *Section 5.2.2*	III

6.1.1 Linear dynamic identification and OMA with reduced amounts of data

The results obtained from the different case studies allow to conclude that the proposed algorithm can properly be used to perform output-only dynamic identification tasks for civil engineering systems under ambient vibrations.

The EMILIA algorithm effectively processes linear structural responses and data, yielding consistent instantaneous values of natural frequencies and mode shapes. Moreover, the statistical analysis and Bayesian inference stage, at the end of the algorithm workflow, allows to generate

accurate static results, namely a set of single values for the natural frequencies, obtained by processing the dynamic instantaneous outputs.

The algorithm's effectiveness is demonstrated by comparing the results against well-established traditional modal analysis methods, such as EFDD and SSI. In the case study of the 2D FE bridge model, this comparison specifically focused on four modes, reliably identified by both alternative estimators and EMILIA, across three different stiffness scenarios analysed. The proposed algorithm accurately identified instantaneous frequencies and shapes for these four selected modes, yielding results analogous to those provided by traditional identification algorithms. Moreover, the results were in excellent agreement with the target numerical solutions obtained through the eigenvalue analysis.

In the case of the 3D FE masonry tower model, the algorithm performed the OMA utilising only the first 30 seconds of recorded data. This short duration captured the structural response to ambient vibrations prior to the onset of strong motion. Despite the probable non-stationarity of the input data and the brief recording duration, EMILIA provided a sufficiently reliable identification of the natural frequencies and mode shapes. These results were successfully compared with the target numerical outcomes obtained through the eigenvalue analysis.

Finally, the algorithm performance was tested against real data collected in a laboratory environment. Here, the algorithm proved the consistency and steadiness of the generated outcomes across various sets of acquisitions conducted at different times of the day and under two structural conditions: undamaged and damaged.

Additionally, the consistency of the results was further tested by performing dynamic identification, over reduced amounts of data, and evaluating the mean and the variance of the obtained instantaneous frequency outputs. The results showed promising levels of accuracy and reliability even with limited data available, including a few seconds.

Traditional modal identification methods based on the decomposition of a weighted matrix, like CPSD or Hankel matrix, commonly require long datasets in order to reduce the influence of noise. On the other hand, the minimum amount of data required by the undecimated discrete wavelet decomposition (MODWPT), which constitutes the core of the first stage of the EMILIA algorithm, is only limited by the number of samples required to support the high- and low-pass filters, that in the case of a Daubechies wavelet is equal to twice the number of vanishing moments of the chosen function. This makes wavelet analysis an extremely fast and accurate TFA that can properly work with short and very short acquisitions, producing instantaneous outputs.

However, the utilisation of extremely short data streams, such as those lasting only a few seconds, hinders the final Bayesian inference based on the instantaneous outputs and may reduce the accuracy of the computed static frequency values.

6.1.2 Non-linear dynamic identification and OMA with strong motion seismic data

The results obtained from the three case studies lead to the conclusion that the proposed algorithm can effectively perform output-only dynamic identification tasks, even in the presence of high-transient non-stationary data. This capability is particularly noteworthy in scenarios involving the damaged non-linear responses of civil engineering systems and constitutes a significant advantage of EMILIA when compared to commonly used well-established dynamic identification algorithms.

For the 2D bridge model, simulated non-linear data were generated by merging the linear data sets acquired under different stiffness configurations. In the case of the 3D masonry tower, non-stationary data were obtained by capturing the structural response to a strong seismic base excitation. Lastly, for the shear-type steel specimen, a continuous acquisition was conducted while manually introducing damage into the system.

In the simulated 2D bridge case study, the algorithm demonstrated remarkable accuracy in tracking the evolution of modal frequencies across the 30-minute dataset, even in the presence of sudden large-extent drops. Furthermore, the graphical outcomes and spectra produced by EMILIA not only captured the changes in the modal parameters but also provided valuable information regarding the clustering and scattering of instantaneous frequency samples and the instant, during acquisition, in which the variation occurs. The dynamic identification of the shear-type steel specimen represented a crucial expansion of the previous problem to a real dataset, encompassing realistic sources of uncertainties and damage scenarios. In this case study, EMILIA accurately identified and monitored the evolution of the instantaneous natural frequencies throughout the acquisition process, effectively capturing the drop induced by the damage.

The robustness and noise tolerance, even with relatively short recordings, and the ability to track non-linear behaviours were particularly tested in the dynamic identification conducted on the 3D masonry tower. This analysis considered the full high-transient, non-stationary data affected by the intense seismic action, which led to the outbreak of damage during data acquisition. The good algorithm performance against non-linear data depends on the MODWPT time domain wavelet data decomposition, in conjunction with the Hilbert transform analysis, core components of EMILIA. During

decomposition, the algorithm reads modal data by computing the area between the wavelet and the data, as illustrated in Figure 3.3. While the previous makes the algorithm highly robust against noise, it also renders it sensitive to the shape of the chosen wavelet function, and to significant differences in energy content of the spectrum. This, indeed, emerged during the main shock of the earthquake, likely inducing a response of the tower predominantly characterised by the whip effect. In this circumstance, the algorithm as well mainly captured and computed this effect, which can be easily mistaken for a sort of bending mode within the bandwidth of higher energy input.

Nonetheless, the analysis of EMILIA outputs in the immediate pre- and post of this strongly transient state demonstrated its capability of correctly identifying the modal properties.

6.1.3 Time-dependent dynamic identification and damage assessment

The results obtained from the linear and non-linear dynamic identification tests demonstrated EMILIA's capability in computing time-dependent natural frequencies, mode shapes and their higher derivatives. Similar to noise tolerance, this capability is mainly due to the combined use of MODWPT decomposition and Hilbert TFA within the core procedures of the algorithm. These mathematical tools enable data analysis in both time and frequency domains with high accuracy.

The good performance was identified against (I) mainly linear signals that suddenly underwent large extent drops, observed in the 2D bridge model; (II) significant non-linear structural responses under strong seismic motion data, as seen in the 3D masonry tower; (III) localised disturbances in real data, observed in the shear-type specimen.

These time-dependent outputs of the algorithm are paramount for informing condition monitoring and early warning upon the outbreak of damage, facilitating online and real-time assessment of the investigated system. This involves resorting to the assessment and detection of sudden changes in the instantaneous frequency outputs.

The consistency and steadiness in the results demonstrated in real data, both before and after damage, are promising, and the algorithm is expected to reliably detect small variations induced by changes in the structural conditions. In addition to its accuracy in computing frequency outputs, the algorithm's robustness to noise and non-stationarity in the data, even with short inputs (as observed in the 3D masonry tower), suggests that EMILIA would be capable of promptly detecting such variations even during or shortly after ongoing high transient phenomena.

Assuming the availability of a sufficient number of sensors, alongside the information provided by shifts in instantaneous frequencies, variations in instantaneous mode shapes have also been

leveraged for damage identification. In particular, a method based on changes in MAC values was adopted while investigating the masonry tower. Here, the instantaneous mode shapes and modal curvatures compared against a reference, undamaged, baseline allowed to support the detection of a residual anomalous behaviour induced by the earthquake.

It is worth noting that a side effect of the time-dependent outputs is the enormous amount of data generated at the conclusion of even a simple computation with the proposed algorithm. Particularly the graphical outputs from the EMILIA algorithm, such as the time-dependent probability spectrums and the Hilbert spectrograms, impose a heavy load on both the RAM memory and the hard drive system of any computer.

6.2 Future lines of research

Given the composite nature of the EMILIA algorithm, which integrates various methods across its three stages, opportunities for further improvement, aiming at general applications as well as case-specific needs, may arise from the adoption of different mathematical tools. This comprises exploring alternative wavelet functions, TFA techniques, and probability distributions, including assessing and optimising their parameter setting. A second significant area of research involves integrating EMILIA within a broader SHM workflow for damage identification. Finally, some aspects affecting the viability of the algorithm in practical applications are worth being addressed.

Considering the main drawbacks identified during the evolution of this work, three priority research needs are outlined below as recommended future directions for enhancing the performance of EMILIA.

The direct identification of the structural modal frequencies by selecting probability peaks from the computed BPDFs, has demonstrated promising results for linear modal analysis. The undecimated MODWPT data decomposition and the abundance of instantaneous outputs should be further leveraged, for instance, through alternative probability analyses and/or employing machine learning strategies. In particular, the definition of more robust identification criteria and thresholds is needed, to automatically estimate modal properties even from data affected by non-linearity and time-variance within the acquisition process, likely resulting in multimodal fitted PDFs.

A great advantage of the MODWPT wavelet decomposition lies in its flexibility to use any orthogonal discrete mother wavelets, such as different versions of the Daubechies mother wavelets or the Coiflets wavelet family, which have already been successfully applied in seismic analysis. Investigating the performance of different wavelets in conducting dynamic identification for civil

engineering purposes is expected to enhance and refine the decomposition stage of the EMILIA algorithm. This exploration is not limited to existing wavelet families as new wavelets can be developed and tailored by analysing earthquake records (Y. Wang 2015). This approach is expected to enable the future identification of the most suitable mother wavelet for a given problem, based on the characteristics of investigated systems, ongoing phenomena, occurring disturbances, and output signals.

Finally, one of the shortcomings of the algorithm is the substantial volume of data generated at the end of computations, often amounting to several gigabytes. Managing this large dataset can pose a challenge, particularly limiting the application of the EMILIA algorithm in tasks requiring higher sampling frequencies or involving long-duration acquisitions necessary for long-term monitoring and damage identification of civil engineering systems. This limitation is not unique to EMILIA but is a common issue with many tools for condition monitoring.

Ongoing advancements in CPUs, hard drives, RAM modules, and especially the emerging developments in quantum computers and networks, will allow to manage higher sampling frequencies. This opens doors for applying the proposed method in various domains including non-linear signal processing, machinery maintenance, preventive conservation, and time-dependent non-linear dynamic identification of airborne and space structures.

In the meantime and parallel to this development, strategies to mitigate the computational burden associated with the processing, storage, and retrieval of data should be explored and implemented to enhance the practical applicability of EMILIA.

BIBLIOGRAPHIC REFERENCES

Abdeljaber, Osama, Onur Avci, Mustafa Serkan Kiranyaz, Boualem Boashash, Henry Sodano, and Daniel J. Inman. 2018. "1-D CNNs for Structural Damage Detection: Verification on a Structural Health Monitoring Benchmark Data." *Neurocomputing* 275:1308–17. https://doi.org/10.1016/j.neucom.2017.09.069.

Abdeljaber, Osama, Onur Avci, Serkan Kiranyaz, Moncef Gabbouj, and Daniel J. Inman. 2017. "Real-Time Vibration-Based Structural Damage Detection Using One-Dimensional Convolutional Neural Networks." *Journal of Sound and Vibration* 388:154–70. https://doi.org/10.1016/j.jsv.2016.10.043.

Allemang, Randall J., and David L. Brown. 1982. "A Correlation Coefficient for Modal Vector Analysis." In *1st International Modal Analysis Conference (IMAC I)*, 110–16. Orlando, USA.

Amezquita-Sanchez, Juan Pablo, Arturo Garcia-Perez, Rene J. Romero-Troncoso, Roque A. Osornio-Rios, and Gilberto Herrera-Ruiz. 2013. "High-Resolution Spectral-Analysis for Identifying the Natural Modes of a Truss-Type Structure by Means of Vibrations." *JVC/Journal of Vibration and Control* 19 (16): 2347–56. https://doi.org/10.1177/1077546312456228.

Anders Brandt. 2023. *Noise and Vibration Analysis: Signal Analysis and Experimental Procedures*. 2nd ed. Wiley.

Arioli, Gianni, and Filippo Gazzola. 2017. "Torsional Instability in Suspension Bridges: The Tacoma Narrows Bridge Case." *Communications in Nonlinear Science and Numerical Simulation* 42 (January):342–57. https://doi.org/10.1016/j.cnsns.2016.05.028.

Avci, Onur, Osama Abdeljaber, Serkan Kiranyaz, and Daniel Inman. 2017. "Structural Damage Detection in Real Time: Implementation of 1D Convolutional Neural Networks for SHM Applications." In *Conference Proceedings of the Society for Experimental Mechanics Series*, 7:49–54. https://doi.org/10.1007/978-3-319-54109-9.

Barontini, Alberto. 2021. "Bio-Inspired Algorithms for Structural Health Monitoring of Civil Engineering Systems." Guimarães: University of Minho.

Barontini, Alberto, Maria Giovanna Masciotta, Paulo Amado-Mendes, Luís F. Ramos, and Paulo B. Lourenço. 2021. "Reducing the Training Samples for Damage Detection of Existing Buildings through Self-Space Approximation Techniques." *Sensors* 21 (21): 7155. https://doi.org/10.3390/s21217155.

Barontini, Alberto, Ricardo Perera, Maria Giovanna Masciotta, Paulo Amado-Mendes, Luis Ramos, and Paulo Lourenço. 2019. "Deterministically Generated Negative Selection Algorithm for Damage Detection in Civil Engineering Systems." *Engineering Structures* 197 (October):109444. https://doi.org/10.1016/j.engstruct.2019.109444.

Bayes, Thomas. 1763. "LII. An Essay towards Solving a Problem in the Doctrine of Chances. By the Late Rev. Mr. Bayes, F. R. S. Communicated by Mr. Price, in a Letter to John Canton, A. M. F. R. S." *Philosophical Transactions of the Royal Society of London* 53 (December):370–418. https://doi.org/10.1098/rstl.1763.0053.

Belouchrani, Adel, Karim Abed-Meraim, Jean François Cardoso, and Eric Moulines. 1997. "A Blind Source Separation Technique Using Second-Order Statistics." *IEEE Transactions on Signal Processing* 45 (2): 434–44. https://doi.org/10.1109/78.554307.

Bendat, Julius S, and Allan G Piersol. 1980. "Engineering Applications of Correlation and Spectral Analysis." *AIAA Journal* 31 (11): 2190–91. https://doi.org/10.2514/3.49131.

Bertha, Mathieu, and Jean-Claude Golinval. 2017. "Identification of Non-Stationary Dynamical Systems Using Multivariate ARMA Models." *Mechanical Systems and Signal Processing* 88 (May):166–79. https://doi.org/10.1016/j.ymssp.2016.11.024.

Bhushan, Bharat. 2009. "Biomimetics: Lessons from Nature–an Overview." *Philosophical Transactions of the Royal Society A: Mathematical, Physical and Engineering Sciences* 367 (1893): 1445–86. https://doi.org/10.1098/rsta.2009.0011.

Bishop, R. E. D., and G. M. L. Gladwell. 1963. "An Investigation Into The Theory of Resonance Testing." *Philosophical Transactions of the Royal Society of London* 255 (1055): 241–80.

Boashash, B. 1992a. "Estimating and Interpreting the Instantaneous Frequency of a Signal. I. Fundamentals." *Proceedings of the IEEE* 80 (4): 520–38. https://doi.org/10.1109/5.135376.

———. 1992b. "Estimating and Interpreting the Instantaneous Frequency of a Signal. II. Algorithms and Applications." *Proceedings of the IEEE* 80 (4): 540–68. https://doi.org/10.1109/5.135378.

Bowman, Adrian W., and Adelchi Azzalini. 2000. *Applied Smoothing Techniques for Data Analysis: The Kernel Approach with S-PLUS Illustrations*. *Oxford Statistical Science Series*. 1st ed. Vol. 18. UK: Oxford University Press.

Bradley, Robert E., and C. Edward Sandifer. 2009. *Cauchy's Cours d'analyse [Cauchy's Analysis Course]*. New York, NY: Springer New York. https://doi.org/10.1007/978-1-4419-0549-9.

Brandt, A. 2019. "A Signal Processing Framework for Operational Modal Analysis in Time and Frequency Domain." *Mechanical Systems and Signal Processing* 115:380–93. https://doi.org/10.1016/j.ymssp.2018.06.009.

Brincker, Rune. 2010. "Recent Advances of Operational Modal Analysis and Applications in Structural Health Monitoring." *Aalborg University*.

———. 2014. "Some Elements of Operational Modal Analysis." *Shock and Vibration* 2014:11. https://doi.org/http://dx.doi.org/10.1155/2014/325839.

Brincker, Rune, Palle Andersen, and Niels-Jørgen Jacobsen. 2007. "Automated Frequency Domain Decomposition for Operational Modal Analysis." *Conference and Exposition on Structural Dynamics IMAC*, no. XXIV, 1–7.

Brincker, Rune, Peter Olsen, Sandro Amador, Martin Juul, Abdollah Malekjafarian, and Mohammad Ashory. 2019. "Modal Participation in Multiple Input Ibrahim Time Domain Identification." *Mathematics and Mechanics of Solids* 24 (1): 168–80. https://doi.org/10.1177/1081286517733034.

Brincker, Rune;, C. E.; Ventura, and P. Andersen. 2001. "Damping Estimation by Frequency Domain Decomposition." In *Proceedings of IMAC XIX*, 698–703. Kissimmee, Florida, USA.

Brincker, Rune, L. Zhang, and P. Andersen. 2000. "Aalborg Universitet Modal Identification from Ambient Responses Using Frequency Domain Decomposition Publication Date :" *MAC 18 : Proceedings of the International Modal Analysis Conference*, 625–30.

Brincker, Rune, and Lingmi Zhang. 2009. "Frequency Domain Decomposition Revisited." *IOMAC 2009 - 3rd International Operational Modal Analysis Conference*, 615–26.

Brincker, Rune, Lingmi Zhang, and Palle Andersen. 2001. "Modal Identification of Output-Only Systems Using Frequency Domain Decomposition." *Smart Materials and Structures* 10 (3): 441–45. https://doi.org/10.1088/0964-1726/10/3/303.

Brown, D. L., R. J. Allemang, Ray Zimmerman, and M. Mergeay. 1979. "Parameter Estimation Techniques for Modal Analysis." *SAE Transactions* 88 (1): 828–46.

Cardoso, Jean François. 1998. "Blind Signal Separation: Statistical Principles." *Proceedings of the IEEE* 86 (10): 2009–25. https://doi.org/10.1109/5.720250.

Carpine, Raphaël, Silvia Ientile, and Pierre Argoul. 2023. "Investigating the Statistical Error on Autocorrelation for Operational Modal Analysis." *Journal of Sound and Vibration* 547 (March). https://doi.org/10.1016/j.jsv.2022.117504.

Catbas, F. N., A. E. Aktan, R. J. Allemang, and D. L. Brown. 1998. "Correlation Function for Spatial Locations of Scaled Mode Shapes - (COMEF)." *Proceedings of the International Modal Analysis Conference - IMAC* 2 (January 1998): 1550–55.

Cawley, P., and R.D. Adams. 1979. "The Location of Defects in Structures From Measurements of Natural Frequencies." *The Journal of Strain Analysis for Engineering Design* 14 (2): 49–57. https://doi.org/10.1243/03093247V142049.

Chang, Chih Chieh, and Lien Wen Chen. 2004. "Damage Detection of a Rectangular Plate by Spatial Wavelet Based Approach." *Applied Acoustics* 65 (8): 819–32. https://doi.org/10.1016/j.apacoust.2004.01.004.

Chun, Pang-jo, Hiroaki Yamashita, and Seiji Furukawa. 2015. "Bridge Damage Severity Quantification Using Multipoint Acceleration Measurement and Artificial Neural Networks." *Shock and Vibration* 2015:11.

Cicone, Antonio, Jingfang Liu, and Haomin Zhou. 2014. "Adaptive Local Iterative Filtering for Signal Decomposition and Instantaneous Frequency Analysis," November. http://arxiv.org/abs/1411.6051.

Civera, Marco, and Cecilia Surace. 2021. "A Comparative Analysis of Signal Decomposition Techniques for Structural Health Monitoring on an Experimental Benchmark." *Sensors* 21 (5): 1825. https://doi.org/10.3390/s21051825.

———. 2022. "The Instantaneous Spectral Entropy for Real-Time, Online Structural Health Monitoring." *Journal of Physics: Conference Series* 2184 (1): 012033. https://doi.org/10.1088/1742-6596/2184/1/012033.

Cochran, W., J. Cooley, D. Favin, H. Helms, R. Kaenel, W. Lang, G. Maling, D. Nelson, C. Rader, and P. Welch. 1967. "What Is the Fast Fourier Transform?" *IEEE Transactions on Audio and Electroacoustics* 15 (2): 45–55. https://doi.org/10.1109/TAU.1967.1161899.

Cole, Henry A., Jr. 1968. "On-the-Line Analysis of Random Vibrations." In *Structural Dynamics and Materials Conference*, 9. Palm Springs: AIAA. https://doi.org/10.2514/6.1968-288.

———. 1973. "On-Line Failure Detection and Damping Measurement of Aerospace Structures by Random Decrement Signatures." *NASA Technical Report*, 78.

Cooley, J., P. Lewis, and P. Welch. 1967a. "Application of the Fast Fourier Transform to Computation of Fourier Integrals, Fourier Series, and Convolution Integrals." *IEEE Transactions on Audio and Electroacoustics* 15 (2): 79–84. https://doi.org/10.1109/TAU.1967.1161904.

———. 1967b. "Historical Notes on the Fast Fourier Transform." *IEEE Transactions on Audio and Electroacoustics* 15 (2): 76–79. https://doi.org/10.1109/TAU.1967.1161903.

Cooley, James W., and John W. Tukey. 2006. "An Algorithm for the Machine Calculation of Complex Fourier Series." *Mathematics of Computation* 19 (90): 297. https://doi.org/10.2307/2003354.

D. J. Ewins. 2009. *Modal Testing: Theory, Practice and Application*. 2nd ed. https://www.wiley.com/en-us/Modal+Testing:+Theory,+Practice+and+Application,+2nd+Edition-p-9780863802188.

Dai, Hongzhe, Guofeng Xue, and Wei Wang. 2014. "An Adaptive Wavelet Frame Neural Network Method for Efficient Reliability Analysis." *Computer-Aided Civil and Infrastructure Engineering* 29 (10): 801–14. https://doi.org/10.1111/mice.12117.

Das, Swagato, P. Saha, and S. K. Patro. 2016. "Vibration-Based Damage Detection Techniques Used for Health Monitoring of Structures: A Review." *Journal of Civil Structural Health Monitoring* 6 (3): 477–507. https://doi.org/10.1007/s13349-016-0168-5.

Daubechies, Ingrid. 1992. *Ten Lectures on Wavelets*. *Society of Industrial and Applied Mathematics, SIAM*. Society for Industrial and Applied Mathematics. https://doi.org/10.1137/1.9781611970104.

Daubechies, Ingrid, Jianfeng Lu, and Hau-Tieng Wu. 2011. "Synchrosqueezed Wavelet Transforms: An Empirical Mode Decomposition-like Tool." *Applied and Computational Harmonic Analysis* 30 (2): 243–61. https://doi.org/10.1016/j.acha.2010.08.002.

DIANA FEA B.V. 2021. "DIANA FEA® R10.5." Delft, The Netherlands.

Döhler, Michael, Palle Andersen, and Laurent Mevel. 2012. "Operational Modal Analysis Using a Fast Stochastic Subspace Identification Method." In *Conference Proceedings of the Society for Experimental Mechanics Series*, 5:19–24. https://doi.org/10.1007/978-1-4614-2425-3_3.

——. 2017. "Variance Computation of Modal Parameter Estimates from UPC Subspace Identification." In *IOMAC - 7th International Operational Modal Analysis Conference*. Ingolstadt, Germany. https://hal.inria.fr/hal-01522137.

Douka, E., S. Loutridis, and A. Trochidis. 2003. "Crack Identification in Beams Using Wavelet Analysis." *International Journal of Solids and Structures* 40 (13–14): 3557–69. https://doi.org/10.1016/S0020-7683(03)00147-1.

Dragomiretskiy, Konstantin, and Dominique Zosso. 2014. "Variational Mode Decomposition." *IEEE Transactions on Signal Processing* 62 (3): 531–44. https://doi.org/10.1109/TSP.2013.2288675.

Dziedziech, K., W. J. Staszewski, and T. Uhl. 2015. "Wavelet-Based Modal Analysis for Time-Variant Systems." *Mechanical Systems and Signal Processing* 50–51:323–37. https://doi.org/10.1016/j.ymssp.2014.05.003.

Fan, Wei, and Pizhong Qiao. 2009. "A 2-D Continuous Wavelet Transform of Mode Shape Data for Damage Detection of Plate Structures." *International Journal of Solids and Structures* 46 (25–26): 4379–95. https://doi.org/10.1016/j.ijsolstr.2009.08.022.

Fang, X., H. Luo, and J. Tang. 2005. "Structural Damage Detection Using Neural Network with Learning Rate Improvement." *Computers and Structures* 83 (25–26): 2150–61. https://doi.org/10.1016/j.compstruc.2005.02.029.

Farrar, Charles R, and Keith Worden. 2007. "An Introduction to Structural Health Monitoring." *Philosophical Transactions of the Royal Society A: Mathematical, Physical and Engineering Sciences* 365 (1851): 303–15. https://doi.org/10.1098/rsta.2006.1928.

Farrar, Charles R., and Keith Worden. 2012. *Structural Health Monitoring: A Machine Learning Perspective*. Wiley. https://doi.org/10.1002/9781118443118.

Feldman, Michael. 2011. *Hilbert Transform Applications in Mechanical Vibration*. First Edit. Chichester: John Wiley & Sons.

Forrest, S., A.S. Perelson, L. Allen, and R. Cherukuri. 1994. "Self-Nonself Discrimination in a Computer." In *Proceedings of 1994 IEEE Computer Society Symposium on Research in Security and Privacy*, 202–12. IEEE Comput. Soc. Press. https://doi.org/10.1109/RISP.1994.296580.

Fourier, Jean Baptiste Joseph. 1822. *Théorie Analytique de La Chaleur [Analytical Theory of Heat]*. 2009 Re-ed. Cambridge: Cambridge University Press. https://doi.org/10.1017/CBO9780511693229.

Frigo, Matteo, and Steven~G. Johnson. 2005. "The Design and Implementation of {FFTW3}." *Proceedings of the IEEE* 93 (2): 216–31.

Gabor, D. 1946. "Theory of Communication." *Journal of the Institution of Electrical Engineers - Part III: Radio and Communication Engineering* 93 (26): 429–41. https://doi.org/10.1049/ji-3-2.1946.0074.

Gelman, Andrew, John B. Carlin, Hal S. Stern, David B. Dunson, Aki Vehtari, and Donald B. Rubin. 2013. *Bayesian Data Analysis*. *The SAGE Encyclopedia of Research Design*. Chapman and Hall/CRC. https://doi.org/10.1201/b16018.

Gene H. Golub, and Charles F. Van Loan. 2013. *Matrix Computations*. 4th ed. Johns Hopkins University Press.

Gersch, W. 1974. "On the Achievable Accuracy of Structural System Parameter Estimates." *Journal of Sound and Vibration* 34 (1): 63–79. https://doi.org/10.1016/S0022-460X(74)80355-X.

——. 1975. "Parameter Identification: Stochastic Process Techniques." *The Shock and Vibration Digest* 7 (11): 71–86.

Gersch, W., and T. Brotherton. 1982. "Estimation of Stationary Structural System Parameters from Non-Stationary Random Vibration Data: A Locally Stationary Model Method." *Journal of Sound and Vibration* 81 (2): 215–27. https://doi.org/10.1016/0022-460X(82)90205-X.

Gersch, W., and R. S.Z. Liu. 1976. "Time Series Methods for the Synthesis of Random Vibration Systems." *Journal of Applied Mechanics, Transactions ASME* 43 (1): 159–65. https://doi.org/10.1115/1.3423768.

Gersch, W., and F. Martinelli. 1979. "Estimation Of Structural System Parameters From Stationary And Non-Stationary Ambient Vibrations: An Exploratory-Confumatory Analysis." *Journal of Sound & Vibration* 65 (3): 303–18.

Gersch, Will. 1970. "Estimation of the Autoregressive Parameters of a Mixed Autoregressive Moving-Average Time Series." *IEEE Transactions on Automatic Control* AC-15 (5): 583–88. https://doi.org/10.1109/TAC.1970.1099560.

Gersch, Will, and David R. Sharpe. 1973. "Estimation of Power Spectra with Finite-Order Autoregressive Models." *IEEE Transactions on Automatic Control* 18 (4): 367–69. https://doi.org/10.1109/TAC.1973.1100350.

Gilbert Strang. 2016. *Introduction to Linear Algebra*. 5th ed. Wellesley-Cambridge Press.

Gilles, Jerome. 2013. "Empirical Wavelet Transform." *IEEE Transactions on Signal Processing* 61 (16): 3999–4010. https://doi.org/10.1109/TSP.2013.2265222.

Giordano, Pier Francesco, Chiara Iacovino, Said Quqa, and Maria Pina Limongelli. 2022. "The Value of Seismic Structural Health Monitoring for Post-Earthquake Building Evacuation." *Bulletin of Earthquake Engineering* 20 (9): 4367–93. https://doi.org/10.1007/s10518-022-01375-2.

Gomez, Hugo C., Hasan S. Ulusoy, and Maria Q. Feng. 2013. "Variation of Modal Parameters of a Highway Bridge Extracted from Six Earthquake Records." *Earthquake Engineering & Structural Dynamics* 42 (4): 565–79. https://doi.org/10.1002/eqe.2227.

Gong, Maosheng, Jing Sun, and Lili Xie. 2014. "Identification of Model Structure Parameters via Combination of AFMM and ARX from Seismic Response Data." *Earthquake Engineering and Engineering Vibration* 13 (3): 411–23. https://doi.org/10.1007/s11803-014-0252-y.

Gonzalez, F., D. Dasgupta, and R. Kozma. 2002. "Combining Negative Selection and Classification Techniques for Anomaly Detection." In *Proceedings of the 2002 Congress on Evolutionary Computation. CEC'02 (Cat. No.02TH8600)*, 1:705–10. IEEE. https://doi.org/10.1109/CEC.2002.1007012.

Goupillaud, P., A. Grossmann, and J. Morlet. 1984. "Cycle-Octave and Related Transforms in Seismic Signal Analysis." *Geoexploration* 23 (1): 85–102. https://doi.org/https://doi.org/10.1016/0016-7142(84)90025-5.

Grenier, Y. 1983. "Time-Dependent ARMA Modeling of Nonstationary Signals." *IEEE Transactions on Acoustics, Speech, and Signal Processing* 31 (4): 899–911. https://doi.org/10.1109/TASSP.1983.1164152.

Greś, Szymon, Michael Döhler, Palle Andersen, and Laurent Mevel. 2021. "Kalman Filter-Based Subspace Identification for Operational Modal Analysis under Unmeasured Periodic Excitation." *Mechanical Systems and Signal Processing* 146 (January):106996. https://doi.org/10.1016/j.ymssp.2020.106996.

Greś, Szymon, Michael Döhler, and Laurent Mevel. 2021. "Uncertainty Quantification of the Modal Assurance Criterion in Operational Modal Analysis." *Mechanical Systems and Signal Processing* 152. https://doi.org/10.1016/j.ymssp.2020.107457.

Gres, Szymon, Martin Dalgaard Ulriksen, Michael Döhler, Rasmus Johan Johansen, Palle Andersen, Lars Damkilde, and Søren Andreas Nielsen. 2017. "Statistical Methods for Damage Detection Applied to Civil Structures." *Procedia Engineering* 199:1919–24. https://doi.org/10.1016/j.proeng.2017.09.280.

Gupta, Madan M., Liang Jin, and Noriyasu Homma. 2003. *Static and Dynamic Neural Networks*. Hoboken, NJ, USA: John Wiley & Sons, Inc. https://doi.org/10.1002/0471427950.

Haar, Alfred. 1910. "Zur Theorie Der Orthogonalen Funktionensysteme." *Mathematische Annalen* 69 (3): 331–71. https://doi.org/10.1007/BF01456326.

Hazra, B., A. Sadhu, A. J. Roffel, and S. Narasimhan. 2012. "Hybrid Time-Frequency Blind Source Separation Towards Ambient System Identification of Structures." *Computer-Aided Civil and Infrastructure Engineering* 27 (5): 314–32. https://doi.org/10.1111/j.1467-8667.2011.00732.x.

He, K., and W. D. Zhu. 2011. "A Vibration-Based Structural Damage Detection Method and Its Applications to Engineering Structures." *International Journal of Smart and Nano Materials* 2 (3): 194–218. https://doi.org/10.1080/19475411.2011.594105.

Hormazábal, Manuel F., Alberto Barontini, Maria Giovanna Masciotta, and Daniel V. Oliveira. 2023. "A Non-Parametric Algorithm for Time-Dependent Modal Analysis of Civil Structures and Infrastructures." *Mechanical Systems and Signal Processing* 204 (December):110802. https://doi.org/10.1016/j.ymssp.2023.110802.

Hormazábal, Manuel F., Maria Giovanna Masciotta, and Daniel V. Oliveira. 2021. "Proposal for a Time-Dependent Dynamic Identification Algorithm for Structural Health Monitoring." In *12th International Conference on Structural Analysis of Historical Constructions*. CIMNE. https://doi.org/10.23967/sahc.2021.196.

Hu, Xiaoya, Bingwen Wang, and Han Ji. 2013. "A Wireless Sensor Network-Based Structural Health Monitoring System for Highway Bridges." *Computer-Aided Civil and Infrastructure Engineering* 28 (3): 193–209. https://doi.org/10.1111/j.1467-8667.2012.00781.x.

Huang, Norden E. 2014. "Introduction to the Hilbert-Huang Transform and Its Related Mathematical Problems." In *Hilbert–Huang Transform and Its Applications*, 1–26. Greenbelt, USA. https://doi.org/doi:10.1142/9789812703347_0001.

Huang, Norden E, and Samuel S P Shen. 2005. *Hilbert-Huang Transform and Its Applications*. Vol. 5. Interdisciplinary Mathematical Sciences. WORLD SCIENTIFIC. https://doi.org/10.1142/5862.

Huang, Norden E., Zheng Shen, Steven R. Long, Manli C. Wu, Hsing H. Shih, Quanan Zheng, Nai-Chyuan Yen, Chi Chao Tung, and Henry H. Liu. 1998. "The Empirical Mode Decomposition and the Hilbert Spectrum for Nonlinear and Non-Stationary Time Series Analysis." *Proceedings of the Royal Society of London. Series A: Mathematical, Physical and Engineering Sciences* 454 (1971): 903–95. https://doi.org/10.1098/rspa.1998.0193.

Huang, Norden E., and Zhaohua Wu. 2008. "A Review on Hilbert-Huang Transform: Method and Its Applications to Geophysical Studies." *Reviews of Geophysics* 46 (2): RG2006. https://doi.org/10.1029/2007RG000228.

Huang, Norden E., Zhaohua Wu, Steven R. Long, Kenneth C. Arnold, Xianyao Chen, and Karin Blank. 2009. "On Instantaneous Frequency." *Advances in Adaptive Data Analysis* 01 (02): 177–229. https://doi.org/10.1142/S1793536909000096.

Hughes, A. J., R. J. Barthorpe, N. Dervilis, C. R. Farrar, and K. Worden. 2021. "A Probabilistic Risk-Based Decision Framework for Structural Health Monitoring." *Mechanical Systems and Signal Processing* 150:107339. https://doi.org/10.1016/j.ymssp.2020.107339.

Hyvärinen, Aapo, Juha Karhunen, and Erkki Oja. 2001. *Independent Component Analysis*. New York: John Wiley & Sons, Inc. https://www.wiley.com/en-us/Independent+Component+Analysis-p-9780471405405.

Iatsenko, D., P. V.E. McClintock, and A. Stefanovska. 2016. "Extraction of Instantaneous Frequencies from Ridges in Time-Frequency Representations of Signals." *Signal Processing* 125 (August):290–303. https://doi.org/10.1016/j.sigpro.2016.01.024.

Ibrahim, S. R. 1977. "Random Decrement Technique for Modal Identification of Structures." *Journal of Spacecraft and Rockets* 14 (11): 596–700. https://doi.org/10.2514/3.57251.

Ibrahim, S. R., and E. C. Mikulcik. 1973. “A Time Domain Modal Vibration Test Technique.” *The Shock & Vibration Bulletin* 43 (4): 21–37.

——. 1977. “Method for the Direct Identification of Vibration Parameters From the Free Response.” *Shock Vib Bull* 4 (47): 183–98.

INGV. 1997. “L AQUILA V. ATERNO CENTRO VALLE (IT.AQV).” 1997. https://itaca.mi.ingv.it/ItacaNet_32/#/station/IT/AQV.

——. 2009a. “AQV 00 IT-2009-0009 2009-04-06 01:32:40 (HN).” Https://Itaca.Mi.Ingv.It/ItacaNet_32/#/Waveform/IT/AQV/00/IT-2009-0009/HN. April 6, 2009. https://itaca.mi.ingv.it/ItacaNet_32/#/waveform/IT/AQV/00/IT-2009-0009/HN.

——. 2009b. “L_AQUILA (IT-2009-0009).” April 6, 2009. https://itaca.mi.ingv.it/ItacaNet_32/#/event/IT-2009-0009.

James, GH, Thomas Carne, and James Lauffer. 1995. “The Natural Excitation Technique (NExT) for Modal Parameter Extraction from Operating Structures.” *Modal Analysis-the International Journal of Analytical and Experimental Modal Analysis* 10 (4): 260.

Jarosińska, Małgorzata, and Stefan Berczyński. 2021. “Changes in Frequency and Mode Shapes Due to Damage in Steel–Concrete Composite Beam.” *Materials* 14 (21): 6232. https://doi.org/10.3390/ma14216232.

Jiang, Shao Fei, Chun Ming Zhang, and Shuai Zhang. 2011. “Two-Stage Structural Damage Detection Using Fuzzy Neural Networks and Data Fusion Techniques.” *Expert Systems with Applications* 38 (1): 511–19. https://doi.org/10.1016/j.eswa.2010.06.093.

Jiang, Shao-Fei, Chun-Ming Zhang, and C. G. Koh. 2006. “Structural Damage Detection by Integrating Data Fusion and Probabilistic Neural Network.” *Advances in Structural Engineering* 9 (4): 445–58. https://doi.org/10.1260/136943306778812787.

Jiang, Xiaomo, and Hojjat Adeli. 2007. “Pseudospectra, MUSIC, and Dynamic Wavelet Neural Network for Damage Detection of Highrise Buildings.” *International Journal for Numerical Methods in Engineering* 71 (5): 606–29. https://doi.org/https://doi.org/10.1002/nme.1964.

Juang, J. N., and R. S. Pappa. 1986. “Effects of Noise on Modal Parameters Identified by the Eigensystem Realization Algorithm.” *Journal of Guidance, Control, and Dynamics* 9 (3): 294–303. https://doi.org/10.2514/3.20106.

Juang, Jer-Nan, and Richard S. Pappa. 1985. “An Eigensystem Realization Algorithm for Modal Parameter Identification and Model Reduction.” *Journal of Guidance, Control, and Dynamics* 8 (5): 620–27. https://doi.org/10.2514/3.20031.

K. F. Riley, M. P. Hobson, and S. J. Bence. 2006. *Mathematical Methods for Physics and Engineering*. 3rd ed. Cambridge University Press.

Kaiser, James F. 1990. “On a Simple Algorithm to Calculate the ‘energy’ of a Signal.” In *ICASSP, IEEE International Conference on Acoustics, Speech and Signal Processing - Proceedings*, 1:381–84. Publ by IEEE. https://doi.org/10.1109/icassp.1990.115702.

Katayama. 2004. *Spectral Methods for System Identification*. *Chemistry & ...*. http://onlinelibrary.wiley.com/doi/10.1002/cbdv.200490137/abstract.

Kennedy, Charles C., and C. D. P. Pancu. 1947. “Use of Vectors in Vibration Measurement and Analysis.” *Journal of the Aeronautical Sciences* 14 (11): 603–25. https://doi.org/10.2514/8.1474.

Kerschen, G., F. Poncelet, and J. C. Golinval. 2007. “Physical Interpretation of Independent Component Analysis in Structural Dynamics.” *Mechanical Systems and Signal Processing* 21 (4): 1561–75. https://doi.org/10.1016/j.ymssp.2006.07.009.

Kijewski-Correa, T., and A. Kareem. 2006. “Efficacy of Hilbert and Wavelet Transforms for Time-Frequency Analysis.” *Journal of Engineering Mechanics* 132 (10): 1037–49. https://doi.org/10.1061/(ASCE)0733-9399(2006)132:10(1037).

Kim, Sunyong, and Dan M. Frangopol. 2011. "Cost-Effective Lifetime Structural Health Monitoring Based on Availability." *Journal of Structural Engineering* 137 (1): 22–33. https://doi.org/10.1061/(ASCE)ST.1943-541X.0000280.

I. Hunt, David. 1992. "Application of an Enhanced Coordinate Modal Assurance Criterion." In .

Li, Peng. 2011. "Structural Damage Localization Using Probabilistic Neural Networks." *Mathematical and Computer Modelling* 54 (3–4): 965–69. https://doi.org/10.1016/j.mcm.2010.11.023.

Lieven, N. A. J., and D. J. Ewins. 1988. "Spatial Correlation of Mode Shapes, the Coordinate Modal Assurance Criterion (COMAC)." In *Proceedings of the 6th International Modal Analysis Conference*, 690–95.

Limongelli, Maria Pina, and Mehmet Çelebi, eds. 2019. *Seismic Structural Health Monitoring. From Theory to Successful Applications. Springer Tracts in Civil Engineering*. 1st ed. Springer.

Liu, Shuaishuai, Rui Zhao, Kaiping Yu, Baopeng Liao, and Bowen Zheng. 2022. "A Novel Real-Time Modal Analysis Method for Operational Time-Varying Structural Systems Based on Short-Time Extension of Multivariate VMD." *Structures* 37 (March):389–402. https://doi.org/10.1016/j.istruc.2021.12.070.

Ljung, Lennart. 2001. "Estimating Linear Time-Invariant Models of Nonlinear Time-Varying Systems." *European Journal of Control*. Vol. 7.

———. 2008. "Perspectives on System Identification." In *IFAC Proceedings Volumes (IFAC-PapersOnline)*. Vol. 17. https://doi.org/10.3182/20080706-5-KR-1001.4277.

Loan, Charles Van. 1992. *Computational Frameworks for the Fast Fourier Transform*. Society for Industrial and Applied Mathematics. https://doi.org/10.1137/1.9781611970999.

Londoño, Julián M., Simon A. Neild, and Jonathan E. Cooper. 2015. "Identification of Backbone Curves of Nonlinear Systems from Resonance Decay Responses." *Journal of Sound and Vibration* 348 (July):224–38. https://doi.org/10.1016/j.jsv.2015.03.015.

Loutridis, S., E. Douka, and A. Trochidis. 2004. "Crack Identification in Double-Cracked Beams Using Wavelet Analysis." *Journal of Sound and Vibration* 277 (4–5): 1025–39. https://doi.org/10.1016/j.jsv.2003.09.035.

Magalhães, Filipe, Álvaro Cunha, Elsa Caetano, and Rune Brincker. 2010. "Damping Estimation Using Free Decays and Ambient Vibration Tests." *Mechanical Systems and Signal Processing* 24 (5): 1274–90. https://doi.org/10.1016/j.ymssp.2009.02.011.

Maia, Nuno Manuel Mendes. 1988. "Extraction of Valid Modal Properties from Measured Data in Structural Vibrations." *Mechanical Engineering*. Doctor of Philosophy Thesis, University of London.

Malekjafarian, A., R. Brincker, M. R. Ashory, and M. M. Khatibi. 2012. "Modified Ibrahim Time Domain Method for Identification of Closely Spaced Modes: Experimental Results." In , 443–49. https://doi.org/10.1007/978-1-4614-2413-0_44.

Masciotta, Maria Giovanna. 2015. "Damage Identification of Structures Based on Spectral Output Signals." University of Minho.

Masciotta, Maria Giovanna, and Daniel Pellegrini. 2022. "Tracking the Variation of Complex Mode Shapes for Damage Quantification and Localization in Structural Systems." *Mechanical Systems and Signal Processing* 169 (April):108731. https://doi.org/10.1016/j.ymssp.2021.108731.

Masciotta, Maria Giovanna, Luís F. Ramos, Paulo B. Lourenço, and Marcello Vasta. 2017. "Spectral Algorithm for Non-Destructive Damage Localisation: Application to an Ancient Masonry Arch Model." *Mechanical Systems and Signal Processing* 84 (February):286–307. https://doi.org/10.1016/j.ymssp.2016.06.034.

Masciotta, Maria Giovanna, Luís F. Ramos, Paulo B. Lourenço, Marcello Vasta, and Guido De Roeck. 2016. "A Spectrum-Driven Damage Identification Technique: Application and Validation through

the Numerical Simulation of the Z24 Bridge." *Mechanical Systems and Signal Processing* 70–71 (March):578–600. https://doi.org/10.1016/j.ymssp.2015.08.027.

Masciotta, Maria Giovanna, João C.A. Roque, Luís F. Ramos, and Paulo B. Lourenço. 2016. "A Multidisciplinary Approach to Assess the Health State of Heritage Structures: The Case Study of the Church of Monastery of Jerónimos in Lisbon." *Construction and Building Materials* 116 (July):169–87. https://doi.org/10.1016/j.conbuildmat.2016.04.146.

Matsumoto, Masaru, Hiromichi Shirato, Tomomi Yagi, Rikuma Shijo, Akitoshi Eguchi, and Hitoshi Tamaki. 2003. "Effects of Aerodynamic Interferences between Heaving and Torsional Vibration of Bridge Decks: The Case of Tacoma Narrows Bridge." *Journal of Wind Engineering and Industrial Aerodynamics* 91 (12–15): 1547–57. https://doi.org/10.1016/j.jweia.2003.09.010.

Messina, A., E. J. Williams, and T. Contursi. 1998. "Structural Damage Detection by a Sensitivity and Statistical-Based Method." *Journal of Sound and Vibration* 216 (5): 791–808.

Michael D. Greenberg. 2000. *Differential Equations and Linear Algebra*. 1st ed. Prentice Hall.

Nagarajaiah, S., and B. Basu. 2010. "Output Only Modal Identification and Structural Damage Detection Using Time Frequency & Wavelet Techniques." *Earthquake Engineering and Engineering Vibration* 8 (4): 583–605. https://doi.org/10.1007/s11803-009-9120-6.

Noël, J. P., and G. Kerschen. 2017. "Nonlinear System Identification in Structural Dynamics: 10 More Years of Progress." *Mechanical Systems and Signal Processing* 83 (January):2–35. https://doi.org/10.1016/j.ymssp.2016.07.020.

Nuttall, A.H., and E. Bedrosian. 1966. "On the Quadrature Approximation to the Hilbert Transform of Modulated Signals." *Proceedings of the IEEE* 54 (10): 1458–59. https://doi.org/10.1109/PROC.1966.5138.

Nyquist, H. 1928. "Certain Topics in Telegraph Transmission Theory." *Transactions of the American Institute of Electrical Engineers* 47 (2): 617–44. https://doi.org/10.1109/T-AIEE.1928.5055024.

Oliveira, C. S., and M. Navarro. 2010. "Fundamental Periods of Vibration of RC Buildings in Portugal from In-Situ Experimental and Numerical Techniques." *Bulletin of Earthquake Engineering* 8 (3): 609–42. https://doi.org/10.1007/s10518-009-9162-1.

Osornio-Rios, Roque A., Juan Pablo Amezquita-Sanchez, Rene J. Romero-Troncoso, and Arturo Garcia-Perez. 2012. "MUSIC-ANN Analysis for Locating Structural Damages in a Truss-Type Structure by Means of Vibrations." *Computer-Aided Civil and Infrastructure Engineering* 27 (9): 687–98. https://doi.org/10.1111/j.1467-8667.2012.00777.x.

Ovanesova, A. V., and L. E. Suárez. 2004. "Applications of Wavelet Transforms to Damage Detection in Frame Structures." *Engineering Structures* 26 (1): 39–49. https://doi.org/10.1016/j.engstruct.2003.08.009.

Overschee, Peter van, and Bart de Moor. 1996. *Subspace Identification for Linear Systems*. *2008 30th Annual International Conference of the IEEE Engineering in Medicine and Biology Society*. Boston, MA: Springer US. https://doi.org/10.1007/978-1-4613-0465-4.

Pandey, A., and M. Biswas. 1994. "Damage Detection in Structures Using Changes in Flexibility." *Journal of Sound and Vibration* 169 (1): 3–17.

Pandey, A., M. Biswas, and M. Samman. 1991. "Damage Detection From Changes in Curvature Mode Shapes." *Journal of Sound and Vibration* 145 (2): 321–32.

Papagiannopoulos, George A., and George D. Hatzigeorgiou. 2011. "On the Use of the Half-Power Bandwidth Method to Estimate Damping in Building Structures." *Soil Dynamics and Earthquake Engineering* 31 (7): 1075–79. https://doi.org/10.1016/j.soildyn.2011.02.007.

Paul C. Krause, Oleg Wasynczuk, and Scott D. Sudhoff. 2002. *Analysis of Electric Machinery and Drive Systems*. Wiley-IEEE Press.

Peeters, Bart, Herman Van Der Auweraer, Frederik Vanhollebeke, and Patrick Guillaume. 2007. "Operational Modal Analysis for Estimating the Dynamic Properties of a Stadium Structure during a Football Game." *Shock and Vibration* 14:283–303. http://www.hindawi.com.

Peeters, Bart, and Guido de Roeck. 2001. "Stochastic System Identification for Operational Modal Analysis: A Review." *Journal of Dynamic Systems, Measurement, and Control* 123 (4): 659–67. https://doi.org/10.1115/1.1410370.

Pellegrini, D., A. Barontini, M. Girardi, P.B. Lourenço, M.G. Masciotta, N. Mendes, C. Padovani, and L.F. Ramos. 2023. "Effects of Temperature Variations on the Modal Properties of Masonry Structures: An Experimental-Based Numerical Modelling Approach." *Structures* 53 (July):595–613. https://doi.org/10.1016/j.istruc.2023.04.080.

Peng, Z.K., Peter W. Tse, and F.L. Chu. 2005. "An Improved Hilbert–Huang Transform and Its Application in Vibration Signal Analysis." *Journal of Sound and Vibration* 286 (1–2): 187–205. https://doi.org/10.1016/j.jsv.2004.10.005.

Poncelet, F., G. Kerschen, J. C. Golinval, and D. Verhelst. 2007. "Output-Only Modal Analysis Using Blind Source Separation Techniques." *Mechanical Systems and Signal Processing* 21 (6): 2335–58. https://doi.org/10.1016/j.ymssp.2006.12.005.

Pourgholi, Mehran, Mohsen Mohammadzadeh Gilarlue, Touraj Vahdaini, and Mohammad Azarbonyad. 2023. "Influence of Hankel Matrix Dimension on System Identification of Structures Using Stochastic Subspace Algorithms." *Mechanical Systems and Signal Processing* 186 (March). https://doi.org/10.1016/j.ymssp.2022.109893.

Rainieri, Carlo, and Giovanni Fabbrocino. 2014. *Operational Modal Analysis of Civil Engineering Structures*. 1st ed. New York, NY: Springer New York. https://doi.org/10.1007/978-1-4939-0767-0.

Ramírez, E., Paulo B. Lourenço, and Michele D'Amato. 2019. "Seismic Assessment of the Matera Cathedral." In *11th International Conference on Structural Analysis of Historical Constructions (SAHC)*, edited by Aguilar R., Torrealva D., Moreira S., Pando M.A., and Ramos L.F., 18:1346–54. Springer, Cham. https://doi.org/http://doi-org-443.webvpn.fjmu.edu.cn/10.1007/978-3-319-99441-3_144.

Ramos, L.F., L. Marques, P.B. Lourenço, G. de Roeck, A. Campos-Costa, and J. Roque. 2010. "Monitoring Historical Masonry Structures with Operational Modal Analysis: Two Case Studies." *Mechanical Systems and Signal Processing* 24 (5): 1291–1305. https://doi.org/10.1016/j.ymssp.2010.01.011.

Ramos, Luís F. 2007. "Damage Identification on Masonry Structures Based on Vibration Signatures." *PhD Thesis*. http://repositorium.sdum.uminho.pt/handle/1822/7380.

Rehman, Naveed ur, and Hania Aftab. 2019. "Multivariate Variational Mode Decomposition." *IEEE Transactions on Signal Processing* 67 (23): 6039–52. https://doi.org/10.1109/TSP.2019.2951223.

Rodrigues, Jorge, R Brincker, and P Andersen. 2004. "Improvement of Frequency Domain Output-Only Modal Identification from the Application of the Random Decrement Technique." *Proceedings of IMAC XXII*, 92–100. ftp://ftp.svibs.com/Download/Literature/Papers/2004/2004_4.pdf.

Rodrigues, Jorge, and Rune Brincker. 2005. "Application of the Random Decrement Technique in Operational Modal Anlysis." *International Operational Modal Analysis Conference (IOMAC)*, 191–200. https://pdfs.semanticscholar.org/d3a5/e41b26871ffb5cea37dd9fd65967f664bb07.pdf.

Ruzzene, M., A. Fasana, L. Garibaldi, and B. Piombo. 1997. "Natural Frequencies And Dampings Identification Using Wavelet Transform: Application To Real Data." *Mechanical Systems and Signal Processing* 11 (2): 207–18. https://doi.org/10.1006/mssp.1996.0078.

Rytter, Anders. 1993. "Vibrational Based Inspection of Civil Engineering Structures." *Fracture and Dynamics* R9314 (44). https://vbn.aau.dk/en/publications/vibrational-based-inspection-of-civil-engineering-structures.

Saito, Tomoo, and James L. Beck. 2010. "Bayesian Model Selection for ARX Models and Its Application to Structural Health Monitoring." *Earthquake Engineering & Structural Dynamics* 39 (15): 1737–59. https://doi.org/10.1002/eqe.1006.

Schmidt, Ralph O. 1979. "Multiple Emitter Location and Parameter Estimation." *Ieee*, no. March, 243–58.

Schwarz, Brian, and Mark Richardson. 2003. "Scaling Mode Shapes Obtained from Operating Data." In *IMAC*, 1–8.

Shannon, C.E. 1949. "Communication in the Presence of Noise." *Proceedings of the IRE* 37 (1): 10–21. https://doi.org/10.1109/JRPROC.1949.232969.

Shi, Weixing, Jiazeng Shan, and Xilin Lu. 2012. "Modal Identification of Shanghai World Financial Center Both from Free and Ambient Vibration Response." *Engineering Structures* 36 (March):14–26. https://doi.org/10.1016/j.engstruct.2011.11.025.

Simon Carbajo, Esther, Ricardo Simon Carbajo, Ciarán Mc Goldrick, and Biswajit Basu. 2014. "ASDAH: An Automated Structural Change Detection Algorithm Based on the Hilbert–Huang Transform." *Mechanical Systems and Signal Processing* 47 (1–2): 78–93. https://doi.org/10.1016/j.ymssp.2013.06.010.

Spitznogle, Frank R., and Azizul H. Quazi. 1969. "Representation and Analysis of Time-Limited Data Samples Using a Complex Exponential Algorithm." *The Journal of the Acoustical Society of America* 46 (1A): 102–3. https://doi.org/10.1121/1.1972432.

Structural Vibration Solutions A/S. 2020. "ARTeMIS Modal™ R6.1." Aalborg, Denmark2020.

Sung, S. H., H. J. Jung, and H. Y. Jung. 2013. "Damage Detection for Beam-like Structures Using the Normalized Curvature of a Uniform Load Surface." *Journal of Sound and Vibration* 332 (6): 1501–19. https://doi.org/10.1016/j.jsv.2012.11.016.

Surace, C., and A. Bovsunovsky. 2020. "The Use of Frequency Ratios to Diagnose Structural Damage in Varying Environmental Conditions." *Mechanical Systems and Signal Processing* 136 (February):106523. https://doi.org/10.1016/j.ymssp.2019.106523.

Surace, Cecilia, and Romualdo Ruotolo. 1994. "Crack Detection of a Beam Using the Wavelet Transform." *Proceedings of the 12th International Modal Analysis Conference*, 1141–1167.

Teager, H. M., and S. M. Teager. 1990. "Evidence for Nonlinear Sound Production Mechanisms in the Vocal Tract." In *Speech Production and Speech Modelling*, 241–61. Dordrecht: Springer Netherlands. https://doi.org/10.1007/978-94-009-2037-8_10.

The MathWorks Inc. 2021a. "MATLAB Wavelet Toolbox™ R2021a." Natick, Massachusetts, USE.

——. 2021b. "MATLAB™ and Simulink™ Student Suite R2021a." Natick, Massachusetts, USA.

Thoft-Christensen, Palle. 2012. "Infrastructures and Life-Cycle Cost-Benefit Analysis." *Structure and Infrastructure Engineering* 8 (5): 507–16. https://doi.org/10.1080/15732479.2010.539070.

Ubertini, Filippo, Gabriele Comanducci, and Nicola Cavalagli. 2016. "Vibration-Based Structural Health Monitoring of a Historic Bell-Tower Using Output-Only Measurements and Multivariate Statistical Analysis." *Structural Health Monitoring* 15 (4): 438–57. https://doi.org/10.1177/1475921716643948.

Ubertini, Filippo, Carmelo Gentile, and Annibale Luigi Materazzi. 2013. "Automated Modal Identification in Operational Conditions and Its Application to Bridges." *Engineering Structures* 46 (January):264–78. https://doi.org/10.1016/j.engstruct.2012.07.031.

Valla, Matthieu, Philippe Gueguen, Béatrice Augère, Didier Goular, and Matthieu Perrault. 2015. "Remote Modal Study of Reinforced Concrete Buildings Using a Multipath Lidar Vibrometer."

Journal of Structural Engineering 141 (1): 1–10. https://doi.org/10.1061/(asce)st.1943-541x.0001087.

Ventura, Carlos E. 2001. "Aalborg Universitet Damping Estimation by Frequency Domain Decomposition Brincker, Rune; Ventura, C. E.; Andersen, P."

Vincent, Julian F.V, Olga A Bogatyreva, Nikolaj R Bogatyrev, Adrian Bowyer, and Anja-Karina Pahl. 2006. "Biomimetics: Its Practice and Theory." *Journal of The Royal Society Interface* 3 (9): 471–82. https://doi.org/10.1098/rsif.2006.0127.

Vistasp M. Karbhari, and Farhad Ansari, eds. 2009. *Structural Health Monitoring of Civil Infrastructure Systems*. *Structural Health Monitoring of Civil Infrastructure Systems*. 1st ed. Cambridge: Woodhead Publishing.

Vold, Harvard, John Kundrat, G. Thomas Rocklin, and Richard Russell. 1989. "A Multi-Input Modal Estimation Algorithm for Mini-Computers." *SAE Technical Paper*, no. 890731, 67–77. https://doi.org/10.4271/890731.

Wahab, M M A, and G D Roeck. 1999. "Damage Detection In Bridges Using Modal Curvatures: Application To A Real Damage Scenario." *Journal of Sound and Vibration* 266 (2): 217–35.

Walden, A. T., and A. Contreras Cristan. 1998. "The Phase–Corrected Undecimated Discrete Wavelet Packet Transform and Its Application to Interpreting the Timing of Events." *Proceedings of the Royal Society of London. Series A: Mathematical, Physical and Engineering Sciences* 454 (1976): 2243–66. https://doi.org/10.1098/rspa.1998.0257.

Wang, Chao, Wei-Xin Ren, Zuo-Cai Wang, and Hong-Ping Zhu. 2013. "Instantaneous Frequency Identification of Time-Varying Structures by Continuous Wavelet Transform." *Engineering Structures* 52 (July):17–25. https://doi.org/10.1016/j.engstruct.2013.02.006.

Wang, Lei, Rui Chen, Lizhao Dai, Ke Huang, Jiabin Zhang, and Cui Tang. 2022. "A Detection Method Integrating Modal Deflection Curvature Difference and Natural Frequency for Structural Stiffness Degradation." *Engineering Failure Analysis* 141 (November):106637. https://doi.org/10.1016/j.engfailanal.2022.106637.

Wang, Yanghua. 2015. "Generalized Seismic Wavelets." *Geophysical Journal International* 203 (2): 1172–78. https://doi.org/10.1093/gji/ggv346.

Welch, P. 1967. "The Use of Fast Fourier Transform for the Estimation of Power Spectra: A Method Based on Time Averaging over Short, Modified Periodograms." *IEEE Transactions on Audio and Electroacoustics* 15 (2): 70–73. https://doi.org/10.1109/TAU.1967.1161901.

Wen, C. M., S. L. Hung, C. S. Huang, and J. C. Jan. 2007. "Unsupervised Fuzzy Neural Networks for Damage Detection of Structures." *Structural Control and Health Monitoring* 14 (1): 144–61. https://doi.org/10.1002/stc.116.

Y. Narkis. 1992. "Identification Of Crack Location In Vibrating Simply Supported Beams.Pdf." *Journal of Sound and Vibration*.

Yan, Guirong, Tiantian Li, Jianxin Yu, Ruoqiang Feng, and Xiaoyun Shao. 2019. "Damage Localization Using Shape Change in Uniform Load Surface for Civil Large-Span Space Structures." *Journal of Intelligent Material Systems and Structures* 30 (9): 1339–54. https://doi.org/10.1177/1045389X18806388.

Yang, J. N., Y. Lei, S. Lin, and N. Huang. 2003. "Hilbert-Huang Based Approach for Structural Damage Detection." *Journal of Engineering Mechanics ASCE* 130 (1): 85–95. https://doi.org/10.1061/(asce)0733-9399(2004)130:1(85).

——. 2004. "Hilbert-Huang Based Approach for Structural Damage Detection." *Journal of Engineering Mechanics* 130 (1): 85–95. https://doi.org/10.1061/(ASCE)0733-9399(2004)130:1(85).

Yang, Kai, Kaiping Yu, and Qiaofeng Li. 2013. "Modal Parameter Extraction Based on Hilbert Transform and Complex Independent Component Analysis with Reference." *Mechanical Systems and Signal Processing* 40 (1): 257–68. https://doi.org/10.1016/j.ymssp.2013.05.003.

Zhang, Chunwei, Asma A. Mousavi, Sami F. Masri, Gholamreza Gholipour, Kai Yan, and Xiuling Li. 2022. "Vibration Feature Extraction Using Signal Processing Techniques for Structural Health Monitoring: A Review." *Mechanical Systems and Signal Processing* 177 (April): 109175. https://doi.org/10.1016/j.ymssp.2022.109175.

Zhang, Z., and A. E. Aktan. 1998. "Application of Modal Flexibility and Its Derivatives in Structural Identification." *Research in Nondestructive Evaluation* 10 (1): 43–61. https://doi.org/10.1080/09349849809409622.

Zhou, Si-Da, Ward Heylen, Paul Sas, and Li Liu. 2014. "Parametric Modal Identification of Time-Varying Structures and the Validation Approach of Modal Parameters." *Mechanical Systems and Signal Processing* 47 (1–2): 94–119. https://doi.org/10.1016/j.ymssp.2013.07.021.

Zhou, X. T., Y. Q. Ni, and F. L. Zhang. 2014. "Damage Localization of Cable-Supported Bridges Using Modal Frequency Data and Probabilistic Neural Network." *Mathematical Problems in Engineering* 2014. https://doi.org/10.1155/2014/837963.

ANNEXE

A.1: EMILIA algorithm outputs basic information and nomenclature

N° : N^{th} EMILIA algorithm output.

MPV : Mean, in Hertz, of the frequency bins that presents the highest probability among all the Kernel distributions computed from the instantaneous frequency data from all the channels for the N^{th} algorithm output.

σ^2 (MPV) : Variance of the previous output.

MEV : Bayes most expected value, in Hertz, calculated from the Kernel probability distributions computed from the instantaneous frequency data from all the channels for the N^{th} algorithm output. This is the key output of the algorithm and the singleton values presented as natural frequency results along the present work.

σ^2 (MEV) : Variance of the previous output.

Max. BPDF : Maximum probability computed on the Bayes updated probability distribution for the N^{th} algorithm output.

A.2: Case I EMILIA algorithm outputs

Table A.1: Case I *ST00* scenario EMILIA output.

N°	MPV	σ^2 (MPV)	MEV	σ^2 (MEV)	Max. BPDF
1	0.49	0.01	0.51	0.00	7.77
2	1.48	0.06	1.39	0.00	10.56
3	1.94	0.01	1.86	0.00	20.48
4	2.79	0.02	2.78	0.00	7.02
5	3.61	0.00	3.61	0.00	12.14
6	4.55	0.02	4.56	0.00	9.27
7	4.97	0.00	4.93	0.00	19.55
8	5.77	0.02	5.63	0.00	14.65
9	6.32	0.16	6.47	0.01	4.75
10	7.25	0.19	7.49	0.00	8.23
11	8.33	0.00	8.32	0.00	8.77
12	9.09	0.00	9.08	0.00	20.48
13	9.10	0.00	9.10	0.00	14.80
14	10.54	0.01	10.49	0.00	9.84
15	11.54	0.10	11.42	0.01	5.22
16	12.37	0.01	12.36	0.00	8.75
17	12.64	0.01	12.67	0.00	6.76
18	13.36	0.03	13.47	0.01	4.79
19	14.35	0.01	14.43	0.01	5.91
20	14.76	0.11	15.12	0.01	3.93
21	14.68	0.90	15.29	0.10	1.20
22	16.77	0.01	16.74	0.00	9.55
23	17.53	0.00	17.54	0.00	9.45
24	18.36	0.00	18.36	0.00	8.44
25	19.01	0.01	19.00	0.00	6.46
26	19.97	0.01	20.00	0.01	5.72
27	20.76	0.03	20.73	0.01	4.57
28	21.91	0.28	21.78	0.02	2.92
29	23.68	1.99	23.06	0.04	2.19
30	25.37	3.34	26.95	0.36	3.13
31	24.48	0.06	24.41	0.02	3.26
32	24.94	0.00	24.95	0.00	9.52
33	25.11	0.00	25.11	0.00	7.68
34	25.62	0.06	25.68	0.02	3.20
35	27.19	0.18	27.28	0.00	12.57
36	27.15	0.56	27.32	0.00	10.46
37	28.34	0.02	28.34	0.02	3.09
38	29.21	0.00	29.22	0.01	4.95
39	30.10	0.00	30.08	0.00	6.52
40	30.95	0.00	30.94	0.00	6.94
41	31.52	0.01	31.53	0.00	6.86
42	32.42	0.00	32.42	0.00	9.90
43	33.17	0.00	33.17	0.00	12.96
44	33.99	0.00	34.00	0.00	8.10
45	34.85	0.00	34.85	0.00	10.31
46	35.56	0.00	35.56	0.00	8.11
47	36.41	0.02	36.36	0.00	13.31
48	37.24	0.02	37.22	0.00	6.49
49	37.62	0.02	37.62	0.00	6.84
50	37.60	1.09	38.47	0.02	3.43
51	39.31	0.01	39.33	0.01	4.33
52	40.38	0.03	40.33	0.00	7.43
53	40.93	0.01	40.85	0.00	10.24
54	41.82	0.00	41.82	0.00	10.32
55	42.56	0.00	42.57	0.00	10.14
56	43.43	0.01	43.43	0.00	7.28
57	44.03	0.01	44.04	0.00	8.10
58	45.04	0.01	45.06	0.00	7.72
59	45.59	0.01	45.54	0.00	13.22
60	46.40	0.01	46.39	0.00	10.88
61	47.22	0.00	47.22	0.00	9.77
62	48.06	0.00	48.06	0.00	11.95
63	48.84	0.00	48.84	0.00	12.21
64	49.63	0.00	49.62	0.00	12.38

Table A.2: Case I *ST01* scenario EMILIA output.

N°	MPV	σ^2 (MPV)	MEV	σ^2 (MEV)	Max. BPDF
1	0.50	0.01	0.52	0.00	9.04
2	1.48	0.05	1.71	0.00	18.80
3	1.91	0.01	1.81	0.00	20.48
4	2.84	0.01	2.84	0.00	9.00
5	3.59	0.00	3.58	0.00	10.33
6	4.47	0.00	4.49	0.00	20.43
7	5.11	0.07	5.17	0.01	5.55
8	5.79	0.03	5.67	0.00	15.02
9	6.41	0.11	6.58	0.00	7.44
10	7.45	0.02	7.51	0.00	9.25
11	8.33	0.00	8.33	0.00	12.07
12	9.37	0.00	9.38	0.00	20.48
13	9.38	0.00	9.38	0.00	20.48
14	10.47	0.01	10.45	0.00	5.57
15	11.47	0.03	11.41	0.01	4.80
16	12.28	0.01	12.28	0.00	9.11
17	12.53	0.01	12.52	0.00	8.79
18	13.40	0.01	13.43	0.01	4.97
19	14.45	0.01	14.52	0.00	7.04
20	14.29	0.53	14.79	0.05	1.67
21	14.58	1.04	15.16	0.05	1.69
22	16.81	0.01	16.83	0.00	12.29
23	17.53	0.00	17.54	0.00	10.02
24	18.44	0.00	18.44	0.00	7.40
25	19.04	0.00	19.04	0.00	6.79
26	19.95	0.00	19.95	0.00	6.14
27	20.90	0.04	20.81	0.01	5.78
28	23.23	1.30	22.40	0.05	2.02
29	23.50	1.16	22.56	0.02	2.74
30	23.56	0.33	23.36	0.02	2.59
31	24.49	0.08	24.44	0.02	3.34
32	24.93	0.00	24.92	0.00	7.49
33	25.12	0.00	25.12	0.00	7.19
34	25.64	0.03	25.71	0.02	3.18
35	26.35	0.16	26.56	0.03	2.46
36	27.71	0.12	28.01	0.00	5.74
37	27.99	0.13	28.19	0.00	6.51
38	29.10	0.02	29.17	0.01	5.35
39	30.07	0.00	30.07	0.00	7.21
40	30.96	0.00	30.96	0.00	8.47
41	31.56	0.00	31.55	0.00	8.07
42	32.41	0.00	32.41	0.00	10.34
43	33.22	0.00	33.22	0.00	10.96
44	34.14	0.01	34.16	0.00	10.37
45	34.56	0.01	34.54	0.00	10.59
46	35.59	0.01	35.56	0.00	6.88
47	36.44	0.01	36.44	0.01	5.04
48	37.35	0.00	37.33	0.00	7.45
49	37.67	0.00	37.67	0.00	7.36
50	38.41	0.00	38.42	0.01	4.22
51	39.39	0.00	39.40	0.01	5.41
52	40.32	0.01	40.34	0.00	8.66
53	40.93	0.01	40.92	0.00	8.79
54	41.80	0.00	41.81	0.00	11.53
55	42.57	0.00	42.57	0.00	9.70
56	43.44	0.00	43.43	0.00	7.99
57	44.01	0.01	44.03	0.00	7.53
58	44.94	0.00	44.93	0.00	11.04
59	45.69	0.00	45.69	0.00	12.23
60	46.62	0.01	46.66	0.00	10.27
61	47.12	0.01	47.14	0.00	9.78
62	48.05	0.00	48.04	0.00	12.40
63	48.83	0.00	48.82	0.00	11.57
64	49.60	0.00	49.60	0.00	13.49

Table A.3: Case I *ST02* scenario EMILIA output.

N°	MPV	σ^2 (MPV)	MEV	σ^2 (MEV)	Max. BPDF
1	0.51	0.01	0.52	0.00	10.14
2	1.50	0.04	1.71	0.00	20.48
3	1.84	0.02	1.71	0.00	20.48
4	2.85	0.00	2.85	0.00	10.18
5	3.66	0.00	3.65	0.00	12.51
6	4.20	0.00	4.20	0.00	20.48
7	5.30	0.02	5.31	0.00	6.85
8	5.76	0.02	5.63	0.00	14.00
9	6.39	0.12	6.60	0.01	7.32
10	7.51	0.01	7.51	0.00	8.34
11	8.34	0.00	8.33	0.00	13.51
12	9.36	0.00	9.36	0.00	14.03
13	9.47	0.00	9.47	0.00	15.71
14	10.43	0.00	10.42	0.00	8.22
15	11.43	0.03	11.40	0.00	6.43
16	12.11	0.02	12.02	0.00	8.39
17	12.44	0.07	12.46	0.01	4.31
18	13.09	0.11	13.26	0.02	2.64
19	14.19	0.02	14.30	0.01	4.73
20	14.29	0.80	14.78	0.04	2.02
21	14.96	0.62	15.27	0.03	2.54
22	16.83	0.00	16.83	0.00	11.47
23	17.60	0.01	17.58	0.00	10.00
24	18.57	0.02	18.54	0.00	8.01
25	19.04	0.01	19.05	0.00	8.80
26	19.89	0.01	19.88	0.00	7.85
27	20.80	0.07	20.71	0.01	5.72
28	22.43	1.27	21.93	0.05	1.82
29	24.11	1.59	23.98	0.22	0.85
30	24.24	1.17	23.97	0.06	1.61
31	24.70	0.07	24.71	0.02	2.68
32	25.01	0.00	24.99	0.00	6.22
33	25.17	0.00	25.18	0.00	8.18
34	25.86	0.01	25.89	0.01	4.16
35	27.14	0.00	27.15	0.00	13.53
36	27.75	0.00	27.76	0.00	6.65
37	28.32	0.00	28.34	0.00	6.72
38	29.13	0.00	29.16	0.01	5.93
39	29.99	0.01	30.02	0.01	5.58
40	30.91	0.00	30.93	0.00	6.60
41	31.53	0.00	31.53	0.00	7.43
42	32.43	0.00	32.43	0.00	9.96
43	33.17	0.00	33.18	0.00	10.46
44	34.01	0.00	34.01	0.00	10.01
45	34.74	0.00	34.74	0.00	9.43
46	35.60	0.00	35.60	0.00	7.49
47	36.52	0.00	36.51	0.00	7.32
48	37.31	0.00	37.32	0.00	6.75
49	37.67	0.00	37.67	0.00	7.48
50	38.46	0.00	38.46	0.01	4.57
51	39.39	0.00	39.39	0.00	6.21
52	40.24	0.00	40.24	0.00	9.06
53	41.00	0.00	40.99	0.00	9.56
54	41.80	0.00	41.80	0.00	12.62
55	42.59	0.00	42.59	0.00	8.81
56	43.45	0.00	43.45	0.00	9.33
57	44.03	0.00	44.03	0.00	8.91
58	44.95	0.00	44.94	0.00	9.57
59	45.70	0.00	45.70	0.00	14.51
60	46.50	0.00	46.50	0.00	10.96
61	47.21	0.00	47.22	0.00	11.00
62	48.05	0.00	48.06	0.00	12.88
63	48.81	0.00	48.82	0.00	13.05
64	49.61	0.00	49.61	0.00	14.42

Table A.4: Case I *ST00+ST01+ST02* mixed scenario EMILIA output.

N°	MPV	σ^2 (MPV)	MEV	σ^2 (MEV)	Max. BPDF
1	0.49	0.01	0.50	0.00	10.11
2	1.49	0.05	1.71	0.00	20.48
3	1.91	0.01	1.86	0.00	20.32
4	2.82	0.01	2.83	0.00	10.32
5	3.62	0.00	3.62	0.00	12.45
6	4.20	0.00	4.20	0.00	20.44
7	5.07	0.03	4.95	0.00	11.47
8	5.77	0.02	5.64	0.00	10.61
9	6.38	0.14	6.57	0.00	5.63
10	7.48	0.01	7.51	0.00	8.39
11	8.33	0.00	8.33	0.00	11.77
12	9.35	0.01	9.37	0.00	20.46
13	9.38	0.00	9.38	0.00	20.48
14	10.46	0.00	10.45	0.00	7.88
15	11.43	0.02	11.41	0.01	5.70
16	12.21	0.03	12.26	0.00	7.42
17	12.57	0.01	12.59	0.00	7.29
18	13.37	0.03	13.44	0.01	4.19
19	14.38	0.01	14.44	0.01	5.79
20	14.50	0.46	15.03	0.02	2.92
21	14.80	0.96	15.23	0.05	1.83
22	16.83	0.00	16.82	0.00	9.09
23	17.55	0.00	17.55	0.00	9.24
24	18.45	0.00	18.44	0.00	7.20
25	19.03	0.00	19.04	0.00	7.70
26	19.94	0.01	19.93	0.00	6.73
27	20.78	0.03	20.75	0.01	5.25
28	22.25	1.19	21.89	0.03	2.38
29	23.39	1.71	22.77	0.09	1.47
30	24.07	1.87	23.52	0.04	2.00
31	24.53	0.06	24.49	0.02	2.89
32	24.95	0.00	24.95	0.00	7.83
33	25.14	0.00	25.13	0.00	7.94
34	25.75	0.02	25.79	0.01	3.40
35	27.22	0.00	27.24	0.00	13.29
36	27.69	0.06	27.76	0.02	4.87
37	28.25	0.00	28.27	0.01	5.72
38	29.17	0.00	29.18	0.01	5.68
39	30.07	0.00	30.06	0.00	6.51
40	30.94	0.00	30.95	0.00	7.73
41	31.54	0.00	31.54	0.00	7.72
42	32.41	0.00	32.42	0.00	10.28
43	33.18	0.00	33.19	0.00	10.56
44	34.06	0.00	34.05	0.00	8.65
45	34.65	0.01	34.70	0.00	6.65
46	35.58	0.00	35.57	0.00	7.20
47	36.39	0.00	36.36	0.00	13.31
48	37.29	0.00	37.30	0.00	6.16
49	37.66	0.00	37.66	0.00	7.27
50	38.47	0.01	38.47	0.01	4.18
51	39.39	0.00	39.38	0.01	5.45
52	40.31	0.01	40.29	0.00	7.68
53	40.94	0.01	40.93	0.00	7.46
54	41.81	0.00	41.81	0.00	12.29
55	42.57	0.00	42.58	0.00	9.91
56	43.43	0.00	43.44	0.00	8.15
57	44.03	0.00	44.03	0.00	7.96
58	44.95	0.00	44.95	0.00	8.21
59	45.69	0.00	45.69	0.00	10.70
60	46.51	0.01	46.49	0.00	8.90
61	47.19	0.00	47.19	0.00	9.10
62	48.05	0.00	48.05	0.00	13.29
63	48.82	0.00	48.83	0.00	12.99
64	49.62	0.00	49.61	0.00	13.53

A.3: Case I six-level MODWPT decomposition time-dependent probability spectrum and Hilbert spectrogram for different stiffness scenarios

ST00 scenario

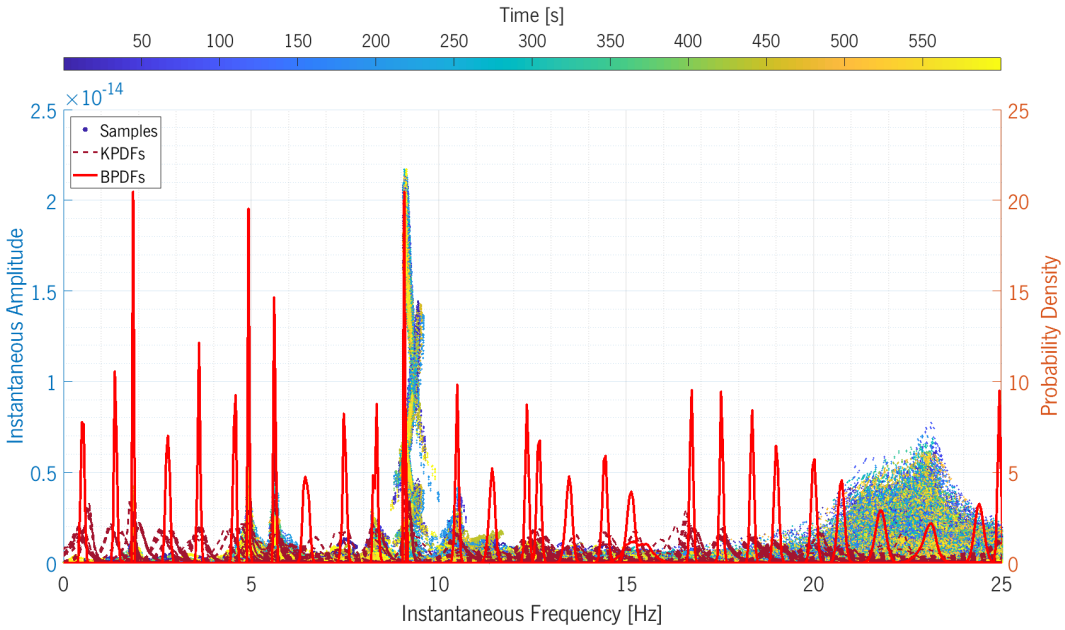


Figure A.1: Case I *ST00* scenario time-dependent probability spectrum.

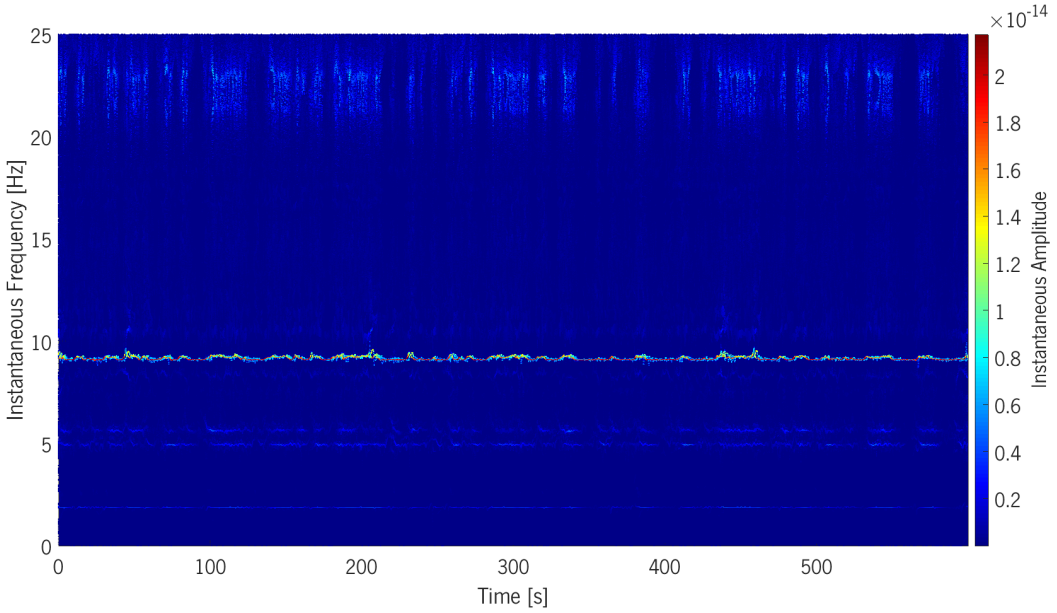


Figure A.2: Case I *ST00* scenario Hilbert spectrogram.

ST01 scenario

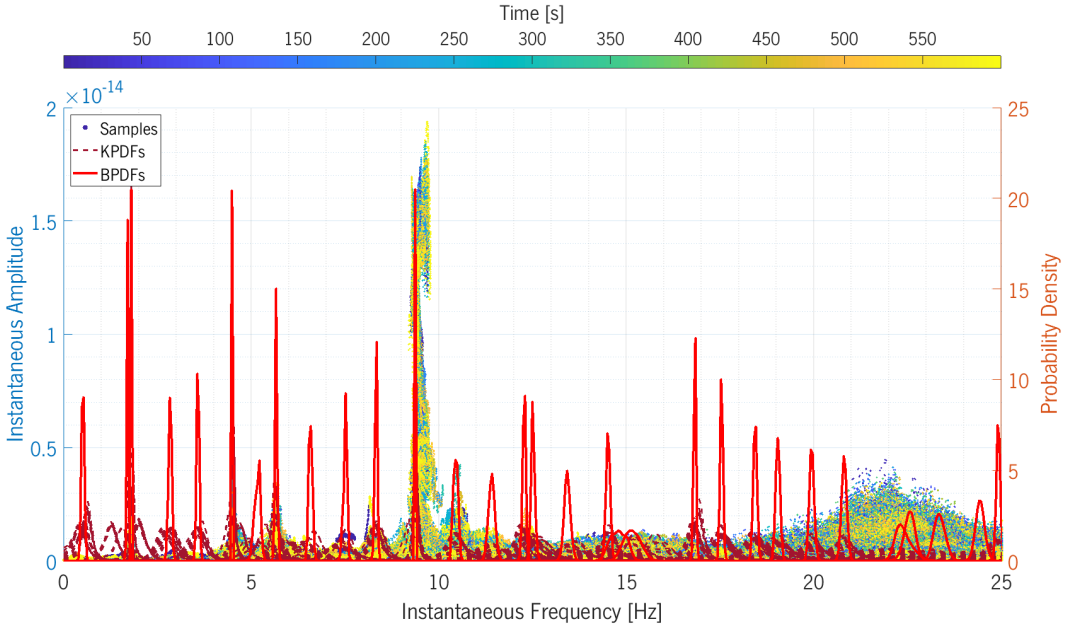


Figure A.3 : Case I *ST01* scenario time-dependent probability spectrum.

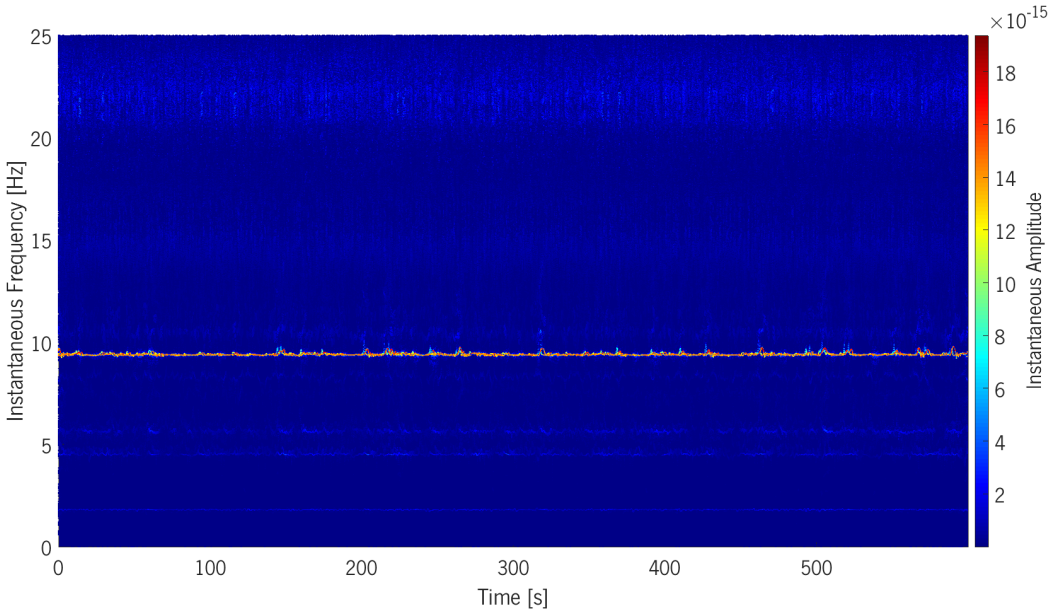


Figure A.4: Case I *ST01* scenario Hilbert spectrogram.

ST02 scenario

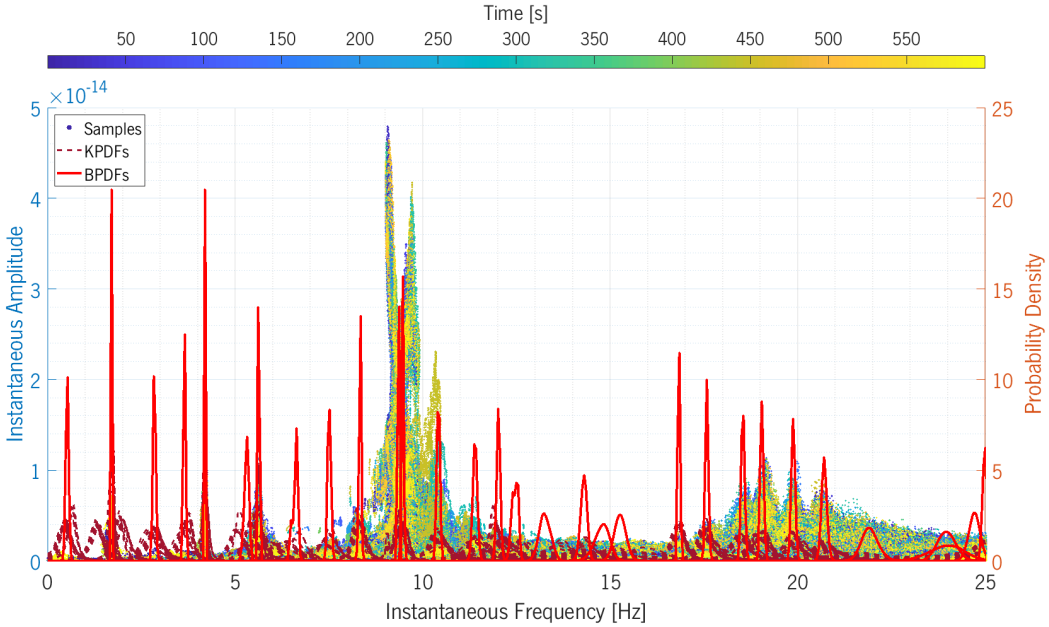


Figure A.5 : Case I *ST02* scenario time-dependent probability spectrum.

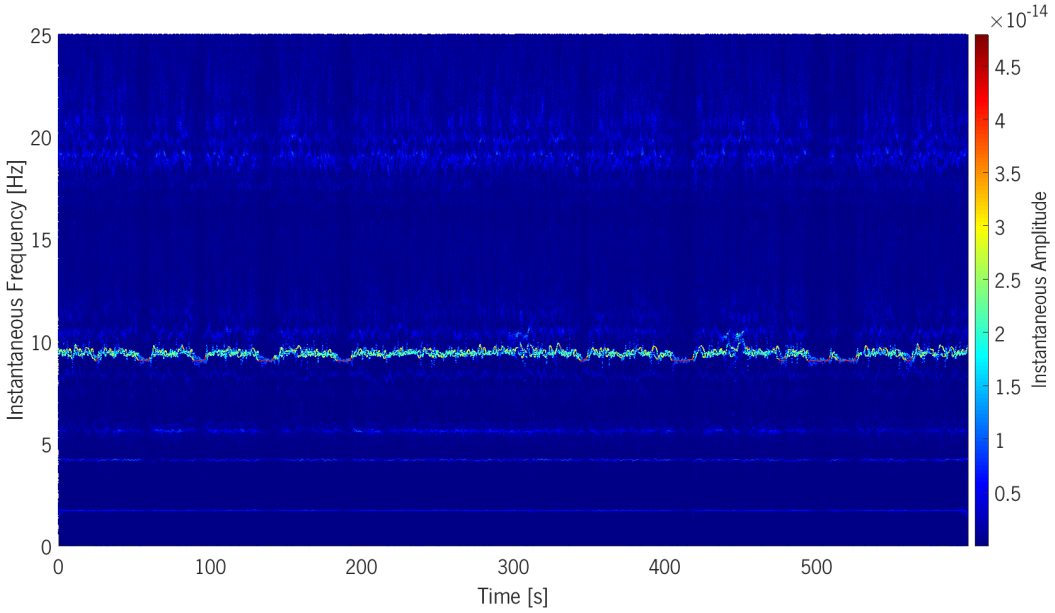


Figure A.6: Case I *ST02* scenario Hilbert spectrogram.

ST00+ST01+ST02 mixed scenario

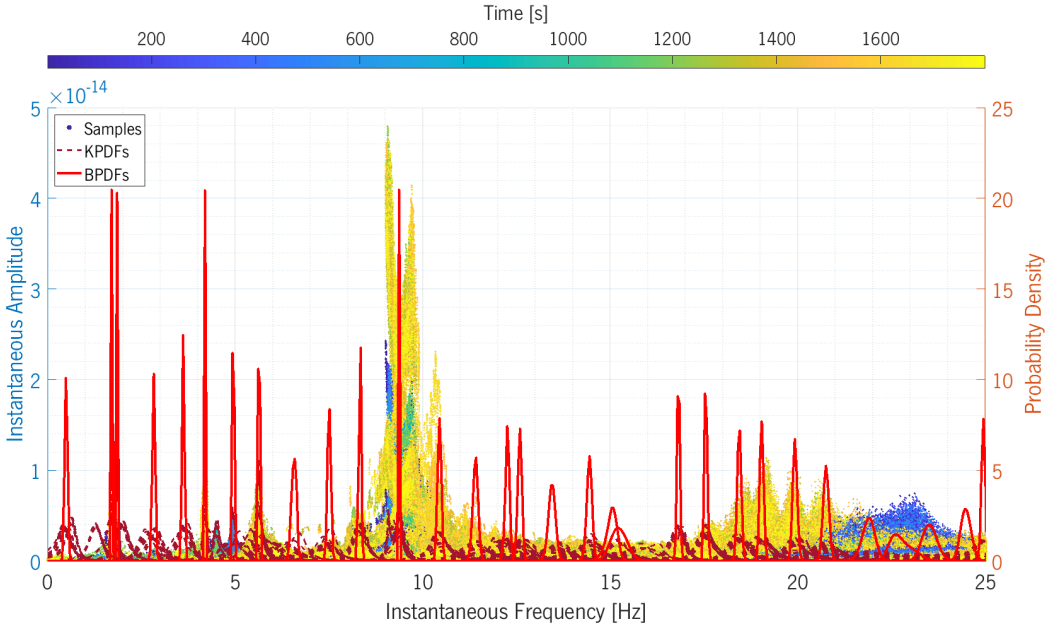


Figure A.7 : Case I *ST00+ST01+ST02* mixed scenario time-dependent probability spectrum.

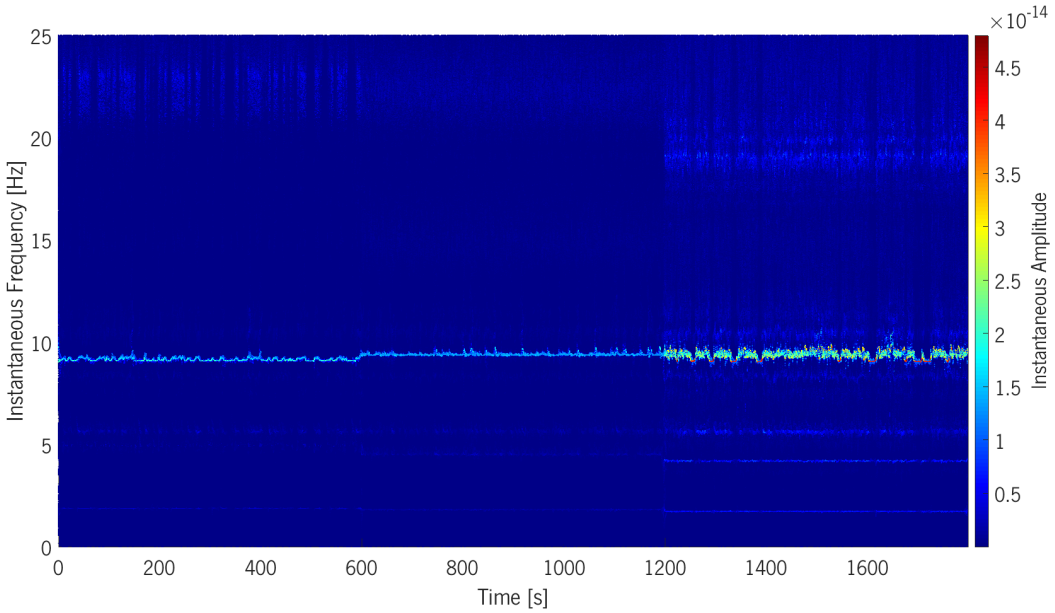


Figure A.8: Case I *ST00+ST01+ST02* mixed scenario six-level Hilbert spectrogram.

A.4: Case I ST00 scenario four-level MODWPT decomposition time-dependent probability spectrum and Hilbert spectrogram (from Table 4.7)

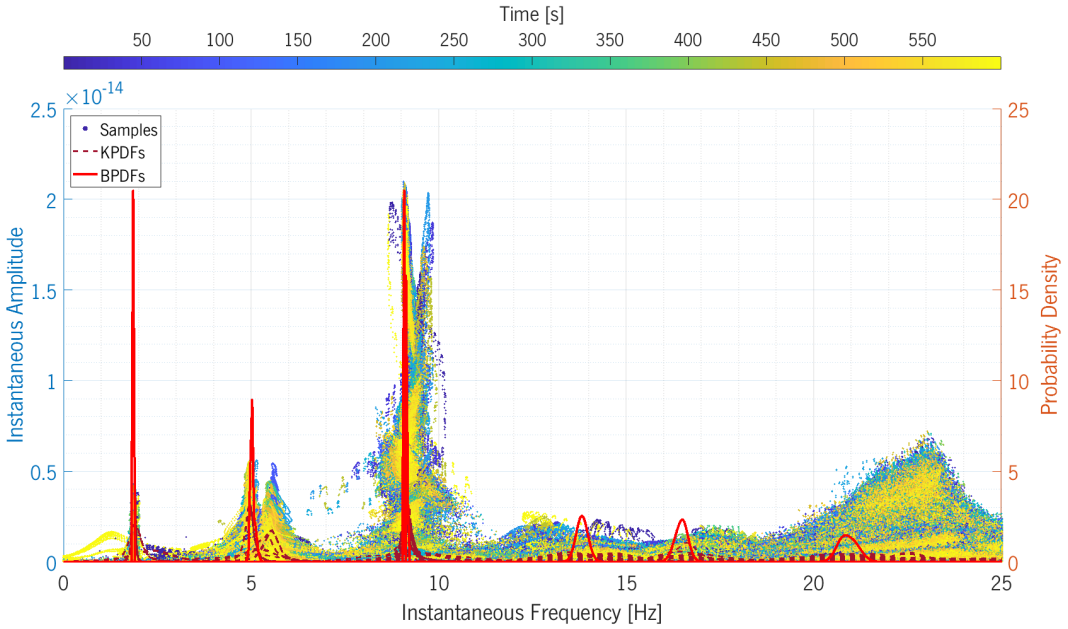


Figure A.9 : Case I *ST00* scenario four-level decomposition time-dependent probability spectrum.

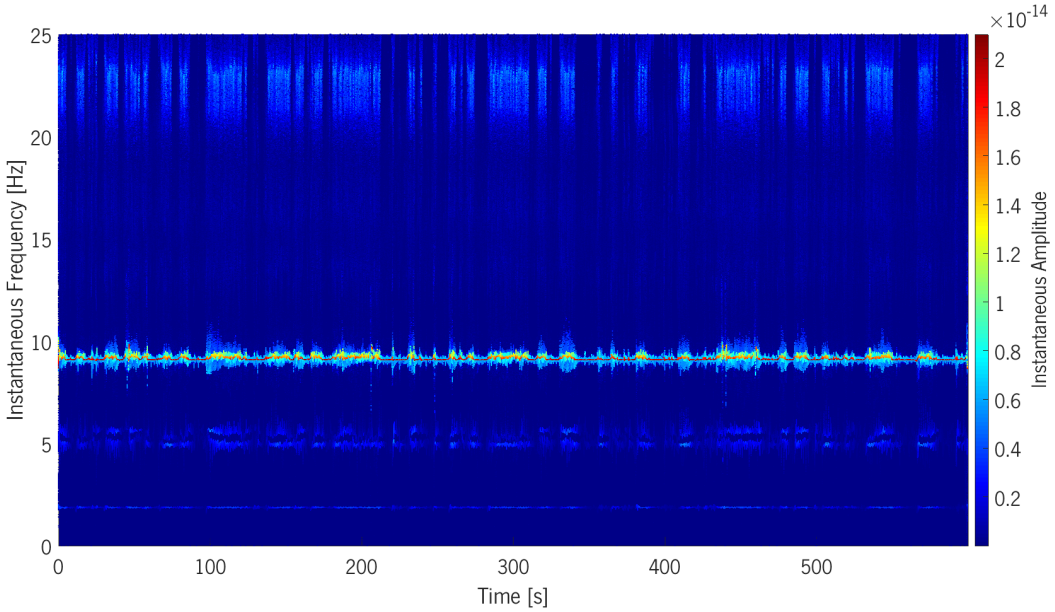


Figure A.10: Case I *ST00* scenario four-level Hilbert spectrogram.

A.5: Case I ST00 scenario two-level MODWPT decomposition time-dependent probability spectrum and Hilbert spectrogram (from Table 4.8)

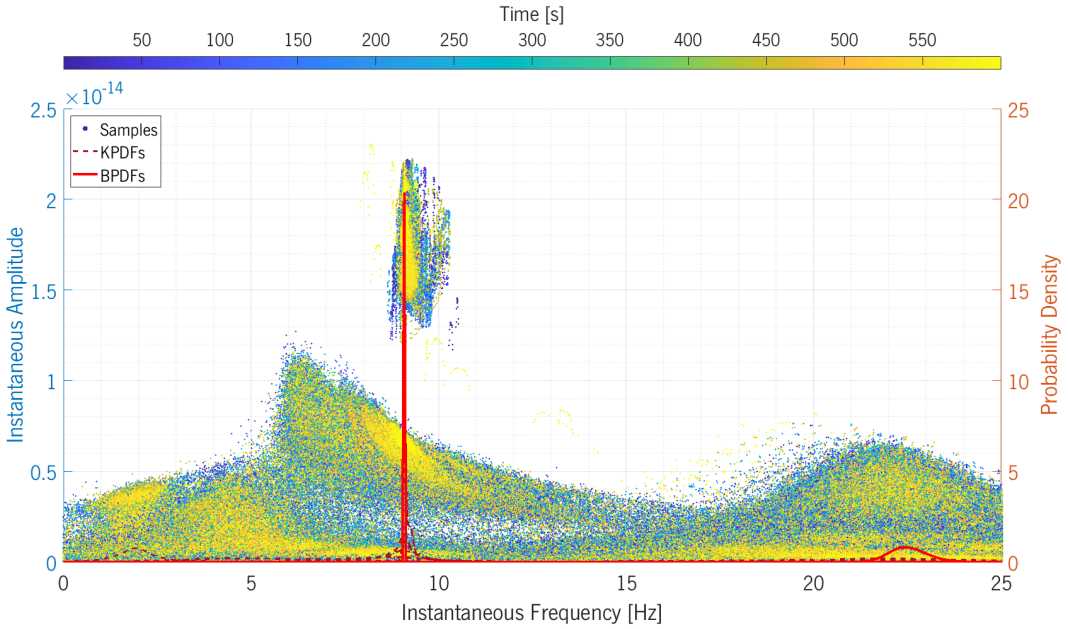


Figure A.11 : Case I *ST00* scenario two-level decomposition time-dependent probability spectrum.

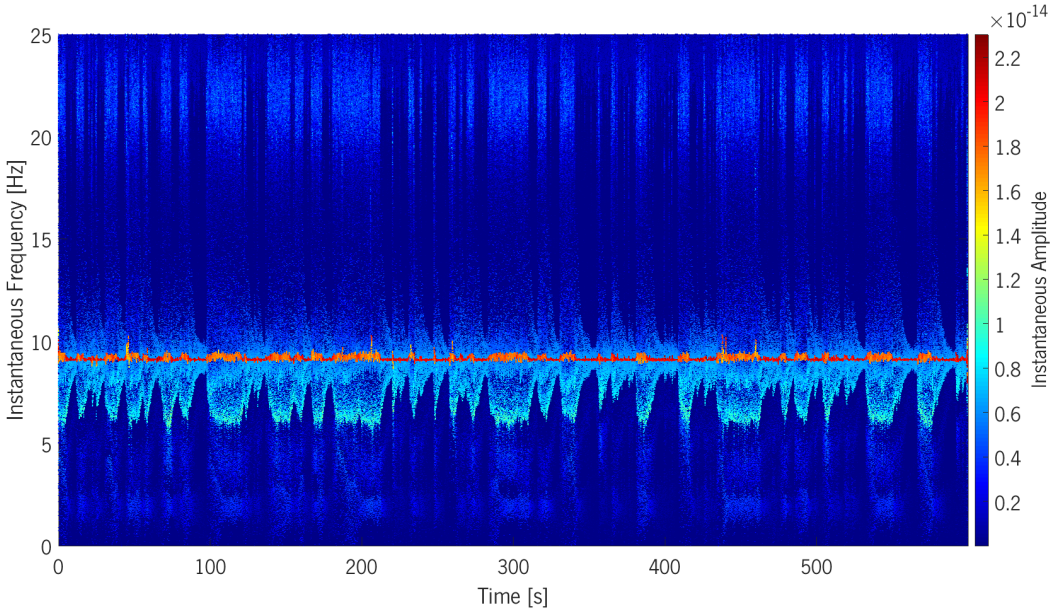


Figure A.12: Case I *ST00* scenario two-level Hilbert spectrogram.